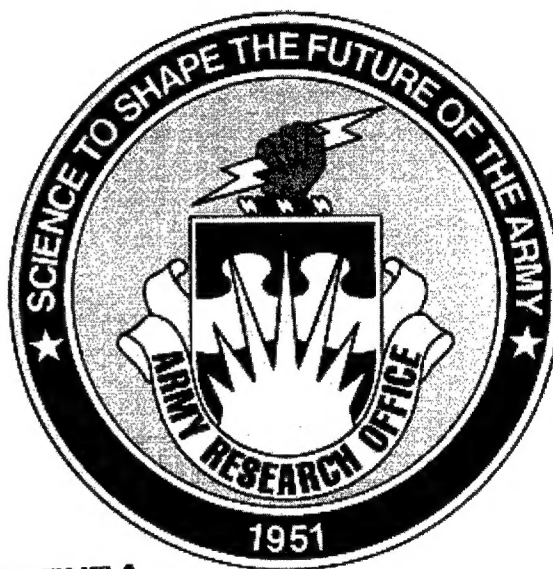


# **ARMY RESEARCH OFFICE AND AIR FORCE OFFICE OF SCIENTIFIC RESEARCH**



**DISTRIBUTION STATEMENT A**  
Approved for Public Release  
Distribution Unlimited

## **2003 CONTRACTORS MEETING IN CHEMICAL PROPULSION**

**20030923 165**

# REPORT DOCUMENTATION PAGE

AFRL-SR-AR-TR-03-

0348

data needed, and completing and reviewing this collection of information. Send comments regarding this burden estimate or any other this burden to Department of Defense, Washington Headquarters Services, Directorate for Information Operations and Reports (0704-4302). Respondents should be aware that notwithstanding any other provision of law, no person shall be subject to any penalty for failing to furnish information if it does not have a valid OMB control number. PLEASE DO NOT RETURN YOUR FORM TO THE ABOVE ADDRESS.

the  
ng  
antly

1. REPORT DATE (DD-MM-YYYY) 08-07-2003		2. REPORT TYPE Technical		3. DATES COVERED (From - To) 01-06-2002 - 31-05-2003	
4. TITLE AND SUBTITLE (U) Army Research Office and Air Force Office of Scientific Research 2003 Contractors Meeting in Chemical Propulsion				5a. CONTRACT NUMBER	
				5b. GRANT NUMBER	
				5c. PROGRAM ELEMENT NUMBER 61102A, 61102F	
				5d. PROJECT NUMBER	
6. AUTHOR(S)  David M. Mann and Julian M. Tishkoff				5e. TASK NUMBER	
				5f. WORK UNIT NUMBER	
				8. PERFORMING ORGANIZATION REPORT NUMBER	
7. PERFORMING ORGANIZATION NAME(S) AND ADDRESS(ES)  Army Research Office                      Air Force Office of Scientific Research Research Triangle Park NC              Research 27709-2211                                  Arlington VA 22203-1954				10. SPONSOR/MONITOR'S ACRONYM(S)	
9. SPONSORING / MONITORING AGENCY NAME(S) AND ADDRESS(ES) AFOSR/NA 4015 Wilson Boulevard Room 713 Arlington VA 22203-1954				11. SPONSOR/MONITOR'S REPORT NUMBER(S)	
12. DISTRIBUTION / AVAILABILITY STATEMENT  Approved for public release; distribution is unlimited					
13. SUPPLEMENTARY NOTES					
14. ABSTRACT  Abstracts are given for 6.1 basic research in chemical propulsion sponsored by the Army Research Office and the Air Force Office of Scientific Research.					
15. SUBJECT TERMS Flames, Propulsion, Gas Turbines, Diesel Engines, Scramjets, Pulse Detonation Engines, Hydrocarbon Fuels, Diagnostics, Spray, Droplet, Turbulence, Combustion, Simulation					
16. SECURITY CLASSIFICATION OF:			17. LIMITATION OF ABSTRACT	18. NUMBER OF PAGES	19a. NAME OF RESPONSIBLE PERSON
a. REPORT	b. ABSTRACT	c. THIS PAGE			Julian M. Tishkoff
Unclassified	Unclassified	Unclassified	UL	189	19b. TELEPHONE NUMBER (include area code) (703) 696-8478

**ARO/AFOSR Contractors' Meeting in Chemical Propulsion**  
**TABLE OF CONTENTS**

Agenda .....	1
AFOSR Sponsored Research in Combustion and Diagnostics	
<i>J.M. Tishkoff, AFOSR/NA</i> .....	5
The Army Research Office Program in Propulsion and Energetics	
<i>D.M. Mann, ARO/Mechanical &amp; Environmental Sciences Division</i> .....	9
Acoustic Sensing and Actuation in Gaseous Flows	
<i>T. Lieuwen, Georgia Institute of Technology</i> .....	11
Chemical Kinetics and Aerodynamics of Ignition	
<i>C.K. Law, Princeton University</i> .....	15
Physical and Chemical Process in Flames	
<i>C.K. Law, Princeton University</i> .....	19
Experimental and Computational Characterization of Combustion Phenomena	
<i>J.R. Gord, AFRL/PRTS</i> .....	23
Transient Engine Behavior and Control	
<i>P.V. Farrell and D. Foster, University of Wisconsin-Madison</i> .....	27
Adaptation of Advanced Diesel Engines for Military Requirements Under Severe Environmental Conditions	
<i>N.A. Henein, Wayne State University</i> .....	31
Thermal Ignition Theory Applied to Diesel Autoignition	
<i>A.M. Mellor, S.L. Plee and R.J. Tabaczynski</i> <i>Vanderbilt University</i> .....	35
Study of In-Cylinder Reactions of High Power-Density Direct Injection Diesel Engines	
<i>K.T. Rhee, Rutgers University</i> .....	39
Development of Linear Engine/Alternator	
<i>P. Famouri and N. Clark, West Virginia University</i> .....	43
Porous Media Combustion Concepts for Propulsion Gas Turbines	
<i>A.K. Agrawal and S.R. Gollahalli, University of Oklahoma</i> .....	47
Concurrent Research on High Gravity (g) Combustion with Enabling Materials	
<i>J. Zelina, AFRL/PRTS</i> .....	53
Pulse Detonation Physiochemical and Exhaust Relaxation Processes	
<i>F. Schauer, AFRL/PRTS</i> .....	57
Measurement of Electrospray Droplet's Charge and Radius Distributions with Quadrupole Mass Spectrometer (Oral Presentation: Establishment of an Electrostatic Atomization Theory and Experiment Program at Prairie View A&M University)	
<i>T-S. Huang, Prairie View A&amp;M University</i> .....	61

Ballistic Imaging in the Primary Breakup Region of Diesel Injector Sprays <i>M. Linne and T. Parker, Colorado School of Mines</i> .....	63
Modeling the Primary Breakup of High Speed Liquid Jets <i>P.V. Farrell and R.D. Reitz, University of Wisconsin-Madison</i> .....	67
PDF Modeling of Turbulent Combustion <i>S.B. Pope, Cornell University</i> .....	71
Filtered Mass Density Function for Subgrid Scale Modeling of Turbulent Diffusion Flames <i>P. Givi, University of Pittsburgh</i> .....	75
Large-Eddy Simulation of Turbulent Combustion <i>H. Pitsch, Stanford University</i> .....	79
A New Class of Hybrid Schemes Based on Large Eddy Simulation and Low-Dimensional Stochastic Models <i>T. Echekki, North Carolina State University</i> .....	83
Towards LES of Turbulent Combustion Using Lattice Boltzmann Method <i>S.S. Girimaji, Texas A&amp;M University and L-S. Luo, National Institute of Aerospace</i> .....	87
Experimental Study of Velocity-Scalar Filtered Joint Density Function and Its Transport Equation <i>C. Tong, Clemson University</i> .....	91
Statistical Interpretation of Scalar Time-Series Measurements in Turbulent Partially Premixed Flames <i>N.M. Laurendeau, G.B. King, and M.W. Renfro, Purdue University</i> .....	95
Ramjet Research <i>C.D. Carter and M.R. Gruber, AFRL/PRA</i> .....	101
Mixing, Chemical Reactions, and Combustion in High-Speed Turbulent Flows <i>P.E. Dimotakis, California Institute of Technology</i> .....	105
<b>Abstracts of Work Units Not Presented at the Meeting</b>	
The Low Temperature Oxidation Chemistry of JP-8 and Its Surrogates at High Pressure <i>N.P. Cernansky and D.L. Miller, Drexel University</i> .....	111
Advanced Supercritical Fuels <i>T. Edwards, C. Bunker, and T. Jackson, AFRL/PRTG</i> .....	115
Experimental and Detailed Numerical Studies of Fundamental Flame Properties of Gaseous And Liquid Fuels <i>F.N. Egolfopoulos, University of Southern California</i> .....	119
Drop/Gas Interactions of Dense Sprays <i>G.M. Faeth, The University of Michigan</i> .....	123
Advanced Stimulated Scattering Measurements in Supercritical Fluids <i>G.W. Faris, SRI International</i> .....	127



Plasma Research for Aerospace Propulsion <i>B.N. Ganguly, AFRL</i> .....	131
Sub- and Super-Critical Evaporation and Combustion of a Moving Droplet <i>G. Gogos, University of Nebraska-Lincoln</i> .....	135
Shock Tube Measurements of Ignition Processes in Diesel-Related Fuels <i>R.K. Hanson, Stanford University</i> .....	139
Advanced Diagnostics for Reacting Flows <i>R.K. Hanson, Stanford University</i> .....	143
Planar Image Particle Analyzer for Whole Field Spray Applications <i>C. Hess and R. Nesbitt, MetroLaser, Inc.</i> .....	147
Stabilization and Blowout of Gaseous- and Spray-Jet Flames <i>K.M. Lyons, North Carolina State University</i> .....	151
Autoignition and Burning Speeds of JP-8 Fuel at High Temperatures and Pressures <i>M. Metghalchi, Northeastern University</i> .....	155
Soot Morphology in Unsteady Counterflow Diffusion Flames <i>W. Roberts, North Carolina State University</i> .....	159
Chemical-Kinetic Characterization of Autoignition and Combustion of Diesel and JP-8 <i>K. Seshadri, University of California, San Diego</i> .....	163
Development and Optimization of a Comprehensive Kinetic Model of Hydrocarbon Fuel Combustion <i>H. Wang, University of Delaware</i> .....	167
Invitees .....	171



# **ARO/AFOSR CONTRACTORS MEETING**

**IN**

## **CHEMICAL PROPULSION**

**Colonial Williamsburg Hotel-Woodlands**

**Williamsburg VA**

**23-25 June 2003**

### **MONDAY, 23 JUNE**

1:30 - 1:45      AFOSR Combustion and Diagnostics Program – Julian Tishkoff

1:45 - 2:00      Army Research Office Overview - David Mann

Topic: Combustion Physicochemical Processes

2:00 - 2:30      Time-Resolved Measurements and Reactive Pathways for  
Hypergolic Bipropellant Combustion  
James Smith, University of Alabama-Huntsville

2:30 - 3:00      Development of Acoustic-Based, "Multi-Tasking" Sensing and  
Actuation Capabilities for Gas Turbine Combustors  
Tim Lieuwen, Georgia Institute of Technology

3:00 - 3:30      BREAK

3:30 - 4:00      Turbulence and Chemical Kinetics in Ignition  
C. K. Law, Princeton University

4:00 - 4:30      Physical and Chemical Processes in Flames  
C. K. Law, Princeton University

4:30 - 5:00      Experimental and Computational Characterization of Combustion  
Phenomena  
James Gord, AFRL/PRTS

5:00 - 7:30      DINNER

7:30 - 9:30      EVENING PANEL DISCUSSION – Working with the U.S.  
Government

Paul Dimotakis, California Institute of Technology  
Gerard M. Faeth University of Michigan  
C.K. Law, Princeton University  
Phil Myers, University of Wisconsin

## **TUESDAY, 24 JUNE**

8:15 - 8:30      Announcements

### TOPIC: Propulsion Concepts

8:30 - 9:00      Transient Engine Behavior and Control  
Patrick Farrell, University of Wisconsin-Madison

9:00 - 9:30      Adaption of Advanced Diesel Engines for Military Requirements  
Under Severe Environmental Conditions  
Naeim Henein, Wayne State University

9:30 - 10:00     DI Diesel Performance and Emission Models  
A. M. Mellor, Vanderbilt University

10:00 - 10:30    BREAK

10:30 - 11:00    Study of In-Cylinder Reactions of High Power-Density Direct  
Injection Diesel Engines  
Kyung Rhee, Rutgers, The State University of New Jersey

11:00 - 11:30    Frequency Effects and Power Density of Linear Alternator/Engine  
Systems  
Parviz Famouri, West Virginia University

11:30 - 12:00    Porous Media Combustor Concepts for Propulsion Gas Turbines  
Ajay Agrawal, University of Oklahoma

12:00 - 1:30     LUNCH

1:30 - 2:00      Concurrent Research on High Gravity (g) Combustion and Enabling  
Materials  
Joseph Zelina, AFRL/PRTS

2:00 - 2:30      Pulse Detonation Physicochemical and Exhaust Relaxation  
Processes  
Fred Schauer, AFRL/PRTS

2:30 - 3:00      BREAK

### TOPIC: Atomization and Sprays

3:00 - 3:30      Establishment of an Electrostatic Atomization Theory and  
Experiment Program at Prairie View A&M University  
Tian-Sen Huang, Prairie View A&M University

3:30 - 4:00      Ballistic Imaging in the Primary Breakup Region of Diesel

Injector Sprays  
Mark Linne, Colorado School of Mines

4:00 - 4:30      Modeling the Primary Breakup of High Speed Liquid Jets  
Patrick Farrell, University of Wisconsin-Madison

4:30 - 7:30      DINNER

7:30 - 9:30      EVENING DISCUSSION – Microcombustion Research

Jeff Jagoda, Georgia Institute of Technology  
Ian Waitz, Massachusetts Institute of Technology

## WEDNESDAY, 25 JUNE

8:15 - 8:30      Announcements

TOPIC: Combustion Modeling and Simulation

8:30 - 9:00      PDF Modeling of Turbulent Combustion  
Steve Pope, Cornell University

9:00 - 9:30      Filtered Mass Density Function for Subgrid Scale Modeling of  
Turbulent Diffusion Flames  
Peyman Givi, University of Pittsburgh

9:30 - 10:00      Large-Eddy Simulation of Turbulent Combustion  
Heinz Pitsch, Stanford University

10:00 – 10:30      A New Class of Hybrid Schemes Based on Large-Eddy  
Simulations and Low-Dimensional Stochastic Models  
Tarek Echekki, North Carolina State University

10:30 – 11:00      BREAK

11:00 – 11:30      Large Eddy Simulation of the Lattice Boltzman Equation for  
Turbulent Combustion  
Sharath Girimaji, Texas A&M University

11:30 – 12:00      Experimental Study of Velocity-Conserved Scalar Filtered  
Joint Density Function for Improving Large Eddy Simulation  
Of Turbulent Combustion  
Chenning Tong, Clemson University

12:00 – 12:30      Statistical Interpretation of Scalar Time-Series Measurements  
in Turbulent Partially Premixed Flames  
Normand Laurendeau, Purdue University

12:30 - 1:30        LUNCH

TOPIC: Supersonic Combustion

1:30 - 2:00        Ramjet Research  
Campbell Carter, AFRL/PRA

2:00 - 2:45        Mixing, Chemical Reactions, and Combustion in High-Speed  
Turbulent Flows  
Paul Dimotakis, California Institute of Technology

2:45 - 3:15        ARO BUSINESS SESSION – Contractors/Grantees in Dr. Mann's  
Program

3:15 - 3:45        AFOSR BUSINESS SESSION – Contractors/Grantees in Dr.  
Tishkoff's Program

3:45                ADJOURN

## **AFOSR SPONSORED RESEARCH IN COMBUSTION AND DIAGNOSTICS**

**PROGRAM MANAGER: JULIAN M. TISHKOFF**

**AFOSR/NA  
4015 Wilson Boulevard, Room 713  
Arlington VA 22203-1954**

**SUMMARY/OVERVIEW:** The Air Force Office of Scientific Research (AFOSR) program in combustion and diagnostics currently is focused on five areas of study: high-speed propulsion, turbulent combustion, diagnostics, supercritical fuel behavior, and plasma-enhanced combustion. An assessment of major research needs in each of these areas is presented.

### **TECHNICAL DISCUSSION**

AFOSR is the single manager for Air Force basic research, including efforts based on external proposals and in-house work at the Air Force Research Laboratory (AFRL). Combustion and Diagnostics is assigned to the AFOSR Directorate of Aerospace and Materials Sciences along with programs in rocket and space propulsion, fluid and solid mechanics, and structural materials.

Interests of the AFOSR Combustion and Diagnostics subarea are given in the SUMMARY section above. Many achievements can be cited for these interests, yet imposing fundamental research challenges remain. The objective of the program is publications in the refereed scientific literature describing significant new understanding of multiphase turbulent reacting flow. Incremental improvements to existing scientific approaches, hardware development, and computer codes fall outside the scope of this objective.

The Combustion and Diagnostics subarea supports the Air Force commitment to aerospace propulsion through the Department of Defense National Aerospace Initiative (NAI). Accordingly, the research in this subarea will address research issues related to chemical propulsion for all Air Force aerospace missions, including combined cycle propulsion for access to space. This program will complement related research activities in space propulsion and energetic materials.



The primary focus of research in turbulent combustion is the creation of computational modeling tools for combustor designers that are both computationally tractable and quantitatively predictive. This research has been directed in two areas: the formulation of augmented reduced chemical kinetic mechanisms for the combustion of hydrocarbon fuels and the development of subgrid-scale models for large eddy simulation of turbulent combustion.

Future airbreathing and chemical rocket propulsion systems will require propellants to absorb substantial thermal energy, raising their temperatures to supercritical thermodynamic conditions. Understanding and controlling fluid properties at these conditions will be crucial for avoiding thermal degradation and for optimizing subsequent processes within the combustor. Research has focused on the role of supercritical transport in the thermal destabilization of hydrocarbon fuel prior to combustion and on primary and secondary fuel breakup under transcritical and supercritical conditions.

Plasma research is one of six AFOSR Theme topics selected for support beginning in Fiscal Year 2001. The focus primarily is on the utilization of plasmas for ignition and flame stabilization in scramjets; however, the extension of this technology to other modes of chemical propulsion and energy conversion also is of interest. The theme research has been supplemented by research coordinated between universities and small businesses under the Department of Defense Small Business Technology Transfer (STTR) Program. The Air Force also supports related research activity in Russia under the Air Force Research Laboratory International Research Initiative. The Theme and Russian research activity was presented as part of a Weakly Ionized Gas Dynamics (WIG) Workshop at the 31<sup>st</sup> AIAA Aerospace Sciences Meeting and Exhibit in January 2003. The next workshop will take place in January 2004.

Decisions on support for research proposals are based on scientific opportunities and technology needs. Researchers interested in submitting proposals should contact Dr. Tishkoff for information on time constraints associated with proposal evaluations. Further information on research interests and proposal preparation can be found on the AFOSR web site, <http://www.afosr.af.mil>. The availability of funds places a major constraint on program redirection and growth. Figure 1 shows the recent trend of funding for basic research in combustion and diagnostics from Air Force and DOD sources. Informal inquiries for new research are encouraged throughout the year. Formal proposals should be submitted by 1 April for peer review by the National Research Council.

The purpose of this abstract has been to communicate AFOSR perceptions of research trends to the university and industrial research communities. However, communication from those communities back to AFOSR also is desirable and essential for creating new

research opportunities. Therefore, all proposals and inquiries for fundamental research are encouraged even if the content does not fall within the areas of emphasis described herein. Comments and criticisms of current AFOSR programs also are welcome.

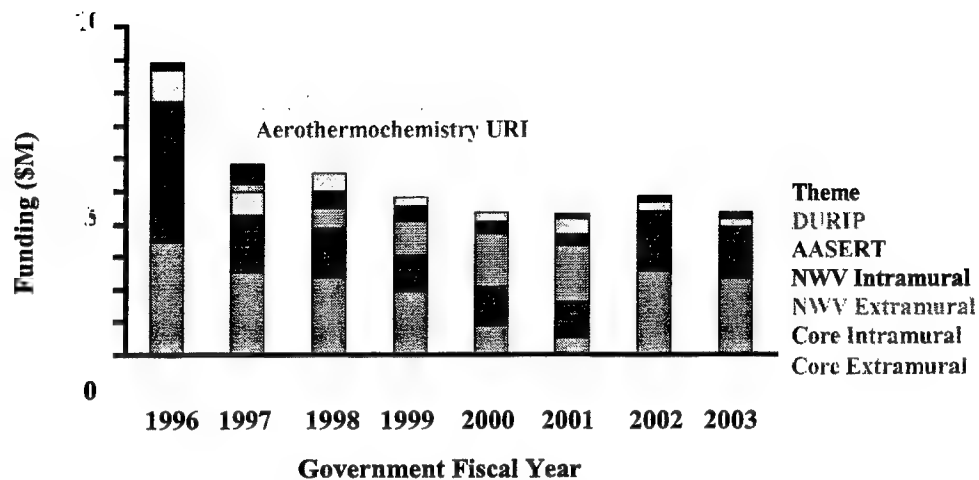


**Figure 1. AFOSR Funding for Combustion and Diagnostics**



## **The Army Research Office Program in Propulsion and Energetics**

David M. Mann  
Mechanical and Environmental Sciences Division  
US Army Research Office

The Army is on a fast-paced path to transformation. That transformation involves the development of new classes of fighting vehicles, the Future Combat System, which are lighter and more mobile, while maintaining the levels of lethality and survivability offered by today's systems, e.g. the M1 Abrams tank. Over the years, ARO propulsion and energetics research has played a vital part in providing the options for the development of the new systems. Research in future years will yield breakthroughs that will enable new capabilities.

The Army Transformation and recent world events have re-emphasized the need for lightweight, high power density, high efficiency engines for air and ground vehicles. The ARO Propulsion program continues to focus on optimizing the combustion processes in diesel and gas turbine engines. Fundamental to that optimization is understanding and developing predictive models for the controlling mechanisms and processes. Particularly important research areas are fuel injection and fuel-air mixing dynamics, ignition, combustion and heat transfer. In order to be applicable to the environments of advanced engines, it is vitally important to address these areas in the appropriate parameter space of temperature, pressure and turbulence level. Ultimately the goal is to combine the detailed understanding of combustion that can be used with active control techniques and health monitoring systems.

Projectile and missile propulsion is the focus of the ARO Energetics program. The emphasis is on the development of higher energy systems, both through the utilization of current energetic materials under higher loading conditions and through the development of higher energy/output energetic materials, e.g. nanoscale materials. In the first instance, fixed volume systems, such as gun and missile combustion chambers, can deliver higher energies if higher charge densities (guns) or more compact combustors (liquid fueled missiles) are used. Here the challenges are the ignition and heat release dynamics at high density. In the second instance, the Army is exploring the potential of nano-scale energetic materials to provide higher energy and higher power for propulsion and explosive uses. In this new field, emphasis is being placed on the preparation and characterization of novel nanostructures and on understanding their reactivity.

Details on submitting proposals to ARO may be found on the ARO web site, [www.aro.army.mil](http://www.aro.army.mil). The site contains the Broad Agency Announcement for the ARO and other Army Research Laboratory Directorates' research efforts. Prospective offerors to ARO are encouraged to informally discuss their research ideas with the appropriate ARO program manager prior to submitting a formal proposal.



## ACOUSTIC SENSING AND ACTUATION IN GASEOUS FLOWS

Contract # DAAD19-01-0571

Principal Investigator: Tim Lieuwen

School of Aerospace Engineering  
Georgia Institute of Technology  
Atlanta, GA 30332-0150

### SUMMARY/OVERVIEW:

This program is developing acoustic techniques for non-intrusive sensing and actuation of gas flows. Although not the primary focus of this work, we have developed a fast, very sensitive method of measuring low levels of water vapor concentration. We have initiated the patent process by filing an invention disclosure and have begun exploring commercialization possibilities. We have also developed a technique that relates the mixing between two gases by measuring the acoustic absorption at several frequencies. We present data below showing a clear change in absorption levels with gas mixedness. Future work is directed at developing inversion techniques to reconstruct spatial mixedness profiles.

### TECHNICAL DISCUSSION:

#### *Background*

The objectives of this program are to develop acoustic techniques for 1) sensing and 2) actuation in gas flows. Work performed to date has focused on the former item. Specifically, this work focused on the use of acoustic absorption measurements to characterize gas mixtures. The objective of this work is two fold: 1) determine the accuracy and sensitivity with which acoustic absorption can be measured in practical environments, and 2) demonstrate the use of acoustic absorption measurements to infer the level of molecular mixedness between constituents in a multi-component gas media.

#### *Water Vapor Concentration Measurements*

Work performed in the first year developed a fast, sensitive technique to measure low levels of water vapor concentration. In this year, we have begun exploring possibilities for commercializing this work into an industrial sensor. We have reviewed current technologies and approaches for measuring low levels of water vapor in air and other gases. The best sensors available use very accurate, but also slow (~1 minute) and expensive (\$10-\$40K) chilled-water hygrometer technology for making these measurements. For our approach, the basic sensing/actuating hardware and signal processing costs will be quite low. If our approach can be packaged at a reasonable cost (something we haven't explored yet), this approach could make a convenient alternative to current technologies. To this end, we have filed an invention disclosure with Georgia Tech and begun conversations with individuals at several companies that make high end humidity sensors.

### *Carbon Dioxide Absorption Characteristics*

As in the first year, carbon dioxide was used in tests during year 2 for characterization of gas mixedness. It was chosen because of its relatively low vibrational temperature, resulting in high levels of absorption at room temperatures. The vibrational relaxation frequency of carbon dioxide is strongly dependent upon the water concentration. Thus, we are using  $\text{CO}_2 - \text{H}_2\text{O}$  mixtures. Using existing databases<sup>1</sup>, we have quantified the dependence of the acoustic absorption coefficient upon frequency and water vapor concentration, see Figure 1. The figure shows the monotonic increase in absorption coefficient magnitude with frequency, as well as its nonmonotonic and nonlinear dependence upon water vapor level.

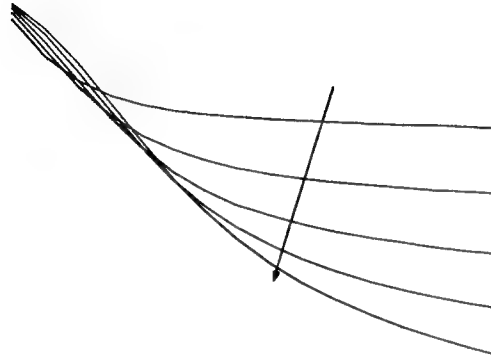


**Figure 1. Dependence of acoustic absorption coefficient upon frequency and water vapor concentration ( $=0, 0.005, 0.01, 0.015$ , and  $0.02\%$  by weight).**

The nonlinear dependence of absorption coefficient upon (in this case) water vapor content is key to the technique being pursued here. Because of this nonlinearity, the total absorption of a sound wave traversing the medium depends upon the local concentration values, and not just the integrated sum across the line of sight. To demonstrate this point, consider the total acoustic absorption across two gas profiles, both of which contain the same total amount of water, see Figure 2.

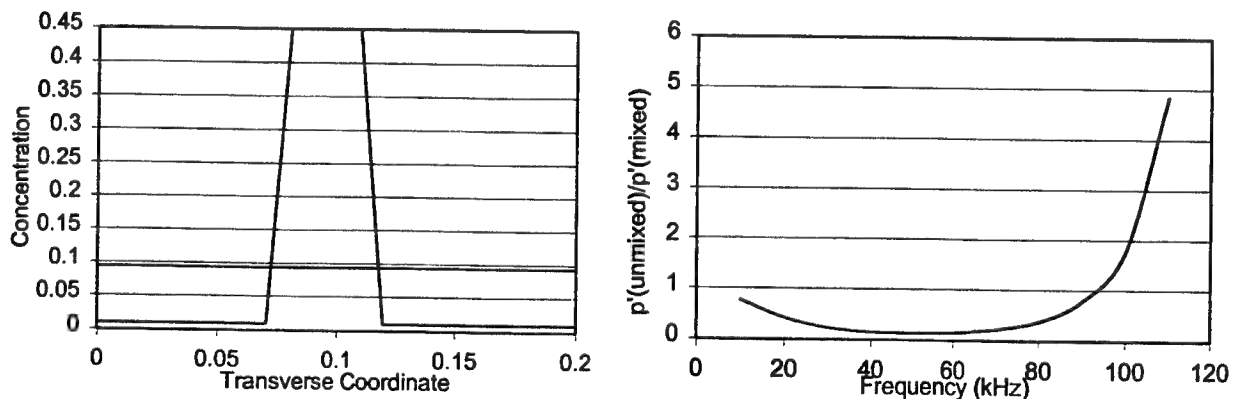


**Figure 2. Two spatial profiles of water vapor concentration used to demonstrate capability of absorption technique to determine gas mixedness levels (left) and ratio of acoustic pressures for these two profiles (right).**

Consider the total acoustic absorption across these two profiles. The figure above plots the ratios of the acoustic pressure measured in the unmixed and perfectly mixed case. The figure shows that this pressure only has a value of unity near 90 kHz and has a high of around 5 and a



low of 0.2. This figure strongly suggests that comparison of the acoustic absorption measured at a few frequencies can be used to infer levels of mixedness. Furthermore, given information from enough frequencies, it also may be possible to extract information about the spatial unmixedness profile, a point we discuss in our ARO report.

### *Facility Development*

Having demonstrated the theoretical feasibility of being able to reconstruct the spatial profile of the gas mixedness levels, we have assembled an experimental facility to attempt to demonstrate this technique. It consists of an 8-foot long, 8 x 11 inch section aluminum duct that is capped at one side and open at the other side. A box with one open end slides inside the duct. Two gases of arbitrary composition, denoted as Gas A and Gas B below, flow through the main chamber and the translating box.

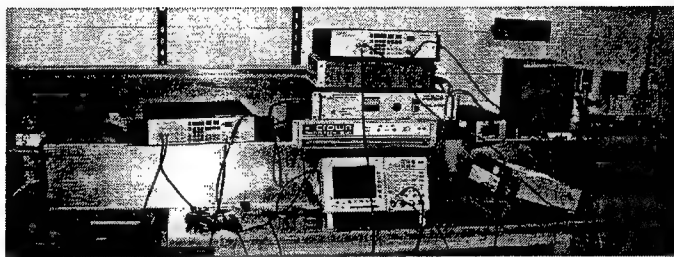


**Figure 3. Photo of facility developed for acoustic mixing measurements.**

For this experiment, gases "A" and "B" simply consisted of two CO<sub>2</sub> sources with different levels of impurity: research grade (99.999% purity) and industrial grade (99.98% purity). The two gas flows are metered with velocities from 1cm/s to 5cm/s. These velocities and lengths were chosen based on diffusive mixing calculations based upon requirements that the two gases could be essentially completely mixed when the box is positioned the farthest distance from the transducer. As such, the degree of gas mixing can be varied via the box location and/or the gas velocity

Acoustic signals are generated with one of two transducers. A 38 mm diameter, type 616341 electrostatic polaroid transducer is used to generate sound in the 30kHz to 65kHz range. A Massa piezoelectric crystal is used to generate sound in the 130-160 Hz range. Acoustic measurements are obtained with a 1/8" type 4191 Bruel and Kjaer microphone. The speaker and microphone are situated near the nozzle end of the duct.

### *Acoustic absorption measurements in Inhomogeneous Gas Flow*

In the experiment, two initially unmixed gas streams enter the duct from upstream. As these gases convect down the duct and mix, the acoustic absorption at different axial locations are measured at several frequencies between 30-65 and 130-160 kHz. For each frequency, two acoustic amplitudes  $A_{avg}(f)$ ,  $A(f)$  are measured by varying the position of box, 1) the box is 1.2 m away from the microphone, where the gas can be regarded as perfect mixed; and 2) the box is near the microphone. The gas is acoustically interrogated by bursts of 10-50 acoustic cycles at the desired frequency, followed by a pause in order to allow the reverberant field to damp out, see Figure 4.

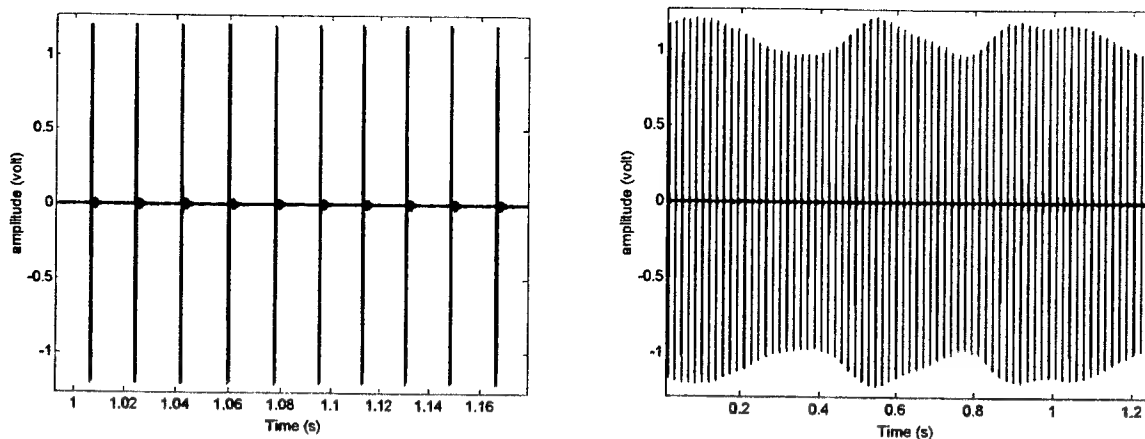


**Figure 4. Time dependence of acoustic pressure, illustrating spaced tone bursts.**

At some axial locations, the flow field is apparently highly unsteady, likely due to vortex shedding at the shear layer between the two gas streams. The unsteady mixing between the two gas streams is highly visible in these pulsed acoustic data, as seen in the right figure above. Although the measurements are not as clean as we would like due to this unsteadiness, we have obtained substantial number of measurements suggesting that the proposed technique is viable and that it is capable of discerning different levels of mixedness. Figure 5 illustrates the amplitude a 45 kHz acoustic signal upon distance between the box and transducer. It shows the monotonic decrease in amplitude with increasing distance (corresponding to increased mixedness). The amplitude of the errorbar corresponds to the fluctuation level of the signal. The large fluctuation at 20 cm is indicative of what are apparently large vortical structures that rapidly mix the flow, as evidenced by the flatness of the amplitude curve for increasing distances. An analogous curve illustrating the frequency dependence of the acoustic absorption at two axial locations is also plotted in on the right. The figure shows the substantial difference in acoustic pressure levels at the two axial levels across almost the entire frequency range.

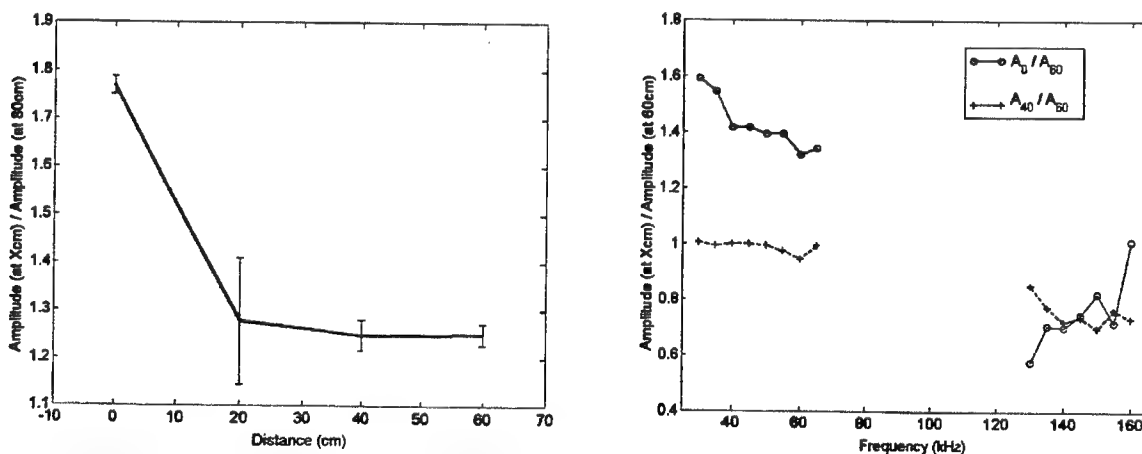


**Figure 5. Dependence of 45 kHz amplitude signal upon axial distance between gas stream origination point and acoustic transducer (left) and dependence of acoustic pressure level upon frequency at two axial locations(right).**

## References

- <sup>1</sup> Bhatia, A, *Ultrasonic Absorption*, Dover Publications: New York, 1967.

# CHEMICAL KINETICS AND AERODYNAMICS OF IGNITION

(ARO Grant No. DAAG19-01-0004)

Principal Investigator: Chung K. Law

Princeton University  
Princeton, NJ 08544

## SUMMARY/OVERVIEW

This program investigates nonhomogeneous ignition by studying premixed and nonpremixed, laminar and turbulent ignition in the counterflow configuration, with emphasis on quantifying the ignition limits of various fuels and identifying the controlling ignition kinetics. Three projects involving both experiment and computation were undertaken during the reporting period. In the first project, laminar premixed ignition was investigated for both hydrogen and propane. Results show that the ignition temperatures of  $H_2$ /air premixture exhibit five limits over the pressure range investigated. The first three limits mimic those of homogeneous explosion, but are shifted to higher temperatures. The fourth ignition limit runs parallel to the crossover temperature but is shifted to lower temperatures, and is attributed to  $HO_2$  becoming part of a propagating route. At the highest pressure range constituting the fifth ignition limit,  $HO_2$  recombination results in the generation of  $H_2O_2$  and consequently  $OH$  to facilitate ignition. Ignition of propane/air mixture at atmospheric pressure was investigated as a comparison. In contrast to hydrogen, the ignition temperature increases as the freestream becomes leaner due to the fact that the ignition kernel is rendered leaner than the freestream because propane is less diffusive than oxygen. The second project extends the previous non-premixed ignition of alkanes to alkenes ( $C_2$ - $C_4$ ), recognizing that small alkenes are important intermediates in hydrocarbon combustion. Experiments showed that the ignition temperature decreases with increasing pressure, which was also observed for alkanes in the past. Numerical simulation is under way to help understand the experimental results on alkenes ignition. In the third project, a two-step process was adopted to model turbulent ignition that takes advantage of the possibility of decoupling the descriptions of turbulence from chemical reaction due to the small amount of heat release prior to ignition. Calculations using different mixing models indicated that turbulence intensity has little effect on the ignition temperature, which is about 30K higher than laminar ignition temperatures.

## TECHNICAL DISCUSSION

### 1. Premixed hydrogen/air and propane/air ignition

A previous study on the ignition of a *lean* premixed hydrogen/air jet by a counterflowing heated nitrogen jet at atmospheric pressure demonstrated that the strong preferential diffusion of hydrogen can lead to substantial hydrogen over-enrichment in the ignition kernel, leading to retarded ignition characterized by increased ignition temperature with increasing freestream fuel equivalence ratio,  $\phi$ . This study has since been extended in two directions: hydrogen ignition at elevated pressures, and propane ignition at atmospheric pressure.

The study on hydrogen/air ignition at elevated pressures was motivated by the recognition that ignition phenomena are inherently sensitive to detailed chemistry, and that such

sensitivity is strongly manifested in terms of pressure variations. Figure 1 compares the characteristic Z-shaped pressure-temperature explosion limits of a homogeneous mixture with the present premixed counterflow ignition temperatures, determined from both experiment and calculations, for 9%  $H_2$  in air mixture ( $\phi = 0.236$ ) versus heated  $N_2$  at a pressure-weighted strain rate of  $k = 216s^{-1}$ . The results show two important distinctions between the homogeneous and the present premixed ignition situations. First, the counterflow ignition response curve is shifted along the crossover temperature path to a higher temperature regime due to the reduced residence time. Second, the ignition temperature exhibits five limits over the pressure range investigated. These five ignition limits have the following characteristics.

The first three ignition limits qualitatively mimic the homogenous case. Quantitatively, the pronounced  $H$  radical loss to the hot inert side pushes the first limit to end at a higher pressure. The steepening of the second limit, which turns and forms the third limit, is due to the increasing importance of R-18 ( $HO_2 + H_2 \rightarrow H_2O_2 + H$ ). This reaction converts the relatively inert  $HO_2$  to the more reactive  $H$  radical and is greatly facilitated by the abundant  $H_2$  within the ignition kernel owing to its preferential diffusion over  $O_2$ . As the concentration of  $H$  is built up with pressure, reactions between  $HO_2$  and  $H$  (R10:  $HO_2 + H \rightarrow H_2 + O_2$  and R11:  $HO_2 + H \rightarrow OH + OH$ ) start to influence ignition. The combined effect is to weaken the termination reaction R9 ( $H + O_2 + M \rightarrow HO_2 + M$ ) by a factor of  $2k_{10}/(k_{10} + k_{11})$ . Ignition occurs at a lower temperature than the crossover temperature, and an extended second limit behavior appears. Finally, as more  $HO_2$  are produced with increasing pressure, its recombination reaction R14 ( $HO_2 + HO_2 \rightarrow H_2O_2 + O_2$ ) generates  $H_2O_2$  which further decomposes to two  $OH$  through R16 ( $H_2O_2 + M \rightarrow 2OH + M$ ). Thus ignition again becomes easier at the fifth limit. As a whole, the five limits of premixed ignition can be interpreted as a global three limits behavior, with the third (explosion) limit interrupted by the extended second limit which is the observed fourth ignition limit.

The counterpart of hydrogen/air ignition is propane/air ignition because propane, being less mobile than oxygen, will render an originally lean mixture more fuel lean in the ignition kernel. Thus while increasing  $\phi$  will facilitate ignition, the extent is expected to be weakened. Figure 2 shows that the ignition temperature decreases with increasing  $\phi$ , although the influence of preferential diffusion cannot be readily separated out.

## 2. Nonpremixed ( $C_2$ - $C_4$ ) alkene ignition

Nonpremixed ignition of ( $C_1$ - $C_8$ ) alkanes was systematical investigated previously. Results showed that the ignition temperature is strongly affected by three factors, namely the reactivity of the alkyl radical, which depends on the fuel structure, the effect of fuel size on diffusivity, and the effect of finite rate kinetics and the complex coupling between reaction and transport for the many intermediate species.

Since small alkenes are important intermediate constituents in the combustion of hydrocarbon fuels, its oxidation processes have a large influence in constructing a framework for the mechanism of hydrocarbon oxidation. We have therefore extended our ignition chemistry study to alkenes.

Five fuels, ethylene, propylene, 1-butene, cis-2-butene and trans-2-butene, were tested experimentally. The ignition response of ethylene and propylene were also numerical simulated using detailed mechanism for experimental comparison. The responses of 1-butene, cis-2-butene and trans-2-butene were not simulated due to the lack of validated chemical mechanisms.

Figure 3 plots the air temperature required to ignite the fuel mixture as a function of pressure for ethylene and propylene. It is seen that the ignition temperature decreases with increasing pressure. Similar results were also observed for the other three alkenes. Figure 3 also shows that ethylene ignites at lower temperatures than propylene, possibly due to the fact that it

is more diffusive and therefore has a higher concentration in the ignition kernel. Molecule structure could of course also play a role in the difference.

The calculated ignition temperatures are about 70K higher than the experimental values. The discrepancy is beyond the experimental error. Two factors may contribute to the disagreement. One is the fuel diffusivity since the ignition temperature strongly depends on the amount of fuel available in the ignition kernel. The other is the chemical mechanism. The sensitivity of ignition on fuel diffusivity and chemical reactions are currently being investigated.

### 3. Modeling study of turbulent nonpremixed ignition

Our previous experimental study on the effects of turbulence on nonpremixed hydrogen ignition showed that optimal conditions for ignition exist in weakly turbulent flows where the ignition temperature is lower than either laminar or strongly turbulent flows at the same pressure. In order to understand this phenomenon, computational simulation was conducted using Monte Carlo techniques to solve a joint scalar PDF equation. The simulation involved calculating the velocity field using a Reynolds stress model, and using this frozen flow field in the subsequent ignition calculation. The decoupling is justified because the small amount of heat release prior to ignition is not expected to affect the flow field. Results show that under most flow conditions, there is a large increase in  $H$  at ignition that is orders of magnitude larger than the background fluctuations. Heat release is shown to be negligible prior to ignition by examining the stochastic particle temperatures conditioned on the mixture fraction. After ignition has occurred, effects of heat release are evident in the conditional temperature data and the partially decoupled reactions are no longer expected to accurately represent the flow conditions.

Figure 4 shows that, at atmospheric pressure, the calculated ignition temperatures are about 30K higher than the calculated laminar ignition temperatures, and no appreciable variation is noted for flows with different turbulence intensities. Similar over-predictions were noted between turbulent and laminar calculations at pressures up to 3-4 atm. At still higher pressures, the turbulent calculations do not clearly exhibit the third limit behavior found in laminar ignition. These results differ from the experiment which did find an effect of turbulence intensity on ignition temperatures and show a decrease in ignition temperature with bulk strain rate instead of the increase shown in the turbulent calculations. At higher pressures, the quantitative agreement between turbulent calculations and experiments improved but it is unclear whether the trends of the two sets of data are qualitatively similar. Further modeling work is being conducted aiming to resolve this discrepancy.

## MAJOR PUBLICATIONS

- [1] "Effects of turbulence on nonpremixed ignition in heated counterflow," by J.D. Blouch and C.K. Law, *Combustion and Flame*, Vol. 132, pp. 512-522 (2003).
- [2] "Ignition of premixed hydrogen/Air in heated counterflow," by X.L. Zheng, J.D. Blouch, D.L. Zhu, T.G. Kreutz and C.K. Law, *Proceedings of the Combustion Institute*, in press.
- [3] "A joint scalar PDF study of nonpremixed hydrogen ignition," by J.D. Blouch, J.Y. Chen and C.K. Law, under revision.
- [4] "Ignition of premixed hydrogen/air by heated counterflow under reduced and elevated pressures," by X.L. Zheng and C.K. Law, submitted.
- [5] "Development of comprehensive detailed and reduced reaction mechanisms for combustion modeling," by C.K. Law, C.J. Sung, H. Wang and T. F. Lu, *AIAA Journal*, in press.

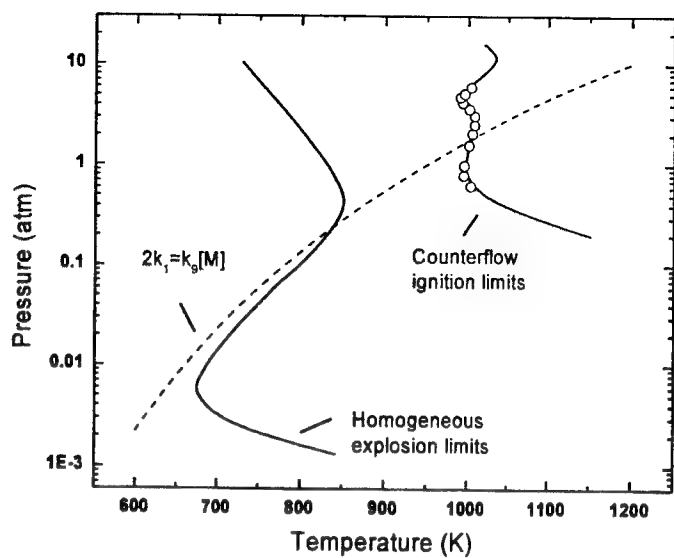


Figure 1: Explosion limits of  $H_2/O_2$  mixture and ignition temperatures under different pressures.

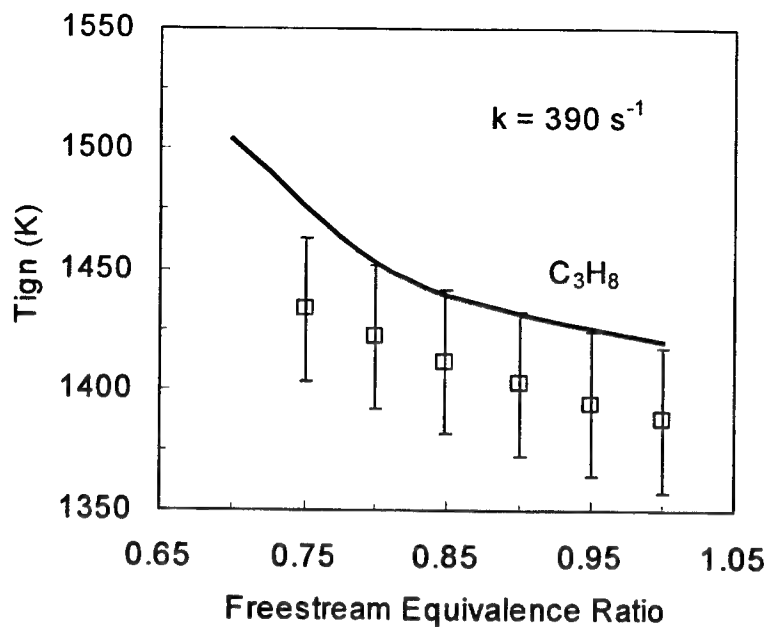


Figure 2: Premixed  $C_3H_8/Air$  ignition temperatures under different freestream equivalence ratios.

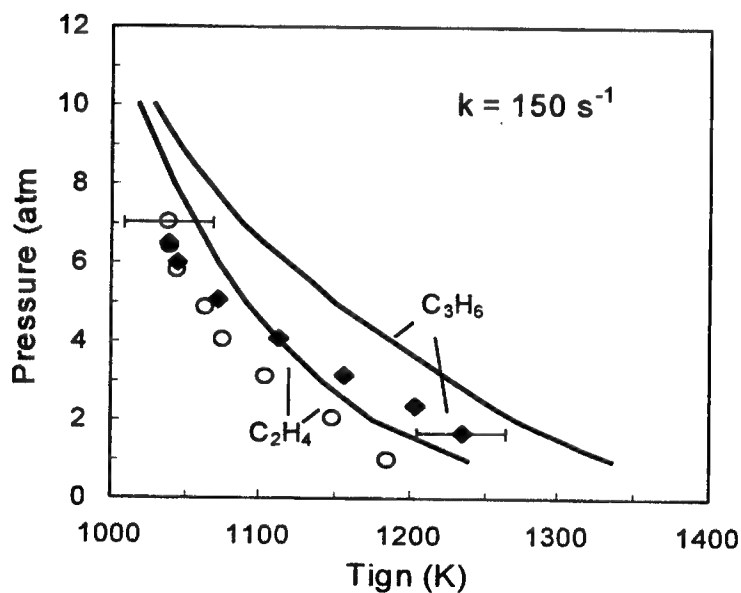


Figure 3: Non-premixed  $C_2H_4/Air$  and  $C_3H_6/Air$  ignition temperatures under different pressures.

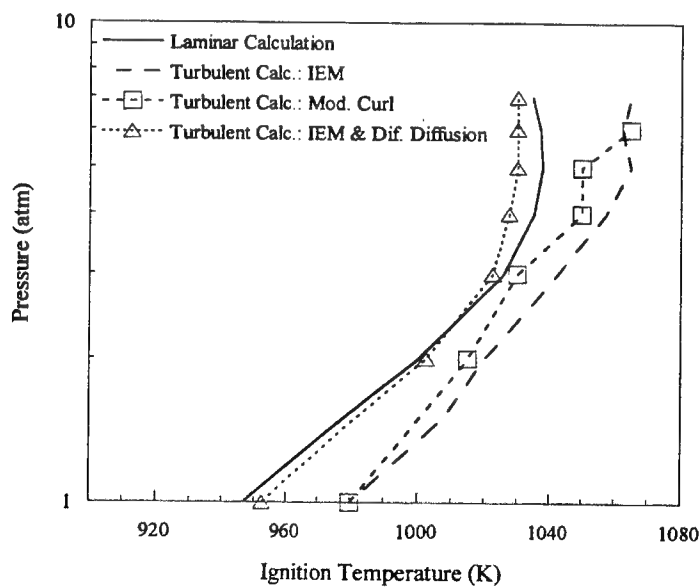


Figure 4: Comparison of the effects of different mixing models on the ignition response to changing pressure.

# PHYSICAL AND CHEMICAL PROCESS IN FLAMES

(AFOSR Grant No. F49620-01-1-0029)

Principle Investigator: Chung K. Law

Department of Mechanical and Aerospace Engineering  
Princeton University, Princeton, NJ 08544

## SUMMARY/OVERVIEW

The objectives of the present program are to develop detailed and simplified chemical kinetics models for hydrocarbon combustion, and to understand and quantify the dynamics of flames. During the reporting period progress were made in the following projects: (1) Skeletal mechanism reduction by the method of directed relation graph (DRG). A skeletal mechanism for ethylene oxidation with 33 species and 205 elementary reactions was derived and validated. (2) Computational cost minimization without accuracy loss was studied. A computer program was developed for automatic mechanism specific code generation. (3) Acquisition of laminar flame speeds of hydrocarbon fuels at elevated pressures. (4) Oscillatory blowoff of flames.

## TECHNICAL DISCUSSION

### 1. Skeletal Mechanism Development Using Directed Relation Graphs

The first step towards reduction of a detailed mechanism is the elimination of unimportant elementary reactions to the level of skeletal mechanism. Previously this procedure was conducted through "experience". In this endeavor we attempt to develop a rational methodology towards elimination. In the present approach the dependence of a species on other species in a large mechanism was transformed to a Directed Relation Graph (DRG), in which each species represent a vertex and there exists an incident directed edge from vertex A to vertex B if and only if it requires the existence of species B to accurately calculate the production rate of species A. The weight of the edge from A to B in the DRG is defined as the normalized contribution of B-related elementary reactions in evaluating the production rate of species A. Weak dependence of a species on another, indicated by an edge weight smaller than a given small threshold value, can therefore be eliminated. A group of species, which are strongly coupled with the major species such as the fuel and the oxidizer, can be identified by a depth first search (DFS), in linear time, starting from these major species. Skeletal mechanisms of different levels can be generated from the strongly coupled group by specifying different small threshold values. For the ethylene/air system, the dependence of species number in the skeletal mechanism on the given threshold value is shown in Fig. 1.1. The jumps in Fig. 1.1 show



the truncation of strongly coupled groups, and the truncation should be performed at one of the jumps. It is also observed that starting from a very small threshold value, the number of species in the skeletal mechanism increases as the threshold value increases and as the threshold value approaches 0, the skeletal mechanism approaches the detailed mechanism. This linear time algorithm for fast mechanism reduction can also be applied for solving large problems exploiting Newton solver, for which searching for the initial guess can be extremely difficult and time consuming.

For ethylene oxidation a skeletal mechanism with 33 species and 205 elementary reactions was derived from a detailed mechanism with 70 species and 463 elementary reactions. The skeletal mechanism yields close agreement with those obtained by using the detailed mechanism for perfectly stirred reactor (PSR), auto ignition, 1-D planar premixed flame, and counter flow diffusion flames over the pressure range of 0.1~30 atm, equivalence ratio range of 0.6~1.5, and an extensive temperature range. The comparison of the skeletal mechanism with the detailed one for PSR and auto ignition is shown in Figs. 1.2-1.3 respectively.

Further validation of the skeletal mechanism for 1-D laminar premixed flames and counter-flow nonpremixed ignition is shown in Figs. 1.4 and 1.5. The agreement can be considered to be quite satisfactory.

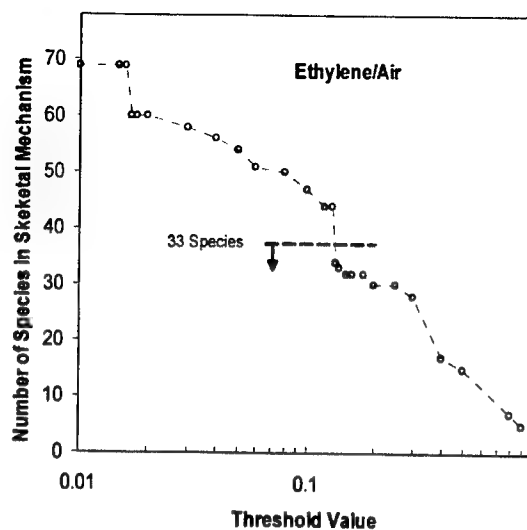


Figure 1.1

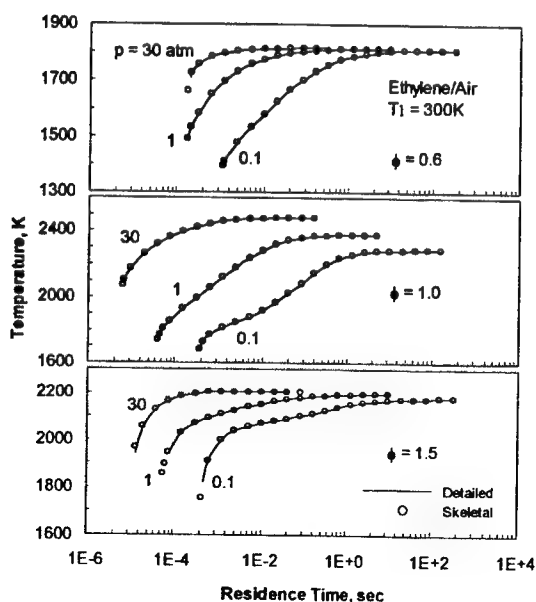


Figure 1.2

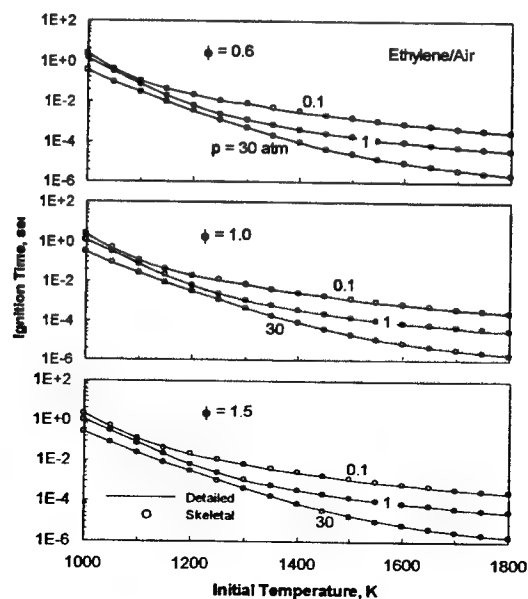


Figure 1.3

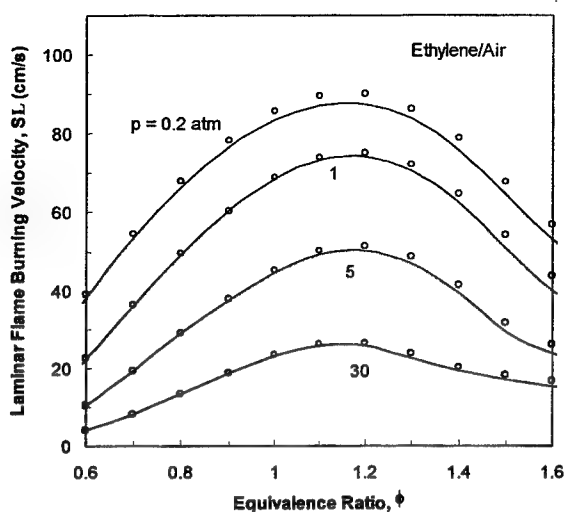


Figure 1.4

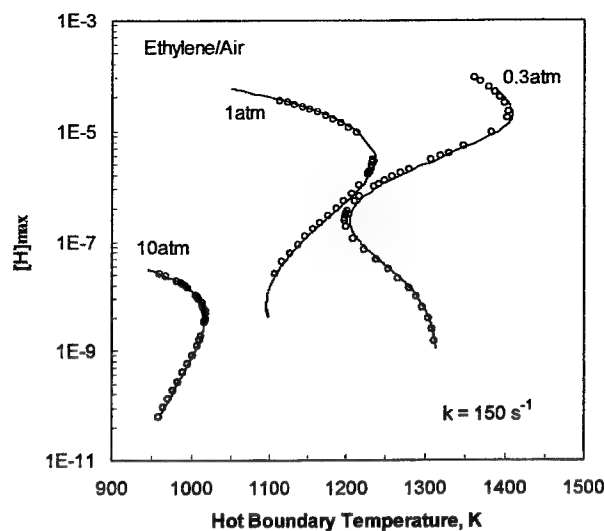


Figure 1.5

## 2. Mechanism Specific Computational Cost Minimization

The computational cost for detailed mechanisms can be reduced significantly through mechanism specific optimization without loss of accuracy. Such optimizations include methods such as redundant or trivial term elimination, pre-calculation of the best sequence of serious operations, dynamic caching of frequently recalculated terms, and employment of special functions for specific parameter ranges. The above methods are obviously mechanism-dependent or even machine dependent. However, it only needs to be done once for one mechanism and can be used forever. Therefore it is highly desirable that every detailed mechanism should come with an optimal computation sequence in the form of a compliant software subroutine.

A computer program has been developed to search for the best or nearly best computational sequence and to generate FORTRAN subroutines for fast calculation of chemical reaction rates. The time savings for skeletal reduction with and without this software optimization are compared with those of the detailed mechanism are shown in Fig. 2.1. It can be seen that the combination of highly accurate skeletal reduction with this software optimization can easily achieve the time savings of more than one order of magnitude.

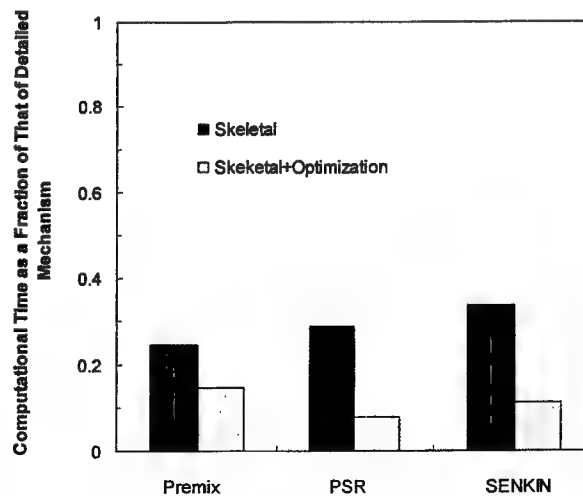


Figure 2.1

### 3. Experimental Determination of Laminar Flame Speeds at Elevated Pressures

Efforts were continuously being expended towards acquisition of laminar flame speed data for practical use as well as for the development of comprehensive oxidation mechanisms for hydrocarbon fuels. Two major directions were initiated during the reporting period. First, the pressure range of determination has been extended to that of 20-60 atmospheres. This was accomplished through the use of a new combustion chamber that allows high and constant pressure combustion with the capability of optical observation. Second, while previous experiments were mainly concerned with alkanes, new experiments were initiated on the major combustion intermediates including the alkenes. Specifically, data were taken on ethane, ethylene, propylene, and iso-butane, with equivalence ratios between 0.7 and 1.40 in increments of 0.1. These data are currently being analyzed.

### 4. Oscillatory Flame Blowoff

Previous efforts on unsteady flame behavior were mainly on flame extinction. In particular, it was shown quite convincingly that  $Le > 1$  flames frequently oscillate before extinction, and as such could modify the extinction boundary based on steady-state extinction consideration. The investigation has now been extended to flame stabilization and blowoff. Since  $Le > 1$  flames are intrinsically pulsatingly unstable, there is reason to believe that the stabilization and blowoff boundaries could also be affected by pulsation. A 2D computer code with detailed chemistry and transport has been under development for this project.

## JOURNAL PUBLICATIONS

1. "Determination of laminar flame speeds of fuel blends using digital particle image velocimetry: ethylene, n-butane, and toluene mixtures," by T. Hirasawa, C.J. Sung, A. Joshi, H. Wang, and C.K. Law, *Proc. Combust. Inst.* Vol. 29, in press.
2. "Outward propagation, burning velocities, and chemical effects of methane flames up to 60 atmospheres," *Proc. Combust. Inst.*, Vol. 29, in press.
3. "Pulsating instability and extinction of stretched premixed flames," by E.W. Christiansen and C.K. Law, *Proc. Combust. Inst.*, Vol. 29, in press.
4. "Oscillatory extinction of spherical diffusion flames," by S.W. Yoo, E.W. Christiansen, and C.K. Law, *Proc. Combust. Inst.*, Vol. 29, in press.
5. "A computational study of oscillatory extinction of spherical diffusion flames," by E. W. Christiansen, S.D. Tse, and C.K. Law, *Combust. Flame*, in press.
6. "Development of comprehensive detailed and reduced reaction mechanisms for combustion modeling," by C.K. Law, C.J. Sung, H. Wang, and T.F. Lu, *AIAA J.*, in press.

# EXPERIMENTAL AND COMPUTATIONAL CHARACTERIZATION OF COMBUSTION PHENOMENA

AFOSR Task No. 02PR01COR

Principal Investigator: James R. Gord

Air Force Research Laboratory  
AFRL/PRTS Bldg 490  
1790 Loop Rd N  
Wright-Patterson AFB OH 45433-7103

## SUMMARY/OVERVIEW

Propulsion systems represent a substantial fraction of the cost, weight, and complexity of Air Force aircraft, spacecraft, and other weapon-system platforms. The vast majority of these propulsion systems are powered through combustion of fuel; therefore, the detailed study of combustion has emerged as a highly relevant and important field of endeavor. Much of the work performed by today's combustion scientists and engineers is devoted to the tasks of improving propulsion-system performance while simultaneously reducing pollutant emissions. Increasing the affordability, maintainability, and reliability of these critical propulsion systems is a major driver of activity as well. This research effort is designed to forward the scientific investigation of combustion phenomena through an integrated program of fundamental combustion studies, both experimental and computational, supported by parallel efforts to develop, demonstrate, and apply advanced techniques in laser-based/optical diagnostics and modeling and simulation.

## TECHNICAL DISCUSSION

While this AFOSR-funded program involves numerous ongoing investigations, just a few recent advances are described in this abstract. Many other ongoing activities have been reviewed during recent AFOSR/ARO Contractors Meetings and are not discussed at length here.

Continuing Collaborative Studies of Vortex-Flame Interactions with École Centrale Paris and ONERA. The investigation of vortex-perturbed counterflow diffusion flames is critical to our understanding of fundamental combustion processes. These interactions represent idealized turbulent combustion phenomena, and their studies will drive the development and evaluation of simplified models to be used in design codes for practical combustion systems. Here we discuss continuing work in two configurations: a counterflow flame perturbed by multiple colliding vortices and a two-phase counterflow flame perturbed by a single vortex.

Initial work in the multiple-colliding-vortex configuration has been focused on the generation of small-scale multiple-vortex-flame interactions to simulate turbulent conditions with improved fidelity. Because the counter-propagating-vortex configuration induces a stationary vortex-flame interaction, the early stages of interaction represent an idealized vortex-induced flame extinction. Current work in this area has been designed to explore the feasibility of extracting a single universal criterion for local flame extinction induced by dynamic strain.

Changes in the structure of a flat counterflow diffusion flame during its interaction with multiple incoming vortices have been investigated using planar laser-induced fluorescence (PLIF) of the hydroxyl radical (OH) and an in-house time-dependent computational fluid

dynamics code with chemistry (CFDC) known as UNICORN. Excellent agreement between experimental and computational data has been achieved, as documented in Figure 1. Three variables were investigated for various incoming vortex velocities to characterize the observed quenching process: the air-side strain rate, fuel-side strain rate, and the scalar dissipation rate. Here, strain rates are defined as the component of the velocity gradient normal to the flame surface, and scalar dissipation is the vector product of the fuel concentration gradient with itself. It is found that none of these variables can individually characterize the quenching process associated with unsteady flames. It is proposed instead that a variable proportional to the air-side strain rate and inversely proportional to the temperature-drop rate at extinction could characterize the unsteady quenching process. Figure 2 shows that the air-side strain rate increases linearly with the temperature-drop rate. Since temperature drop directly correlates the balance between the reactant influx and its consumption in the flame zone (extent of non-equilibrium nature of the reactions), Fig. 2 suggests that the quenching value of the air-side strain rate increases with the extent of non-equilibrium chemistry taking place in the flame zone. By defining a variable that is proportional to the air-side strain rate and inversely proportional to the temperature-drop rate, a universal term for describing the quenching process in unsteady flames can be obtained. For example:

$$\sigma = T_{\infty} \frac{K_a}{(dT/dt)_{ext}}$$

where  $\sigma$  is the extinction parameter,  $K_a$  is the air-side strain rate,  $T$  is temperature,  $t$  is time, and  $T_{\infty}$  is the unperturbed temperature.

In the two-phase vortex flame configuration (Fig. 3), early work was focused on demonstrating the experimental technique and discerning the effects of fuel composition, droplet seeding levels, and PAH fluorescence on the CH PLIF signal. Recent work has been focused on detailed analyses of the rate of CH layer extinction and the evolution of flame surface area during the two-phase counterflow flame inter-

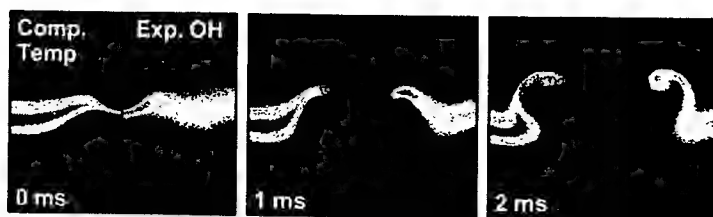


Figure 1. Computed temperature vs. OH PLIF data for a flat counterflow diffusion flame perturbed by multiple vortices.

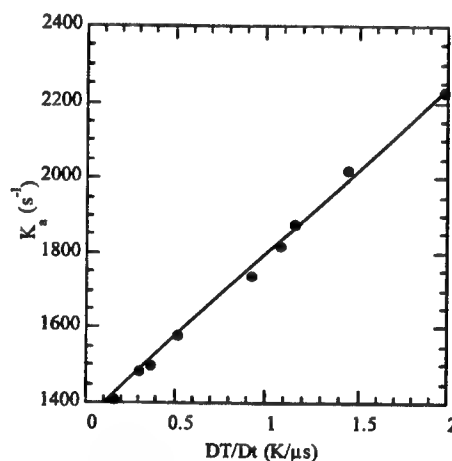


Figure 2. Proportionality of air-side strain rate with temperature-drop rate at extinction.

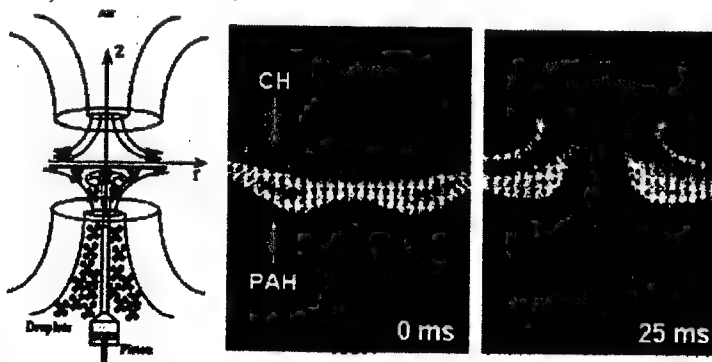


Figure 3. Flow configuration (left) and simultaneous PLIF/PIV images during two-phase vortex-flame interactions (middle and right).

action with fuel-side vortices of varying size and strength. Detailed analysis of the strain rate along the centerline has also been performed using PIV data acquired simultaneously with CH PLIF, as shown on the left in Fig. 4. Vortices of similar initial circulation but differing size show widely disparate peak strain rates and CH decay rates due to varying levels of flame-induced vortex dissipation. As shown in the center plot of Fig. 4, the CH decay rate is nearly linear in time with increasing slopes at higher fuel-side strain rates. These data are useful for evaluating the extinction behavior of two-phase vortex-flame interactions in the context of the universal criterion suggested above as modified for the case of a single fuel-side vortex.

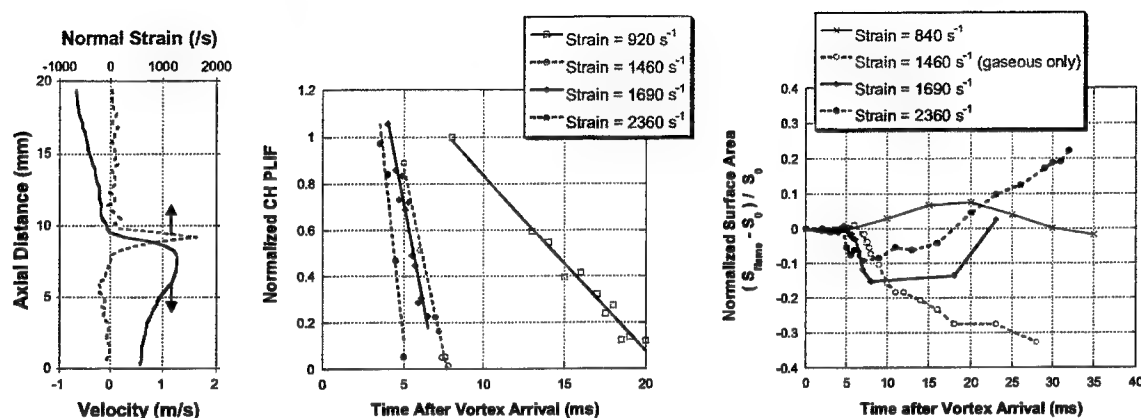


Figure 4. Experimentally measured normal strain rate along the centerline (left), normalized CH PLIF as a function of strain rate and time after vortex arrival (middle), and evolution of normalized flame surface area as a function of strain rate and time after vortex arrival (right).

Dual-Pump, Dual-Broadband Coherent Anti-Stokes Raman Scattering for Characterization of Liquid-Fueled Combustors. Our FY02 abstract described collaborative development with Prof. Bob Lucht (Purdue University) and his team at Texas A&M University of triple-pump CARS. That effort has been expanded to yield a dual-pump, dual-broadband CARS system for simultaneous detection of temperature and three species concentrations in reacting flows. In this CARS system, the rotational transitions of N<sub>2</sub>/O<sub>2</sub> and the rovibrational transitions of N<sub>2</sub>/CO<sub>2</sub> are probed. The CARS spectra of each molecule pair are observed within a distinct wavelength band, allowing two molecule pairs to be measured simultaneously using a detection system that includes two spectrometers and two cameras. Since nitrogen is a common species in each molecule pair, it can be used as a reference for normalizing species concentrations and for

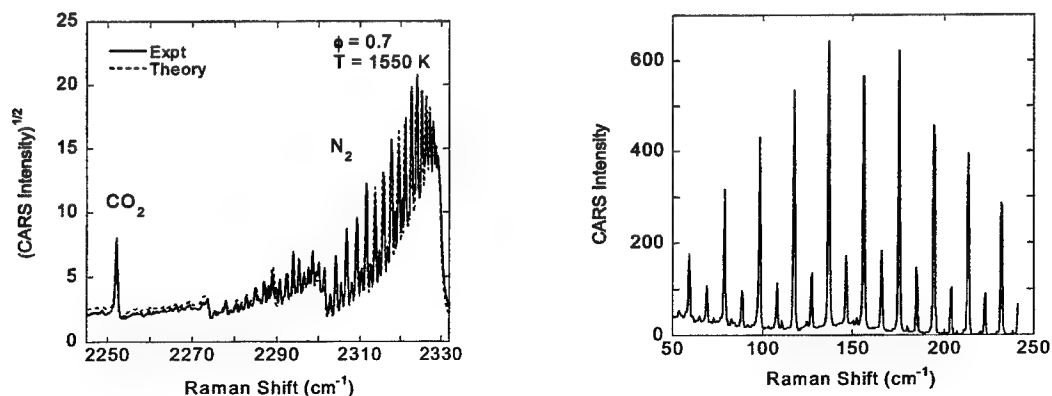


Figure 5. CARS signals obtained in the exhaust stream of the CFM56 combustor. Rovibrational spectra for N<sub>2</sub> and CO<sub>2</sub> are depicted on the left. Rotational spectra for N<sub>2</sub> and O<sub>2</sub> acquired simultaneously with the N<sub>2</sub>/CO<sub>2</sub> spectra are depicted on the right.

improving the accuracy and dynamic range of temperature measurements. Demonstration of this measurement technology has been accomplished in the exhaust of a liquid-fueled, swirl-stabilized CFM56 combustor. These measurements were performed to investigate the exhaust-stream temperatures and CO<sub>2</sub> concentrations for various jet fuels over a range of equivalence ratios. The effects of fuel additives on these combustor parameters were explored as well. Representative data are captured in Figure 5.

**Transient-Grating Thermometry in a Trapped-Vortex Combustor.** Transient grating spectroscopy (TGS, also known as laser-induced thermal acoustics or LITA) is a nonlinear optical technique that can be applied to measure gas temperature, sound speed, thermal diffusivity, and various other parameters of interest in reacting flowfields. Two pulsed pump beams derived from the same laser are crossed to generate a laser-induced grating in the probe volume via nonresonant absorption. The local hydrodynamic response produces two counter-propagating sound waves that scatter a phase-matched probe beam to yield a beam-like signal. In turbulent environments, single-shot signals are acquired and analyzed to produce probability density functions (PDF's) of the inferred temperature.

As part of our continuing effort to develop and apply this technique, transient grating thermometry has been performed in the rich flame zone of a TVC operating under turbulent, pressurized, JP-8-fueled conditions. Measurements were accomplished at pressures of 50, 75, and 100 psi with local equivalence ratios in the range 1–1.25. The pump beams were derived from the 565-nm output of a Nd:YAG-pumped dye laser. The cw output of a vanadate laser (532 nm) provided the probe beam. While the pump lasers were not tuned to a particular molecular resonance, the detected signals showed clear signs of thermalization and the absence of nonresonant electrostriction. Soot particles and soot precursors are the likely absorbers responsible for signal generation. Beam steering was clearly evident in the form of variable pointing and random spatial modulation of the exiting beams. Due to such adverse affects, signal was not obtained on all laser shots; however, useful signals were generated with sufficient frequency to permit meaningful temperature measurements.

A typical single-shot signal is depicted in Figure 6. A temperature PDF constructed from ~800 analyzed single shots is depicted in Figure 7. The resulting PDF is centered at 2000 K. The breadth of the PDF largely reflects the local dynamic nature of the reaction zone as pockets of fluid in different relative states of combustion maturity pass through the probe volume. The far wings of the PDF also contain contributions from electronic noise (particularly at high frequency) and processing noise (particularly at low frequency). Note that all signals were processed with no discrimination against those with very low signal-to-noise ratios.

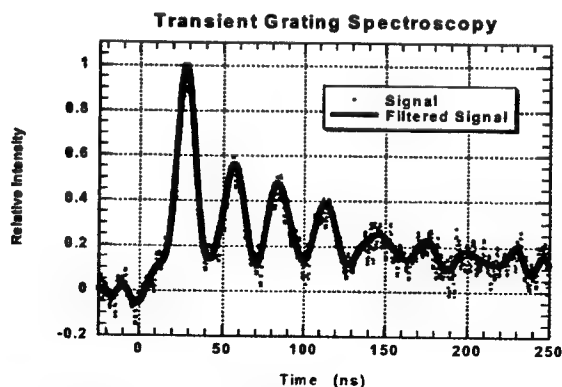


Figure 6. Single-shot TGS signal acquired in the rich flame zone of a TVC operating under turbulent, pressurized, JP-8-fueled conditions.

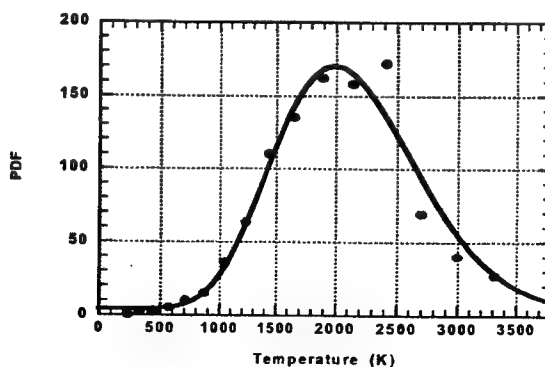


Figure 7. Temperature PDF constructed through analysis of ~800 single-shot signals acquired in a TVC operating at a pressure of 100 psi.



## TRANSIENT ENGINE BEHAVIOR AND CONTROL

(DAAD19-00-1-0487)

Principal Investigator(s): P.V. Farrell and D. Foster

Engine Research Center  
University of Wisconsin-Madison  
1500 Engineering Drive, Madison, WI 53706

### SUMMARY/OVERVIEW:

This thrust is aimed at understanding transient engine performance. The work described here has two thrusts: clarifying how engine performance and emissions change with engine operating conditions and understanding engine performance during changes in operating conditions. A general expectation is that future Army powertrains may employ smaller displacement, higher speed engines that can provide higher power density output for smaller and lighter future vehicles, with a potential for improved fuel economy as well. As these powertrains are likely to operate under highly transient conditions, understanding of the characteristics and limits of transient operation is important.

### TECHNICAL DISCUSSION

#### **Engine and Transient Dynamometer System**

A transient engine dynamometer is a hydraulic-based dynamometer system, similar to those constructed in the PCRL at UW-Madison [1]. The system consists of a test engine that is connected to a positive displacement hydraulic pump. The flow, and therefore the pressure, of the fluid entering and exiting the pump are computer controlled with a high-speed servo valve and the pump displacement is variable as well. The pressure difference across the dynamometer pump generates the torque needed to control the engine, while the variable displacement affects the flow rate and resulting speed of the pump. Software written using LabVIEW, is used to loop through interrogation of the sensors, estimation of output results based on simple feed-forward models, and checking of those results.

The results for the system in its current state are illustrated in figs 1, 2, and 3. Figure 1 shows the system response to a step change in torque request when operating in a motored condition. The measured torque follows the torque request with some rise time delay. The oscillations in the measured torques signal are artifacts of the torque variation as each of the 4 engine cylinders goes through a compression stroke. At higher torque values, these oscillations are not as evident. Figure 2 shows the requested torque and measured torque in a condition in which the requested torque varies somewhat sinusoidally with time. Figure 1.4 shows a trace for the dynamometer with a step change in speed requested. The measured speed follows the request with a time lag. Note also the torque spike needed to rapidly adjust the speed to match the request.

#### **Cavity Ring-Down Spectroscopy for Particulate Measurement**

For transient engine experiments to be really useful, transient emission measurements are necessary. Commercial devices are available to measure HC and NOx with small time

constants ( $\sim 2$  ms), but similar measures for particulates are not available. This project is aimed at developing a method for high speed particulate measurement, with possible extension to other engine out constituents.

The method under investigation is Cavity Ring-Down Spectroscopy (CRDS) which is a method employing light absorption in a multipass optical cell [c.f. 2,3]. The unique feature of CRDS is that the actual measurement is not total attenuation, but the rate of change of attenuation as a laser pulse is multipassed through the cell and gradually decays due to absorption. A schematic of a simple CRDS system is shown in fig. 4.

A pulsed DPSS laser with a high rep rate (2 kHz), low power (1 mJ) pulse, and a relatively long pulse length was used, primarily because of its compact dimensions. As it is not injection seeded, the line-width is not as narrow as for an injection-seeded Nd:YAG (used in initial evaluations) resulting in shorter ringdown times. To assure resonance in the cavity, one of the mirrors was mounted on a piezoelectrically driven mount to allow axial scanning of the mirror through a distance of about one wavelength. Ringdown intensities varied significantly for in-resonance vs. out-of-resonance conditions. The DPSS CRDS is shown in fig. 5.

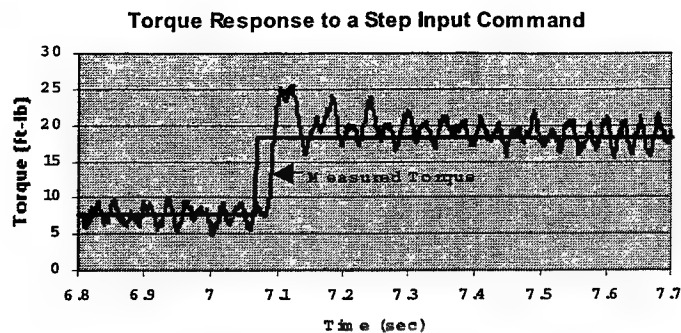
Sample results for the DPSS system are shown in fig. 6. Figure 6 shows an overall set of results for a wide range of absorption using a soot surrogate (DCF). The range of likely interest in a diesel engine is indicated by the BSU (Bosch Smoke Number) indicators. For this data, the mass of DCF in the test cell was varied to produce over an order of magnitude change in absorption coefficient. Note that in fig. 6 the sensitivity of the ringdown time to gas absorption is poor. Most gas-phase CRDS systems use light sources tuned to an IR absorption (emission) band of the gas of interest to dramatically increase the sensitivity of the measurement. As 532 nm (doubled Nd:YAG) is far from any resonance for these molecules, gas phase sensitivity using this wavelength is poor. Since particulates are usually considered broadband absorbers, wavelength selection should be less critical for particulate measurements.

#### **Particulate Composition Variation with Operating Conditions**

As mentioned above, in considering engines operating under a range of conditions and experiencing frequent changes in conditions, understanding of the impact of varying operating conditions is important.

One indicator of engine behavior is the detailed composition and size of the particulates produced. The mass of the elemental carbon, organic carbon and the sulfate contained within the particulate changes significantly as the engine load is changed. These trends are shown in fig. 7 for two different engine speeds. As the load increases the proportion of the particulate matter that is elemental carbon increases and the proportion of the particulate matter that is organic carbon decreases. The proportion of the particulate matter that is sulfates also increases as the load increases. This trend occurs at both engine speeds tested. The insert in each figure gives the fraction of the particulate matter that is respectively elemental or organic carbon, and shows how that fraction changes with load. As the particulate emission is indicative of incomplete air utilization, and hence an indication of approaching the limit of the power density, these data indicate that the details of the chemical energy conversion processes at these power limiting conditions, are different for these two operating conditions.

Data for trace metals, magnesium, calcium, manganese, iron and lead, for different engine loads at speeds of 1200 RPM and 1800 RPM are shown in fig. 8. Note the values of calcium are divided by 20, in order to display them on the same scale as the other trace metals. That is, calcium is the dominant trace metal measured in these experiments. Calcium is not present in the fuel, so these data can be used to assess the participation of the lubricating oil in the combustion process and show that the lubrication oil contributes to the particulate matter in



different amounts at different engine operating conditions. The iron measured in the particulate is most likely from engine wear.

Figure 1. Torque response for transient dynamometer

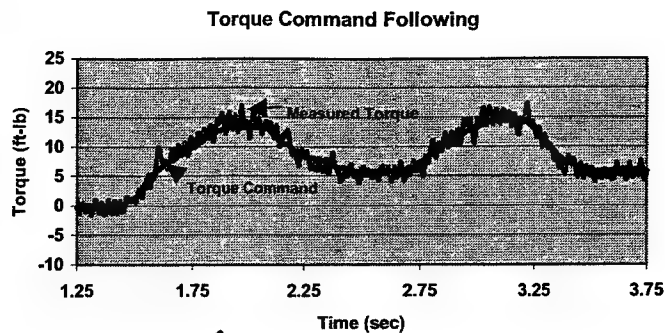


Figure 2. Torque following

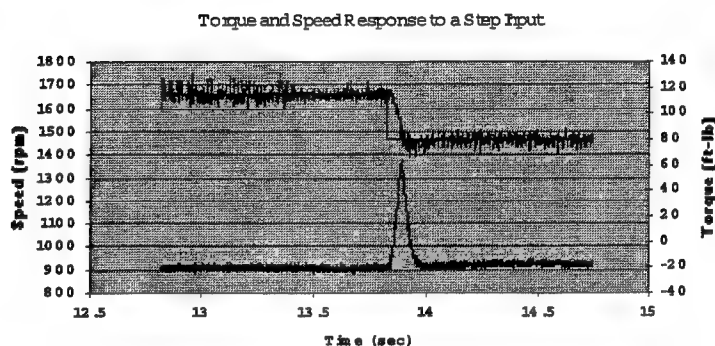


Figure 3. Speed response for transient dyno.

#### Principle (empty cavity)



#### Beer-Lambert law

$$I_t = I_0 \cdot \exp(-\sigma \cdot L \cdot N) = I_0 \cdot \exp(-k \cdot L)$$

#### Decay time of laser light (Cavity-Ringdown time: $\tau$ )

$$i_t = i_0 \cdot \exp\left[-\left(\frac{\text{number of reflections}}{\text{round trip}}\right) \left(\frac{\text{loss}}{\text{reflection}}\right) (\text{number of round trips})\right]$$

$$i_t = i_0 \cdot \exp\left[-\left[(1-R) + k_{\text{gas}}L\right] \left(\frac{t \cdot c}{L}\right)\right] \quad \text{PMT signal} = A \cdot \exp\left(-\frac{t}{\tau}\right)$$

#### Absorption coefficient in an empty cavity

$$k_{\text{Gas}}L = \frac{L}{\tau \cdot c} - (1-R)$$

Figure 4. CRDS system basics.

#### Q-switched DPSS laser system

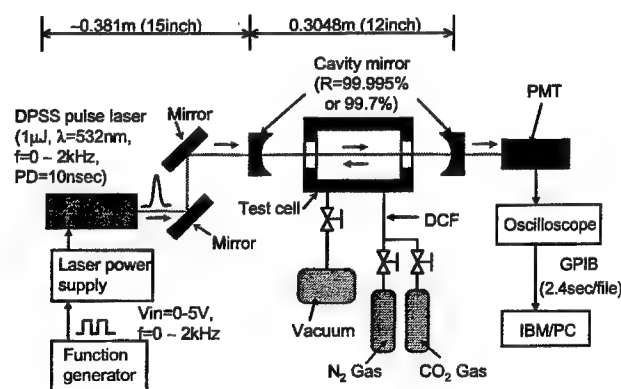
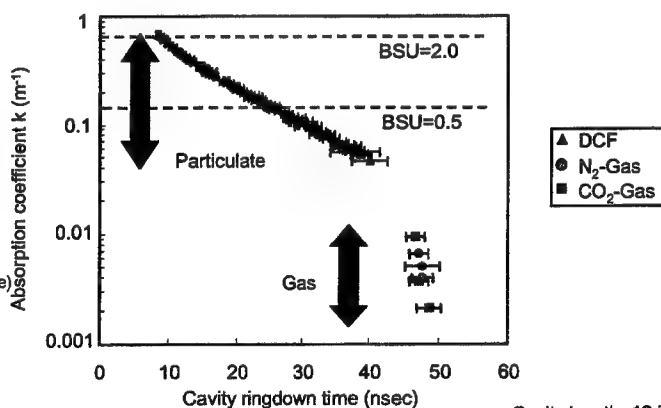


Figure 5. DPSS CRDS system

#### Absorption coefficient



Cavity length: 12 inch  
Laser: Q-switched DPSS

Figure 6. Absorption results for CRDS

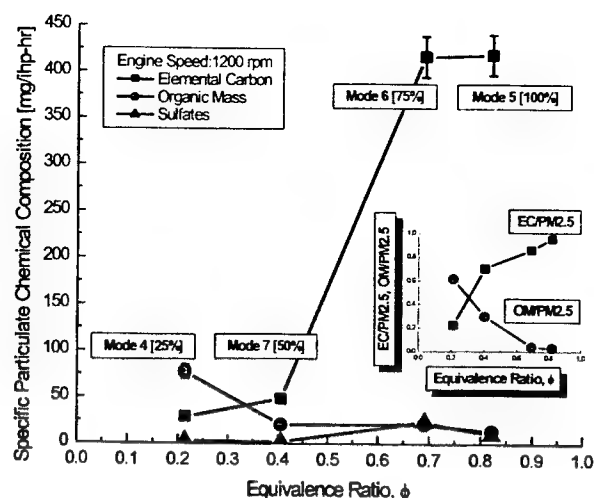
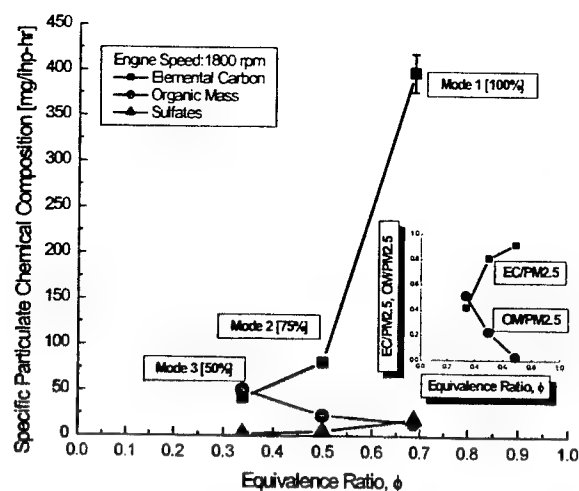


Figure 7. Distribution of Elemental Carbon, Organic Carbon and Sulfate within the Particulate versus Equivalence Ratio for 1200 RPM and 1800 RPM

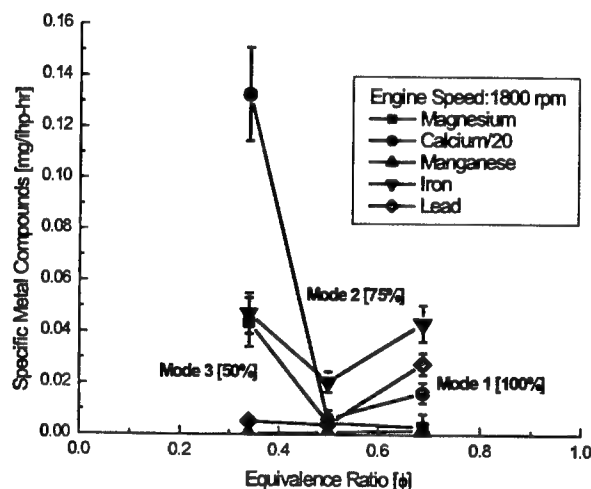
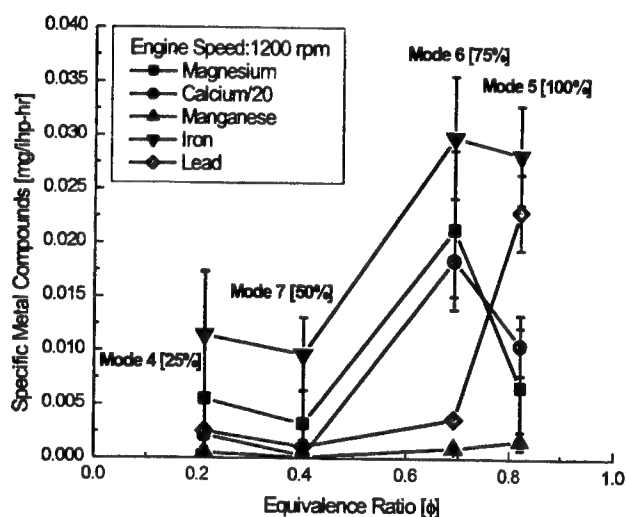


Figure 8. Metal compounds as a function of equivalence ratio and engine speed.

#### References:

1. G. R. Babbitt, and J. J. Moskwa, "Implementation Details and Test Results for a Transient Engine Dynamometer and Hardware in the Loop Vehicle Model," Proc. of the IEEE Conf. on Control Applications/Computer Aided Control System Design (CCA/CACSD), August 22-27 1999, Hawaii
2. P. Zalicki and R. Zare, "Cavity ring-down spectroscopy for quantitative absorption measurements" *J. Chem. Phys.* 102, pp. 2708-2717, (1995).
3. R. VanderWal and T. M. Ticich, "Cavity ringdown and laser-induced incandescence measurements of soot", *Applied Optics* 38, pp. 1444-1451 (1999).

# **ADAPTATION OF ADVANCED DIESEL ENGINES FOR MILITARY REQUIREMENTS UNDER SEVERE ENVIRONMENTAL CONDITIONS**

(Grant Number DAAD 19 02-1-0372)

Principal Investigator: Naeim A. Henein

Wayne State University  
Center for Automotive Research  
Engineering Building  
Detroit, MI 48202  
Tel.(313) 577 3887, Fax: (313) 577 8789  
email:henein@eng.wayne.edu

## **SUMMARY**

Military requirements cannot be met by commercial diesel engines designed to meet the stringent emission standards. The goal of this program is to develop a computer based adaptation tool to determine the engine control strategy needed to achieve the military goals of best fuel economy, high power density without any black smoke or excessive stresses on key engine parts, reliable cold starting without emitting white smoke. Further more, the strategy would enable the engine to run on JP-8 instead of the regular DF-2 fuel. The scope of this paper is to develop a model to predict the cold starting behavior of the engine if DF-2 is replaced by JP-8. JP-8 is more volatile and has a lower Cetane Number, CN, than DF-2 fuel. The model predictions are compared with experimental data on a single cylinder diesel engine tested in a cold room under various ambient low temperatures.

## **Background**

Commercial heavy-duty diesel engines are required to meet stringent emission standards for nitrogen oxides (NO<sub>x</sub>), particulate matter (PM) and Hydrocarbons. To achieve these goals, Exhaust Gas Recirculation (EGR) is used to reduce NO<sub>x</sub>, with a side effect of increase in PM. To reduce PM, very high injection pressures are required. The higher the injection pressure, the more is the energy consumed in driving the pump. To further reduce NO<sub>x</sub>, the EGR is cooled. This adds a substantial load on the engine cooling system which requires a larger coolant circulating pump, larger radiator area and larger fan. All these devices add to the volume and mass of the power train, in addition to their negative impact on peak power and fuel economy.

## **Adaptation of Commercial Engines to run on JP-8**

Military vehicles are required to run on JP-8 instead of DF-2. These two fuels have different distillation ranges, volatilities and CNs. Figures 1 and 2 show a gas chromatographic analysis of JP-8 and DF-2 respectively. JP-8 fuel contains lighter hydrocarbons than DF-2. Lighter hydrocarbons are known to be more volatile have lower CN.

The issue is to find out how would JP-8 affect the cold startability of the diesel engine at low ambient temperatures. Engine starting consists of two modes of operation:

1. Engine motoring during the cranking period

2. Engine acceleration after the start of combustion.  
The scope of this paper is to find the effect of running the commercial direct injection diesel engine on JP-8.

## Objectives

1. Develop a mathematical model that would account for the effects of fuel volatility and CN on the cranking period.
2. Determine the effect of using JP-8 fuel instead of DF-2 on the length of the cranking period. at low ambient temperatures.

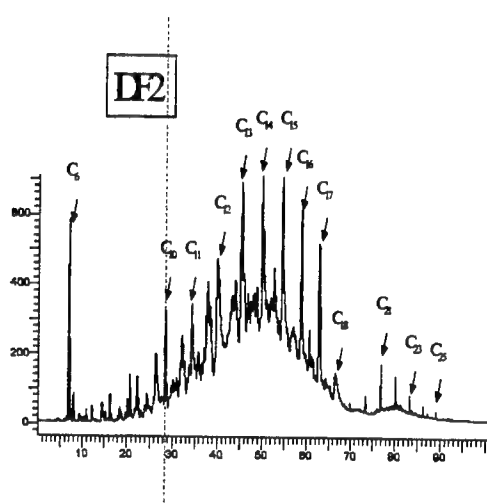


Figure 1. GC trace showing the constituents of DF-2

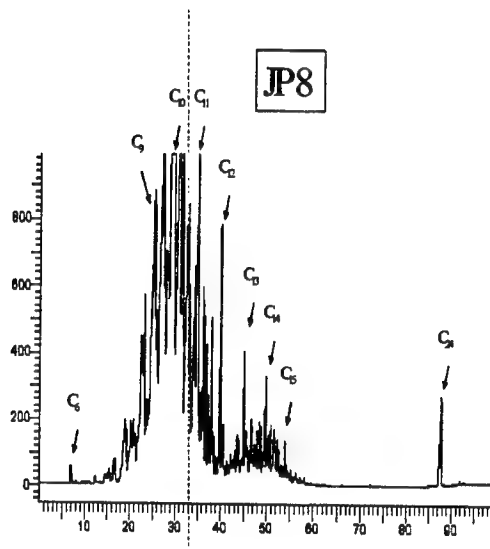


Figure 2. GC trace showing the constituents of JP-8

## A New Mathematical Model for Cranking Period

The model consists of the following sub models

1. Compression Pressure And Temperature Sub Model
  - (a) Effect of cranking period on wall temperature sub model
  - (b) Effect of accumulated fuel on compression ratio sub model
  - (c) Effect of cranking speed sub model
2. Fuel Vapor Concentration Sub Model
  - (a) Spray evaporation sub model.
  - (b) Liquid film accumulation on the wall and evaporation sub model
  - (c) Recycled fuel vapor sub model

## A New Autoignition Index (AI)

This index combines the effects of gas temperature and fuel vapor concentration

- (a) To determine the first firing cycle
- (b) To determine the length of the cranking period.

$$AI = \int_{t_{inj}}^{t_{end}} k_0 [F] \exp\left(-\frac{E}{RT}\right) dt$$

(c) For this first generation model, the engine runs on a single paraffin hydrocarbon. The analysis covered hydrocarbons having different number of carbon atoms.

The following assumptions are made

1. Autoignition occurs when AI reaches a critical value
2. The numerical value of critical AI is determined from the cold start test at normal room temperature.

AI shows that the three factors that affect the number of cranking cycles are:

1. [F], the concentration of the fuel vapor.
2. [T], the gas temperature, T
3. t, the period after the start of injection

Figure 3.

Relationship between number of carbon atoms, saturation pressure at 425 K and CN.

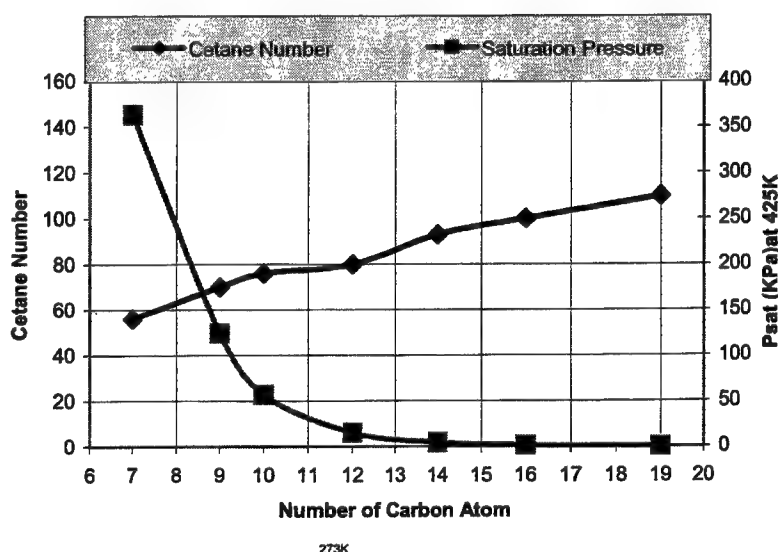
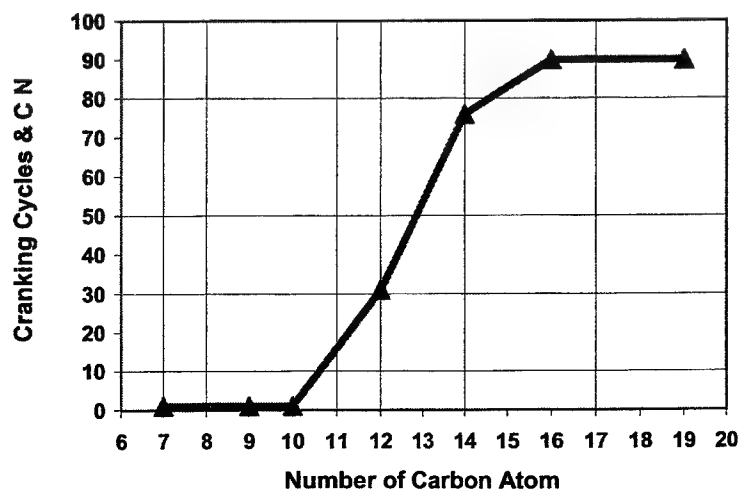


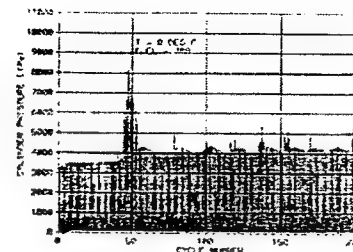
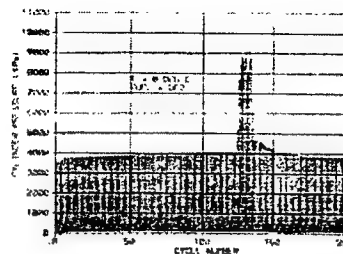
Figure 4.

Effect of the number of carbon atoms in the hydrocarbon molecule on the number of cranking cycles predicted by the model.

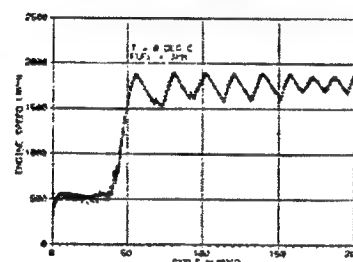
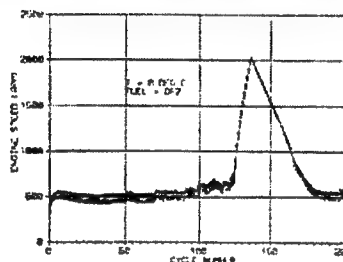


## Comparison Between The Starting Of A Single Cylinder Diesel Engine On DF-2 and JP-8. Fuel At Room Temperature = 0°C.

Cylinder gas pressure for the first 200 cycles



Instantaneous engine speed for the first 200 cycles



### Conclusions

- 1 A first generation simulation model for the cold-start cranking-period has been developed. The model indicated the following:
  - a. CN alone is not a good indicator of the number of cranking cycles.
  - b. Fuel volatility is as important as CN in controlling the cranking period.
2. A new auto-ignition index (AI) has been developed to combine the effects of volatility and the CN.
3. The model predictions indicated that the volatile paraffin components of the DF2 and JP8 are the initiators of the autoignition process at the end of cranking period.
4. The model predictions agreed with the results of experiments on a single-cylinder diesel engine

### Future Work

1. Develop a second generation model based on experimental data for the vapor pressure of the actual fuels as a function of temperature.
2. Combine the combustion instability model and the cranking prediction model to predict the HC (white smoke) emissions.
3. Extend the model to multi-cylinder heavy duty diesel engines.
4. Apply the model to determine the electronic controls strategies to reduce the cranking period, combustion instability and HC (white smoke) emissions.

### Acknowledgement

This research is a part of a program sponsored by U.S. Army Research Office, Contract number DAAD 19 02-1-0372, under the direction of Dr. David Mann.



# THERMAL IGNITION THEORY APPLIED TO DIESEL AUTOIGNITION

(Grant/Contract Number DAAG55-98-I-0433)

Principal Investigators: A. M. Mellor\*, S. L. Plee, R. J. Tabaczynski

\*Vanderbilt University, VU Station B 35192  
2301 Vanderbilt Place, Nashville, TN 37235-1592

## SUMMARY/OVERVIEW:

The focus of the program is developing engineering models for direct injection (DI) diesel engine performance and emissions. Present work is focused on development of phenomenological DI diesel ignition, combustion, and NO<sub>x</sub> models for inclusion in cycle simulation type codes that predict engine performance and emissions. Over the past year study of the ignition of hydrocarbon fuels in strained flow fields, like those found in DI diesel engines, has received primary emphasis. One phase of this work involves analysis of counterflow and liquid pool experiments using thermal ignition theory to determine global chemical ignition delay activation temperatures and is discussed below.

## TECHNICAL DISCUSSION

**Introduction:** The DI diesel engine community has used one-equation models for ignition delay in engines for many years. Wolfer [1] was the first to propose the use of an inverse Arrhenius expression for ignition delay of diesel sprays,

$$\tau_{id} = Ap^{-n} \exp(E_A / RT) \quad (1)$$

where A, n, and E<sub>A</sub> (apparent activation energy) are model constants, p and T are the charge pressure and temperature, and R is the ideal gas constant. Equation (1) lumps liquid fuel evaporation, mixing of fuel with charge, and chemical delay into one chemical kinetic term. As a result, correlations apply only to the injector/engine tested and exhibit activation energies or temperatures that can be as much as ten times lower than those obtained in well-mixed, controlled systems used to isolate and study the chemical delay. Here classical thermal ignition theory is extended to the relatively straightforward fluid mechanic environment of a counterflow burner to clarify how both chemistry and mixing can be included in a more general one-equation model. This new model is validated with ignition limit data for ethane or ethene with O<sub>2</sub>/N<sub>2</sub> either premixed or unmixed in the counterflow arrangement and liquid diesel fuel in a pool configuration. Since the overall mixing time in this burner is known *a priori*, the data can be manipulated to yield global chemical ignition delay activation temperatures for these fuels.

**Experimental:** Under ARO funding Seshadri and co-workers performed autoignition experiments at atmospheric pressure using counterflow and liquid pool configurations for three cases [2-3]. Case 1 utilizes cool premixed reactants flowing toward a heated inert gas moving in the opposite direction, case 2 involves cool gaseous fuel approaching an opposed flow of heated oxidizer, and case 3 employs a pool of liquid fuel heated by the oxidizer flow directed normal to the pool surface. For ignition in the unmixed cases, cases 2 and 3, fuel is provided from a duct

or pool (stream 1) at room temperature,  $T_1$ , and various velocities,  $V_1$ , with nitrogen as an inert diluent when the fuel is gaseous. The oxidizer and nitrogen enter from the other duct (stream 2) at velocities,  $V_2$ , and elevated temperatures,  $T_2$ , both of which are variables in the tests. The hot oxidizer from stream 2 is the heat source for the fuel, and the opposed flow induces fuel-oxygen contact at the stagnation region where the flow turns radially outward and the flame appears upon ignition. The premixed configuration, case 1, is similar, except that the gaseous fuel and oxidizer are premixed in stream 1, and stream 2 is composed of nitrogen that provides the thermal energy.

Ethane and ethene over a range of equivalence ratios were studied [2] for both the unmixed and premixed counterflow configurations. Mobil DF-2 fuel was utilized for the liquid pool ignition experiments [3]. For all fuels, the stream 2 temperatures were slowly increased from room temperature up to a critical temperature where ignition was sustained. The critical conditions for autoignition were determined by the appearance of a visible flame.

Seshadri [2] reports the stream 2 temperature ignition limit data for gaseous fuels in terms of the strain rate on the oxidizer side of the stagnation plane,  $a_2$ , defined as:

$$a_2 = \frac{2|V_2|}{L} \left( 1 + \frac{|V_1|\sqrt{\rho_1}}{|V_2|\sqrt{\rho_2}} \right) \quad (2)$$

where  $L$  is the distance between the two ducts, and  $\rho$  is density. For the case where DF-2 vapor is supplied from the pool of liquid fuel in place of the lower jet, Payer [3] simplifies Eq. (2) to

$$a_2 = \frac{2|V_2|}{L} \quad (3)$$

**Thermal Ignition in Counterflow Burner Configurations:** In his development of thermal ignition theory, Frank-Kamenetskii [4] analyzes the premixed fuel-oxidizer contents of a constant volume vessel with no ignition source other than hot walls. He finds that ignition will occur for Damköhler numbers above a constant critical value, as shown by

$$Da = \frac{\tau_{sl}}{\tau_{hc}} \geq \left( \frac{\tau_{sl}}{\tau_{hc}} \right)_{crit} = \text{constant} \quad (4)$$

where  $\tau_{sl}$  is the heat transfer time and  $\tau_{hc}$  is the kinetic time.

Thermal ignition theory is applied to the three experiments to be examined here by Mellor et al. [5]. In their derivation the heat transfer time is taken inversely proportional to the strain rate. The resulting critical value for the Damköhler number is given by

$$Da_{crit} = \left( \frac{\tau_{sl}}{\tau_{hc}} \right)_{crit} = \text{constant} = i^{-a} A e^{-E/RT_2} c_{O_2,0}^n \frac{EQ}{RT_2^2} \frac{1}{\rho c_p a_2} \bigg|_{crit} \quad (5)$$

where  $i$  is the number of moles of  $O_2$  per mole of fuel in the global reaction,  $a$  and  $n$  are the fuel and overall reaction orders in the global reaction,  $A$  and  $E$  are the pre-exponential factor and activation energy for the global reaction,  $Q$  is the fuel heating value,  $c_{O_2,0}$  is the concentration of  $O_2$ ,  $\rho$  is density, and  $c_p$  is the constant pressure specific heat. In the first experiment, oxygen and fuel enter the combustion region in stream 1 at 298 K. Substituting these values into Eq. (5), replacing concentration with mol fraction ( $x$ ), and rearranging, the ignition criterion becomes:

$$\left( \frac{\tau_{sl}}{\tau_{hc}} \right)_{crit} = \text{constant} = i^{-a} A e^{-E/RT_2} \left( \frac{x_{O_2,1}}{RT_1} \right)^n \frac{EQ}{c_p T_2} \frac{p^{n-1}}{a_2} \bigg|_{crit} \quad (6)$$

In the second and third experiments, both involving diffusion flames, fuel enters in stream 1 at 298 K, while oxygen and nitrogen are provided by stream 2 at  $T_2$ . For these cases, Eq. (5) can be written to give the ignition criterion as:

$$\left( \frac{\tau_{sl}}{\tau_{hc}} \right)_{crit} = \text{constant} = i^{-a} A e^{-E/RT_2} X_{O_2,2}^n \frac{E}{R} \left( \frac{p}{R} \right)^{n-1} \frac{Q}{c_p T_2^{n+1}} \frac{1}{a_2} \Big|_{crit} \quad (7)$$

If all constant terms in Eq. (6) or (7) are combined and the logarithm of the result is taken, Eq. (8) is obtained:

$$\ln \left( a_2 p^{1-n} T_i^n T_2 \right) = -\frac{E}{RT_2} + B \quad (8)$$

where  $i = 1$  for premixed cases,  $i = 2$  for unmixed cases, and  $B$  is a constant. Following Spadaccini and TeVelde [6],  $n$  might be assigned values of 1 or 2, at least for DF-2. Equation (8) indicates how a semi-logarithmic graph involving the strain rate, pressure, and hot stream temperature at the ignition limit can provide an overall activation temperature ( $E/R$ ) from the test results.

**Results:** The counterflow burner ignition data from Seshadri [2] are graphed in the form of Eq. (8) in Fig. 1 for  $n$  equal to two. The activation temperatures ( $E/R$ ) and constant terms ( $B$ ) determined from the best-fits shown in Fig. 1 and from a similar graph for  $n$  equal to one are presented in Table 1 along with the fit statistics.

**Table 1: Activation temperature ( $E/R$ ), y-intercept ( $B$ ), and fit statistic for each fuel and test configuration for  $n = 1$  and  $n = 2$ .**

	$n = 1$			$n = 2$		
	( $E/R$ ) (K)	$B$	$R^2$	( $E/R$ ) (K)	$B$	$R^2$
ethane (premixed)	18918	33.54	0.9990	18918	27.71	0.9990
ethene (premixed)	19448	34.13	0.9999	19448	28.29	0.9999
ethane (unmixed)	21204	38.27	0.9900	22358	34.80	0.9908
ethene (unmixed)	23206	40.73	0.9872	24315	37.22	0.9883
diesel (liquid pool)	22067	38.18	0.9987	23242	34.72	0.9988

The correlated values of activation temperature range from 18900 to 24300 K for all test cases. Higher global activation temperatures are indicated for the unmixed cases than for the premixed case, indicating a relative ease for oxidative pyrolysis. However, at similar strain rates ignition occurs at lower temperatures for the unmixed cases. The assumed value of  $n$  does not contribute to the correlated values of activation temperatures for the premixed test case (the stream 2 temperature term on the left side of Eq. (8) is independent of  $n$ ) and contributes only slightly to the values for the unmixed and liquid pool test cases since the range of  $T_2$  temperatures is small and the pressure is maintained at one atmosphere for all tests. The activation temperatures reported in Table 1 for ethane and ethene are comparable to those presented in the literature for premixed or well-mixed fuel-oxidizer systems in similar ranges of temperature, pressure, and equivalence ratio, confirming the validity of the approach suggested here [5]. No comparison of this type is possible for diesel fuel.

**Future Efforts:** Thermal ignition theory has been applied to DI diesel sprays in a manner similar to that discussed above [7]. The results presented here indicate that the activation temperature of diesel fuel is  $\sim 23000$  K. With the diesel fuel global ignition delay activation

temperature known, an appropriate expression for the mixing time in a diesel spray is now being investigated using results of injection into a constant volume bomb and DI diesel engine tests.

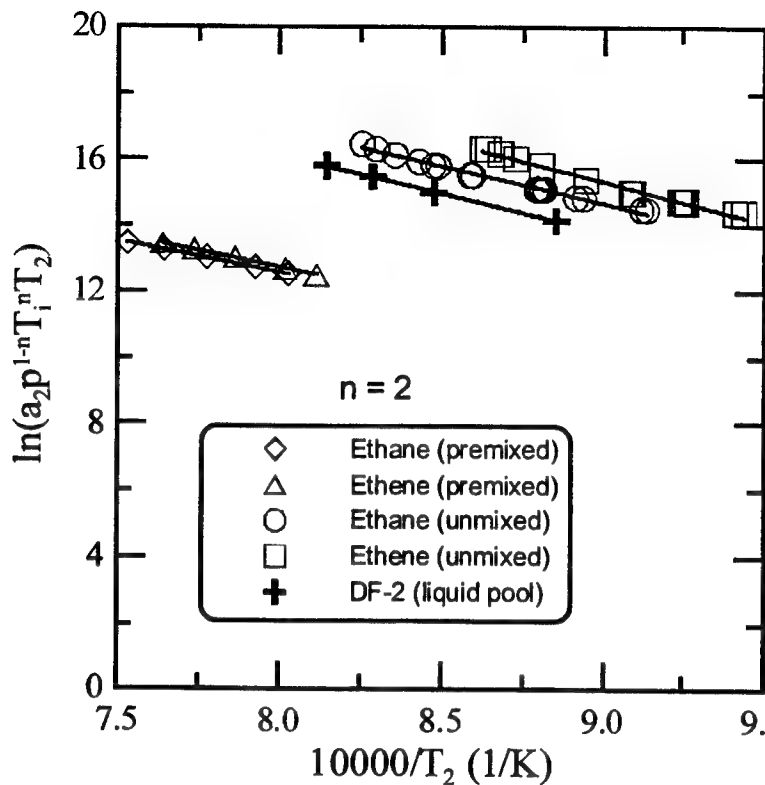


Figure 1: Results of model given by Eq. (8) applied to counterflow burner data for  $n = 2$ . Index  $i = 1$  for premixed cases and  $i = 2$  for unmixed/liquid pool cases.

#### References:

- 1) Wolfer (1938), "Ignition lag in diesel engines," VDI-Forschungsheft No. 392, Translated by Royal Aircraft Establishment, Farnborough Library No. 358, Aug. 1959.
- 2) Seshadri, K. (2002), "Chemical kinetic characterization of autoignition and combustion of diesel and JP-8," ARO/AFOSR Contractors Meeting in Chemical Propulsion, Dayton, OH.
- 3) Payer, W. (2002), "Chemical-kinetic characterization of autoignition and combustion of liquid fuels," presentation dated 24 May.
- 4) Frank-Kamenetskii, D. A. (1969), Diffusion and Heat Transfer in Chemical Kinetics, Second Edition, Plenum Press, New York.
- 5) Mellor, A. M., Russell, S. C., Humer, S., and Seshadri, K. (2003), "Thermal ignition theory applied to diesel engine autoignition," paper submitted to the Journal of Engine Research.
- 6) Spadaccini, L. J. and TeVelde, J. A. (1982), "Autoignition characteristics of aircraft-type fuels," Combustion and Flame, Vol. 46, pp. 283-300.
- 7) Mellor, A. M., Plee, S. L., and Tabaczynski, R. J. (2002), "A phenomenological model for autoignition in direct injection diesel engines," ARO/AFOSR Contractors Meeting in Chemical Propulsion, Dayton, OH.

# STUDY OF IN-CYLINDER REACTIONS OF HIGH POWER-DENSITY DIRECT INJECTION DIESEL ENGINES

(ARO Contract no. DAAD19-01-1-0766)

Principal Investigator: KT Rhee

Rutgers, The State University of New Jersey  
Mechanical and Aerospace Engineering Department  
98 Brett Road  
Piscataway, NJ 08855-0909

## OVERVIEW:

Direct-injection (DI) Diesel or compression-ignition (CI) engine combustion process is investigated when new design and operational strategies are employed in order to achieve a high power-density (HPD) engine. This goal is being achieved by developing quantitative imaging and speciation methods of in-cylinder reaction processes.

New methods being used in the study include: (1) a digital imaging system with consisting of five (5) units of high-speed cryogenically cooled infrared focal plane arrays operated by a single electronic-control-package, (2) a four-color-method (FCM); (3) an optical DI-CI engine, (4) Rutgers Animation Program (RAP) and (5) new electronic packages for imaging system.

During the reporting period, the construction of new five-camera system comes to near completion, which will permit acquisition of four sets of spectral digital image and a set of spectra distribution. An entirely new data processing method (i.e., FCM) is being constructed in order to process raw data from the imaging system. For this, a new optical DI-CI engine (using a Cummins 903 unit) has been constructed. In addition, for handling and processing of results from the above, a new RAP program has been developed. Also a new electronic control system is being fabricated.

## TECHNICAL DISCUSSION

**Five-Camera-Imaging-System.** In addition to improvements (as explained later) made on the existing four-camera high-speed spectral infrared imaging system (SIS), a new optical package has been *designed and fabricated* that includes a unit of high-speed IR digital cameras (Modified Czerny-Turner IR Spectrometer, MCTIRS) as shown in Fig. 1. This is placed right above the SIS so that when both systems are operated four sets of spectral images and a spectra distribution are simultaneously captured at successive instants of time. The MCTIRS has been designed to capture distributions of spectra within the spectral range the SIS. When four geometrically identical images in respective spectral bands and a spectra distribution are simultaneously obtained at high rates from the combustion chamber during the preflame and combustion periods, an improved understanding of complex DI-CI

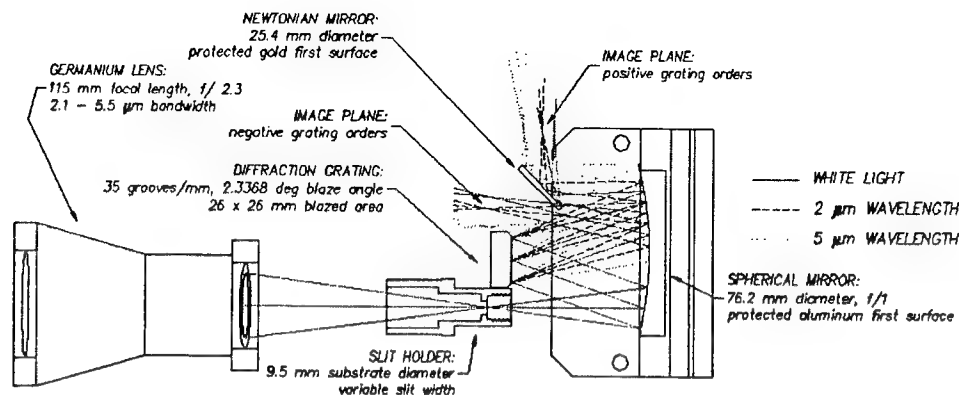


Fig. 1. Modified Czerny-Turner Infrared Spectrometer.

engine processes will be achieved. Since pressure-time history is also included in analysis of those results obtained at high rates in the SIS-MCTIRS system, a new animation program of displaying six images for each experiment is required, which is being done as explained later. The new unit will be explained more in the presentation.

**Four-Color Method (FCM).** Because of limitations and difficulties of *our* earlier spectral methods of achieving quantitative imaging (i.e., determination of distributions of temperature, and species within combustion products), an “entirely” new data processing method is introduced. Mentioning the limitations/difficulties, the mapping method (we introduced earlier) is effective in solving low degree problems (e.g. two spectra data processing) but when the number of unknowns increases (degree of 3 or 4, like we face at present), generation and manipulation of “spatial” iso-intensity curves becomes difficult to achieve. Also due to its extreme sensitivity to “imperfect” measurements, the error rate is expected to be high. Our new band ratio method (including pressure effects) is applicable in optically thin objects with the assumption that other strong radiation effects (e.g. from soot) may be neglected, which, however, is effective in simple cases (e.g. SI engine operated by gaseous fuel) but not in real-world complex engines (e.g. compression engine environment). Our multi-band iteration method was to “theoretically” eliminate/minimize those problems mentioned above. It is often difficult, however, for the iteration to converge in high dimension-coupled-problems, which stems from, as we found later, that there are multiple solutions to a set of (measured) radiation intensities. (Typically, one scenario of a higher wall temperature with low soot concentration versus another having a low wall temperature and high concentration/temperature soot.) The iteration, therefore, has hit the so-called intervention area.

The new FCM technique has been developed based on approaches employed in non-engineering fields, as briefly explained next. First, the basic idea of the approach is to divide the 4D unknown space ( $T_{\text{gas}}$ ,  $T_{\text{wall}}$ , [water], and [soot]) to form localized sub-domains, as indicated by

$$I_{\lambda_i} = f_{\lambda_i, P, L, \epsilon_{wall}}(T_{gas}, T_{wall}, [water], [soot]), I = 1, 2, 3, 4 \quad (1)$$

where,  $S = \{T_{gas}, T_{wall}, [water], [soot]\}$  is the combustion state vector and  $I_{\lambda_i}, I = 1, 2, 3, 4$  is the intensity vector.

Thereby escaping from the intervention areas, within each sub-domain, the solution(s) are found, i.e., a “divide-and-conquer” approach. One of the methods explored for such area/domain subdivision problems may be the famous “postal office problem.” Briefly, it is to distribute sets of “postal offices” (sites) onto a planner area and then divide the area into subdivision according to those sites such that traveling from a point to the office in the same division cost less than traveling to any other post offices in the area (e.g. Vornoi assignment model and Voronois diagram). Basically, we consider all solutions of the FCM as “sites.”

Among difficulties is to determine subdivisions in close matches (such as Voroni diagrams leading to information about “sites” i.e., solutions). After some considerable amount of evaluation we found that our possible solutions are finite in the order of dimension and therefore “sites” in the space are geometrically sparse and leave a lot of space for subdivision manipulation.

When allowing approximately five-percent errors in individual spectral intensities numerous groups of 4D solutions are identifies, by using a step of the pattern recognition/classification method. Note the pattern classification has been widely explored in the field of artificial intelligence (AI) in non-engineering fields, including medical imaging, stock-market analysis, marketing, language modeling, electronic commerce, and speech recognition. (More discussion in the presentation.)

However convenient the migration idea it might be, there is no ready-to-use training database for our FCM. Rather we need a training database consisting of “experienced” data with proven credibility. Note that in the past we processed data from the *NASA* handbook and built a simulation model in analytical form, from which we generated intensity sets from desired combustion states. However, there is an alternative way to represent the model, i.e. to represent it by data instead of analytic relations, we see the model as a mapping from a combustion state vector space  $R^4(S)$  to an intensity vector space  $R^4(I_{\lambda_i})$ , consisting of data entries. That is, *NASA* model (data):  $R^4(S) \Rightarrow R^4(I_{\lambda_i})$ . Again, relation shown here demonstrates representation of *NASA* single-line-group (SLG) radiation model by data as specified in relationship in Eq. (1), instead of analytical equations.

Transformation of the model into data form is to acquire an un-biased *training database*. This includes discretizing the “continuous valued patterns” in combustion states, indexing and organizing entries for fast access, etc. A training database should be implemented to ensure completeness and compactness, i.e., the classification results based on it is complete without false dismissals while keeping the training set as compact as possible. A great deal of effort has been made to investigate a substantial subset that satisfies both requirements.

After all possible solutions are obtained, they are discriminated against other factors such as engine running conditions, a corresponding crank angle, air/fuel ratio, and also expected species concentrations. Thereby abnormal results are discarded to find the final solution. More details are explained in the presentation.

**Optical DI-CI Engine.** In addition to the existing single-cylinder Cummins 903 engine with optical access via the cylinder head, construction of a new optical Cummins 903 V-2 engine has been completed during the reporting period. Unlike the limited view of a single spray in the former engine, images of multiple spray images can be obtained in the new engine having a hollow extended piston.

In order to achieve HPD CI processes, the engine will be mated with the most advanced high-pressure electronically controlled injection system to be introduced in the field. The core purposes of developing a new optical engine based on a real-world engine is to achieve the same engine design details (that are known to deliver the most desirable power output and emission characteristics) in this engine for in-cylinder investigation. Details of engine construction and results will be shown in the presentation.

**New Rutgers Animation Program (RAP).** The Rutgers Super Imaging System (SIS) having four high-speed digital camera, a part of the five-camera system explained earlier, has greatly been improved as follows. Unlike the conventional high-speed imaging method of obtaining successive images from only a single cycle at a time, the present SIS has been advanced to be capable of achieving the same in four spectral bands from as many as 100 *consecutive cycles*. This was achieved by incorporating the SIS with the most advanced digital handling units introduced in the field supported by our new software packages. When even merely a set of results is obtained by using this SIS, the amount of data to be reviewed is beyond the ability of the existing RAP. An entirely new RAP (called RAP II) has been developed in order to meet need of handling such massive amounts of images, which will be explained in the presentation.

**New Electronic Circuit Package.** Electronic control packages of the SIS for the performance explained above have been all designed and fabricated in our laboratory, which have experienced various limitations, including erratic function and failure of electronic components. Often some malfunction of the system units last for a long period time without knowing the source of problems.

In order to achieve more predictable data acquisition, and trouble-free operation, the circuit boards have all been newly designed and fabricated by an outside specialty company. In spite of its high cost and (also high hope), the delivery has greatly been delayed to date when this report is being prepared.

When the finished boards are delivered, construction of the five-camera system mentioned earlier will be greatly expedited. It is hoped to present some results by the time of our meeting in Williamsburg.



# DEVELOPMENT OF A LINEAR ENGINE/ALTERNATOR

Grant/Contract Number: DAAD19-01-1-041

Principal Investigators: Parviz Famouri\* and Nigel Clark\*\*

*West Virginia University*

*\*Lane Department Of Computer Science and Electrical Engineering*

*\*\* Department of Mechanical and Aerospace Engineering  
Morgantown, WV 26506*

## Summary/Overview

Internal combustion engines convert the chemical energy of fuel into kinetic energy during combustion, resulting in linear motion of the pistons. In conventional engine/alternator sets, the slider-crank mechanism converts the linear reciprocating motion of the piston into rotating motion. A rotating generator converts this kinetic energy into electrical energy. Motion conversion from linear to rotating is eliminated in linear engine/alternators by solidly linking the moving parts of the alternator to the pistons, improving the overall efficiency of the system.<sup>1</sup> The result is a simple engine/alternator set comprised of half as many components as a conventional engine/alternator, potentially reducing manufacturing costs and engine maintenance.<sup>2</sup> This report outlines the progress of the research and development of a 2<sup>nd</sup> generation two-stroke, diesel, dual piston, two-cylinder linear engine/alternator unit. A time-based dimensionless numerical simulation program was used to test and predict the performance of the linear engine for a variety of dimensions and operating conditions, with results indicating that compression is strongly affected by the fuel/air ratio. An electromagnet linear alternator (EMLA) is being developed with the goal of providing enough force to actuate the engine assembly until the compression ratio that will support spark-ignited fuel combustion is reached. A prototype has been constructed and operated with limited success.

## Technical Discussion

### *Linear Engine Time-Based Dimensionless Modeling*

A numerical simulation program was developed using the principles of a previous four-stroke compression ignition linear engine model, with changes made to make it possible to investigate the two-stroke compression ignition linear engine in this study.<sup>3</sup> To generalize results, the program was altered to provide output dimensionless parametric analysis. Dimensionless displacement, mass, and time were defined with respect to effective stroke length, moving assembly mass, and exhaust port pressure immediately after port closure. The program inputs are bore to effective stroke length,  $\lambda$ , dimensionless injection position, dimensionless load constant for the alternator, and premixed and diffusive combustion ratios. The outputs of the program are dimensionless frequency, dimensionless indicated power, dimensionless friction force, dimensionless average velocity, dimensionless instantaneous velocity, indicated efficiency, compression ratio, dimensionless indicated power/generator mass, dimensionless energy/generator mass, dimensionless indicated power/cylinder volume, and dimensionless energy/generator volume.

The study revealed that with  $\lambda$ , or air to fuel ratio relative to stoichiometric air to fuel ratio, of 3, indicated efficiency increased with increasing bore/effective stroke length ratio, as illustrated in Figure 1(a). Figure 1(b) illustrates that the highest compression ratio occurred for a bore/effective stroke ratio of 2.2. Changing the bore/effective stroke ratio above or below 2.2 resulted in a lower compression ratio. Highest dimensionless indicated power per generator mass was for a bore/effective stroke ratio of 2. Results also indicated that injecting the fuel when the piston approaches the cylinder head during the compression stroke, and burning the fuel with a premixed combustion ratio of 20% with 80% high diffusive combustion would enhance the indicated efficiency, relative to injecting the fuel while the piston far from cylinder head during compression stroke or burning the fuel with a premixed combustion ratio of 40% with 60% high diffusive combustion. The decrease in the indicated efficiency when burning the fuel with a premixed combustion ratio more than 20% was due to the rapid increase in the in-cylinder pressure and the increase in the heat loss associated to this increase.

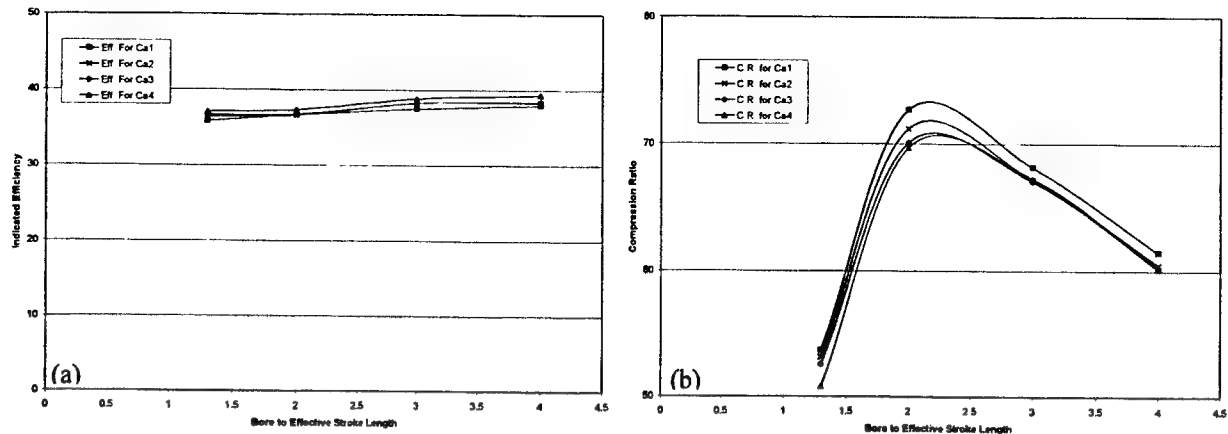


**Figure 1: (a) Indicated Efficiency Versus Bore to Effective Stroke Length for  $\Lambda = 3$ , and Dimensionless Injection Position=0.081. (b) Compression Ratio Versus Bore to Effective Stroke Length for  $\Lambda = 3$ , and Dimensionless Injection Position=0.081.**

### *Linear Alternator Electromagnetic Modeling*

An Electromagnet Linear Alternator (EMLA) has been modeled for inclusion on the linear engine. Compared to permanent magnet linear alternators (PMLA), the EMLA has several advantages.<sup>4</sup> The major advantage is that the field flux of the machine is controllable, allowing active regulation of the output voltage. This design allows for easy starting of the engine by controllable electro-magnetic force with the alternator operating as an actuator, and is smaller and more efficient than PMLA. Disadvantages of the EMLA include the need for connection to the external excitation source, and heating that can limit the current density of the field windings, resulting in strength of field.

To accomplish the design and optimization of the alternator, a finite element analysis package was employed to determine the distribution of various design parameters, including the armature and field slot size, the number of stator teeth, and the number of poles. Additional analysis was performed to determine other parameters, such as the wire size, and the number of winding turns for a given wire gauge and current density. A parametric study was performed to determine the effects of changes to each of the machine parameters on the operation of the system, the flux distribution, and thrust force at different moving position along the stroke length. The alternator will work as an actuator to crank the engine, providing enough force to create the necessary pressure and temperature condition to start the engine. The 4-pole linear alternator was modeled for 5 KVA of output power at a frequency of 51 Hz, with an efficiency of 90% and  $13 \times 10^3 \text{ N/m}^2$  of specific thrust. Figure 2(a) and (b) show axis-symmetric flux density and flux lines at the zero position, indicating a field current density of  $3.6 \text{ A/mm}^2$ . The airgap density is around 1.4 Tesla. Figure 2(c) shows the parametric simulation result of the flux linkages for each coil at each position for a full stroke length.

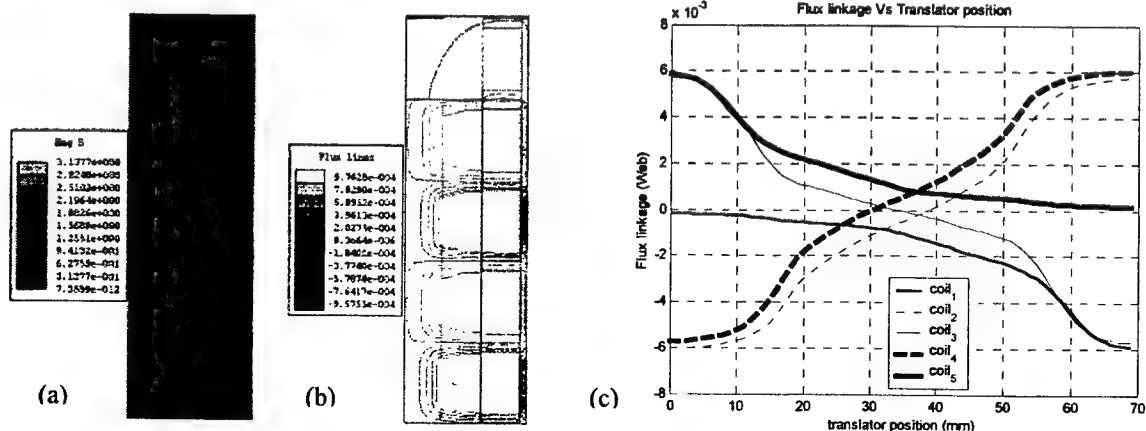


**Figure 2. (a) Flux density and (b) flux lines at zero position. (c) Stator coil #1 -#5 flux linkage**

### Prototype Design and Operation

Design and prototyping of a 2<sup>nd</sup> generation linear/engine is underway. The current stage of this research employs an iron slug linear actuator, similar in size and weight to the EMLA discussed earlier, which is used to start the dual-piston, two-stroke, compression-ignition linear engine, illustrated in Figure 3(a), in order to develop the optimum starting parameters. After stable operation of the engine is achieved, the iron slug will be replaced by the EMLA. To decrease development cost, the engine has been constructed from off-the-shelf components. For the same reason, the design utilizes loop scavenging, performed by pressurized (80 psi) house air. Although there is no side force on the diesel-lubricated piston, lubricant was added to the air via an air tool lubricator unit to prevent excessive wear. The design is based on Kawasaki motorcycle components (cylinders and pistons), with a bore of 76 mm. The engine uses a Bosch common rail direct diesel injection system, with a pump and injectors from a 1.9L Mercedes common rail diesel engine. The maximum stroke is 74 mm, restricted by the cylinder heads. The rest of the engine has been manufactured in house. At this stage of development, two sets of coils are used as stators, with the iron slug attached to the connecting rod to move the piston assembly. The starter solenoids are supplied by automotive batteries via isolated gate bipolar transistors (IGBTs), with a cranking signal provided from a signal generator. This method allows the engine to have a variable cranking frequency, which aids in finding the highest compression ratio during cranking.

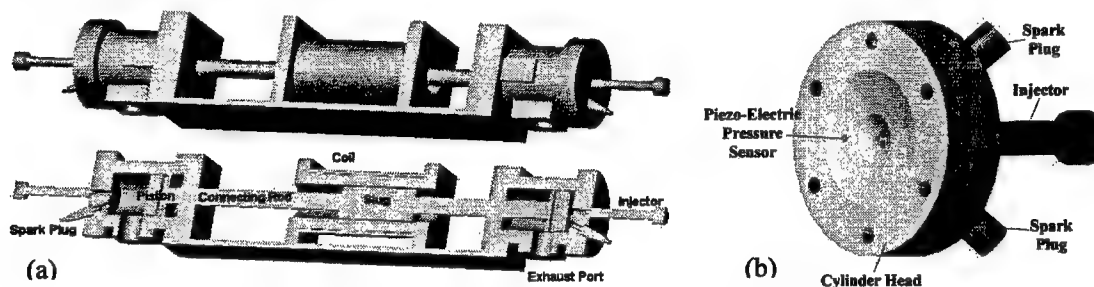


Figure 3: (a) Prototype engine design and (b) detailed view of the cylinder head.

Each cylinder head includes an injector, a piezoelectric pressure sensor, and two spark plugs (Figure 3(b)). The ground electrode has been removed from each spark plug, resulting full isolation between plugs and cylinder heads. A fuel furnace ignition coil has been used to provide continuous arc between the two plugs for each cylinder while starting the engine. This starting aid is necessary because, even with the variable cranking frequency, the iron slug actuator is unable to deliver a high enough compression ratio to start the engine. Using 60 V at a cranking frequency of 23 Hz, a compression ratio of 4:1 was measured without the continuous arc, too low to start the engine. The continuous arc improved this situation by igniting the injected fuel during engine start. In theory, after the first ignition, the arc can be switched off because ignition in the continuous-arc cylinder creates a high enough compression ratio in the other cylinder for the fuel to auto-ignite, allowing the engine to sustain operation. To date, the iron slug actuator provides sufficient starting force, but combustion in both cylinders is sporadic, with the majority of linear engine operational tests resulting in single cylinder combustion. However, an injector controller has been designed that gives a reliable injector timing sequence, and improved operation is anticipated.

### Injector Controller

The injector control system is comprised of a MICRO-EPSILON inductive potentiometric position sensor, a Microchip 40 MHz microcontroller, and two signal shaping, high-pressure injection drivers. The main task of the microcontroller is to operate the high-pressure injectors in correlation with shaft position. The microcontroller reads the analog signal from the shaft-mounted position sensor and converts it to a digital value that can be used in determining injection timing. The user can adjust the timing of the left and right injection by setting the triggering variables on the microcontroller. When the position sensor output reaches the desired triggering value, the microcontroller signals the injection shaping circuits to fire. Figure 4(a) illustrates injector timing response using signal generator input to simulate pressure sensor output. Since the injector solenoids require a slightly higher current at opening time, a simple signal-shaping circuit was applied to the output of the microcontroller to sink enough current to overcome constrictive forces. Figure 4(b) shows actual injector solenoid operation during linear engine operation using the potentiometric position sensor signal as the control input.

Research is progressing toward the goal of a functioning linear engine/alternator system. Modeling of engine combustion and alternator geometry is being refined, and design modification of the prototype engine to achieve continuous ignited combustion operation is underway. After reliable operation is achieved, implementation and testing of the alternator in place of the iron slug actuator will begin.

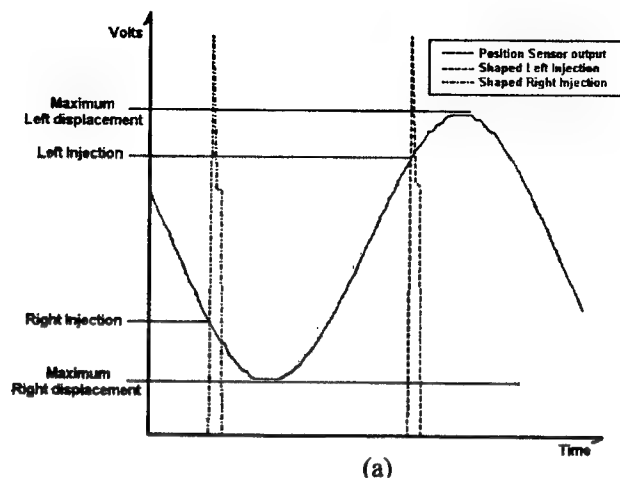
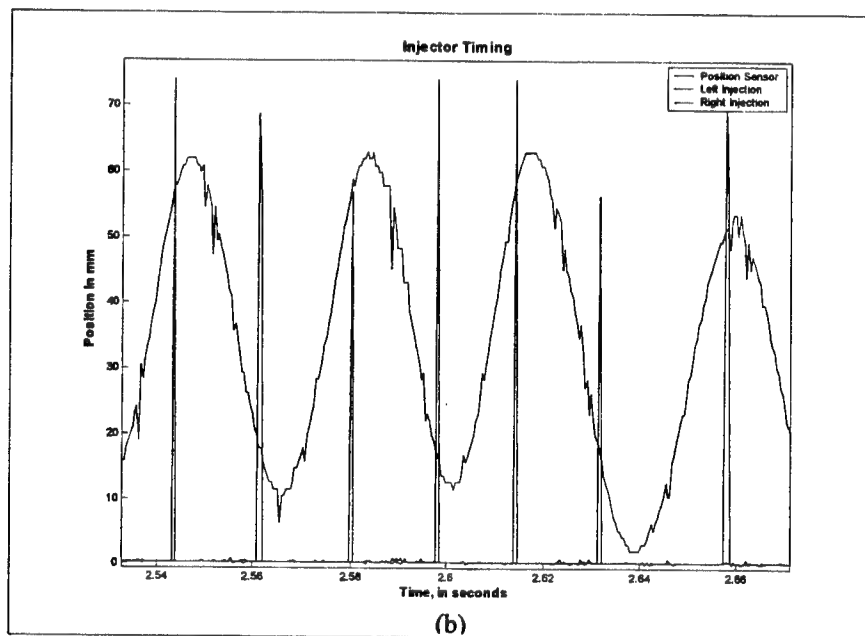


Figure 4: (a) Simulated injector timing sequence and (b) injector timing data during linear engine operation.



## References

1. Shoukry, E.; Taylor, S.; Clark, N.; Famouri, P.; "Numerical simulation for parametric study of a two-stroke direct injection linear engine," SAE-2002-01-1739, 2002.
2. Braun, A. T.; Schweitzer, P. H.; "The braun linear engine," SAE-730185, 1973.
3. S. Petreanu; "Conceptual Analysis of a Four-Stroke Linear Engine," Dissertation, West Virginia University, 2000.
4. Brombowski, A.; Cheskis, L.; Podlesak, T.; Famouri, P.; Clark, N. N.; Taylor, S.; "Analysis of a permanent magnet diesel alternator," ARO internal report.

# POROUS MEDIA COMBUSTION CONCEPTS FOR PROPULSION GAS TURBINES

(Grant/Contract Number DAAD 190210082)

Principal Investigators: Ajay K. Agrawal, and Subramanayam R. Gollahalli

School of Aerospace and Mechanical Engineering  
University of Oklahoma, Norman, OK 73019

## SUMMARY/OVERVIEW:

Combustion using porous inert media offers several benefits for propulsion gas turbines such as high power density, stable operation over a wider range, homogeneous temperature field, lower combustion noise and reduced emissions of NO<sub>x</sub> and CO. In this study fuel atomization, fuel/air mixing, and combustion processes using silicon carbide coated Carbon-Carbon composite porous materials are investigated experimentally and computationally. Combustion and pre-combustion processes are studied independently to isolate the underlying physics of fuel preparation and exhaust emissions. Kerosene fuel is atomized using an air-assist injector placed upstream of the porous combustor. Experimental facilities for both types of studies have been developed and qualified. Preliminary spray characteristics and fuel/air mixing were obtained. Evaporation histories of fuel vapor have been computed with and without the porous media. Combustion experiments were conducted with flame stabilized either on the surface or inside the porous media. Results demonstrate extension of lean-blow off limit with flame stabilized inside the porous media leading to lower NO<sub>x</sub> and CO emissions.

## TECHNICAL DISCUSSION

Porous media combustion operates on the concept of recirculating energy from products to reactants or the "excess enthalpy flame" introduced by Hardesty and Weinberg [1976]. The flame may be stabilized on the surface or inside the porous inert media as illustrated in Figure 1. For interior combustion, an upstream fine pore region is used to prevent propagation of the flame stabilized in the coarse pore region.

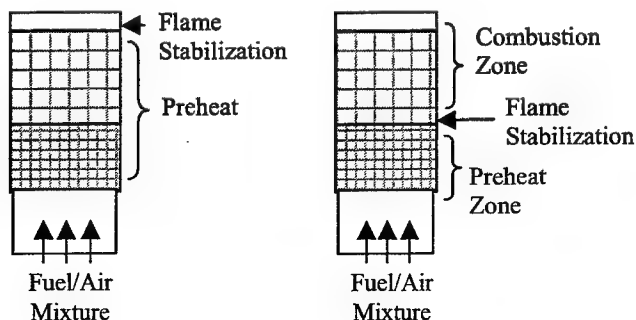


Figure 1. Schematic Representation of (a) Surface Combustion, (b) Interior Combustion

Howell et al. [1996], Viskanta [1995], and Trimis and Durst [1996] have reviewed the PIM combustion research. Kotani and Takeno [1982] found that a porous burner increased the laminar flame speed by more than an order of magnitude. Subsequently, various aspects of combustion with PIM have been investigated experimentally and numerically. Recently, Pickenacker et al. [1999] have developed several commercial concepts involving combustion inside PIM. Previous research in PIM combustion has typically focused on combustion of gaseous fuels. Kaplan and Hall [1995] have demonstrated that a stable, low-emission burner for liquid fuels is possible. In their configuration, heptane was sprayed on the combustion section of a porous ceramic burner using an oil spray nozzle. They reported stable combustion for heptane at equivalence ratios ranging from 0.57-0.67. Further, they reported very low emissions of CO and NO<sub>x</sub>; CO varied from 3 to 7 ppm and NO<sub>x</sub> varied from 15 to 20 ppm when corrected for 3% oxygen.

A crucial component of the PIM combustion is the porous material. Unlike porous ceramics considered in previous studies, we are considering silicone-carbide coated carbon-carbon composites. When manufactured properly, the C-C composites have the highest specific strength of any known material and retain their strength at high temperatures. Figure 2 shows sample materials with 32 and 4 pores per cm (ppcm).

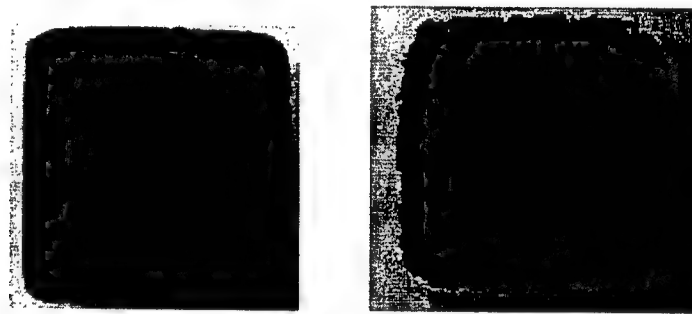


Figure 2. Silicon-carbide coated C-C composite porous materials, (a) 33ppcm, (b) 4ppcm

We are investigating fuel atomization, fuel/air mixing and combustion processes using Kerosene fuel. Figure 3 illustrates experimental configuration used for these studies. It consists of four sections: the inlet section, the fuel vaporization/mixing section, the PIM section, and the exhaust or emissions shield. The fuel is atomized using an air-assist injector located upstream of the PIM section. The injector can be traversed to control the distance between the injection point and the PIM inlet. Two test sections were built; one to study fuel atomization and fuel/air mixing processes upstream of the PIM. This test section shown in Figure 4 contains transparent windows for optical measurements using phase-Doppler particle analyzer. In this setup, the porous matrix is heated electrically to simulate the thermal feedback from the combustion zone. A test section similar to that in Figure 5, without the optical windows, was used for combustion experiments.

The fuel evaporation process with and without the porous media was simulated computationally assuming point injection. Non-Darcy flow is considered in the porous media, assumed as a

momentum sink. Effective thermal conductivity of the porous medium is calculated by taking the volumetric average of fluid and solid media. Turbulence was modeled using the standard  $k-\epsilon$  turbulence model. A control-volume based discretization method is adopted to solve the governing equations. Computations were performed for air and fuel inlet temperatures of 473K and 298K, respectively and porous media temperature varying between 473K and 583K. Radial profiles of kerosene vapor concentrations were captured downstream of the injection point.

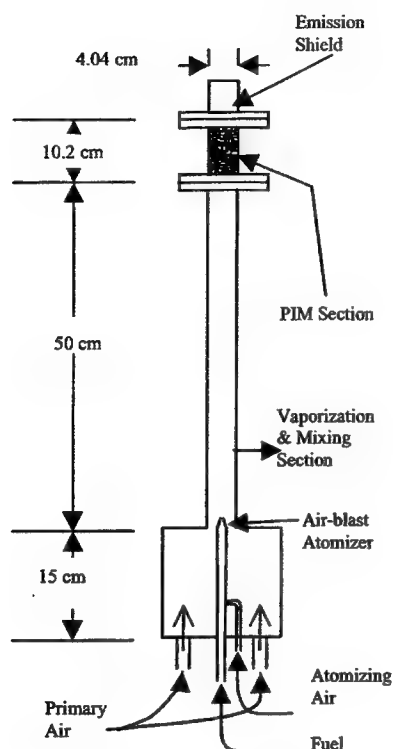


Figure 3. Schematic Diagram of the Experimental Setup

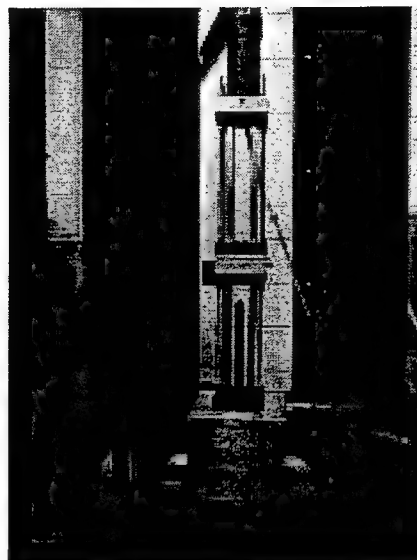


Figure 4. Transparent Test Section for Fuel Atomization and Fuel/Air Mixing Studies

Figure 5a shows vapor concentration profiles at various axial locations (measured from the PIM inlet) when the porous media and air temperature are the same, i.e., 473K. In this case, little fuel evaporation is observed. Moreover, the vapor concentration profiles with and without the porous media were found to be nearly the same. Increasing the porous media temperature to 583K significantly improved fuel evaporation and mixing rates as shown in Figure 5b.

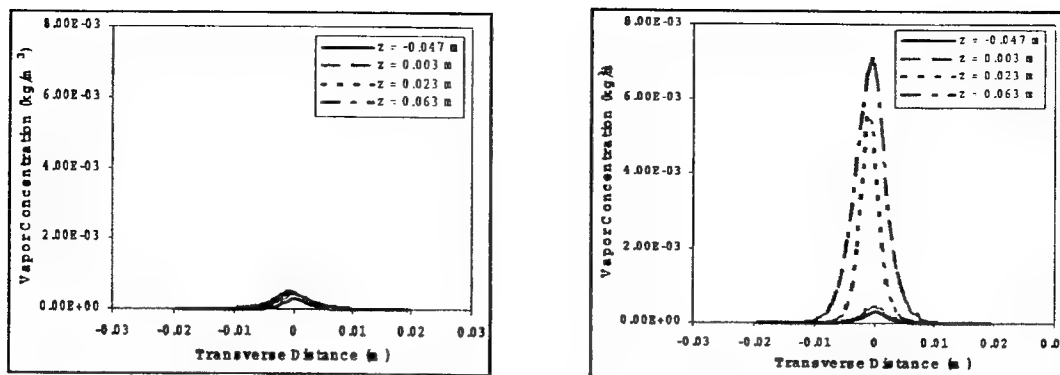


Fig. 5. Vapor Concentration Profiles with Porous Media at (a) 473K (left), and (b) 583K (right).

Measured spray characteristics using water showed an increase in drop diameters in the radial direction attributed to (i) evaporation of small droplets near the spray co-flow interface, and (ii) swirling of co-flow. Combustion experiments were conducted to investigate the effects of equivalence ratio, primary air temperature, and heat release rates on emissions of NO<sub>x</sub> and CO for porous media operated in surface and interior combustion modes.

Figure 6 depicts the two types of combustion at equivalence ratio of 0.75, primary air temperature of 510K, and heat release rate of 3.7kW. Surface combustion illustrated in Fig. 6a, is characterized by a visible blue flat flame. The combustion noise was similar to the sound produced by a Bunsen burner. Interior combustion depicted in Fig 6b produced a bright orange glow and was essentially noiseless. Figure 7 depicts NO<sub>x</sub> and CO concentrations versus equivalence ratio at different primary air temperatures for interior and surface combustion modes. Interior combustion is shown to extend the lean flammability limit compared to that for the surface combustion mode. Lower NO<sub>x</sub> and CO emissions were achieved with interior combustion. Details results are provided in Marbach and Agrawal [2003] and Heatly et al [2003].

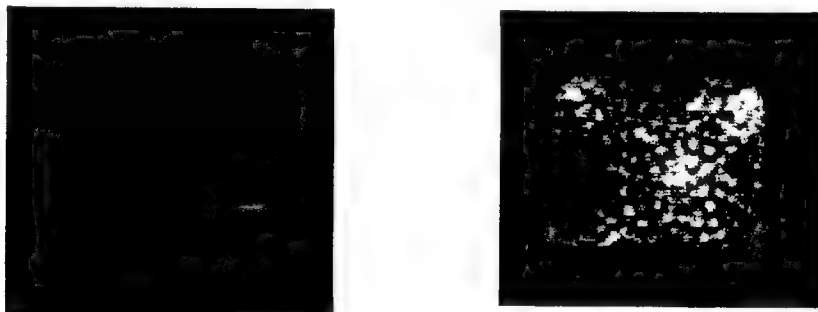




Figure 6. Visual Images of a) Surface combustion, b) Interior combustion

#### REFERENCES

- Hardesty, D.R. and Weinberg, F.J., 1976, Combust. Sci. Tech., vol. 12, pp. 153-157.
- Heatly, R., Marbach, T.L., and Agrawal, A.K., 2003, Paper PG01, Proc. 3<sup>rd</sup> Joint Meeting of the U.S. Sections of the Combustion Institute, Chicago, IL.
- Howell, J.R., Hall, M.J., and Ellzey, J.L., 1996, Prog. Energy Combust. Sci., vol. 22, pp. 121-145.
- Kaplan, M. and Hall, M.J., 1995, Exp. Thermal Fluid Science, vol. 11, pp. 13-20.
- Kotani, Y., and Takeno, T., 1982, Proc. of the Combustion Institute, vol. 19, pp. 1503-1509.
- Marbach, T.L., and Agrawal, A.K., 2003, ASME Paper GT2003-38713, accepted for J of Eng Gas Turbines & Power.
- Pickenaker, O., Pickenacker, K., Wawrzinek, K., Trimis, D., Pritzkow, W.E.C., Muller, C., Goedtke, P., Papenburg, U., Adler, J., Standke, G., Heymer, H., Tauscher, W., and Jansen, F., 1999, Interceram, vol. 48, No. 5 and 6, pp. 1-12.
- Trimis, D., and Durst, F., 1996, Combust. Sci. Tech., vol. 121, p. 153.
- Viskanta, R., 1995, Interaction of Combustion and Heat Transfer in Porous Inert Media, in Transport Phenomena in Combustion, Ed. S.H. Chan, pp. 64-87, Taylor and Francis.

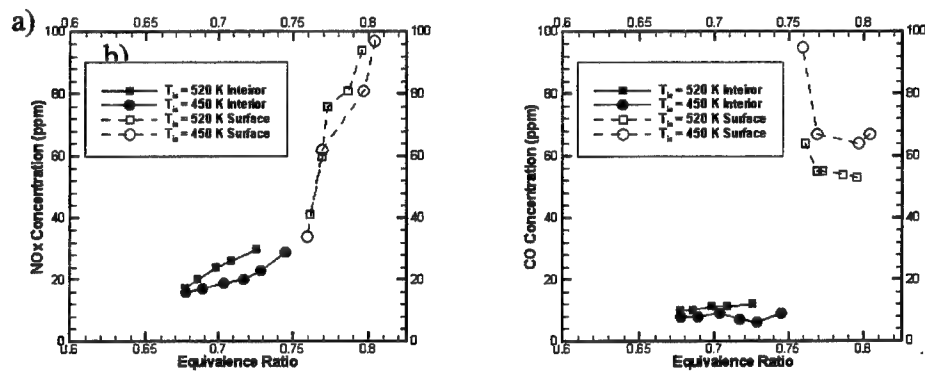


Figure 7. Comparison of Temperature Effect on a) NOx and b) CO



# CONCURRENT RESEARCH ON HIGH GRAVITY (g) COMBUSTION WITH ENABLING MATERIALS

(LRIR: 99PR12ENT)

Principal Investigator(s): Dr. Joseph Zelina

Air Force Research Laboratory  
AFRL/PRTS  
WPAFB, OH 45433

## SUMMARY/OVERVIEW:

A gas turbine combustor concept that uses high g-loading in the circumferential cavity is being tested at AFRL to provide a low-emissions, ultra-compact, high performance combustion system for future military and commercial aircraft. This work comprises experimental testing, modeling and simulation, and cycle analysis of different combustor concepts whereby the UCC can be used as a main combustor or an inter-turbine burner. The testing includes aerodynamic and high-temperature materials performance. Initial tests indicate that, by using highly swirling flows, the combustor performance can be enhanced in the form of improved combustor efficiencies at reduced combustor length. Understanding the impact of high g-loading on the pollutant emissions, operability limits, and combustor durability are three major areas where the AFOSR program will progress the scientific understanding of the processes in this novel combustion system.

## TECHNICAL DISCUSSION

A gas turbine engine has been proposed that uses a near constant temperature (NCT) cycle and an Inter-Turbine Burner (ITB) to provide large amounts of power extraction from the low-pressure turbine. This level of energy is achieved with a modest temperature rise across the ITB. The additional energy can be used to power a large fan for a high bypass ratio transport aircraft or to drive a generator for electrical power extraction. Conventional gas turbine engines cannot meet such power extraction demands without a loss of engine thrust. A second power source to provide energy for such applications would be necessary, adding considerable cost and weight to the system. This current work focuses on Ultra-Compact Combustor (UCC) technology to serve as an ITB or main combustor in the NCT engine. Reducing the size of the main combustor and ITB is essential to reducing or maintaining overall engine weight and size.

We have begun experiments on a UCC which will combine the combustor with the compressor exit guide vanes and the turbine inlet guide vanes. To illustrate this revolutionary design, a conventional combustor is shown in Fig. 1a. Air enters the combustion chamber through dome swirlers and liner holes that provide mixing air and cooling air to the system. In conventional design, the residence time in the combustor is mainly a function of axial length of the system; therefore, engine length is needed to complete the combustion process. The mixture is burned, and then exits the combustor through turbine inlet guide vanes, which direct the flow at the correct angle at the high pressure turbine rotor.

In the UCC design, a trench, or cavity, runs around the outer circumference of the vanes as seen in Fig. 1b. Aligned with this cavity, within each vane, will be a radial cavity. The idea is to

burn rich in the circumferential cavity, allowing much of the required combustion residence time to take place in the circumferential direction of the engine, rather than the axial as is done conventionally. The flow within this cavity will be swirled to generate high “g” loading and reduce the chemical residence time. Flame stabilization occurs as combustion products are recirculated in the cavity. The intermediate products of combustion will be transported into one or more radial cavities in the vane where combustion will continue at reduced equivalence ratio. Finally, across the leading edge of the vanes, again in a circumferential orientation, there will be a flame holder (if necessary) where products will be entrained and distributed into the main flow.

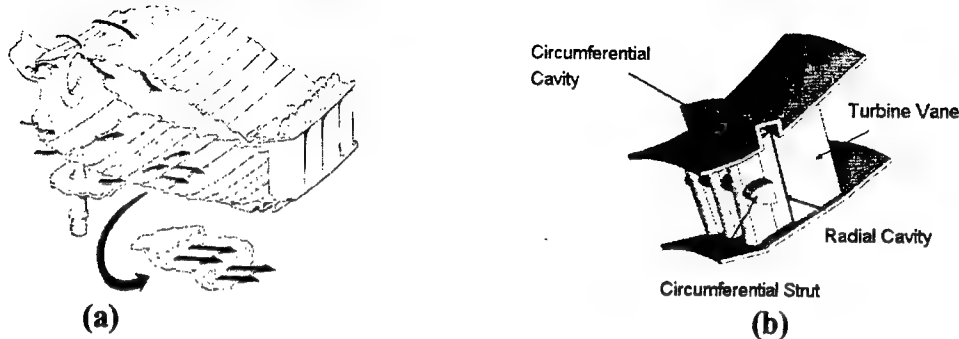


**Figure 1: (a) Conventional Gas Turbine Combustor Design Showing Dome, (b) Ultra-Compact Combustor Design showing Integral Circumferential Cavity and Turbine Vanes.**

A series of nine combustor configurations were tested in AFRL's atmospheric pressure combustion facility, using different fuel injection schemes, as seen in Table 1. These tests were run at combustor pressure drop ranging from  $1.5\% < dP/P < 5\%$ ,  $0.015 < \text{overall fuel air ratio (OFAR)} < 0.035$  ( $0.9 < \phi_{\text{cav}} < 2.2$ ) and inlet temperature  $T_3 = 500$  F. JP-8 + 100 fuel was used. Cavity airflow remained nearly constant, at 24-32% of the total airflow to the system. The variation was due largely to the different effective areas of the individual fuel injectors. The cavity airflow includes air entering around the fuel injector as well as cavity air jets.

**Table 1: Test Matrix for UCC/ITB.**

Conf	Inj Swirl	Inj Angle	Conf.	Inj Swirl /Direction	Inj. Angle	Conf	Inj Swirl/ Direction	Inj. Angle
A	0°	0°	D	45° CW	0°	G	45° CCW	0°
B	0°	20°	E	45° CW	20°	H	45° CCW	20°
C	0°	37°	F	45° CW	37°	I	45° CCW	37°

CW = clockwise, CCW = counter-clockwise

### **Combustion Stability and Lean Blowout**

Combustor lean blowout (LBO) was investigated for the nine configurations. The LBO was plotted against the combustor loading parameter (LP) which is defined as:

$$LP = \frac{Wa}{\delta_{3.0}^{1.75} V_c e^{\frac{T_3}{540}}}$$

$$\text{Eq. (1) where, } \delta = \frac{P_{T3}}{14.696} \quad \text{Eq. (2)}$$

where  $Wa$  is the inlet air flowrate,  $V_c$  is the combustor volume,  $T_3$  is the inlet temperature, and  $P_{T3}$  is the inlet pressure. These tests were run at 500 °F inlet air temperature. As shown in Fig. 2a, the OFAR ~0.007 to 0.012 as the combustor LP increases from 0.5 to 2.5. Some tests were run to investigate rich blowout (RBO) in the combustor, which would identify the upper end of

the RQL-type approach to this UCC system design. In most configurations, the RBO was never achieved. The cavity is very stable for  $0.6 < \phi_{cav} < 2.5$ .

The LBO limits were measured experimentally for all of the test configurations, and this data is shown in Fig. 2b. Considerable differences are noticed between the combustor designs. In general, Configuration F showed the lowest LBO limit, and Configuration A showed the highest LBO value. Interestingly, for Configuration E, H and I, the LBO limit seems to be constant or slightly decrease with combustor loading. Repeat data points were taken to verify the initial results and were found to agree with the first data sets.

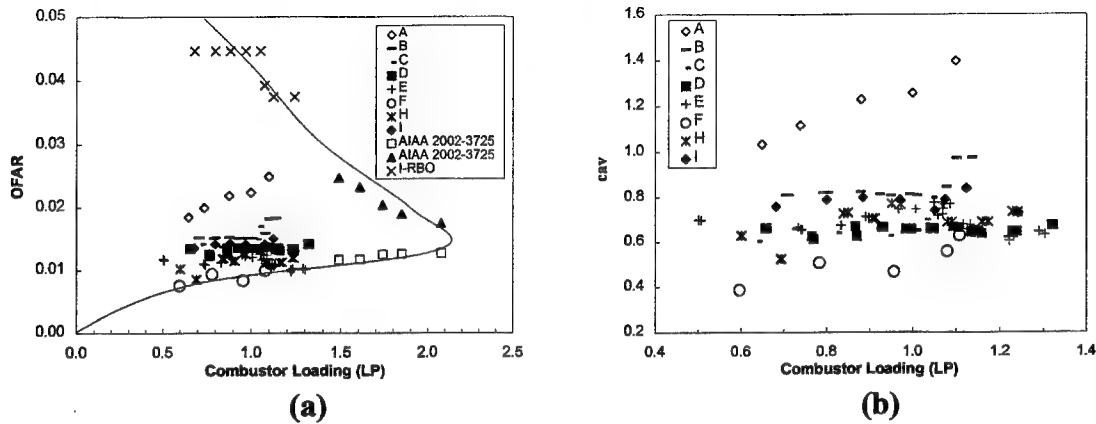


**Figure 2: (a) Stability Loop for the UCC cavity-only operation, and (b) Lean Blowout (LBO) performance for different combustor designs.**

It is believed that the combustor operates in two modes. The first mode is fuel injection-stabilized, where the flame is anchored on individual fuel injectors. The second mode is bulk swirl-stabilized, where the cavity velocity and the turbulent burning velocity are balanced to allow for re-ignition of products from adjacent fuel site locations. Further testing with high-speed photography, OH imaging, and fuel-air ratio sensors are planned to validate this process. In general, however, the LBO data is consistent with conventional design, however, needs to still be improved in future design iterations.

### **Combustion Efficiency**

Combustion efficiency was plotted as a function of g-loading in the cavity. Although a somewhat difficult to define, estimates of g-loading were calculated using continuity, where:

$$V_{tan} = \frac{Wa_{cav}}{\rho_{cav} A_{ex}} \frac{1}{\tan \beta} \quad \text{Eq. 3}$$

The density term was calculated based on the bulk temperature in the cavity (calculated from  $\phi_{cav}$ ). The cavity exit area,  $A_{ex}$ , was  $19.15 \text{ in}^2$ . Angle  $\beta$  was determined from modeling and simulation predictions using the FLUENT code, and found to be  $23 < \beta < 28$  degrees. Once  $V_{tan}$  is known, the g-loading can be calculated using the equation:

$$g = \frac{V_{tan}^2}{g_c r_{cav}} \quad \text{Eq. 4}$$

where  $r_{cav}$  is the average cavity radius. Estimated g-loading ranged from 500 to 3300 g's.

With 0-degree injection angle and C-series injectors, the efficiency increased to 2300 g's, then decreased with increasing loading, as shown in Fig. 3a. Adding swirl to the injector, as well

as angling the injector at 37 degrees, as in Fig. 3b, efficiency remained constant with increased g-loading for  $\phi_{cav}$ .

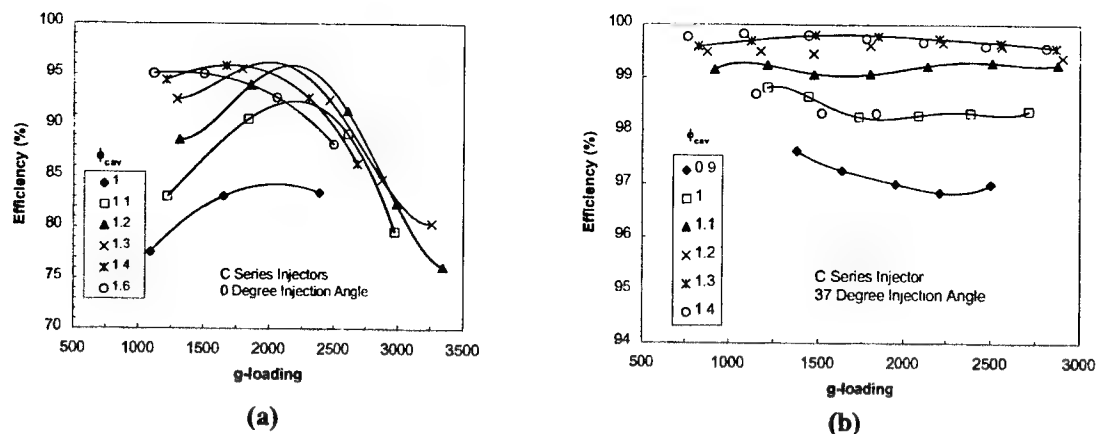


**Figure 3: Combustion Efficiency as a function of g-loading for (a) 0° Injection Angle and (b) 37° Injection Angle Using Fuel Injectors Without Injection Swirl.**

The data suggests that, by keeping the fuel/air mixture in the cavity via fuel injection swirl, the g-loading eventually takes over and increases the burning rate. The increased burning rate results in higher efficiencies. The enhanced burning rate is due to the stratification effect that high g-loading causes in the cavity. Similar to a centrifuge, the higher density mixture propagates to the outer diameter, where it can remain in the cavity, evaporate, mix, and burn. The lower density, high temperature gases migrate toward the cavity centerline where they enter the main airflow. When the fuel injection angle is more radial without injection swirl to help compact the mixture via local recirculation, some of the unburned mixture enters the main flow and is rapidly quenched. In addition to injection angle, the injector swirl direction is important. When the swirl is in a direction to enhance main airflow, the combustor efficiency is improved and shows an increase with increasing g-loading.

### Summary

A parametric experimental investigation of a high g-loaded combustion system has been successfully conducted in an atmospheric pressure rig. Key features of the combustion system include:

1. Short flame lengths (50%) compared to conventional combustor designs.
2. Acceptable LBO performance with Config. F (45° CW swirl, 37° injection angle). LBO performance was greatly impacted by the combustor design.
3. Excellent combustion efficiency which is a strong function of injector type and injection angle. Data suggests 2 modes of operation, where the flame is injector-stabilized at low loadings, and becomes bulk-flow stabilized at high loadings.
4. Increased g-loading resulted in improved combustion efficiencies.
5. Despite the fact that efficiencies increase, NOx emissions decrease for several design configurations, indicating emissions technology improvements rather than NOx-CO trades (not shown in current abstract).

Additional experiments are underway to investigate the impact of turbine vanes in the cavity flowpath. These tests will be conducted at atmospheric and high pressure conditions.

# PULSE DETONATION PHYSIOCHEMICAL AND EXHAUST RELAXATION PROCESSES

LRIR 01PR02COR

Principal Investigator: Dr. Fred Schauer (AFRL/PRTS)

AFRL/PRTS  
1790 Loop Road North, Building 490  
Wright-Patterson AFB OH 45433-7103

## SUMMARY/OVERVIEW:

The objective of this program is to establish the scientific knowledge of detonation initiation, propagation, and blow-down needed to develop a pulse detonation engine (PDE) that will function on hydrocarbon fuels. The complex interaction of chemistry, gas dynamics, turbulent mixing, and geometry are responsible for the success or failure of the detonation phenomena required to operate a PDE. Detonation tube exhaust blow-down conditions, which are predicted to have a significant impact upon performance, will be explored in order to achieve basic understanding of the relationships between detonations, nozzles, and multiple detonation tube interactions.

## TECHNICAL DISCUSSION

The technological motivation for this program is the need to develop low-cost high-performance PDE's that can operate on hydrocarbon fuels. PDE's rely upon detonation combustion to produce a pressure rise in the combustion chamber instead of the expensive rotating machinery used in gas turbine engines. Consequently, the most expensive and maintenance-intensive components of a conventional turbine engine, namely the compressor and turbine stages, will not be necessary in PDE's. PDE's operates on a near-constant-volume heat addition cycle as opposed to the constant-pressure cycle employed in nearly all conventional aero-propulsion systems. The constant volume cycle offers improvements to specific thrust, specific fuel consumption, and specific impulse at a greatly reduced cost. In theory, the PDE can efficiently operate at Mach numbers from zero to above four without using a combined cycle/rocket approach. However, there are some major technical problems that must be resolved before the full potential of PDE's can be realized.

Foremost among the hurdles for a practical PDE system are the requirements for initiation and successful propagation of a detonation with hydrocarbon fuels in air. Although this has not been achieved in 60 years of PDE research, modern computational fluid mechanics (CFD), laser diagnostics, and high-speed instrumentation have not been applied to this challenge until recently. CFD and experimental studies of deflagration-to-detonation transition (DDT) and propagation are being carried out in order to explore the parameters controlling detonation

initiation including: geometry effects, plasma ignition, hybrid fueled pre-detonators, and endothermic fuels. In addition to existing high-frequency instrumentation, an optically accessible test section will be coupled with our high-framing rate cameras to observe the deflagration to detonation transition processes and compare with models. The imaging and laser diagnostics experience obtained from our AFOSR Combustion Research program will also be used to study the detonator tube blow down. High-frequency Schlieren, PLIF, and/or planar Raman imaging will be used to investigate the exit boundary conditions influence on thrust. Two-dimensional nozzles are used in these investigations, and an optical test section will be employed to study both the nozzle flow conditions and multi-tube interactions. CFD calculations are used to gain an understanding of the mechanisms whereby the thrust is influenced by the conditions established when the detonation wave reaches the exit plane.

Previously, techniques for developing hydrocarbon/air deflagration to detonation transition (DDT) were demonstrated without the use of excess oxygen. This work has continued and scaling mechanisms have become better understood to enable DDT in a wide range of detonator tube sizes. However, one of the limitations of DDT techniques with practical fuels is the long chemical induction time required for the preliminary deflagration ignition. Using CFD and experiments, studies of branching detonations were conducted, enabling a detonation to be split from the main detonator tube without quenching. As shown in Figure 1, the split off detonation could then be propagated through a crossover tube to a second detonator tube. Previously, we demonstrated an 85% reduction in DDT time by employing this technique. Through better understanding of the interaction of ignition and confinement, the technique was able to achieve direct or near direct detonation initiation of the second detonator

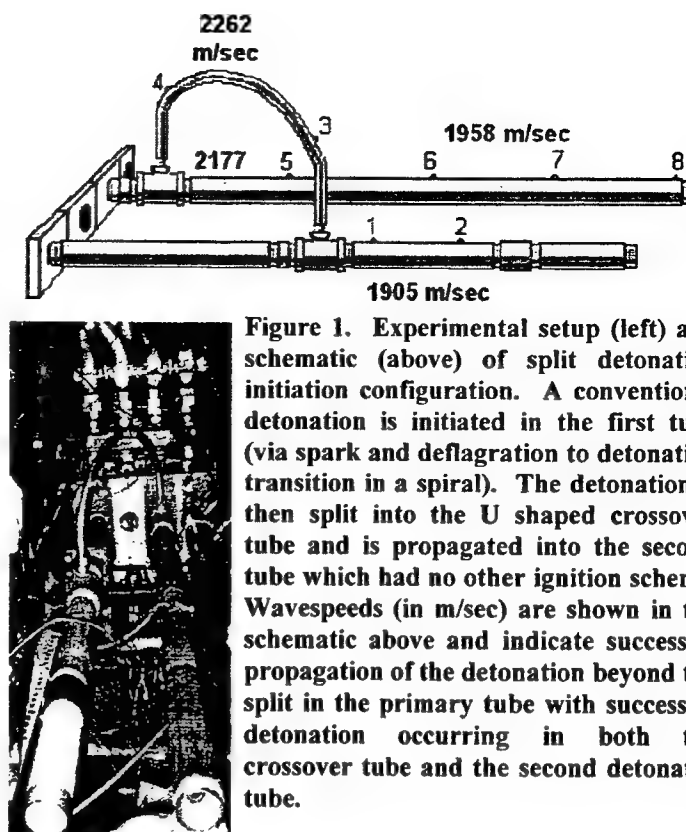


Figure 1. Experimental setup (left) and schematic (above) of split detonation initiation configuration. A conventional detonation is initiated in the first tube (via spark and deflagration to detonation transition in a spiral). The detonation is then split into the U shaped crossover tube and is propagated into the second tube which had no other ignition scheme. Wavespeeds (in m/sec) are shown in the schematic above and indicate successful propagation of the detonation beyond the split in the primary tube with successful detonation occurring in both the crossover tube and the second detonator tube.

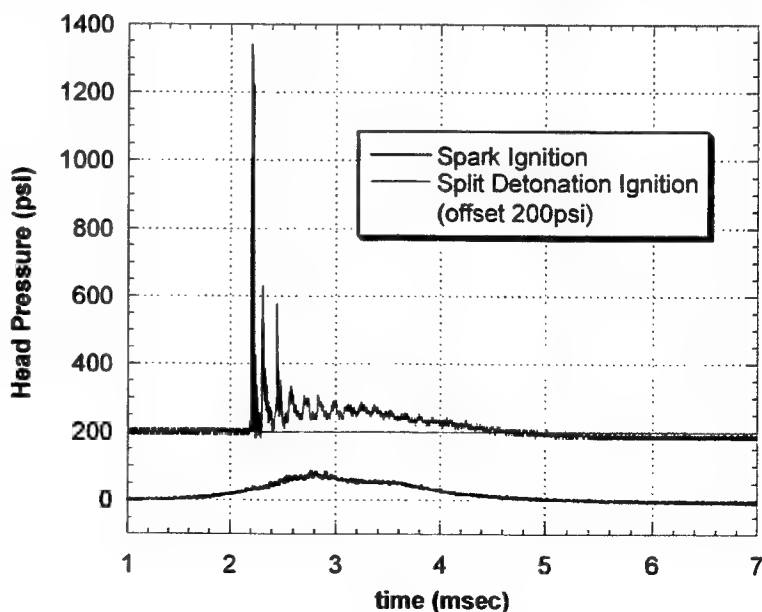


Figure 2. Head pressure versus time for spark ignition (with deflagration to detonation transition) versus split detonation ignition (near direct initiation). The split detonation ignition trace is offset 200 psi for clarity.



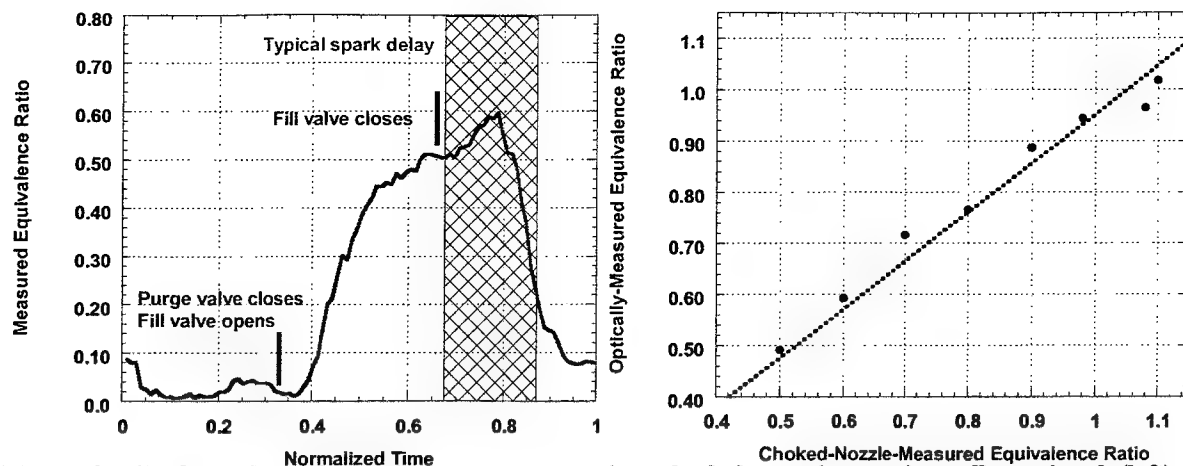


Figure 3. Hydrocarbon absorption measurement in pulsed detonation engine. Raw signal (left) and measured equivalence ratio (rate) versus normalized cycle time.

tube. As shown in the comparison of spark ignition with DDT versus split detonation ignition in Figure 2, a dramatic shortening of the initiation time is accomplished along with greatly increased thrust pressures. Split detonation ignition is much more robust and also simpler without the need for individual igniters for each detonator tube.

In our last annual report, we described the sensitivity of DDT to proper mixture and demonstrated an in-situ measurement of equivalence ratio based upon OH emission. However, the technique was limited to measurement only in the detonation front, lacking resolution in time and space. Utilizing the broad 3.39 micron hydrocarbon absorption feature, a diagnostic technique was developed which enabled in-situ measurement of vapor-phase fuel equivalence ratio in both detonating and cold-flow experiments. This allowed the charge mixing and stratification to be assessed as shown in Figure 3. When compared to the actual equivalence ratio which was regulated by choked nozzles, the results demonstrated that the technique can produce quantitative data even in the unsteady and harsh PDE environment. In fact, the results shown above were obtained using published absorption coefficients for propane with no 'fitting' required. Other hydrocarbon fuels (without validated absorption coefficients) required a simple calibration procedure in a fuel cell. This technique proved so robust, it is currently being used to quantify and calibrate fuel injector performance in a PDE demonstration at Mach 3 flight conditions.

The influence of nozzles upon PDE performance has been found to be highly sensitive to initial detonation conditions, which are strongly influenced by the unsteady nozzle behavior. Figure 4 clearly shows the unsteady nature of the PDE flow in the cold flow condition. Significant compression and expansion waves are created by purge and fill cycles interacting

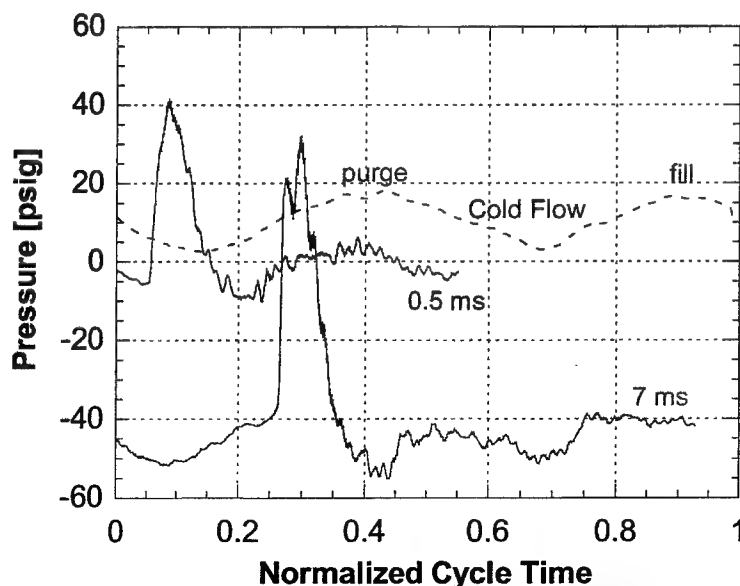


Figure 4. Head pressure (not zeroed) versus normalized cycle time for cold flow (humps correspond to purge and fill cycles so denoted), 0.5 msec ignition delay, and 7.0 msec ignition delay.

with the exit nozzle. These phenomena in turn produce much different behavior in the detonation event depending upon whether ignition occurs in an expansion (0.5 msec ignition delay) or compression wave (7 msec ignition delay). It was found that the unsteady gas dynamics are highly sensitive to nozzle configuration.

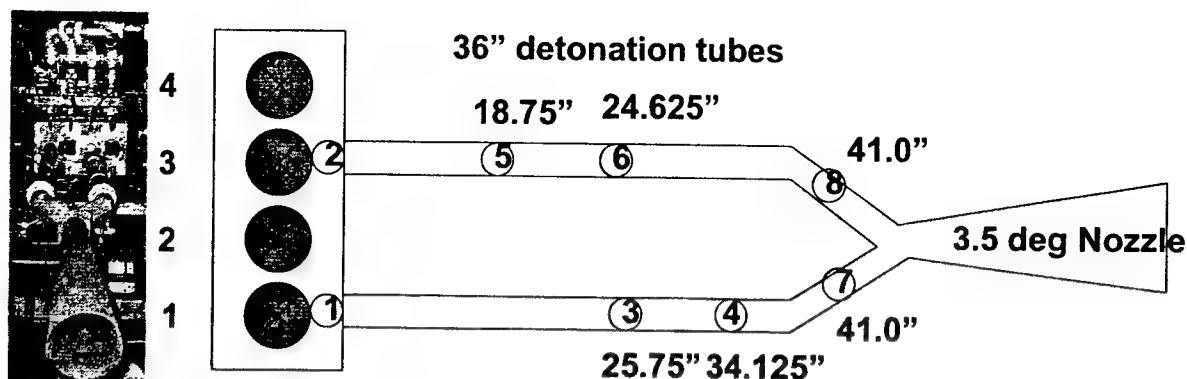


Figure 5. Picture (left) and schematic (right) of multi-tube common nozzle. Pressure transducer locations are demarked by circled numbers along with distance from head.

One approach to solving unsteady nozzle performance is to couple multiple detonator tubes with a common nozzle in an effort to obtain quasi-steady flow downstream of the nozzle. This unvalidated approach remains popular because a common nozzle may produce back-pressurization of the detonation tubes at altitude and enable the application of conventional nozzle theory downstream of the common nozzle throat.

Preliminary experiments were conducted using the setup depicted in Figure 5. Results were obtained with only one ignition event (upper plot of Figure 6) to observe the multi-tube interaction effects. The detonation blast wave was observed to 'wrap' around the common nozzle and pressurize the second tube. When the second tube is ignited (lower plot), higher pressures are observed due to this multi-tube interaction. In addition, blow down times are prolonged in both tubes. Both mechanisms may provide higher performance, but further study is required to efficiently obtain thrust from these unsteady events.

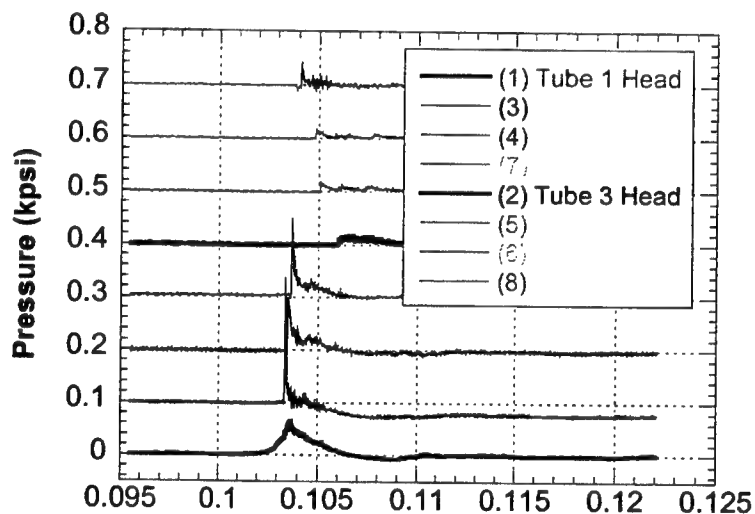
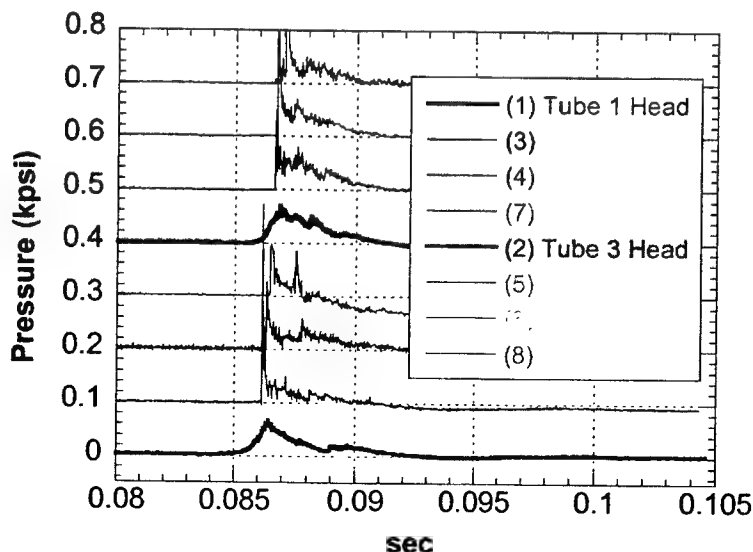


Figure 6. Pressure versus time for common nozzle with single (above) and dual tube (below) ignition.



MEASUREMENT OF ELECTROSPRAY DROPLET'S CHARGE AND RADIUS  
DISTRIBUTIONS WITH QUADRUPOLE MASS SPECTROMETER  
(Oral Presentation: Establishment of an Electrostatic Atomization Theory and  
Experiment Program at Prairie View A&M University)

Principal Investigator: Tian-Sen Huang

Prairie View A&M University

#### SUMMARY

In the first year of the project, we rebuilt the quadrupole mass spectrometer apparatus, and conducted, with student participation, a series of the experiments to analyze the charge and radius distributions of electrospray droplet. The experiments concentrated on the liquids of octoil and wood's metal. The experiments have been continuously improved, and compared with the experiment conducted previously by other labs. Now, a new type of experiments are planned.

#### TECHNICAL DISCUSSION

To start this project, we first rebuilt the high charge quadrupole mass spectrometer/electrometer spray apparatus transferred from Princeton Plasma Physics Lab. Since the quadrupole mass spectrometer apparatus was built in 1980's and operated by different teams in the past, it has been damaged very seriously and has no manuals with it. To make it working, a group consisting of faculty, staff and students disassembled, repaired, and assembled the whole apparatus, including the mechanical pump and diffusion pump, the electrospray system, the filter operation system, and the charge detector system. Through the rebuilding of apparatus, our group has been familiar with the structure of the apparatus and its operation.

The experiments of charging droplet analysis were made first for the liquid octoil because there were more experiments of octoil that have been done. We completed about thirty experiments of charging octoil droplet analysis for different charge/mass ratios and different resolutions. (Each experiment takes about one day.)

In the beginning of the octoil experiments, a special material tetrabutyl ammonium picrate is needed to prepare as an additive to increase the conductivity of testing liquid. Because the additive is an uncommon chemistry material and explosive in its solid state, we compounded it ourselves with tetrabutylammonium hydroxide and picrate acid that were purchased from chemistry material company. Then the octoil is doped with the additive to achieve the conductivity required for electrospray.

In measuring the charge and mass distributions, the mass quadrupole filter works in the basic (lowest) stability region that is commonly used for electrospray experiments. In the experiments, the bias voltage, the oscillating voltage, and the oscillating frequency that fed into the two pairs of poles of the spectrometer were adjusted for measuring the charge distribution of the droplets for the certain value of the ratio of charge to mass. The multichannel analyzer gives charge distribution in 254 or 510 equally divided channels. The mass (or radius) distribution of the droplets can be derived from the charge distribution, and the voltage/charge conversion factor.

In the measurements, the resolution of charge/mass ratio filter is critical. The practical value of resolution in our experiments seems low although its value from the theory is high. As we improved our experimental skills, the resolution was getting higher. In addition, the value of conversion factor of the droplet charge to the measured voltage is very important parameter. A direct measurement of the ratio of the charge to the voltage imposed on the detector has been done. In order to confirm the value, an experiment with radioactive ion source will be conducted.

Our experiments for octoil have been compared with the previous work [Okuda and Kelly, 1996]. We observed two peaks in the charge (radius) distribution that is consistent with Okuda and Kelly's results. Experiments for wood's metal are undertaking.

Now, we are planning to conduct experiments regarding diesel fuel electrospray, and experiments concerning electrospray's application for nano-tech. The electrospray experiments with large flow will be conducted. For this purpose, a new experiment apparatus, the phase Doppler anemometry (PDA) system, is required. (The Yale University's electrospray group has used this device successfully for charged droplet experiments.) In addition, we need a two-channel data acquisition board and a 100 MHz mixed signal oscilloscope, which are used to enhance the capability of PDA system for more experiments.

# BALLISTIC IMAGING IN THE PRIMARY BREAKUP REGION OF DIESEL INJECTOR SPRAYS

Contract Number DAAD19-02-1-0221

Mark Linne and Terrence Parker

Division of Engineering  
Colorado School of Mines  
Golden, CO 80401

## SUMMARY/OVERVIEW:

The Colorado School of Mines is developing a technique for imaging the near-field, liquid core in the primary breakup region of a diesel spray, under operating temperatures and pressures typical of a diesel engine. This technique, called "ballistic imaging", has been used primarily in the medical community for imaging through tissue. To-date, the existence and behavior of a liquid core for diesel sprays have been a subject of debate. Our goal is to contribute to the understanding of the liquid spray core and its primary breakup by adapting ballistic imaging to this important flowfield.

## TECHNICAL DISCUSSION

When light (either continuous or pulsed) passes through a highly turbid medium, some of the photons actually pass straight through without scattering, exiting the medium within roughly the same solid angle that they entered (see Figure 1a). These relatively few photons are termed "ballistic". Because they travel the shortest path, they also exit first (see Figure 1b). A somewhat larger group of photons is called "snake-like", because they are scattered just once or twice. They exit the medium in the same direction as the input light but with a somewhat larger solid angle than the ballistic photons. Because they travel a bit further, they exit just after the ballistic photons. Light exiting the medium that has scattered multiply has a larger photon number density, but it also is scattered into a very large solid angle and it exits last.

Due to their undisturbed path, ballistic photons retain an undistorted image of structures that may be embedded within the turbid material. If used in a shadowgram arrangement, the ballistic photons can provide diffraction limited imaging performance of these structures. In most highly scattering and/or

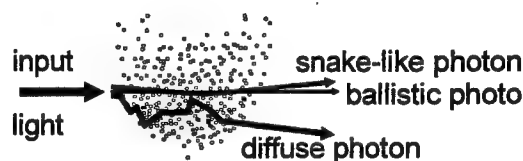


Figure 1a. Geometric schematic of ballistic imaging.

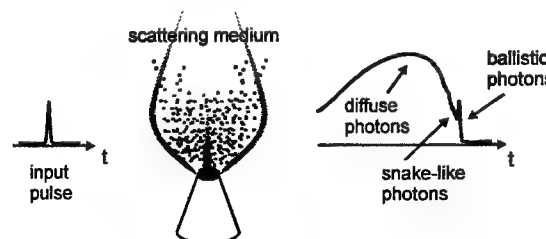


Figure 1b. Time-domain schematic of ballistic imaging with a short pulse.

absorbing environments, the number of transmitted ballistic photons is often insufficient to provide the necessary signal to noise ratios (SNR) to form an image. In such a case, the snake-like photons retain slightly distorted information and can be used in imaging, together with the ballistic photons, with little degradation of resolution. In contrast, diffuse photons retain no memory of the structure within the material. If allowed to participate in the formation of an image, the various paths these multiply scattered photons take through the material will cause any image point they form to appear as if it came from an entirely different part of the object, and this will seriously degrade resolution. Unfortunately, diffuse photons are the most numerous when light is transmitted through highly scattering media. The problem of obtaining a high-resolution image through highly scattering materials is thus a matter of separating and eliminating the diffuse light from the ballistic and snake-like light. This can be done using discrimination methods that make use of the properties that are retained by the ballistic and snake-like light but are lost in multiple scattering events. As already alluded, the direction taken by transmitted light, together with exit time, can help to segregate diffuse photons from the imaging photons. Furthermore, ballistic photons are coherent with the input light and they retain the input polarization.

Based upon a careful evaluation of ballistic imaging techniques described in the literature, we settled upon the time-gated system shown in Figure 2 (based primarily on work by the group of Alfano in New York<sup>1</sup>). Because diesel sprays are transient, it was necessary to find a technique that could acquire rapid transients (fast, still images of single events in this case) and this approach offers that possibility. A 1-kHz repetition rate Spectra-Physics Spitfire Ti:Sapphire regenerative amplifier, seeded with a Spectra-Physics Tsunami Ti:Sapphire mode-locked laser, generates 80 fs, 1mJ pulses centered at  $\sim 800$  nm. The linearly polarized beam is split into OKE gating and imaging beams; 30% of the optical power is used as the imaging beam while the remaining power is used to create the OKE time gate.

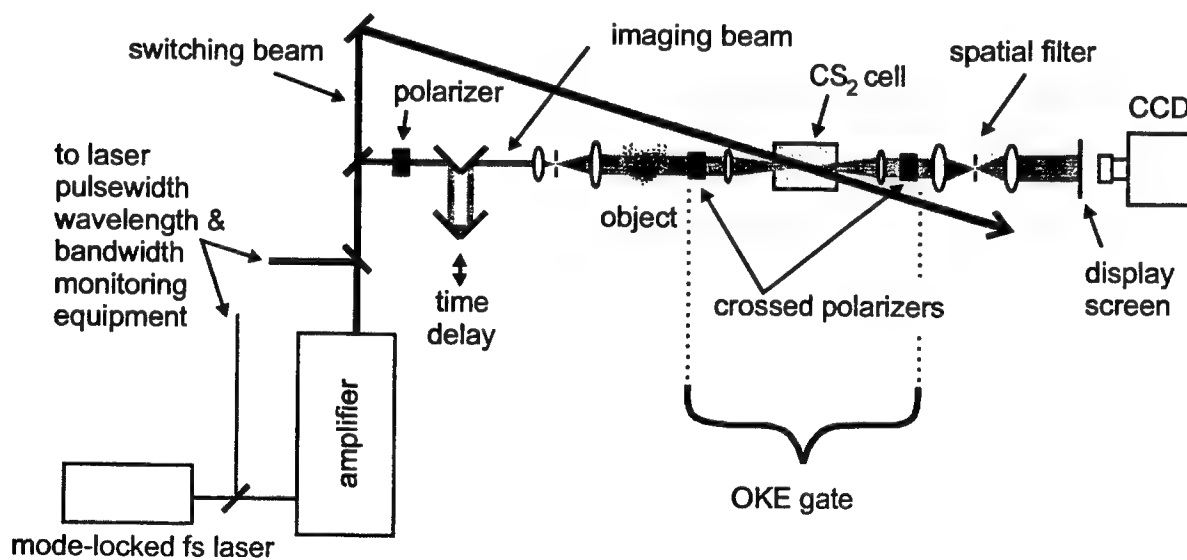


Figure 2. Layout of OKE-switched ballistic imaging system at CSM.

<sup>1</sup> Wang, Ho, Liu and Alfano, "Ballistic 2-D Imaging Through Scattering Walls Using an Ultrafast Optical Kerr Gate", *Science*, 253:769, (1991), Wang, Liu, and Alfano, "Ballistic Imaging of Biomedical Samples Using a Picosecond Optical Kerr Gate", *Proceedings of the SPIE*, 143:97, (1991), Yoo, Das, Liu, Xing and Alfano, "Femtosecond Time-gated Imaging of Translucent Objects Hidden in Highly Scattering Media", *Springer Series in Chemical Physics: Ultrafast Phenomena VIII*, 55:124, (1993).

The polarization state of the imaging beam is first cleaned up with a polarizer, because the OKE gate relies upon polarization switching. The imaging beam is then time delayed using an adjustable length delay arm, to control the delay between the arrival of the switching and imaging pulses at the OKE gate. The imaging beam then passes through an optics train consisting of a telescope (with spatial filter) that controls the imaging beam size at the object, a system to relay the beam through the OKE switch, and a combined spatial filter/telescope for imaging onto a display screen. Our first implementation of this system had serious problems with image distortion. The normal laboratory approach of simply inserting available optics into the beam path does not work. A second system, therefore, has been carefully designed using OSLO®, a commercial ray-trace code. By careful choice of optics, we have ensured that the optical train itself is diffraction limited. There are no spurious aberrations or distortions introduced by the imaging optics themselves in this system.

As mentioned above, one signature of ballistic and snake-like photons is their directionality. Diffuse photons, on the other hand, are multiply scattered; locating their energy in a full  $4\pi$  sr. One passive approach to ballistic imaging takes advantage of this fact by using a fairly hard spatial filter in the imaging beam. At first this seems like a simple and easy solution, but spatial filters also remove high spatial frequency components (small features, including sharp edges) of the image itself. This is because the pinhole of the spatial filter must be placed at a lens focus. That focal plane is the Fourier plane, where high frequency components of the image can be found off axis. The pinhole blocks them, together with the diffuse photons, and the image is thus seriously blurred. Any optical train is a spatial filter of sorts, however, and if careful design is applied one can eliminate a good deal of the diffuse photons while preserving image fidelity. Even a spatial filter can be used if it has been shown not to degrade imaging performance itself. The system shown in Figure 2 thus has an inherent passive ballistic imaging system built into it, while maintaining good image fidelity.

Because the image is transferred in a laser beam, there can be a problem identifying an object plane for the camera. An alternative, but equivalent, explanation is that the phase fronts of the imaging beam are somewhat mixed and this makes it difficult to construct a high-fidelity image at the camera imaging plane, since the beam is coherent. For this reason, most experimentalists use a display screen as shown in Figure 2. The camera then focuses on the screen, and the screen defines the object plane for the camera.

The OKE gate works in the following manner. When there is no switching pulse present, no image is transferred to the display screen. This is because the OKE gate uses crossed calcite polarizers. The first polarizer in the OKE gate (second polarizer used in the imaging beam) is oriented to pass the polarization orientation of the imaging beam. The second OKE polarizer is oriented normal to the first, blocking an unperturbed imaging beam. The measured extinction ratio of the polarizers is  $>10^5$ ; without a switching pulse present there is  $<10^{-5}$  transmission of the imaging beam through the second polarizer. After the first polarizer, the imaging beam is focused into the Kerr active liquid ( $\text{CS}_2$  in this case) with an F/#5 achromat, and then up-collimated with a second F/#10 achromat. At the arrival of a switching pulse, the intense electric field of the pulse causes the  $\text{CS}_2$  dipoles to align along the polarization vector of the switching beam, creating temporary birefringence in the liquid. This birefringence rotates the polarization of the imaging beam (about  $\pi/3$  radians for switching with the fundamental of Ti:sapphire), allowing most of the imaging beam ( $\sim 70 - 75\%$ ) to pass through the second polarizer. The imaging beam time delay is adjusted while switching for maximum signal transmission through the OKE gate. This OKE induced birefringence is limited in time by either the duration of the laser pulse or the molecular response time of the Kerr medium, whichever is longer. In our case, the incident laser pulse is of much shorter

duration than the molecular relaxation time of  $\sim 2$  ps for  $\text{CS}_2$ ; our gate time of 2 ps has been confirmed by direct measurement.

Typically, when an OKE shutter is used in imaging applications the first harmonic of the laser forms the imaging beam while the second harmonic is used for switching. This makes it possible to reject switching light with a low-pass optical filter. The Spitfire output pulse is centered at  $\sim 800$  nm. Consequently, the second harmonic wavelength is  $\sim 400$  nm. This wavelength falls just within the absorption band of  $\text{CS}_2$ . It can be used, but the  $\text{CS}_2$  degrades over time (approximately one half hour). Due to the difficulties associated with this problem, we have evaluated two separate cases. In the first case, the OKE gate is switched with the first harmonic of the laser system, while in the second case, the OKE gate is switched with the second harmonic.

During the phase of work where we have developed and tested techniques, the "object" in Figure 2 has been a high-resolution test chart consisting of lines of varying spatial frequencies (in "line pairs per mm", or lp/mm) placed inside a 10 mm pathlength cell. This cell contains a controllable scattering medium: a solution of distilled water containing various concentrations of  $0.7\text{ }\mu\text{m}$  diameter polystyrene (PS) spheres. In order to compare techniques, the modulation transfer function (MTF) was measured for imaging transmission through the resolution test chart immersed within various concentrations of polystyrene spheres that emulate the environment of a diesel spray. The outcome was that several systems that use a red switch provide optimum single-image results, and the choice of which among these is best will depend upon exactly which spray is interrogated.

In the next phase, we have set up a steady water jet experiment that will allow us to prove the technique without concern for triggering. The system we are using is depicted in Figure 3.

It uses a piston-accumulator system to provide high pressure (2,000 psi) over about 1 minute of spray time. The jet under study is a stock spray nozzle modified to omit internal components that destroy the solid core. Thus, this jet approaches the simplicity of the diesel nozzle, which is typically a short length (typical  $l/d$  of 2 to 6) hole, submillimeter in diameter (100 to 300  $\mu\text{m}$ ), with atomization totally dependent on the conversion of pressure to velocity in the orifice. Jet diameters for nozzles that we have procured range from 0.018 to 0.031 inches (0.5 to 0.8 mm). The jet under study is interesting in its own right, however, and the results can stand alone as a publication. The pressure control available in this system provides access to a range of Reynolds and Weber numbers along with the associated range of expected liquid core lengths. The system should put us into the atomization regime for a single-hole atomizer spray. A ballistic imaging system for this setup has been aligned and we are in the early stages of image acquisition.

In the next year, we plan to acquire images of the quasi-steady spray under various conditions of interest to the spray community while at the same time optimizing ballistic imaging for sprays. Following that, we will design a system for use in the CSM diesel simulator and set it up.

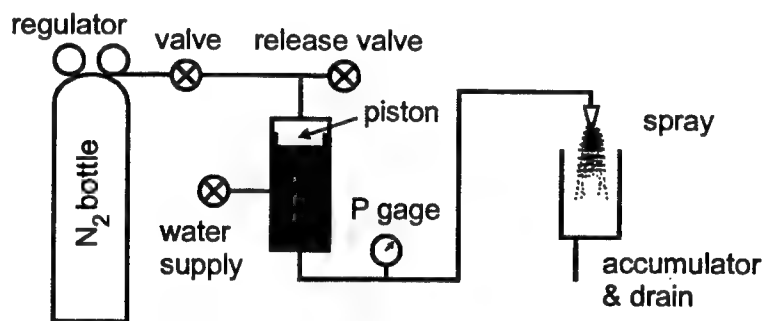


Figure 3. Schematic of quasi-steady spray facility.



# MODELING THE PRIMARY BREAKUP OF HIGH SPEED LIQUID JETS

(DAAD19-00-1-0487<sup>1</sup>)

Principal Investigator(s): P.V. Farrell and R.D. Reitz

Engine Research Center,  
University of Wisconsin-Madison  
1500 Engineering Drive  
Madison, WI 53706

## SUMMARY/OVERVIEW:

There is considerable uncertainty about the structure of the dense core region of diesel sprays, and conventional atomization models that are based on linear stability theory contain numerous assumptions that are difficult to verify. A quasi-two-dimensional non-linear jet breakup model is proposed that eliminates many of these assumptions. The primary breakup is modeled by tracking the wave growth on the liquid-gas interface. The continuity and momentum equations are reduced to one-dimensional forms to calculate the growth of waves on the jet surface, and the gas pressure is obtained by solving for the two-dimensional potential flow using the source panel method. A Fast Fourier Transform (FFT) is used to capture the surface wave structure, and the drop size distribution is calculated from the Fourier coefficients. The model has been validated by comparing with experimental data for both low-speed and high-speed jets. Comparison of diesel combustion and emissions predictions using the new and standard breakup models shows that the primary breakup process has significant influence on predicted soot emissions.

## TECHNICAL DISCUSSION

Spray atomization is an important process in many practical applications including diesel engines. The local vapor distribution that is determined by the atomization and evaporation processes directly influences combustion and pollutant formation. Jet primary breakup is particularly important because it initiates the atomization process and provides the initial conditions for the subsequent spray breakup [1]. However, since the primary breakup usually occurs in the dense spray region, its mechanism is not yet fully understood because of the difficulty of experimental observation.

The present modeling approach combines Lagrangian and Eulerian methods to describe the breakup process. In the method, the continuous jet is discretized into series of liquid 'blobs'. A Lagrangian method is used to track the movement of the blobs, and the breakup of each blob is calculated by a one-dimensional Eulerian method.

---

<sup>1</sup> Financial support of ARO contract number DAAD19-00-1-0487, Caterpillar, and DOE Sandia Laboratories is gratefully acknowledged.

The one-dimensional model consists of the continuity and momentum equations for the liquid phase [2,3]

$$\frac{\partial R^2}{\partial t} + \frac{\partial R^2 u}{\partial x} = 0 \quad (1)$$

$$\frac{\partial R^2 u}{\partial t} + \frac{\partial R^2 u^2}{\partial x} = -\frac{R^2}{\rho_l} \left( \frac{\partial p_l}{\partial x} + \frac{\partial p_g}{\partial x} \right) + 2\nu \frac{\partial}{\partial x} \left( R^2 \frac{\partial u}{\partial x} \right) \quad (2)$$

where  $t$  is time,  $x$  is the axial coordinate with its positive direction pointing in the jet's flow direction,  $R = R(t, x)$  is the radius of the liquid jet as a function of time and axial position, and  $u = u(t, x)$  is the flow velocity within the liquid jet. The liquid pressure is assumed to be uniform at any axial location and is given by [4]

$$p_l = \frac{\sigma}{R} \left[ \frac{1}{\sqrt{1 + (\partial R / \partial x)^2}} - \frac{R (\partial^2 R / \partial x^2)}{\sqrt{1 + (\partial R / \partial x)^2}^3} \right] \quad (3)$$

The effect of the gas phase on the jet surface wave growth is reflected in the gas pressure term, which is obtained by solving for the potential flow over the jet surface using a source panel method [5]. In order to get the required initial conditions, the cavitating flow inside the nozzle was simulated using a nozzle flow model [6]. This model provides velocity, jet diameter and turbulence parameters at the nozzle exit. The time scale of the cavitation-induced disturbances was calculated from the bubble dynamics [7], and was used to specify a reference wavelength of the initial disturbances.

The amplitude of the initial disturbance is assumed to be  $\eta_0 = r_{nozzle} - r_{jet}$  where

$r_{nozzle}$  and  $r_{jet}$  are the radii of the nozzle and the jet, respectively. The initial disturbance is then represented by a Gaussian distribution of surface waves where the standard deviation is found from the turbulence fluctuating velocity provided by the nozzle flow model. A symmetric initial condition and periodic boundary conditions are applied to both ends of the blob [2,3]. A fourth-order Runge-Kutta method is used to solve the equations, and the jet surface structure and wavelengths are monitored by Fourier analyzing the waves with a FFT.

Since multidimensional effects cannot be neglected for high-speed jets, the two-dimensional surface is modeled by reflecting the Fourier series in the peripheral direction on the jet surface (isotropic wave assumption). The drop size distribution was derived from the Fourier series by assuming that drop diameters are proportional to the wavelengths in the Fourier series, and that the mass associated with each drop size is proportional to the magnitude of its corresponding Fourier coefficient [3]. The breakup is assumed to occur when the surface area of the shed drops would be equal to the surface area of the waves on the jet surface. For low speed jets, the cross-section of the blob at each axial position is assumed to be circular [2]; for high-speed jets, the surface area of the blob is obtained by integrating over the 2-D jet surface numerically [3].

The new breakup model was used to predict breakup characteristics, including the breakup time and drop size, for jet primary breakup under various operating conditions [8]. It was found that the effect of the choice of reference wave's wavelength on the breakup time and drop size was negligible, but the effect of the wave's amplitude on the breakup characteristics was important and was found to be correlated adequately with [8]

$$\frac{\tau_{BU}}{\tau_{BU}^*} = f^{-0.066} \quad \text{and} \quad \frac{SMD}{SMD^*} = f^{0.014} \quad (4)$$

where  $\tau_{BU}^*$  and  $SMD^*$  are the predicted breakup time and drop size for a reference initial wave amplitude with,  $\eta_{0,s} = 0.2 \mu m$ , and  $f = \eta_0 / \eta_{0,s}$ . These corrections account for the effects of the nozzle internal flow and the previous breakup events. For implementation in multidimensional models, the primary drop breakup time and drop size were correlated with the operating conditions. It was found [8] that for low-speed jets, when  $We_g \leq We_{g,c}$ ,

$$\tau_{BU} = C_{\tau,1} \left( \frac{\rho_l}{\rho_g} \right) \left( \frac{1}{Re_l We_l} \right)^{0.2} \frac{D_0}{U_0} \quad \text{and} \quad SMD = C_{SMD,1} \left( \frac{\rho_l}{\rho_g} \right)^{0.1} \left( \frac{1}{We_g} \right)^{0.2} D_0 \quad (5)$$

and for high speed jets, when  $We_g > We_{g,c}$ ,

$$\tau_{BU} = C_{\tau,2} \left( \frac{\rho_l}{\rho_g} \right)^{0.5} \frac{D_0}{U_0} \quad \text{and} \quad SMD = C_{SMD,2} \left( \frac{\rho_l}{\rho_g} \right)^{0.05} \left( \frac{1}{We_g} \right)^{0.03} D_0 \quad (6)$$

where  $C_{\tau,1} = 5.0$ ,  $C_{\tau,2} = 1.0$ ,  $C_{SMD,1} = 0.15$ , and  $C_{SMD,2} = 0.05$  and  $We_{g,c} = 1000$ . In these equations,  $\rho$  is density, and subscripts l and g refer to the liquid and gas, respectively.

The Weber number is  $We = \rho U^2 D / \sigma$  and the Reynolds number is  $Re = UD / \nu$ .

The new breakup model was implemented in the KIVA code [9] to replace the standard Kelvin-Helmholtz linear stability model for primary breakup prediction. As in the standard KIVA code, the liquid jet is simulated using discrete parcels. The liquid jet is simulated by injecting 'blobs', and the breakup of each injected blob was calculated using Eqs. (5) or (6). Secondary breakup of drops from the injected blobs was calculated by a Kelvin-Helmholtz / Rayleigh-Taylor hybrid model [10]. The standard model requires an assumed breakup length, beyond which the RT model is initiated [11]. The new model removes this ad hoc requirement and calculates the breakup time for each breakup event. The breakup of all child drops is predicted by the KH-RT model.

To test the model, vaporizing diesel fuel jets were studied using the experimental data of Siebers [12]. Figure 1 shows the effect of gas temperature on the liquid penetration length as the ambient gas density was varied from 3.6 to 59  $kg/m^3$ , and the gas temperature was varied from 700 to 1300 K. The injection pressure was 135 MPa, and the nozzle diameter was 246  $\mu m$ . It found that the new breakup model captures the trends of penetration length as a function of the gas temperature more accurately than the standard model whose predicted penetration length is a much weaker function of the gas temperature [8, 13]. One controlling factor for the temperature dependence is the vaporization rate, which is directly related to the drop size distribution. The improved results indicate that the new breakup model predicts a more realistic drop size distribution.

The new breakup model has also been applied to diesel combustion simulations by Yi and Reitz [13], who found that engine emissions (particularly soot) are significantly influenced by the details of the primary atomization model. It is interesting to note that the primary atomization model had less effect on gross quantities such as cylinder pressure, heat release or liquid penetration lengths.

## REFERENCES

1. R. D. Reitz and R. Diwakar, Structure of High Pressure Fuel Sprays, SAE Paper 870598, SAE Transactions, Vol. 96, Sect. 5, pp. 492-509, 1987.
2. Yi, Y., and Reitz, R.D., "A One-dimensional Breakup Model for Low Speed Jets" Atomization and Sprays, Vol. 12, pp. 667-685, 2002.
3. Yi, Y., and Reitz, R.D., "Modeling the Primary Breakup of High-speed Jets," Accepted for publication, Atomization and Sprays, 2003.
4. V. G. Levich, *Physicochemicals*, Prentice-Hall, Englewood Cliffs, NJ, 1962.
5. C. A. J. Fletcher, *Computational Techniques for Fluid Dynamics, II*, 2<sup>nd</sup> Edition, pp. 130, Springer-Verlag, 1991.
6. C. V. K. Sarre, S-C. Kong, and R. D. Reitz, Modeling the Effects of Injector Nozzle Geometry on Diesel Sprays, SAE Paper 1999-01-0912, 1999.
7. C. Arcoumanis, M. Gavaises, and B. French, Effects of Fuel Injection Processes on the Structure of Diesel Sprays", SAE Paper 970799, 1997.
8. Yi, Y., "Numerical Modeling of Spray Primary Breakup with Application to Diesel Engines," PhD. Thesis, University of Wisconsin-Madison, 2002.
9. Amsden, A.A., "KIVA-3: A KIVA Program with Block-Structured Mesh for Complex Geometries", Los Alamos National Labs, LA-12503-MS, 1993.
10. Beale, J.C. and Reitz, R.D., " Modeling Spray Atomization with the Kelvin-Helmholtz/Rayleigh-Taylor Hybrid Model", Atomization and Sprays, Vol.9, pp.623-650, 1999.
11. Xin, J., Ricart, L., and Reitz, R.D., "Computer Modeling of Diesel Spray Atomization and Combustion", Combustion Science and Technology, Vol. 137, p. 171, 1998.
12. Siebers, D.L., "Liquid-Phase Penetration in Diesel Sprays", SAE Paper 980809, 1998.
13. Yi, Y., and Reitz, R.D., "Modeling the Effect of Primary Atomization on Diesel Engine Emissions," SAE paper 2003-01-1041, 2003.

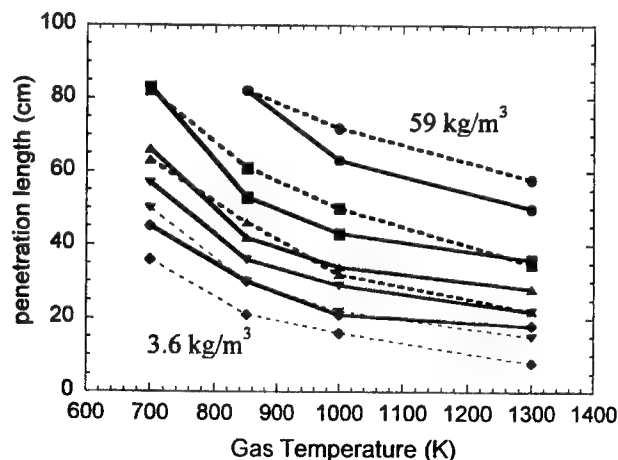


Fig. 1 Liquid penetration length as a function of gas temperature for gas densities from 3.6 to 59  $\text{kg/m}^3$ . The injection pressure is 135 MPa. The fuel and orifice diameter are DF2 and 246  $\mu\text{m}$ . Solid and dashed lines represent the computed and measured data, respectively.

# PDF MODELING OF TURBULENT COMBUSTION

AFOSR Grant F-49620-03-1-0015  
Principal Investigator: Stephen B. Pope

Mechanical & Aerospace Engineering  
Cornell University  
Ithaca, NY 14853

## SUMMARY

The overall goal of the research is to develop and demonstrate improved computational approaches for turbulent combustion. In both space and aircraft applications, the design of combustors in propulsion systems remains a significant technical challenge. Computational modeling is used extensively in the design process: our work is aimed at increasing the accuracy and efficiency of such models. In the last year significant advances have been made in two areas. First, we have used PDF calculations to explore the processes involved in the lifted flames studied experimentally by Cabra et al. (2002). These flames are formed as a cold fuel jet issues into a vitiated air stream. Autoignition is an important process in the stabilization mechanism, and consequently the calculated lift-off height is found to be sensitive to the kinetics. Second, a new method has been developed for combustion chemistry reduction. This is an extension of earlier work using rate-controlled constrained equilibrium (RCCE), but the implicit assumption of an orthogonal projection is improved upon, with favorable impact on the method's accuracy. These two topics are described more fully below. In addition, in collaboration with a group at the University of Pittsburgh, we continue to develop the combination of LES and PDF approaches for turbulent combustion (e.g., Sheikhi et al. 2003).

## PDF CALCULATIONS OF LIFTED TURBULENT FLAMES

In this work, more fully described by Masri et al. (2003), PDF calculations with detailed chemistry are performed of the lifted hydrogen flames studied experimentally by Cabra et al. (2003). The fuel jet mixes with co-flowing combustion products and heated air and subsequently auto-ignites forming a lifted flame stabilized at about ten jet diameters downstream of the exit plane. This burner, developed by Cabra et al. (2002), has the advantage of representing both liftoff and auto-ignition in a rather simple and well-defined flow configuration. However, it should be noted that lifted flames issuing in vitiated co-flow are different from those stabilized in still air. The temperature and composition of the co-flow impose different conditions such that the controlling processes and the dynamics of flame stabilization are different from a regular lifted flame.

The computations presented here use the FLUENT code which solves Reynolds Averaged Navier Stokes (RANS) equations for the mean conservation of mass, momentum and energy, together with the  $k$ - $\epsilon$  turbulence model equations. A transport equation for the composition PDF is coupled and solved using a Lagrangian particle-based Monte Carlo method, and using the modified Curl (MC) mixing model. A detailed chemical kinetic mechanism and a thermodynamic data base are read in and the change in composition due to chemical reaction is

then handled by the In-Situ-Adaptive Tabulation (ISAT) method (Pope, 1997). The use of ISAT is novel in this hybrid RANS-PDF approach.

Two chemical mechanisms are used for hydrogen. One is developed by Mueller et al. (1999) and involves 10 species ( $H_2$ ,  $H$ ,  $O$ ,  $O_2$ ,  $OH$ ,  $H_2O$ ,  $HO_2$ ,  $H_2O_2$ ,  $Ar$ ,  $N_2$ ) and 21 reactions. The other is generated from the GRI-2.1 mechanism for methane by stripping out all the carbon and NO containing species and reactions. This mechanism involves the same species as the Mueller mechanism but with 28 reactions.

As an illustration of the results obtained, Fig. 1 shows radial profiles of the mean mass fractions of  $H_2$  and  $OH$  according to the two different chemical mechanisms. As may be seen, the GRI calculations indicate ignition earlier than the experiments, whereas the Mueller mechanism is in closer agreement with the data.

An interesting observation from the calculations is that ignition occurs first for extremely lean mixtures, because these have the highest temperature.

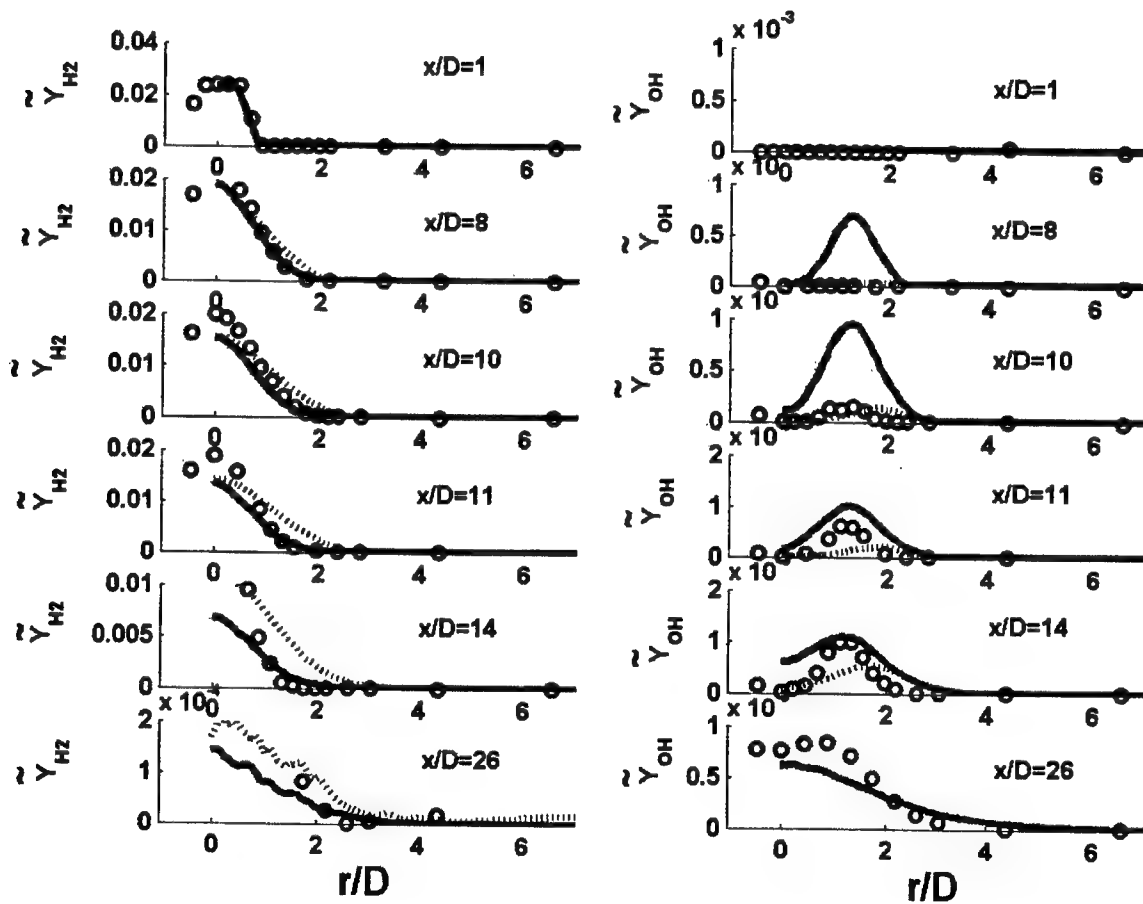


Figure 1: Measured and computed radial profiles of mean mass fractions of  $H_2$  and  $OH$ ,  $\tilde{Y}_{H_2}$  and  $\tilde{Y}_{OH}$  for the lifted flame. Plots on the LHS are for  $\tilde{Y}_{H_2}$  and plots on the RHS are for  $\tilde{Y}_{OH}$ . Each column shows six plots for axial locations  $x/D=1, 8, 10, 11, 14$  and  $26$  respectively. The symbols in each plot represent measurements, the solid line is computed using the GRI21-  $H_2$  mechanism and the dotted line represents computations from the Mueller- $H_2$  mechanism.

## DIMENSION REDUCTION OF COMBUSTION CHEMISTRY

In the past two decades, one of the most important triumphs in combustion research is the numerical simulation of laminar flames in one or two spatial dimensions, taking account of detailed transport and chemical kinetics. However, for most practical reacting flows featuring three dimensional geometric complexity and turbulence, a detailed numerical simulation will remain computationally prohibitive, even on the largest supercomputers. To make calculations of turbulent combustion with realistic chemistry feasible, it is necessary to reduce the computational cost of solving the complex thermo-chemical system.

The recent work of Tang and Pope (2000) describes a unified dimension reduction/storage retrieval methodology which can be used to implement detailed hydrocarbon chemistry efficiently in turbulent combustion calculations. Dimension reduction is achieved through rate-controlled constrained equilibrium (RCCE) (Keck & Gillespie 1971); and storage/retrieval through *in situ* adaptive tabulation (ISAT). In this context, RCCE is preferred over other reduction methodologies, such as quasi-steady state assumption (QSSA) and intrinsic low-dimensional manifold (ILDM) (Maas & Pope 1992), because of the guaranteed existence and smoothness of the implied low-dimensional constrained equilibrium manifold (CEM). However, RCCE is solely based in thermodynamics, whereas QSSA and ILDM are appropriately based on dynamical-systems approached to the chemical kinetics. Its "efficiency" is questionable, therefore, since it is not clear that the implied reduction assumptions are near optimal.

In this study, an orthogonal projection contained in the traditional RCCE method, which projects the rate equation of the chemical system onto the constrained equilibrium manifold, is identified. A more accurate projection, which we refer to as the close parallel inertial manifold (CPIM) is then constructed. The CPIM assumption introduces the chemical kinetics directly through the local Jacobian of the chemical reacting system, and hence leads to greater accuracy than RCCE.

As an illustration of the methodology, Fig. 2 shows calculations for the autoignition of a methane-air mixture initially at 1500K. As may be seen, the CPIM results are almost indistinguishable from those from the detailed mechanism, while RCCE overpredicts the ignition delay time by about a factor of two.

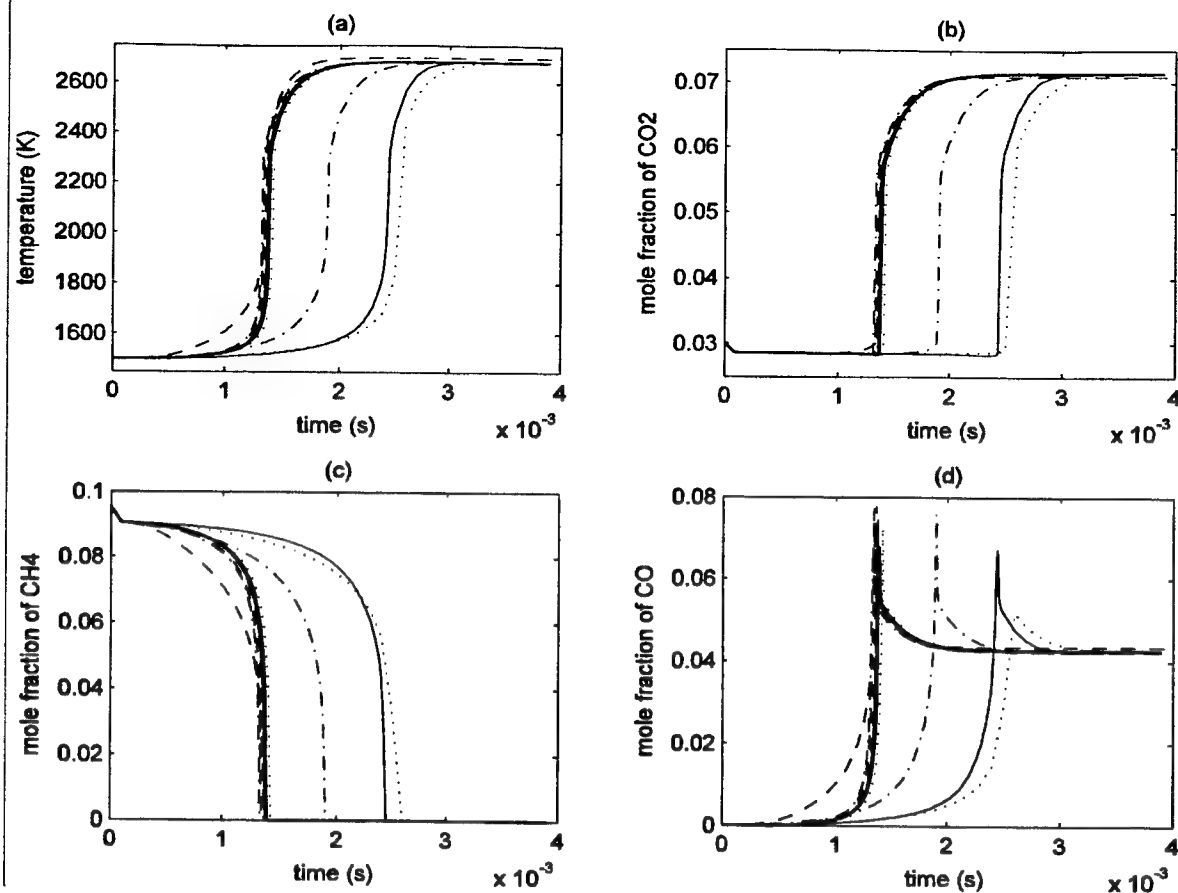


Figure 2: Comparisons of major species mole fractions against time calculated using RCCE and CPIM ( $T_0 = 1500$  K,  $p = 1$  atm, and  $\Phi = 1$ ). Black: exact solution; Red: CPIM; Blue: RCCE.

## REFERENCES

- R. Cabra, T. Myrvold, J.Y. Chen, R.W. Dibble, A.N. Karpetics and R.S. Barlow, (2002) "Simultaneous Laser Raman-Rayleigh-LIF measurements and numerical modeling results of a lifted turbulent H<sub>2</sub>/N<sub>2</sub> jet flame in a vitiated coflow," *Proc. Combust. Inst.*, 29: in press.
- J.C. Keck and D. Gillespie, (1971) *Combust. Flame*, 17:237-241.
- U. Maas and S.B. Pope, (1992) *Combust. Flame*, 88:239-264.
- A.R. Masri, R. Cao, S.B. Pope and G.M. Goldin (2003) "PDF Calculations of Turbulent Lifted Flames of H<sub>2</sub>/N<sub>2</sub> issuing into a vitiated co-flow," *Combust. Theory and Modelling*, (submitted).
- M.A. Mueller, T.J. Kim, R.A. Yetter, and F.L. Dryer, (1999) "Flow Reactor Studies and Kinetic Modeling of the H<sub>2</sub>/O<sub>2</sub> Reaction," *International Journal of Chemical Kinetics*, 31:113-125.
- M.R.H. Sheikhi, T.G. Drozda, P. Givi and S.B. Pope (2003) "Velocity-scalar filtered density functions for large eddy simulation of turbulent flows," *Phys. Fluids*, (to be published).
- Q. Tang and S.B. Pope (2002) *Proc. Combust. Inst.*, to appear.
- S.B. Pope (1997) *Combust. Theory and Modelling*, 1:41-63.



# FILTERED MASS DENSITY FUNCTION FOR SUBGRID SCALE MODELING OF TURBULENT DIFFUSION FLAMES

Grant Number F49620-03-1-0022

Principal Investigator: Peyman Givi

Department of Mechanical Engineering  
University of Pittsburgh  
Pittsburgh, PA 15261

## SUMMARY/OVERVIEW:

The specific objectives of this work are:

- (i) To further develop and improve the "filtered density function" (FDF) methodology for closure of the subgrid scales (SGS) in turbulent reacting flows.
- (ii) To implement the resulting SGS closure for large eddy simulation (LES) of turbulent diffusion flames.

## TECHNICAL DISCUSSION

The filtered density function (FDF) [1] methodology has proven effective for large eddy simulation (LES) of turbulent reacting flows. The fundamental property of the FDF method is exhibited by the closed form nature of the chemical source term appearing in the transport equation governing the FDF. This property is very important as evidenced in several applications of FDF for LES of a variety of turbulent reacting flows; see Ref. [2] for a review. The encouraging results attained thus far warrant further improvements and implementations of LES/FDF for a wider class of reacting flows. Our efforts within the past year have been concentrated on doing exactly that. Specifically, we have been working on:

- (I) Development of the joint velocity-scalar FDF methodology.
- (II) Implementation of our previously developed scalar filtered mass density function (FMDF) for LES of turbulent methane jet flames.
- (III) Development of the joint velocity-scalar FMDF methodology.

The efforts pertaining to (I) are documented in Ref. [3]. In this work, a methodology termed the "velocity-scalar filtered density function" (VSFDF) is developed. This method is basically a combination of the marginal scalar [4] and the marginal velocity [5] FDF schemes. Compared to conventional LES and velocity FDF, this approach has the advantage of treating chemical reaction in a closed form; and compared to scalar FDF, has the advantage of treating convective transport (of momentum and species) in closed form. An exact transport equation is derived for the VSFDF in incompressible turbulent flows. In this equation, the unclosed terms are modeled in a fashion similar to probability density function (PDF) methods as used in Reynolds-averaged simulations (RAS) [6]. A system of stochastic differential equations which yield statistically equivalent results to the modeled VSFDF transport equation is constructed. These SDEs are solved numerically by a Lagrangian Monte Carlo procedure in which the Ito

character of the SDEs is preserved. The consistency of the proposed SDEs and the convergence of the Monte Carlo solution are assessed in a format similar to that in our previous work [4,5].

In efforts pertaining to (II), we have used our previously developed scalar filtered mass density function (SFMDf) [7] methodology for LES of a piloted jet flame configuration as considered in the experiments of the Combustion Research Facility at the Sandia National Laboratories [8]. This flame has been the subject of broad investigations by other computational/modeling methodologies [9]. In the experiments, three basic flames are considered, identified by Flames D, E, and F. The geometrical configuration in these flames is the same, but the jet inlet velocity is varied. In Flame D, the fuel jet velocity is the lowest and the flame is close to equilibrium. The jet velocity increases from flames D to E to F, with noticeable non-equilibrium effects in the latter two. We have completed LES of Flame D. For this simulation, combustion is modeled via the equilibrium methane-oxidation model. This model is enacted via "flamelet" simulations which consider a laminar counterflow (opposed jet) flame configuration [10]. The full methane oxidation mechanism of the Gas Research Institute (GRI) [11] accounting for 53 species and 325 elementary reactions is used. At low strain rates, the flame is close to equilibrium. Thus, the thermo-chemical variables are determined completely by the "mixture fraction." This flamelet library is coupled with our LES/SFMDf solver in which transport of the mixture fraction is considered. It is important to emphasize that the PDF of the mixture fraction is not "assumed" a priori (as done in almost all other flamelet based LES [12-16]). Rather, it is calculated explicitly via the SFMDf.

One of the most important element of LES/SFMDf is associated with the consistency of the FMDF solver. This issue has been the subject of broad investigations in PDF methods (for latest results see Ref. [17]). We have used a hybrid (and highly coupled) finite-difference (FD)/ Monte Carlo (MC) solver in which some of the computations are conducted by FD, some by MC, and some by both. The latter "redundancy" is very important in ensuring the consistency and accuracy of the overall solution procedure. The first and simplest consistency check is via flow visualization. For example, Fig. 1 shows the instantaneous temperature contours of the methane jet flame as obtained by the two methods. Such a consistency is checked for all the other variables and is further assessed via statistical analysis of data generated by the two methods. The predictive capability of SFMDf is demonstrated in Fig. 2 which shows the radial distributions of the time averaged, filtered values of the mixture fraction, the temperature and the mass fractions of some of the species. The agreement shown in this figure is observed for all of the other mean values.

In efforts pertaining to (III), we have just finished the mathematical formulation for the "velocity-scalar filtered mass density function" (VSFMDf). Compared to VSFDF, this methodology has an added advantage that it allows for variable density effects. An exact transport equation is derived for the VSFMDf. A system of stochastic differential equations which yields statistically equivalent results to the modeled VSFMDf transport equation is being constructed. Work is underway in selecting the parameters of the SDEs in such a way that the compressibility effects are taken into account accurately.

## WORK IN PROGRESS

Our current work is concentrated on the following issues: (1) Fine-tuning and further implementation of the LES/SFMDf methodology for prediction of Sandia Flame D. (2) Extension of LES/SFMDf methodology for LES of Sandia's other flames. (3) Completion of

the work on LES/VSFMDf by assessing its consistency and also its predictive capability by the procedure followed in our previous work on LES/VSFDF [3].

## ACKNOWLEDGMENT

We are indebted to Professor Stephen B. Pope (Cornell University) for his valuable collaboration on various aspects of this work.

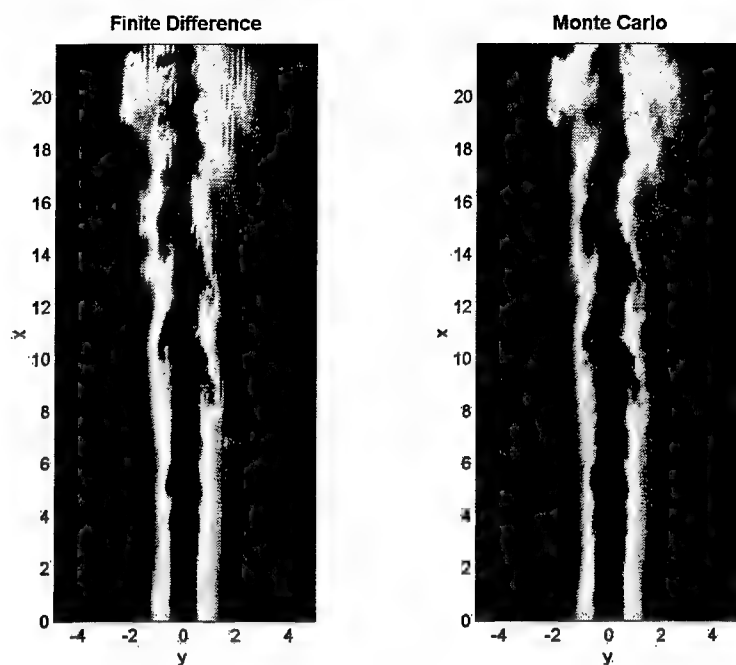


Figure 1. Consistency Assessment of the SFMDf for LES of Sandia Flame D

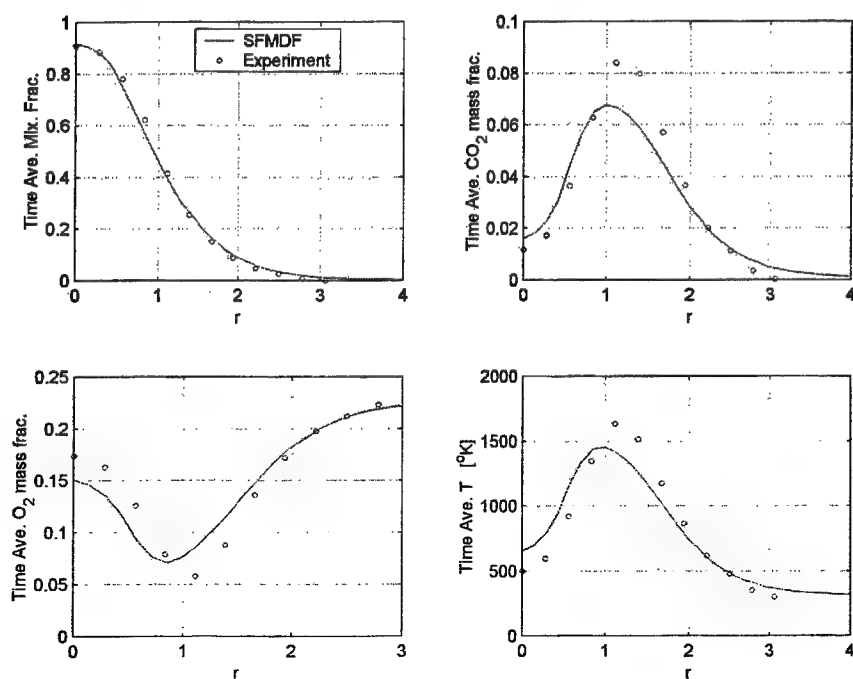


Figure 2. Comparison of LES/SFMDf Predictions with Sandia Data

## REFERENCES

- [1] Pope, S. B., *Turbulent Flows*, Cambridge University Press, Cambridge, UK, 2000.
- [2] Givi, P., A Review of Modern Developments in Large Eddy Simulation of Turbulent Reacting Flows, in Liu, C., Sakell, L., and Herklotz, R., editors, *DNS/LES-Progress and Challenges*, pp. 81-92, Greyden Press, Columbus, OH, 2001.
- [3] Sheikhi, R.M., Drozda, T.G., Givi, P. and Pope, S.B., Velocity-Scalar Filtered Density Function for Large Eddy Simulation of Turbulent Flows, (2003), Submitted for publication.
- [4] Colucci, P.J., Jaber, F.A., Givi, P. and Pope, S.B., *Phys. Fluids*, **10** (2): 499-515 (1998).
- [5] Gicquel, L. Y. M., Givi, P., Jaber, F. A., and Pope, S. B., *Phys. Fluids*, **14** (3): 1196-1213 (2002).
- [6] Pope, S.B., *Ann. Rev. Fluid Mech.*, **26**: 23-63 (1994).
- [7] Jaber, F. A., Colucci, P. J., James, S., Givi, P., and Pope, S. B., *J. Fluid Mech.*, **401**:85-121 (1999).
- [8] Nooren, P. A., Versiuis, M., Van der Meer, T. H., Barlow, R. S., and Frank, J. H., *Applied Physics*, **B71**: 95 (2000).
- [9] Barlow, R. S., Sandia National Laboratories, TNF Workshop website, <http://www.ca.sandia.gov/tdf/Workshop.html>, 2002.
- [10] Peters, N., *Turbulent Combustion*, Cambridge University Press, Cambridge, UK, 2000.
- [11] Smith, G. P., Golden, D. M., Frenklach, M., Moriarty, N. W., Eiteneer, B., Goldenberg, M., Bowman, C. T., Hanson, R., Song, S., Gardiner, W. C., Lissianski, V., and Qin, Z., <http://www.me.berkeley.edu/gri-mech>
- [12] De Bruyn Kops, S. M., Riley, J. J., Kosály, G., and Cook, A. W., *Combust. Flame*, **60**:105-122 (1998).
- [13] DesJardin, P. E. and Frankel, S. H., *Combust. Flame* **119**:121-132 (1999).
- [14] Pitsch, H. and Steiner, H., *Phys. Fluids*, **12**(10): 2541-2554 (2000).
- [15] Ladeinde, F., Cai, X., Sekar, B., and Kiel, B., AIAA Paper 2001-0634, 2001.
- [16] Kempf, A., Forkel, H., Chen, J. Y., Sadiki, A., and Janicka, J., *Proc. Combust. Inst.*, **28**:35-40 (2000).
- [17] Muradoglu, M., Pope, S.B. and Caughey, D.A., *J. Comp. Phys.*, **172**:841-878 (2001).

# LARGE-EDDY SIMULATION OF TURBULENT COMBUSTION

Grant number: F49620-03-1-0258

Flow Physics and Computation Division  
Department of Mechanical Engineering  
Stanford University  
Stanford, CA 94305-3030

## SUMMARY/OVERVIEW

The present research program has two major components: (i) the development of improved turbulence/chemistry interaction models for large-eddy simulations (LES), and (ii) the development of reduced kinetic mechanisms for JP-8 surrogate fuels, including the definition of surrogate fuels and the systematic reduction of the detailed chemical mechanisms. The LES combustion models will be based on the flamelet approach, will be applicable to premixed, non-premixed, and partially-premixed turbulent combustion, and will be of sufficient accuracy for predictions of pollutant formation. The second part of this work aims at the development of a fuel component library, which consists of skeletal mechanisms for different single component fuels using the same base chemistry. These can then be combined in different ways to form a hierarchy of reduced mechanisms for surrogate fuels of different complexity.

## TECHNICAL DISCUSSION

Since the project started only in April 2003, we will here only describe the project and present some relevant preliminary results.

### Combustion Models for Large-Eddy Simulation

In recent years, Large Eddy Simulation (LES) has been successfully applied to non-premixed and premixed turbulent combustion problems [1, 2, 3]. However, in most technical combustion applications, the pure non-premixed or premixed combustion models are no longer valid, since partially premixed combustion has to be taken into account. An example is the stabilization region of a lifted non-premixed flame. To overcome this problem, a Combined Conserved Scalar/Level-Set Flamelet model has been proposed [4, 5], which allows for the computation of reactive flows, where both premixed and non-premixed combustion occurs. In this formulation, the  $G$ -equation method is used to describe partially premixed flame propagation and to distinguish between burned and unburned regions. The reacting gases in the post-flame region are described by a laminar diffusion flamelet approach. The principal roadmap for the further development and validation of these models is to develop and validate the appropriate methods for the pure premixed and non-premixed combustion situations, and

combine the resulting models for a more general formulation. Much of this work has been done in the past. We have developed unsteady flamelet models for LES of non-premixed turbulent combustion [1, 2], and a level-set method for LES of premixed turbulent combustion [3]. These models have been validated with premixed and non-premixed turbulent jet flame experiments. Preliminary simulations with a Combined Conserved Scalar/Level-Set Flamelet Model have already been performed [6, 5].

Recently, we have developed a new consistent formulation of the  $G$ -equation approach for LES [7]. The solution of the instantaneous unfiltered  $G$ -equation has physical meaning only at the instantaneous flame front location. The definition of the remaining  $G$ -field is arbitrary. Hence, in a filtering procedure, applied to derive the appropriate LES equation, only states on the instantaneous unfiltered flame surface can be considered, which excludes the use of conventional volumetric LES filters. A new filter kernel has been developed, which averages along surfaces. Using this filter, the  $G$ -equation for the filtered flame front location can be derived as

$$\frac{\partial \check{G}}{\partial t} + \hat{\mathbf{v}}_u \cdot \nabla \check{G} = s_{T,u} |\nabla \check{G}|. \quad (1)$$

This equation has two unclosed terms. Since the new filter kernel only considers states at the instantaneous flame front, the convection velocity appearing in this equation is an average conditioned on the location of the flame surface. To relate  $\hat{\mathbf{v}}_u$  to the unconditionally Favre-filtered velocity  $\tilde{\mathbf{v}}$ , which is known from the solution of the momentum equations, a model for this quantity has also been developed. The resulting equation for the filtered flame front location is

$$\frac{\partial \check{G}}{\partial t} + \tilde{\mathbf{v}} \cdot \nabla \check{G} = \frac{\rho_u}{\bar{\rho}} s_{T,u} |\nabla \check{G}|. \quad (2)$$

The second unclosed term involves the turbulent burning velocity. A model for this term has also been developed. A length scale equation for the sub-grid flame brush thickness has been derived. An analytic expression for the turbulent burning velocity follows from the assumption that production equals dissipation in this equation.

Interestingly, because of the use of the new filtering procedure, a propagation term proportional to the curvature of the mean front, which appeared in earlier formulations of the filtered  $G$ -equation, is no longer present in Eq. (2). This is an important difference, since the curvature term has a stabilizing effect on the flame front and therefore leads to a decreased resolved flame wrinkling.

This new formulation offers many opportunities for future developments, especially for a dynamic model for the turbulent burning velocity. This will be a major goal of our future developments. We will also improve the sub-grid models for quantities, such as the turbulent kinetic energy, which are used in the computation of the turbulent burning velocity. In addition, we will improve the fidelity of the models when the limits of the applicability of flamelet models are approached.

## Development of Reduced Kinetic Mechanisms for JP-8 Surrogate Fuels

Numerical simulations of practical combustion systems, such as furnaces, pool fires, and even engines often lack an adequate description of the involved chemistry. The reason is, first of all, that real fuels are composed of many single components, involving, for instance,

aliphatic, aromatic, and alkylated aromatic components, but also cyclo-paraffins and possibly oxygenated components. Only for some of these components, detailed chemical kinetic mechanisms are already available. These mechanisms typically consist of thousands of reactions and up to one thousand chemical species. It is clear that it is impossible to model the true chemistry of a realistic fuel. Hence, for numerical simulations, appropriate surrogate fuels have to be used, which consist of one or more chemical components and reproduce the behavior of the real fuel as well as possible.

For the future, the US Air Force and the US Army are planning to use only one single fuel for Diesel engine and aircraft engine applications. This fuel will be JP-8, which is composed of approximately 65 % paraffins, 23 cycloparaffins, and 12 % aromatics. This suggests that these types of fuels should be considered as possible ingredients of JP-8 surrogate fuels. However, it should also be considered that the chemical behavior of branched chain paraffins differs substantially from straight chain paraffins, so that composites with at least four essentially different structures can be identified. The possible candidates representing the different chemical groups in the surrogate fuels have to be limited to chemical species, for which detailed chemical reaction schemes are available or might be available in the near future.

The first step for the present work is to identify appropriate surrogate fuels, which represent the physical and chemical properties of the real fuel as closely as possible. Possible chemical and physical requirements that might have to be satisfied by a particular surrogate fuel are the specific heat release, which can be expressed by the C/H ratio, the liquid or gaseous fuel density, specific heats, boiling point, critical pressure and temperature, formation of pollutants, such as NO<sub>x</sub> and soot, burning velocity, and auto-ignition characteristics. However, it is important to recognize that not all of these criteria are important in all applications. For instance, low temperature auto-ignition characteristics are important in the application to Diesel engine combustion, but irrelevant for aircraft gas-turbine engine combustion.

For the present work, to achieve high flexibility, we will identify surrogate fuels of different complexity by using available experimental data. For all the involved components we will identify appropriate detailed kinetic mechanisms. The accuracy for each single component will then be assessed by comparing simulations with experimental data. For the choice of individual components it is interesting to note that the base components might have to be changed, when going to higher complexity surrogate fuels. It is for instance well known that *n*-heptane is a good choice for a one-component surrogate fuel for Diesel engine combustion, because the auto-ignition characteristics are similar to real Diesel fuel. However, accounting for an aromatic component in a two-component surrogate fuel strongly delays auto-ignition, such that the aliphatic component has to be changed from *n*-heptane to a longer chain aliphatic fuel, which provides a lower auto-ignition delay time.

Differently from previous approaches, here, we will first develop skeletal mechanisms of different complexity for each single fuel component. The simplest mechanisms describe only the heat release, response to strain, and laminar burning velocities correctly. Higher levels of complexity will also include the hydrocarbon chemistry important for NO<sub>x</sub>, soot formation and low temperature auto-ignition chemistry. These skeletal mechanisms will form a component library. From this library, surrogate fuels of different complexity can be defined,

The great advantage of the component library approach is that mechanisms for surro-

gates with the same components, but for different application can be developed relatively easily by just combining the skeletal mechanisms of the single components with appropriate complexity. The second advantage is that, if new components should be added in the future, then these can just be added to the skeletal mechanism component library and the reduction procedure does not have to be repeated for the entire detailed multi-component mechanism.

Different surrogates for JP-8 have been suggested, for instance, by Viola et al. [8] and Agosta et al. [9]. We will most likely start with the six-component surrogate fuel by Viola et al. [8]. The next steps will be to identify a detailed kinetic mechanism for this surrogate fuel, validate with experiments, particularly with the UCSD extinction and counterflow ignition data by Seshadri. With a good set of test cases, we can then computationally define simpler surrogate fuels and build the component library of skeletal mechanisms.

## References

- [1] H. Pitsch and H. Steiner. Large-eddy simulation of a turbulent piloted methane/air diffusion flame (Sandia flame D). *Phys. Fluids*, 12(10):2541–2554, 2000.
- [2] H. Pitsch. Improved pollutant predictions in large-eddy simulations of turbulent non-premixed combustion by considering scalar dissipation rate fluctuations. *Proc. Combust. Inst.*, 29, 2002. to appear.
- [3] H. Pitsch and L. Duchamp de Lageneste. Large-eddy simulation of premixed turbulent combustion using a level-set approach. *Proc. Combust. Inst.*, 29, 2002. to appear.
- [4] N. Peters. *Turbulent Combustion*. Cambridge University Press, 2000.
- [5] H. Pitsch, P. Trouillet, C. D. Pierce, E. Tribbett, C. M. Sipperley, C. F. Edwards, and C. T. Bowman. A joint experimental/large-eddy simulation study of a model gas turbine combustor. *Western States Section Meeting of the Combustion Institute, 2002, San Diego, CA*, pages WSSCI 02S-59, 2002.
- [6] H. Pitsch and L. Duchamp de Lageneste. Large-eddy simulation of lifted turbulent diffusion flames. *2<sup>nd</sup> Joint meeting of the US sections of the Combustion Institute, Oakland, CA*, page paper 263, 2001.
- [7] H. Pitsch and L. Duchamp de Lageneste. A g-equation formulation for large-eddy simulations of premixed turbulent combustion. *CTR Annual Research Briefs*, 2002. to appear.
- [8] A. Violi, S. Yan, E. G. Eddings, A. F. Sarofim, S. Granata, T. Faravelli, and E. Ranzi. Experimental formulation and kinetic model for jp-8 surrogate mixtures. *Comb. Sci. Tech.*, 174:399–417, 2002.
- [9] A. Agosta, D. B. Lenhert, D. L. Miller, and N. P. Cernansky. Development and evaluation of a jp-8 surrogate that models preignition behavior in a pressurized flow reactor. *3<sup>rd</sup> Joint meeting of the US sections of the Combustion Institute, Chicago, OH*, page paper E07, 2003.



# A NEW CLASS OF HYBRID SCHEMES BASED ON LARGE EDDY SIMULATION AND LOW-DIMENSIONAL STOCHASTIC MODELS

(Grant/Contract Number F49620-03-1-0023)

Principal Investigator: Tarek Echekki

North Carolina State University  
2601 Stinson Drive, Raleigh, NC 27695-7910

## SUMMARY/OVERVIEW

The objective of this study is to develop and validate a novel class of hybrid schemes to simulate turbulent mixing and combustion flows. The schemes are based on the coupling of large-eddy simulation (LES) to compute complex flows with One-Dimensional Turbulence (ODT) to resolve important subgrid scale phenomena that govern the so-called "turbulence-chemistry interactions."

## TECHNICAL DISCUSSION

**Introduction:** The prediction of finite-rate chemistry effects presents challenges to the state-of-the-art models in turbulent combustion. The key challenge is the difficulty to account for the detailed coupling between turbulence and chemistry over a wide range of length and time scales. In recent years, there has been increased interest in applying LES approaches to reacting flows. Turbulent combustion models that have been proposed in recent years include extensions of already demonstrated models in RANS approaches with their recognized limitations. These limitations are associated with the representations of unresolved physics of mixing, transport and reaction models, such as the prediction of ignition or extinction events. Other limitations may involve the prediction of transitions in the burning mode (e.g. diffusion to premixed), in the burning regime (e.g. flamelet to distributed reaction) or in the flow regime (e.g. laminar to turbulent).

Alternative strategies in turbulent combustion modeling have been developed by Kerstein: the Linear-Eddy Model (LEM) (Kerstein 1989, 1990, 1991, and 1992) and the One-Dimensional Turbulence (ODT) model (Kerstein 1999). The two approaches address the difficulty of adequately predicting mixing-reaction coupling at all scales by spatially and temporally resolving the processes of turbulent advection, molecular transport and chemistry on one dimension in physical space. The models are based on a mechanistic distinction between turbulent transport and molecular processes (diffusion and chemistry). Molecular processes are implemented deterministically by solution of the unsteady reaction-diffusion equations. Turbulent transport is implemented stochastically by using discrete stirring events implemented on segments of the domain. The principal distinction between LEM and ODT stems from the solution of one or more components of the velocity vector in ODT. The additional transport equations provide information about the velocity field, thereby a mechanism for "driving" turbulence. In contrast to LEM, which is a "mixing model", ODT is a self-contained turbulence model. In LEM, the frequency and the eddy size distribution of the stirring events are prescribed so as to reproduce a predefined energy spectrum and a characteristic turbulent Reynolds number; while, in ODT the frequency and the eddy size distribution of the stirring events are not prescribed in advance. Instead, the local flow field determines them.

In recent studies, Echekki et al (2001, 2002) and Hewson and Kerstein (2001) have demonstrated the stand-alone ODT model for the prediction of finite-rate chemistry effects in self-stabilized hydrogen-air, and CO/H<sub>2</sub>-air and piloted methane-air jet diffusion flames. In nearly parallel flows, the ODT 1D domain may be implemented as a radial line along the transverse plane to the mean flow. This line's evolution in time is then interpreted as a downstream evolution from the inlet through advection of the ODT domain. Qualitative examinations of the inherent mechanisms that govern mixing and entrainment (Echekki et al 2001) indicate that the model reproduces some of the salient features associated with 3D developing boundary layers, even if the dynamics of these complex flows may not be adequately captured with a 1D formulation. Moreover, the model shows very good agreement with experimental statistics of thermo-chemical scalars, including minor species (NO) and intermediates (OH) (Echekki et al 2001) and differential-diffusion effects. The recent simulations by Echekki et al (2002) and Hewson and Kerstein (2001) also illustrate the model capability to predict extinction-reignition events in jet diffusion flames.

**Objectives:** The objective of this study is to develop and validate a novel class of hybrid schemes to simulate turbulent mixing and combustion flows. The schemes are based on the coupling of large-eddy simulation (LES) to compute complex flows with One-Dimensional Turbulence (ODT) to resolve important subgrid scale phenomena that govern the so-called "turbulence-chemistry interactions."

**Requirements for Hybrid Approaches and General Methodology:** In many respects, the LES-LEM methodologies that were developed by Menon and co-workers and McMurtry and co-workers (see for example the review by Menon et al 1993) may be implemented without significant modification to LES-ODT; but the self-contained ODT formulation provides better coupling between subgrid and LES-grid scales through the ODT and LES-filtered momentum equations. This coupling enables a more robust implementation of LES-ODT, and extends the application of these hybrid schemes to a wider class of complex flows. One important limitation of LES-LEM implementation is the use of 'splicing events' for turbulent transport of scalars across LES grids. They involve the exchange of segments of the individual LEM domains (which reside in the LES grid). However, these splicing events do not recognize the portions of the LEM domains that should be exchanged across LES boundaries, and therefore result in unrealistic mixing events (e.g. mixing and fuel and oxidizers without crossing a flame).

An LES-ODT formulation may potentially extend individual representative ODT domains, or elements, across LES cell boundaries, and remove the requirement for splicing. Moreover, the solution of the components of the velocity in the ODT solutions provides a measure of subgrid scales stresses, thereby an alternative model for the subgrid stresses in LES. Therefore, the implementation of LES-based and ODT-based subgrid stresses must be compatible, either by adopting one or combining them into a mixed model. Most importantly, ODT elements can be advected across LES grids to better reflect large scale transport and history effects in combustion phenomena. The LES-ODT methodology is stated below:

- LES resolves transport equations for the momentum and selected scalars to provide a global measure of the flow field and the progress of chemistry and mixing.
- ODT resolves transport equations for subgrid or fluctuating velocity components, and the species and energy equation— The ODT momentum equations are obtained by constructing 1D residual equations from the balance of the instantaneous and filtered momentum equations. The species and energy equations are solved in their unsteady forms on the ODT grid with their filtered and fluctuating velocity contributions expressed explicitly.

Two representations of ODT domains may be implemented that reflect the coupling of ODT with LES: *Eulerian* and *Lagrangian* representations. In the Eulerian representation,

the ODT domains are fixed *a priori* in the computational domain of the coarse-grained simulations. In the Lagrangian representation, the ODT domains are transported with the mean flow. The Lagrangian representation eliminates partially or completely the contribution of mean advective terms in the governing equations of ODT. Distribution requirements of ODT elements in Lagrangian representations are similar to those adopted for related Eulerian-Lagrangian formulations, such as vortex methods (Cottet and Koumoutsakos, 2000). Similar requirements have already been addressed in PDF approaches in turbulent combustion (Pope 1985) and in the more recent Representative Interactive Flamelets approach (Pitsch *et al* 1998).

Figure 1 illustrates a conceptual Eulerian implementation of representative ODT domains for the simulation of an expanding kernel inside the cylinder of an IC engine. The ODT domains may be implemented to “see” the cylinder boundaries, thereby a fine-grained representation of important processes near the cylinder walls (e.g. flame-wall interactions, wall heat transfer, surface chemistry).

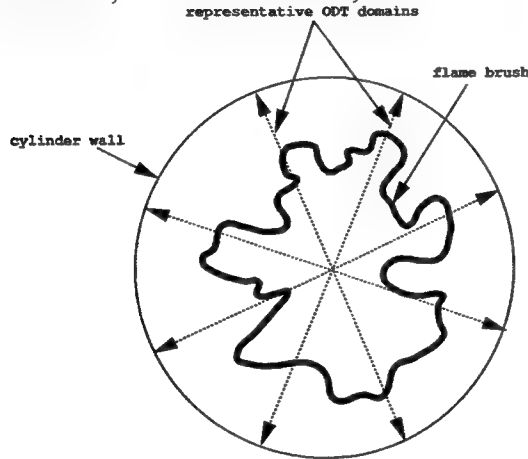


**Figure 1.** Hybrid LES-ODT Approaches – By placing “representative” ODT domains in the computational domain for the LES in a manner consistent with the required resolution of the coarse-grained scheme, spatial resolution of subscale mixing and chemical effects may be achieved. In LES-ODT hybrid schemes, averaged or filtered equations are solved using LES-filtered Navier-Stokes equations. In ODT, the fluctuating velocity components and the thermo-chemical scalars are solved on a finer grid.

The ODT solutions require the specification of initial and boundary conditions, which must be compatible with the LES solutions. ODT elements may extend to the boundaries of the LES domain or imbedded without extension to these boundaries. In the latter approach, implementations of buffer domains or forcing of the governing equations at the ODT boundary points may be implemented.

**Formulation of Filtered and Residual Equations:** The formulation is based on splitting the unsteady Navier-Stokes equations into filtered and residual equations. The residual equations are projected into 1D domains or elements. The LES and ODT governing equations for continuity, momentum and scalars are presented in Table 1 for a Lagrangian representation of ODT elements.

	LES	ODT (Lagrangian Formulation)
<b>Continuity</b>	$\frac{\partial \bar{\rho}}{\partial t} + \frac{\partial}{\partial x_j} (\bar{\rho} \bar{u}_j) = 0$	none
<b>Momentum</b>	$\frac{\partial \bar{\rho} \bar{u}_i}{\partial t} + \frac{\partial}{\partial x_j} (\bar{\rho} \bar{u}_j \bar{u}_i) =$ $\frac{\partial \bar{\tau}_{ij}}{\partial x_j} - \frac{\partial}{\partial x_j} \left[ \bar{\rho} (\bar{u}_i^* \bar{u}_j^* - \bar{u}_i \bar{u}_j) \right], \quad i = 1-3$ <p>where</p> $\tau_{ij} \equiv \mu \left[ \left( \frac{\partial u_i}{\partial x_j} + \frac{\partial u_j}{\partial x_i} \right) - \frac{2}{3} \frac{\partial u_k}{\partial x_k} \right] - \delta_{ij} \frac{\partial P}{\partial x_i},$	$\rho \frac{\partial u_i^*}{\partial t} = \frac{\partial}{\partial \eta} \left( \mu \frac{\partial u_i^*}{\partial \eta} \right) + \frac{\partial}{\partial x_j} \left[ \bar{\rho} (\bar{u}_i^* \bar{u}_j^* - \bar{u}_i \bar{u}_j) \right],$ $i = 1-3$
<b>Scalars</b>	<ul style="list-style-type: none"> <li>Scalars to track progress of mixing and chemistry</li> </ul>	<ul style="list-style-type: none"> <li>Species</li> </ul> $\rho \frac{\partial Y_k}{\partial t} = \frac{\partial}{\partial \eta} (\rho Y_k V_k) + \omega_k^* W_k, \quad k = 1-K.$

$\frac{\partial \bar{\rho} \tilde{Z}_\alpha}{\partial t} + \frac{\partial}{\partial x_j} (\bar{\rho} \tilde{u}_j \tilde{Z}_\alpha) = \frac{\partial}{\partial x_j} \left( \bar{\rho} \left[ D_\alpha \frac{\partial \tilde{Z}_\alpha}{\partial x_j} \right] \right)$ $- \frac{\partial}{\partial x_j} \left[ \bar{\rho} (\tilde{u}_j^* Z_\alpha - \tilde{u}_j'' \tilde{Z}_\alpha) \right] + \bar{S}_\alpha(Z_\alpha), \alpha = 1, N$	<p>• Energy</p> $\rho c_p \frac{\partial T}{\partial t} = \frac{\partial P}{\partial t} + \sum_{k=1}^N c_{p,k} Y_k V_k \frac{\partial T}{\partial \eta} +$ $\frac{\partial}{\partial \eta} \left( \lambda \frac{\partial T}{\partial \eta} \right) - \sum_{k=1}^N h_k \omega_k W_k.$
--	--

**Table 1.** Governing equations for LES and ODT. The coordinates on the 1D domain is  $\eta$ . The scalars  $Z_\alpha$  are derived scalars based on the resolved scalars  $T$  and  $Y_k$ . They are measures of the progress of reaction and mixing (e.g. reaction progress variable, mixture fraction, dissipation rate). Their closure terms (diffusive transport, subgrid fluxes and source terms) are evaluated using the ODT resolved solutions based on the ODT elements residing at the selected grid.

In the hybrid scheme, ODT provides information about velocity-scalar correlations, the filtered density, the mean viscosity and species diffusivities (and diffusive fluxes), and the mean reaction rate. The LES simulation provides mean velocity components. Subgrid stresses may be computed using the coarse-grained approach or ODT (see Fig. 2). The two solution techniques may be coupled numerically using a fractional step approach for temporal integration.

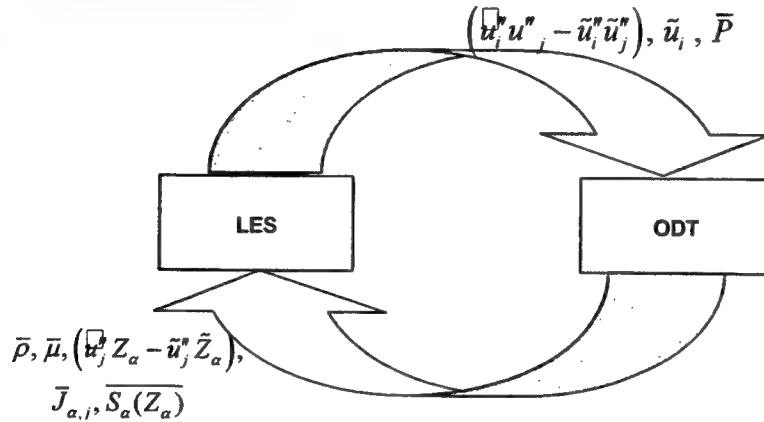


**Figure 2.** Schematics of the hybrid Solution algorithm. ODT provides averaged or filtered flux terms for species and temperature, and averaged and filtered diffusive flux and chemical source terms for species and temperature. LES provides filtered velocity components and the pressure. Subgrid stresses may be evaluated using ODT, or may be provided through the coarse solution, and used to dynamically specify the ODT model parameter.

## References

1. Cottet, G.-H., and Koumoutsakos, P.D., *Vortex Methods*, Cambridge University Press, 2000.
2. Echekki, T., Kerstein, A.R., Dreeben, T.D., and Chen, J.Y., *Combust. Flame*, Vol. 125, pp. 1083-1105 (2001).
3. Echekki, T., Kerstein, A.R., and Chen, J.Y., submitted to *Combust. Flame*, 2002.
4. Hewson, J.C., and Kerstein, A.R., *Combust. Theo. Model.*, Vol. 5, pp. 669-697, 2001.
5. Kerstein, A.R., *Combust. Flame*, Vol. 75, pp. 397-413 (1989).
6. Kerstein, A.R., *J. Fluid Mech.*, Vol. 216, pp. 411-435 (1990).
7. Kerstein, A.R., *J. Fluid Mech.*, Vol. 231, pp. 361-394 (1991).
8. Kerstein, A.R., *Combust. Sci. Tech.*, Vol. 81, pp. 75-96 (1992).
9. Kerstein, A.R., *J. Fluid Mech.*, Vol. 392, pp. 277-334 (1999).
10. Menon, S., McMurtry, P.A., and Kerstein, A.R., in *Large Eddy Simulation of Complex Engineering and Geophysical Flows*, (B. Galperin and S.A. Orszag, Eds.), Cambridge University Press, New York, 1993, pp. 287-314.
11. Pitsch, H., Chen, M., and Peters, N., *Proc. of the Combustion Institute*, Vol. 27, The Combustion Institute, Pittsburgh, 1998, pp. 1057-1064.
12. Pope, S.B., *Prog. Energy Combust. Sci.*, Vol. 11, pp. 119-192 (1985).

# **TOWARDS LES OF TURBULENT COMBUSTION USING LATTICE BOLTZMANN METHOD**

AFOSR GRANT Number F49620-01-1-0142

Principle Investigators: Sharath S. Girimaji \*, Li-Shi Luo \*\*

\* Aerospace Engineering Department, Texas A&M University, College Station, TX 77843-3141

\*\* National Institute of Aerospace (NIA), 144 Research Drive Hampton, VA 23666

## **SUMMARY/OVERVIEW:**

The objective of the proposed research is to develop the fundamentals of Lattice-Boltzmann method (LBM) to enable large-eddy simulations (LES) of turbulent combustion. The physical and computational advantages of the Lattice Boltzmann equation over the Navier-Stokes (NS) based methods for the turbulent combustion application are now even more evident than before. Our goal is to compete with NS methods in their strength areas and provide a superior computational capability in problems that are not easily tractable by the NS method.

## **TECHNICAL DISCUSSION**

Lattice Boltzmann method (LBM) continues to grow as a viable alternative to traditional CFD methods for computing complex fluid flow. For flows involving multi-species mixing, multi-phase interaction and reaction, the advantages of the LBM over traditional methods lay both in physical accuracy and computational characteristics. From the physics point of view, LBM is especially well suited for turbulent reacting flows for it is capable of incorporating thermodynamics, fluid dynamics and chemistry in one internally-consistent unified description. In recent years, LBM has made significant strides in theory and application. On the theoretical front, rigorous mathematical proof now exists demonstrating that the LBM is a special finite difference scheme of the continuous Boltzmann equation that governs all fluid flow <sup>[1]</sup>. (Recall that the Navier-Stokes (NS) equation also has its roots in the Boltzmann equation.) It has also been shown that the LBM can be related to some conventional CFD methods and the proof brings to light the advantages of the LBM. Preliminary numerical studies with the LBM demonstrate the power and the potential of this new method. The main computational advantages of the LBM 'discrete' physics model over the continuum physics model are now well established. Throughout the report the terms LBM and LBE method are used synonymously.

Turbulent combustion is a culmination of several physical processes occurring individually and collectively. The first step towards making LBM a computationally viable tool for turbulent combustion entails the development of models for several phenomena not considered in the basic method. We identify seven different areas in which the LBM needs to be developed from fundamental principles before they can be combined to perform turbulent combustion calculations. These research sub-areas are 1) Molecular mixing, especially between species of vastly different molecular weights. 2) DNS and LES of turbulence. 3) Laminar flames. 4) Effects of heat release on flow dynamics. 5) Multi-phase effects. 6) Chemical kinetics and its reduction. 7) Treatment of complex geometry and boundary conditions.

Under the present grant, aspects of sub-areas (1), (2), (3), (5) and (6) were addressed and suitable LBM models are being developed<sup>[2]-[8]</sup>. The most significant progress has been made in the area of multi-species mixing. We have developed high-fidelity LBM models for multi-component mixing which represents a very important step toward enabling LBM calculations of combustion<sup>[2]-[3]</sup>. Comparison of the mixing model against NS-based DNS data shows very good agreement<sup>[4]</sup>. As demonstrated in the above references, this approach offers several advantages over continuum-based methods for turbulent combustion, especially when reactants of vastly different molecular weights are involved. Yet, much needs to be done before the full potential of LBM for LES of turbulent combustion can be realized. In this report we will present in some detail the progress made in two other areas: DNS of isotropic turbulence in inertial and rotating frames and chemistry reduction.

**DNS/LES with LBM:** Evolution of homogenous isotropic turbulence in a 3D periodic cube is an important benchmark problem in the field of DNS. In an effort to evaluate the capability of LBM in turbulence, simulations of homogeneous isotropic turbulence are performed for the first time in both inertial and rotating frames. A brief description of this study is now provided.

A homogeneous isotropic turbulence velocity field is generated in Fourier space according to a prescribed energy spectrum:  $E(\kappa, 0) = 0.038\kappa^4 \exp(-0.14\kappa^2)$  with pre-selected wave numbers in the range  $(1 \leq \kappa \leq 8)$ . Incompressibility condition is automatically satisfied by (randomly) selecting the velocity amplitude vector in a plane normal to the wavenumber vector. The wavenumber vectors are uniformly distributed on a sphere of the appropriate radius. The decay of turbulence is then investigated in inertial and rotating reference frames. The low-wavenumber scaling of the spectra and the long-time kinetic energy and dissipation decay exponents are evaluated.

For the case without reference frame rotation, the LBM-calculated evolutions of kinetic energy and dissipation are shown in Fig. 1. Simple analysis shows that the decay laws for kinetic energy and dissipation are given by  $k(t) = k_0(t/t_0)^{-n}$  and  $\varepsilon(t) = \varepsilon_0(t/t_0)^{-(n+1)}$  respectively. The experimental values reported for the decay exponent  $n$  are generally in the range 1.15-1.45. From Fig. 1, it can be seen that the computed values of the decay exponents are 1.4 for kinetic energy and 2.4 for dissipation, in good agreement with experimental data. Energy spectra at different time steps for the same case are shown in Fig. 2. Initially, energy is contained in small wave number range as prescribed. Soon the energy spreads to higher wavenumbers (smaller scales) due to the non-linear cascade process. This in itself is quite significant since the advection (the source of non-linearity) is handled very differently in LBM. At this stage, the spectra scale as  $E(\kappa) \sim \kappa^2$  in the low wavenumber scales. (Figure 2 shows the compensated spectra). This is the expected behavior (at this stage of evolution) as energy is conserved during spectral cascade. Subsequently, the spectra start to decay, more rapidly in the large wavenumbers and slowly in the small wavenumbers (small scales).

The effect of frame rotation on turbulence is to inhibit the spectral cascade and thus slow down the decay. Apart from reducing the decay rate, rotation also renders the turbulence anisotropic. In our simulation, we take the axis of frame rotation to be along 3-direction with an angular velocity  $\vec{\Omega} = (0, 0, \Omega)$ , where  $\Omega = \kappa_p u' / R_0$ ,  $R_0$  is the Rossby number and  $\kappa_p = (\kappa_{\max} + \kappa_{\min})/2$  is a constant characterizing the energy containing wave number at  $t = 0$ . Simulations are performed for several Rossby numbers. Fig. 3 shows the evolution of kinetic energy with parameters  $u' = 0.01$ ,  $\tau = 0.62$  ( $128^3$  calculation) for various Rossby numbers. The decay rate decreases with decreasing Rossby number as expected. Closer inspection of the spectra

(figure not shown) clearly indicates that the energy cascade is inhibited by rotation, again consistent with known physics.

**Reduced chemistry for LBM:** Due to the simple explicit nature of LBM, it is anticipated that the time-step size will be smaller than a comparable NS method. In inert flows, the increase in the number of time steps is amply compensated for by the significantly reduced computational effort per time step in LBM. In turbulent combustion flows, the advantage may be reduced unless reaction is handled efficiently. Therefore, for efficient implementation of LBM, it is crucial to develop reduction techniques that are computationally inexpensive.

Currently, a variety of approaches are available in literature for reducing large kinetic mechanisms. For LBM, the simplest of the reduction procedures, the quasi steady state approximation (QSSA) is computationally most suitable, but it is of unreliable accuracy. In search of an inexpensive but reliable reduction procedure for LBM, (i) we will develop fundamental (realizability) constraints which any reduced system must satisfy at a minimum; and (ii) derive simplest models that satisfy these conditions.

Currently, there is no established criterion for judging what constitutes an adequate reduction method. Towards this end, we propose three fundamental or consistency constraints that a reduced system may be mandated to satisfy to be deemed physically acceptable.

1. The reduced system must preserve the fundamental physical properties of the state variables of the full system. This requirement is akin to the realizability constraint in turbulence modeling.
2. The mathematical character of the reduced system must be consistent with that of the full system.
3. The dynamics of the reduced system must be a realizable subset of the full-system behavior. That is, the dynamics of the reduced system cannot be inconsistent with that of the full system. The reduced manifold must be a realizable solution of the full system.

Surprisingly, most current analytical methods (including the sophisticated ones) do not satisfy these minimal requirements. We derive two QSSA-type reduction schemes that possess the following important attributes which are lacking in the traditional QSSA: (i) improved accuracy; (ii) insensitiveness to the choice of retained (slow) and discarded (fast) variables; and, (iii) possibility of customizing the invariant manifold calculation for a specific situation by choosing appropriate reference point.

#### References:

- [1]. X. He and Li-Shi Luo, Theory of the lattice Boltzmann method: From the Boltzmann equation to the lattice Boltzmann equation, *Physical Review E*, **56**, 6811(1997).
- [2]. L.-S. Luo and S. S. Girimaji, Lattice Boltzmann Model for Binary Mixtures, *Physical Review E*, **66**, 035301(2002).
- [3]. L.-S. Luo and S. S. Girimaji, Theory of the Lattice Boltzmann Model: Two-fluid model for Binary Mixtures, *Physical Review E*, **67**, 036302(2003).
- [4]. H. D. Yu, L.-S. Luo, and S. Girimaji, Scalar Mixing and Chemical Reaction Simulations Using Lattice Boltzmann Method, *International Journal of Computational Engineering Science*, **3**, 73(2002).
- [5]. D. d'Humières, I. Ginzburg, M. Krafczyk, P. Lallemand, and L.-S. Luo, Multiple-relaxation-time lattice Boltzmann models in three-dimensions, *Philosophical Transactions of the Royal Society of London, A*, **360**, 437(2002).
- [6]. M. Krafczyk, J. Tölke, and L. -S. Luo, Large-eddy Simulations with a multiple-relaxation-time LBE model, *International Journal of Modern Physics, C*, **17**, 33(2003).
- [7]. P. Lallemand, and L. -S. Luo, Hybrid finite-difference Thermal Lattice Boltzmann Equation, *International Journal of Modern Physics, C*, **17**, 41(2003).
- [8]. P. Lallemand, and L. -S. Luo, Lattice Boltzmann Method for Moving Boundaries, *Journal of Computational Physics*, **184**, 406(2003).



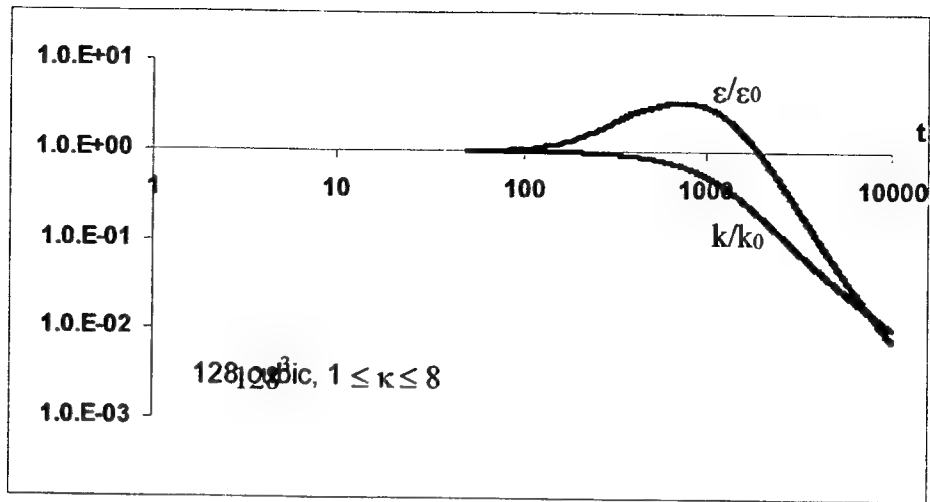


Fig 1 Power-law decay of kinetic energy and dissipation without rotation

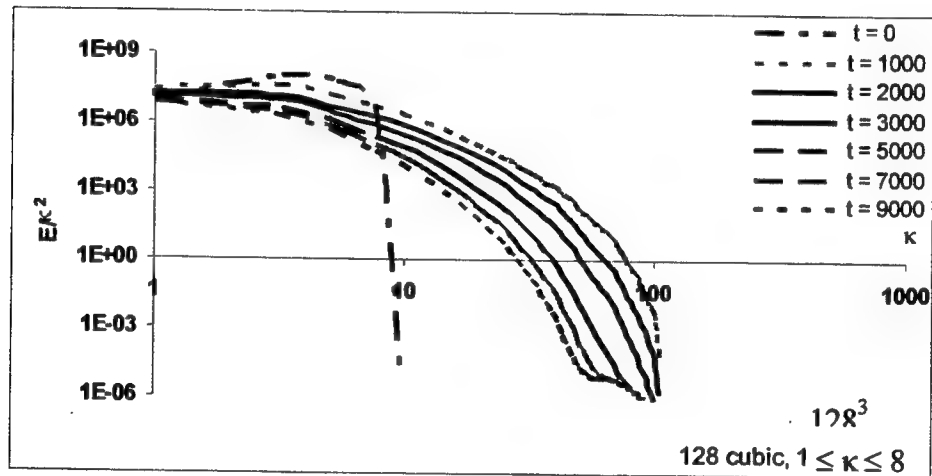


Fig 2 Energy spectrum evolution without

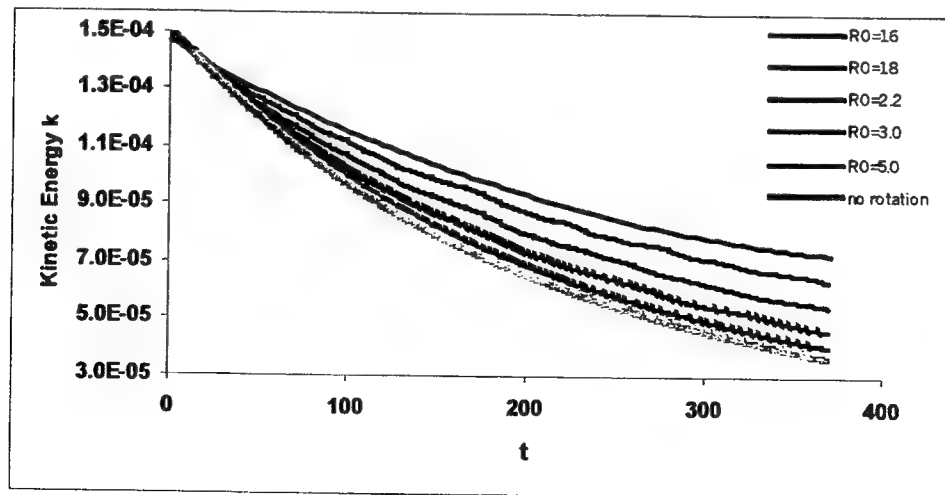


Fig 3 Energy spectrum evolutions with different  $R_0$



# EXPERIMENTAL STUDY OF VELOCITY-SCALAR FILTERED JOINT DENSITY FUNCTION AND ITS TRANSPORT EQUATION

AFOSR Grant F-49620-02-1-0130  
Principal Investigator: Chenning Tong

Department of Mechanical Engineering  
Clemson University  
Clemson, SC 29634-0921

## SUMMARY

Velocity-scalar filtered joint density function (FJDF) and its transport equation used in PDF-based large eddy simulation (LES) of turbulent combustion are studied experimentally in an axisymmetric turbulent jet. The FJDF and the unclosed terms in its transport equation are analyzed using their conditional averages. The FJDF is found to have qualitatively different characteristics depending on the instantaneous subgrid-scale (SGS) scalar variance and kinetic energy. In particular, when both are large compared to their mean values, the scalar mixing depends strongly on the SGS velocity, and the dependence is expected to be Reynolds number independent. The SGS fields are similar to the velocity and mixture fraction structure for laminar flamelets. The results further demonstrate that it is important for mixing models to depend on velocity and to account for different velocity and scalar structures.

## TECHNICAL DISCUSSION

PDF-based LES approaches for computing turbulent combustion have shown great promise. A method recently established by Peyman Givi's group (Skeikhi et al. 2003) solves the velocity-scalar FJDF transport equation in which the SGS scalar transport term is in closed form. More importantly, this approach allows mixing models to depend on velocity, thus has the potential to provide a more realistic description of the SGS mixing which is key to the accuracy of PDF base approaches. Here we study the FJDF and its transport equation for improving the velocity-scalar FJDF method. The velocity FJDF and its transport equation have been shown to be Galilean invariant (Tong 2003).

The velocity-scalar FJDF is defined as

$$f_{u\phi}(\mathbf{V}, \hat{\phi}; \mathbf{x}, t) = \int \prod_{i=1}^3 \delta[u_i(\mathbf{x}', t) - V_i] \delta[\phi(\mathbf{x}', t) - \hat{\phi}] G(\mathbf{x}' - \mathbf{x}) d\mathbf{x}', \quad (1)$$

where  $\mathbf{V}$ ,  $\hat{\phi}$ ,  $\delta$ , and  $G$  are the sample-space variable for  $\mathbf{u}$  and  $\phi$ , the Dirac delta function, and the filter function, respectively. The integration is over all physical space. The FJDF represents the weighted joint distribution of the velocity components and the scalar in a grid cell. The transport equation of the FJDF is obtained using the Navier-Stokes equations and the scalar transport equation:

$$\begin{aligned} \frac{\partial f_{u\phi L}}{\partial t} + V_j \frac{\partial f_{u\phi L}}{\partial x_j} &= \frac{\partial \langle p \rangle_L}{\partial x_j} \frac{\partial f_{u\phi L}}{\partial V_j} + \frac{\partial}{\partial V_j} \left\{ \left\langle \frac{\partial p'}{\partial x_j} \right| \mathbf{u} = \mathbf{V}, \phi = \hat{\phi} \right\rangle_L f_{u\phi L} \right\} \\ - \frac{\partial}{\partial V_i} \left\{ \left\langle \nu \frac{\partial^2 u_i}{\partial x_j \partial x_j} \right| \mathbf{u} = \mathbf{V}, \phi = \hat{\phi} \right\rangle_L f_{u\phi L} \right\} &- \frac{\partial}{\partial \hat{\phi}} \left\{ \left\langle D \frac{\partial^2 \phi}{\partial x_j \partial x_j} \right| \mathbf{u} = \mathbf{V}, \phi = \hat{\phi} \right\rangle_L f_{u\phi L} \right\}. \end{aligned} \quad (2)$$

where  $\langle \cdot | \mathbf{u} = \mathbf{V}, \phi = \hat{\phi} \rangle_L$  denotes a conditionally filtered variable conditional on the velocity vector and the scalar. The left hand side represents the time rate of change of the FJDF

and transport of FJDF in physical space. The terms on the right hand side are transport of the FJDF in velocity space by resolvable-scale pressure gradient, SGS pressure gradient, viscous acceleration, and molecular diffusion. An alternative term to the conditionally filtered scalar diffusion is the conditionally filtered scalar dissipation  $\langle \chi | \mathbf{u} = \mathbf{V}, \phi = \hat{\phi} \rangle_L$ , where  $\chi = D \frac{\partial \phi}{\partial x_j} \frac{\partial \phi}{\partial x_j}$  is the scalar dissipation rate.

The FJDF is a random process and requires statistical descriptions. We employ conditional sampling and averaging techniques. Our previous studies of conserved scalar FDF, the FDF transport equation, and velocity FJDF using these techniques (Tong 2001, Wang and Tong 2002 and 2003) have shown that the SGS velocity and scalar are in equilibrium and non-equilibrium for small and large *instantaneous* SGS energy and variances, respectively. The non-equilibrium SGS scalar contains diffusion layers and the FDF is bimodal, thus the SGS scalar is similar to a nonpremixed scalar field. For nonequilibrium SGS velocity the velocity FJDF is approximately uniform, suggesting that the SGS velocity is under local rapid distortion, which may be modeled using the velocity-wavevector model (Slooten and Pope 1997). The results suggest that mixing models that can better predict the non-equilibrium regime are needed. In this work we investigate the statistical dependence between the SGS velocity and scalar and the effects of the SGS velocity on SGS scalar mixing. The FJDF and the SGS terms in the its transport equation are analyzed using their conditional means with the SGS scalar variance  $\langle \phi''^2 \rangle_L$  and the SGS kinetic energy,  $k_L = (\langle u_1''^2 \rangle_L + \langle u_2''^2 \rangle_L)/2$  as conditioning variables.

Our measurements were made in an axisymmetric turbulent jet at 80 jet nozzle diameters ( $D = 15$  mm) downstream. The jet Reynolds number  $UD/\nu$  is 40000. A sensor array consisting of three hot-wire probes is used to obtain data for performing filtering operations in both the streamwise ( $x$ ) and transverse ( $y$ ) directions. The filter size is varied from 63 to 250 Kolmogorov scales. This technique enables us to acquire a large amount of data ( $10^8$  samples) necessary to achieve sufficient statistical convergence.

### A. Velocity-scalar FJDF

The mean FJDF conditional on the SGS energy, the resolvable-scale velocity, the SGS scalar variance, and the resolvable-scale scalar has qualitatively different forms depending on the conditioning variables. For small  $k_L$  ( $< \langle k_L \rangle$ ) and  $\langle \phi''^2 \rangle_L$  ( $< \langle \phi''^2 \rangle$ ), the conditional FJDF is close to joint-Gaussian (not shown), similar to the JPFD in a fully developed turbulent jet, which is in quasi-equilibrium. For large  $\langle \phi''^2 \rangle_L$  the FJDF is bimodal at  $\phi''/\langle \phi''^2 \rangle_L \approx \pm 1$  regardless of the values of  $k_L$  (Fig. 1), consistent with a scalar diffusion layer structure. For small  $k_L$  [Fig. 1(a)] the correlation between the SGS scalar and the velocity component  $u_1$  is low, indicating small conditional SGS flux. For large  $k_L$  [Fig. 1(b)] the correlation is strong and the two peaks of the FJDF are also separated in the velocity space with a “neck” near  $u_1 = 0$ . Thus scalar mixing is expected to be most intense near this point and depends strongly on the velocity, further demonstrates the need for mixing models to depend on the velocity. This FJDF shape is consistent with a scalar diffusion layer associated with a local plane strain (converging-diverging) velocity field. In such a structure the scalar gradient is the largest in the diffusion layer where the SGS velocity is the smallest. The structure is similar to the counter-flow model for laminar flamelets. The FJDF peaks in Fig. 1(a), on the other hand, overlaps in the velocity space; thus mixing can occur over a wide range of SGS velocity and is less dependent on the velocity.

### B. Conditionally filtered scalar diffusion and dissipation

In the present study the scalar diffusion and dissipation are obtained using the streamwise derivatives. For small  $\langle \phi''^2 \rangle_L$  the diffusion generally has linear dependence on both the SGS velocity and scalar. Figure 2(a) shows the conditionally filtered diffusion for small  $k_L$

$(0.52\langle k_L \rangle)$ . In the center portion the isocontours can be approximated by equally-spaced straight lines, consistent with a previous linear model. For large  $k_L$  the isocontours have larger slope, indicate stronger dependence on  $u_1$ . The results are consistent with velocity-scalar fields having a joint normal JPDP.

For large SGS variance the surface plot of the diffusion is S-shaped and depends on  $u_1$  for certain ranges of  $k_L$  values. Figure 2(b) shows the conditionally filtered diffusion for large  $\langle \phi''^2 \rangle_L$  ( $6.09\langle \phi''^2 \rangle$ ) but small  $k_L$ . In addition to an approximately linear trend, an S-shaped dependence on  $\phi$  exists for all  $u_1$  values. This is consistent with the FJDF in Fig. 1(a) which shows that the bimodal scalar distribution spans a wide range of velocity. For large  $k_L$  the S-shaped region appears to be limited to near  $u_1 = 0$  (not shown), suggesting that large magnitudes of diffusion occur at small SGS velocity. This is further discussed in the following along with the dissipation.

The conditionally filtered scalar dissipation provides an alternative to the conditionally filtered scalar diffusion to close the FJDF equation. For small  $\langle \phi''^2 \rangle_L$  the dissipation generally depends weakly on both the velocity and scalar (not shown), consistent with the approximately joint normal FJDF. For small  $k_L$  and large  $\langle \phi''^2 \rangle_L$  the dissipation shown in Fig. 3(a) has a bell-shaped dependence on  $\phi$  but is weakly dependent on  $u_1$ . The dependence on  $\phi$  is consistent with the FJDF in Fig. 1(a) and the S-shaped the diffusion plot in Fig. 2(b). For large  $k_L$  and  $\langle \phi''^2 \rangle_L$  the dissipation is the largest at  $\phi = 0$  and  $u_1 = 0$  [Fig. 3(b)] and decreases as velocity increases, indicating strong dependence on the SGS velocity. This is consistent with the FJDF in Fig. 1(b) and the notion that the diffusion layer is associated with a converging-diverging (e.g., plane strain) velocity field. In such a structure the velocity component normal to the diffusion layer is small near the layer. This also suggests that the S-shaped surface for the scalar diffusion is limited to small  $u_1$  values. Since diffusion layers have been shown to exist at very high Reynolds numbers, the observed dependence of scalar diffusion and dissipation on the velocity is expected to be Reynolds number independent.

The present study show that there is strong statistical dependence between scalar mixing (dissipation-scale scalar) and the SGS velocity field. The scalar and velocity structure for large SGS variance (especially when the SGS energy is also large) is similar to structure of laminar flamelets, thus the ability of mixing model to reflect such a structure and the localness of mixing is important. The scalar diffusion conditional on the SGS velocity under such conditions is expected to be non-zero and independent of Reynolds number. The results further demonstrate the importance of the velocity in mixing and of including velocity in mixing models.

## REFERENCES

- Sheikhi, M. R. H., Drozda, T. G., Givi, P., and Pope, S. B. (2003) Velocity-scalar filtered density function for large eddy simulation of turbulent flows. Submitted to Phys. Fluids
- Tong, C. (2001) Measurements of conserved scalar filtered density function in a turbulent jet. Phys. Fluids **13**, 2923–2937.
- Tong, C. (2003) Galilean invariance of velocity probability density function transport equation. To appear in Phys. Fluids **15**.
- Van Sooten, P. R. and Pope, S. B. (1997) PDF modeling for inhomogeneous turbulence with exact representation of rapid distortions. Phys. Fluids **9**, 1085–1105.
- Wang, D. and Tong, C. (2002) Conditionally filtered scalar dissipation, scalar diffusion, and velocity in a turbulent jet. Phys. Fluids **14**, 2170–2185.
- Wang and Tong (2003) Experimental investigation of velocity-scalar filtered density function for large eddy simulation. In preparation.

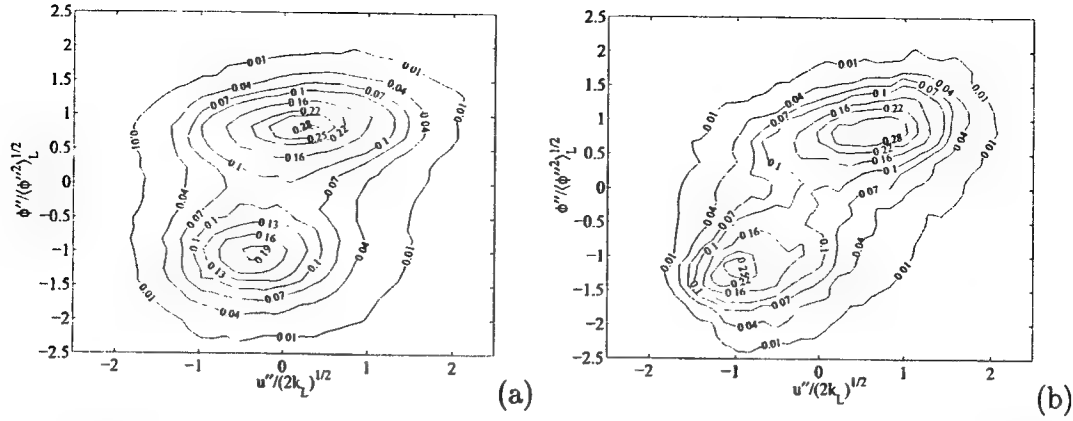


Figure 1: Mean FJDF conditional on  $k_L$ ,  $\langle u \rangle_L$ ,  $\langle \phi'^2 \rangle_L$ , and  $\langle \phi \rangle_L$  on the jet centerline for  $\langle u_1 \rangle_L = \langle u_1 \rangle$  (3.07 m/s) and  $\langle u_1 \rangle_L = 0$ : (a)  $k_L/\langle k_L \rangle = 3.04$  and  $\langle \phi'^2 \rangle_L/\langle \phi'^2 \rangle = 6.09$ ; (b)  $k_L/\langle k_L \rangle = 0.64$  and  $\langle \phi'^2 \rangle_L/\langle \phi'^2 \rangle = 6.09$ . The bimodal FJDF in (b) is strongly asymmetric in  $u_1$ , indicating large SGS flux and suggesting that mixing occurs primarily near  $u_1 = 0$ .

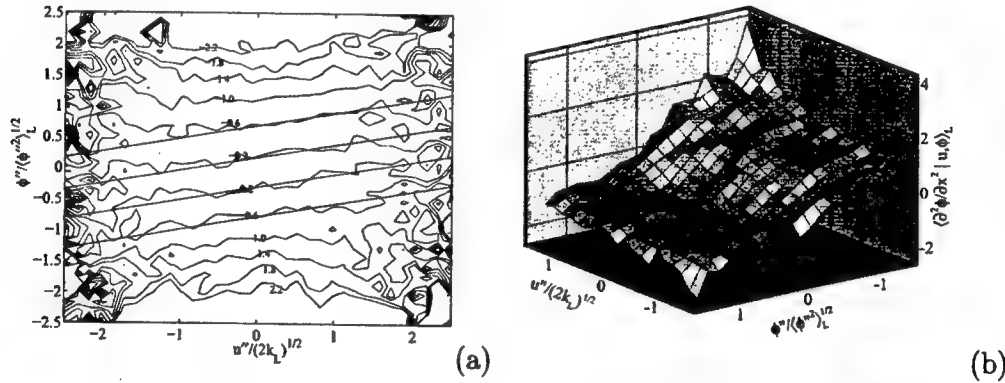


Figure 2: Mean conditionally filtered scalar diffusion: (a)  $k_L/\langle k_L \rangle = 0.8$  and  $\langle \phi'^2 \rangle_L/\langle \phi'^2 \rangle = 0.94$ ; (b)  $k_L/\langle k_L \rangle = 0.52$  and  $\langle \phi'^2 \rangle_L/\langle \phi'^2 \rangle = 6.09$ . The diffusion in (a) can be approximated using a previous linear model (straight lines) whereas that in (b) has a S-shaped region.

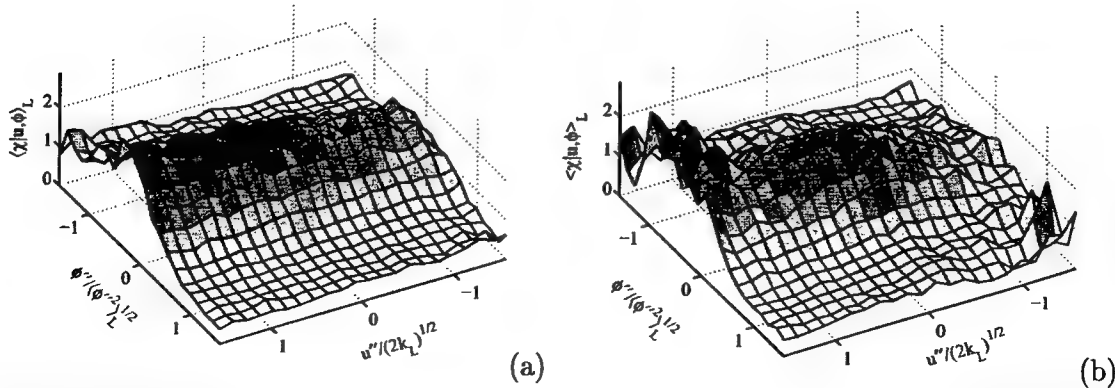


Figure 3: Normalized mean conditionally filtered scalar dissipation: (a)  $k_L/\langle k_L \rangle = 0.64$  and  $\langle \phi'^2 \rangle_L/\langle \phi'^2 \rangle = 4.67$ ; (b)  $k_L/\langle k_L \rangle = 2.43$  and  $\langle \phi'^2 \rangle_L/\langle \phi'^2 \rangle = 4.67$ . The dissipation in (b) shows that mixing occurs primarily near  $u_1 = 0$ .

# STATISTICAL INTERPRETATION OF SCALAR TIME-SERIES MEASUREMENTS IN TURBULENT PARTIALLY PREMIXED FLAMES

AFOSR Grant Number F49620-03-1-0026

Principal Investigators: Normand M. Laurendeau, Galen B. King and Michael W. Renfro

School of Mechanical Engineering, Purdue University, West Lafayette, IN 47907-1288  
Department of Mechanical Engineering, University of Connecticut, Storrs, CT 06269-3139

## SUMMARY/OVERVIEW

This research is concerned with systematic comparisons of scalar autocorrelation functions, power spectral densities, and integral time scales measured by picosecond time-resolved laser-induced fluorescence (PITLIF) and predicted by large-eddy simulations (LES) for turbulent non-premixed and partially premixed jet diffusion flames. These comparisons include both single-point and two-point measurements of OH and CH so as to capture both spatial and temporal correlation statistics. Interpretations of both measured and predicted statistical correlations are aided by flamelet simulations. Such assessments should lead to the development of improved LES models for turbulent combustion processes crucial to practical gas-turbine combustors.

During this past year, hydroxyl time-series have been obtained using PITLIF in turbulent  $H_2/N_2$  jet diffusion flames. Large-eddy simulations for the same flames have been used to predict OH, density and mixture fraction temporal statistics. The measured and predicted power spectral densities for OH were found to collapse to the same shape when normalized by their integral time scales. However, the integral time scales predicted by LES were systematically low by a factor of two-three. These data represent the first reported assessment of LES-predicted fluctuation rates in turbulent reactive flows.

## TECHNICAL DISCUSSION

Scalar fluctuations in turbulent flames display power spectra spanning many orders-of-magnitude in frequency. In many cases the distribution of these fluctuations is self-similar and can be described by a single integral time scale. For non-premixed reacting flows, the local time scale includes information on fluctuation rates arising from both mixing and flame motion. Large-eddy simulations (LES) are capable of predicting such temporal information at moderate Reynolds numbers.<sup>1</sup> Assessment of LES predictions has previously been limited to probability density functions (PDFs) and their moments, including associated mean and rms values. For this work, LES fluctuation rate predictions were examined by comparison to measured scalar time series. In particular, OH fluctuations were measured in a non-premixed hydrogen jet flame. While mixture fraction would be a preferable scalar for validating LES predictions, its measurement is much more difficult and associated fluctuation rates are not generally available. However, since OH exists only in high-temperature regions of non-premixed flames, OH fluctuations are dominated by large-scale flame motion.<sup>2</sup> The OH time scales are insensitive to the OH con-

<sup>1</sup> Pitsch, H. and Steiner, H., *Phys. Fluids*, 10:2541 (2000); Kempf, A., Forkel, H., Chen, J. Y., Sadiki, A., and Janicka, J., *Proc. Combust. Inst.* 28:35 (2000).

<sup>2</sup> Renfro, M. W., Guttenfelder, W. A., King, G. B., and Laurendeau, N. M., *Combust. Flame* 123:389 (2000); Renfro, M. W., King, G. B., and Laurendeau, N. M., *Combust. Flame* 122:139 (2000).

centrations in the flame yet are very sensitive to the flame width and motion.<sup>3</sup> Therefore, OH time-series statistics are expected to be indicative of flame motion, and its comparison to LES is expected to be a useful mechanism for testing the statistical capabilities of LES models.

In the present study, comparisons to LES are limited to a single 50% H<sub>2</sub>/50% N<sub>2</sub>, Re=10,000 flame. The chosen fuel mixture and flame geometry is a standard flame (H3) in the Turbulent Nonpremixed Flame Workshop and has been studied previously by Meier *et al.*<sup>4</sup> using single-shot Raman scattering, by Pfuderer *et al.*<sup>5</sup> using laser-doppler velocimetry (LDV), and by Neuber *et al.*<sup>6</sup> using combined laser-induced fluorescence (LIF) and Raman scattering. These authors report mean values and standard deviations of the temperature and major-species concentrations for this flame. The time-series measurements reported in this study further characterize a standard flame and thus complement the previous data for this flame.

The laser system and detection system used for the present OH measurements is identical to that employed by Renfro *et al.*<sup>7</sup> The system consists of a mode-locked laser and a photon counting system that records the LIF signal and fluorescence lifetime with temporal resolution and bandwidth sufficient for time-series measurements. For the current measurements, the spatial resolution was 100×100×60 μm<sup>3</sup> based on the beam diameter and the monochromator entrance slit width for the detection system. In previous experiments, a fixed sampling rate was chosen to resolve the regions of the flame with the fastest fluctuations. This resulted in excessive temporal resolution in regions with slower fluctuations. In this work, the bandwidth was altered at each point based on the measured power spectra, resulting in improved signal-to-noise ratios.

The burner for the turbulent nonpremixed flame was identical to that used by Meier *et al.*<sup>4</sup> and consisted of an 8-mm tube with a thinned rim at the exit. Co-flowing air with an exit velocity of 0.3 m/s was provided using a contoured 140-mm nozzle. The burner could be translated in axial and radial directions to change the position of the measuring location. Fifty time series of 4096 points were collected at each measurement location. PDFs, PSDs, autocorrelation functions, and integral time scales were computed in the same manner as reported by Renfro *et al.*,<sup>7</sup> including a correction for the measured contribution of shot noise. The statistics were averaged over fifty time series to reduce noise.

The large-eddy simulations were performed on a structured cylindrical grid with 60 radial, 32 circumferential, and 256 axial staggered grid cells. For each simulation, 200,000 time steps were computed requiring approximately two weeks on a 2-GHz processor. For the H3 flame

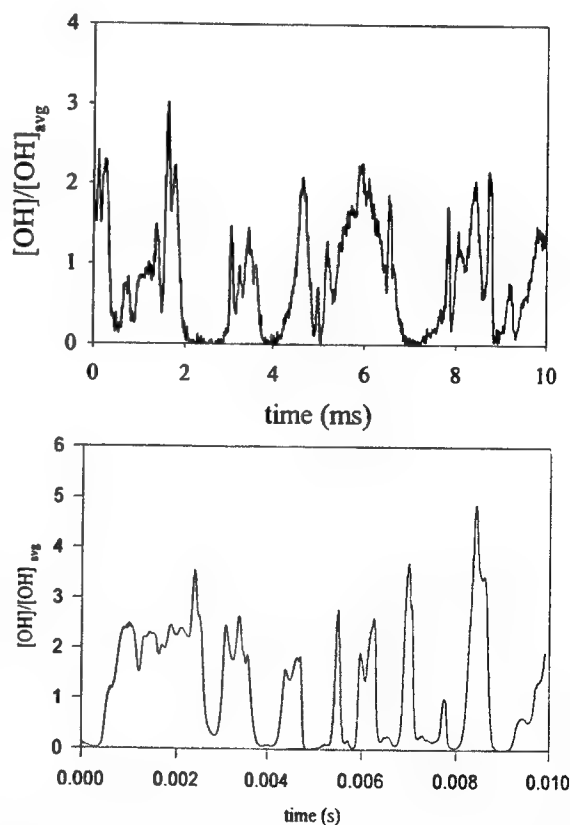


Fig. 1: Hydroxyl time series at  $x/D=10$  (top) measured by PITLIF and (bottom) from LES.

<sup>3</sup> Renfro, M. W., Gore J. P., and Laurendeau, N. M., *Combust. Flame* 129:120 (2002).

<sup>4</sup> Meier, W., Prucker, S., Cao, M.H., Stricker, W., *Combust. Sci. and Tech.* 118:293 (1996).

<sup>5</sup> Pfuderer, D. G., Neuber, A. A., Früchtel, G., Hassel, E. P., and Janicka, J., *Combust. Flame* 106:301 (1996).

<sup>6</sup> Neuber, A., Krieger, G., Tacke, M., Hassel, E., and Janicka, J., *Combust. Flame* 113:198 (1998).

<sup>7</sup> Renfro, M. W., King, G. B., and Laurendeau, N. M., *Appl. Opt.* 38:4596 (1999); Renfro, M. W., Gore, J. P., King, G. B., and Laurendeau, N. M., *AIAA J.* 38:1230 (2000).

simulations, the grid spanned 0.24 m in the radial direction and 0.40 m in the axial direction, corresponding to a maximum axial height of approximately 40 cm. The solver utilized a second-order central scheme for convection and diffusion of momentum, and an explicit third-order Runge Kutta scheme for time integration. A mixture fraction approach was utilized for all scalars. The scalar diffusivity was computed using a second-order central scheme with a constant turbulent Schmidt number of 0.45.<sup>1</sup> An eddy viscosity turbulence model was employed for turbulent transport of momentum and scalars. The Smagorinsky model<sup>8</sup> was used to compute the turbulent viscosity. In each filtered cell, the chemical state was computed using the filtered mixture fraction and an assumed sub-grid Beta-PDF distribution. For the PDF, the scalar dissipation was assumed to be constant on the sub-grid scale. Flamelet state relationships were then applied to this PDF.<sup>9</sup>

For each LES, a development period was required to converge from the initial conditions to statistically stationary turbulence. For the H3 flame, the 200,000 time steps spanned a period of  $\sim 0.25$  s. Time series for further analysis were extracted from the entire LES. The simulated time series of filtered OH mass fraction and density were used point-by-point to create a time-series of OH mole fraction for direct comparison to the PITLIF measurements. The LES time series had uneven step sizes necessary to resolve the fastest velocities in the simulation, but were always around 2  $\mu$ s. The simulated OH time series were re-sampled with a fixed sampling rate of 100 kHz by linearly interpolating OH values every 10  $\mu$ s. This even-step time series was then processed using the same procedure as used for the measured time series.

A representative time series measurement at the peak radial location for  $x/D=10$  is shown in Fig. 1. The trace represents the first 10 ms of data collected and visually demonstrates fluctuations in [OH] fluorescence as the [OH] layer fluctuates with respect to the fixed laser beam. Figure 1 also shows the OH time series at nearly the same location from LES. The measured and simulated time series are visually similar with high levels of intermittency and similar structures in the fluctuations. However, some differences in the shapes of the OH bursts in the time series are apparent, and the noise level in the two series are evidently different.

Autocorrelation functions at the jet centerline for 11 different axial locations were determined from the time series in the range  $x/D=20$  to  $x/D=40$ . The autocorrelation functions were then normalized using their respective integral time scales. The collapse proved to be excellent, as expected along the jet centerline, where the average velocities are high and the influence of the shear layer is minimal. Similarly, PSDs at these same locations demonstrate equally good collapse, thus verifying the expected self-similar behavior along the jet centerline. Predicted PSDs derived from LES are compared to measured PSDs for OH mole fraction in Fig. 2. As with the measurements, good collapse occurs along the centerline; thus, both measurements and LES show that the distribution of OH fluctuations is the same from one point in the flow to another. Therefore, the variation in fluctuation rates can be described by a single integral time scale.

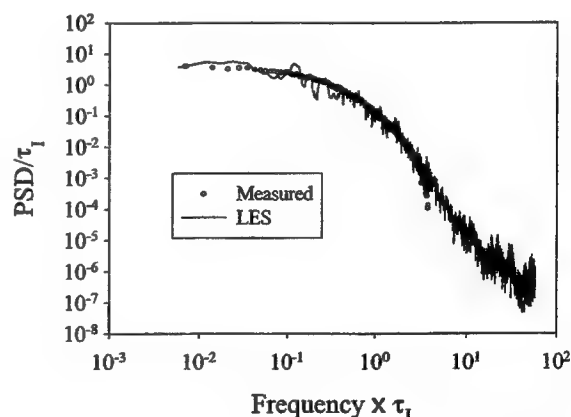


Fig. 2: Comparison of measured and simulated PSDs after normalization for OH in flame H3.

<sup>8</sup> Smagorinsky, J. S., *Monthly Weather Rev.* 91:99 (1963).

<sup>9</sup> Chen, J.-Y., *Personal Communication* (2002).



Figure 3 shows measured integral time scales as a function of radial location ( $r/x$ ) for three different axial heights. For these heights, the time scales range from 0.7 to 2.1 ms. The integral time scales at peak [OH] locations for  $x/D=20$  and  $x/D=30$  are almost equal and that for  $x/D=40$  is almost twice as large. The OH time scales in an  $H_2/CH_4/N_2$  flame were previously observed to be constant within the jet; i.e., below the flame tip and on the fuel side of the reaction layer.<sup>2</sup> The same trend is observed here for  $x/D=20$  and  $x/D=30$ , where the integral time scales on the fuel side are nearly constant until the peak OH location and increase rapidly towards the air-side into the mixing layer. At  $x/D=40$ , the peak OH concentration occurs at the centerline past the flame tip, which has previously not been examined by PITLIF measurements.

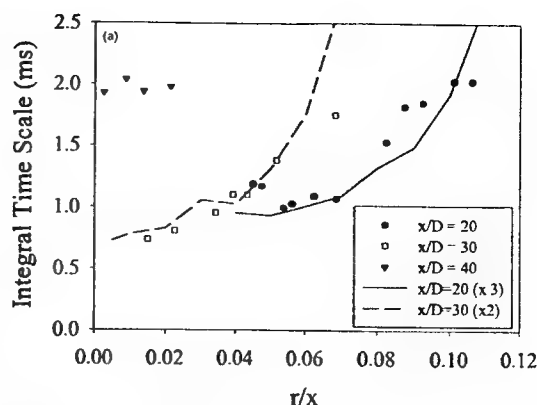


Figure 3: Comparison of measured and predicted time scales versus radial position. The LES time scales have been increased by a constant factor of 2- to facilitate comparison of the radial profile shapes.

Figure 4 shows integral time scales from both PITLIF and LES as a function of axial height along the jet centerline. The measured  $\tau_1$  values range from 0.8 to 1.7 ms and dip to a minimum value at  $x/D = 34$ . This axial location corresponds to the peak in mean [OH] concentration. The time scales,  $\tau_1$ , are nearly constant in the  $x/D = 20$  to 25 range, decrease somewhat until  $x/D = 34$ , and then increase rapidly to significantly higher values farther downstream of the flame tip. In the simulation, the time scales also increase substantially above the flame tip, as compared to simulated values below the flame tip. However, the simulations do not show a local minimum. Furthermore, as for the radial measurements of Fig. 3, the LES predictions for integral time scale are often about a factor of two-three below their measured values.

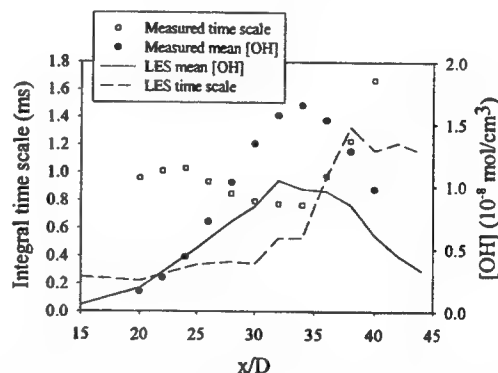


Figure 4: Comparison of measured and LES-predicted mean [OH] and [OH] time scales along the H3 flame centerline.

The measured minimum at  $x/D=34$  is similar to the trend observed in the  $\tau_1$  radial profiles. In particular, we have demonstrated that the peak [OH] location results in a local reduction in the integral time scale for OH owing to its narrow distribution in mixture fraction space.<sup>10</sup> Essentially, small mixture fraction fluctuations that cross the stoichiometric value sample both sides of the OH profile. Hence, a small sinusoidal fluctuation in  $Z$  can become a large fluctuation with twice the frequency for OH. However, LES does not appear to capture this subtle feature of the PITLIF measurements as the simulated time scales grow monotonically with increasing radial or axial position.

The most significant disagreement between the simulated and measured time scales is in their quantitative values. In general, LES is predicting fluctuations that are too fast. Even if improvements in predicted time scales do not impact important parameters such as mean concentration, it is still important to optimize the predicted time scales. For example, LES for a gas turbine combustor may be used to assess the effect of design changes on the pattern factor and on spatial and temporal scales for temperature fluctuations entering the turbine. These parameters

<sup>10</sup> Renfro, M. W., Gore J. P., and Laurendeau, N. M., *Combust. Flame* 129:120 (2002).



describing the thermal field are important in predicting convective heat transfer to the leading turbine blades and in identifying secondary flow losses<sup>11</sup>.

---

<sup>11</sup> Hermanson, K. S. and Thole, K. A., *J. Turbomachinery* 124:623 (2002).



## RAMJET RESEARCH

### AFOSR TASK 2308BW

Principal Investigators: Campbell D. Carter  
Mark R. Gruber

Aerospace Propulsion Division (PRA)  
Propulsion Directorate  
Air Force Research Laboratory  
Wright-Patterson AFB OH 45433

#### SUMMARY/OVERVIEW

This research task includes work in three primary focus areas: (1) multiphase flows relevant to fuel injection into high-speed, oxidizing streams, (2) shock-boundary interactions within the scramjet flowpath, and (3) multidisciplinary laser measurements for benchmarking modeling and simulation and for elucidating the physics of high-speed flows. Within each of these areas, there is a strong relevance to the scramjet propulsion system, and that relationship helps frame the context of our research. Aeration has been studied as a means of improving atomization (and penetration) of the liquid JP-7 during the "cold-start" process; though this approach shows much merit, understanding of the physics of the breakup process is still lacking. Shock-boundary interactions are important for their influence cavity-flameholder stability, and ongoing studies are enabling improved (i.e., robust) fueling schemes. Finally, laser diagnostics provides the means for non-intrusively studying the injection process and cavity flameholding and for determining scramjet engine performance.

#### TECHNICAL DISCUSSION

Areas of focus in the past year have included the following:

- 1) Study of two-phase, aerated injection of a fuel into a high-speed crossflow. The purpose here is to simulate injection of the cold JP-7 into a Mach-2 crossflow during the "cold-start" phase of the Scramjet flight envelope. (The other part of the "cold-start" problem is ignition, and for this part the efficacy of plasmas is being investigated.) To quantify the role of aeration on the atomization and penetration of the aerated jet, a phase-Doppler particle analyzer (PDPA) has been employed.
- 2) Study of the injection of supercritical fuels into a quiescent, subcritical environment. For this study the cracked JP-7 is simulated with a mixture of ethylene and methane.
- 3) Investigation of cavity flameholding, particularly the range of fueling for which the cavity flame remains lit and the stability as the combustor transitions from supersonic (before main-duct ignition) to subsonic flow (after ignition).
- 4) Development/Application of laser diagnostic techniques for use in scramjet testing. Advanced techniques that are being employed include the following: a) tunable diode laser absorption for measurements of water vapor concentration and temperature in a direct-connect scramjet engine (with R. Hanson and J. Jeffries, Stanford Univ.); b) single-shot holography (with G. Faith and K. Sallam, Univ. of Michigan) to investigate the breakup of an aerated spray in a Mach-2 crossflow; c) stereo particle image velocimetry in the cavity shear-layer region; d) planar laser-induced fluorescence (PLIF) of the OH radical within the cavity

flameholder to determine how the flame stabilizes vis-à-vis the supersonic-subsonic mode transition.

Regarding the cavity, it is a pervasive feature of scramjet combustion piloting. Its function is to capture a small portion of the high-speed core flow and establish a stable combustible mixture that provides heat and radicals to hold the core-flow flame. Ideally, it would perform this function insulated from the fluctuations of the core (flow and pressure), interacting with the shock system like a locally thick boundary layer. Unfortunately, it does not. Expansion fans and shocks dominate the mass exchange between cavity and core flow, and local stoichiometry varies widely in all three spatial dimensions and in time. Consequently, the cavity as a flameholder has been a particular point of emphasis. Our study of it has been focused on the means to improve stability for a wide range of fueling rates and/or entrainment rates and as the combustor flow changes from supersonic to subsonic. Of course, the relevance here is that when the combustor ignites, say at a flight Mach number of 4.5, the core flow transitions from supersonic with a Mach number of about 2 to high subsonic; furthermore, the

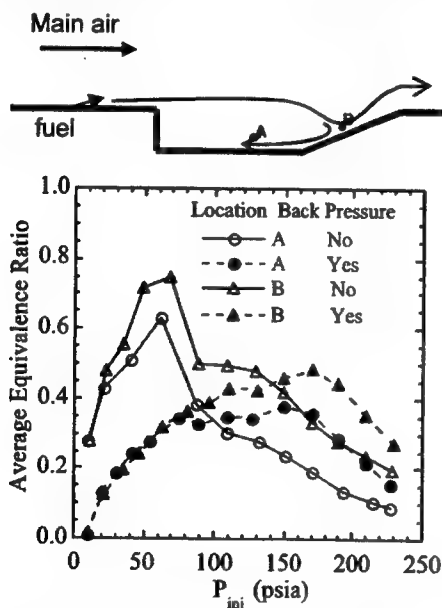


Fig. 2. Fuel distribution within cavity—along the central span—for the case of passive, upstream fueling.

ing of the duct-cavity flow and after backpressuring (again, to simulate the effect of main-duct combustion). Note that the shock system that is anchored on the lip of the cavity with backpressuring is very unstable (the shadowgraph exposure was 200  $\mu$ s to “freeze” the flow); further-

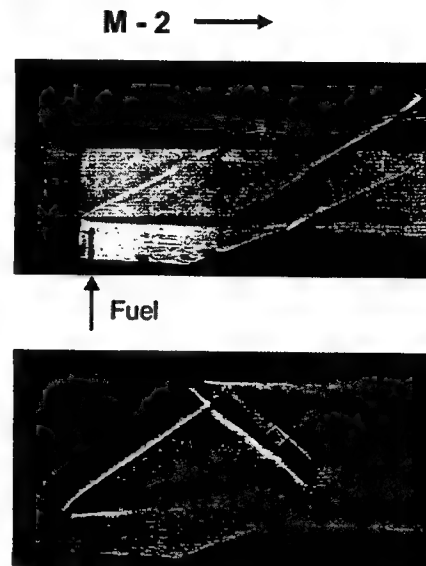


Fig. 1. Shadowgraph of flow over a cavity. Top: baseline case of Mach-2 core flow. Bottom: backpressure case simulating effects of combustion heat release.

cavity shear layer lifts, as shown in Fig. 1, and the entrainment rate changes. As a consequence of this mode change, air entrainment into the cavity changes dramatically with the potential result that the cavity flame is blown out; of course, once the cavity flame blows out, the primary flame of the combustor will also blow out. This indeed has been observed in our direct-connect scramjet facility.

To simulate this mode transition (induced by combustion heat release) within our “nonreacting” (Test Cell 19) supersonic flow facility, a valve downstream of the test section is used; different levels of heat release can thus be simulated simply by opening or closing this valve. The valve position was “calibrated” by comparing the wall static pressure, in relation to the cavity location, to those recorded in the flowpath of our direct-connect scramjet facility. At increasing levels of heat release (or valve blockage) the shock system is pushed forward and peak pressures approach normal shock pressure rise. The results of one of these tests are shown in Fig. 1. Here, two shadowgraph images reveal the flow structure around the cavity before backpressur-

more, as noted above, the shear layer lifts upward, influencing cavity entrainment. The influence of backpressuring on the fuel distribution is also shown in Fig. 2. Here, spontaneous line-wise Raman scattering (of the injectant, ethylene, and nitrogen, representing air), allowed us to deduce equivalence ratio along the line of the laser beam (produced from a Coherent Verdi cw laser). This figure shows that as the duct is backpressured—creating subsonic core flow—the cavity equivalence ratio changes dramatically, in fact becoming much more uniform with backpressuring. Clearly, this sort of change in cavity stoichiometry does not make for a stable situation, leading us to the conclusion that a more actively controlled approach to cavity fueling is required rather than the reliance on passive entrainment of fuel and air across the separated shear layer. More recent efforts where fuel is directly injected into the cavity are showing significant promise for improved combustion stability.

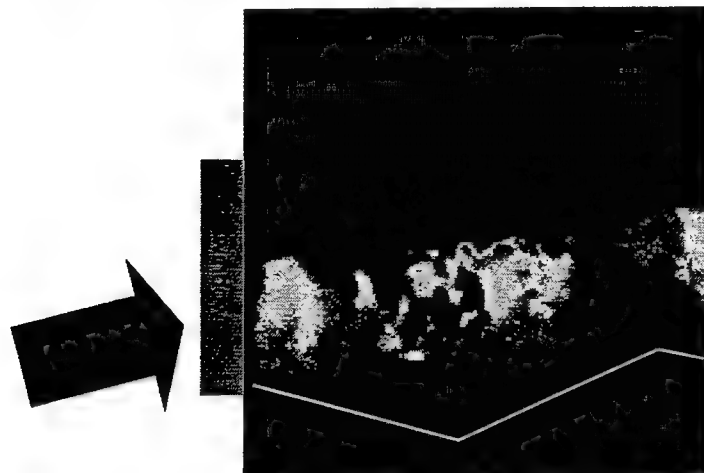


Fig. 3. Instantaneous spanwise image of OH distribution with cavity flame. The cavity outline is indicated by the white line.

Fig. 1). This image shows considerable non-uniformity in the instantaneous OH distribution, though, of course, the frame-averaged result is much more uniform. Still, these images show that the cavity flame is very dynamic. Incidentally, this fueling configuration is less than ideal as well. With the combustor mode change, a substantial amount of the fuel penetrates beyond the cavity, again influencing the cavity flame stability.

As noted above, advanced laser diagnostic methods have been applied and in some cases developed to study high-speed flows. In particular, a collaboration was begun with Prof. R. Hanson and Dr. J. Jeffries of Stanford University to develop tunable diode laser absorption sensors for our scramjet test facility. Our primary goals have been to 1) advance the state of the art in diode laser techniques (making them more robust, especially in relation to scramjet testing and possible control) and 2) evaluate combustor performance in a spatially resolved manner. This latter goal was motivated by CFD simulations showing a

In an effort to study the uniformity of the cavity flame under the influence of main-duct pressure and various fueling configurations, a planar laser-induced fluorescence system for detecting OH was set up. Here an Nd:YAG-pumped dye laser (Lumonics Hyperdye 300) was tuned to the  $Q_1(8)$  transition of the  $A^2\Sigma^+ - X^2\Pi$  (1,0) band of OH, while single-shot fluorescence images were recorded with an intensified CCD camera. A sample half-span, single-shot image is shown in Fig. 3; here the cavity was fueled independently through ports just downstream of the cavity leading edge (as shown in the top image of

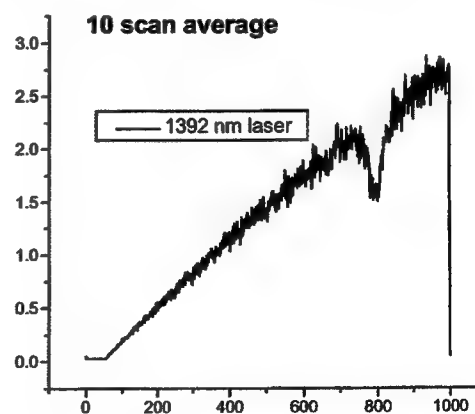


Fig. 4. 10-scan average of transmission for diode laser operating at 1392 nm; the laser along with ones operating near 1335 and 1343 nm, were scanned at 1 kHz. The absorption feature is from water vapor.

distinct height-wise variation in combustion products and temperature, resulting from poor combustion of fuel on the combustor wall opposite the cavity. To probe across the combustor height, a traversing system was designed and implemented such that laser transmitting and receiving optics could be translated in the vertical dimension of the combustor (while the laser probe spatially integrates the result across the spanwise combustor dimension). Initial measurements, however, were constrained to a single traverse, owing to the need to eliminate etaloning effects (by angling of the probe beams downward across the engine). A sample scan from a multiplexed, fiber-coupled sensor (with the combustor operating at an equivalence ratio of 1) is shown in Fig. 4. More recently, the downstream window-port has been redesigned to allow a wedged window to be used; this will eliminate the etalon formed by surface reflection from the window (and therefore permit height-wise probing of the combustor). Nonetheless, our initial measurements have been promising, and they have allowed our Stanford collaborators the opportunity to test different water-vapor absorption schemes.



Fig. 5. Near-field holograms for pure liquid spray (left) and spray with 2% (by mass) gas loading (right).

A similar collaborative effort, this one with Prof. G. Faith and Dr. Khaled Sallam of the University of Michigan, involves the application of pulsed holography to study the near-field breakup of the aerated jet in the Mach-2 crossflow. Sample holograms—ones that show the strong influence of aeration on the jet breakup—are displayed in Fig. 5. In our initial effort, two small Nd:YAG lasers (Continuum Surelite lasers) were employed. Though only a single laser is needed for holography, two were used in this initial experiment so that jet and droplet velocities could also be obtained through double-exposure shadowgraphy. Unfortunately, due to the limited coherence length,  $\sim 1$  cm, of the normal Q-switched Nd:YAG, the quality of the holograms was modest, at best (since the reference and ob-

ject path lengths must be matched roughly within the coherence length). More recently, though, an injection-seeded Nd:YAG laser has been used. The role of seed laser is to induce the Nd:YAG to produce laser light at a single longitudinal mode (one that matches the frequency of the seed laser); with proper seeding the Nd:YAG laser pulse is coherent over its entire length, and the holograms that result are of a very high quality. To make this scheme feasible, however, requires that the laser be run continuously (so that the seeding control electronics function properly). As a consequence it was necessary to use a shutter capable of 1) shuttering around a single laser pulse and 2) reflecting/absorbing the high-powered laser pulse. Control of the laser firing and shutter opening was accomplished with the Quantum Composer delay generator. An initial result from this research is that the near-field mean droplet size is not strongly dependent upon the gas-loading ratio.

#### Acknowledgements:

Drs. Steven Lin, Taitech, Inc., and Mark Hsu, Innovative Scientific Solutions, Inc., lead our efforts in studying fuel injection (both aerated fuel and the supercritical fuel) and cavity flameholding, respectively. Dr. Jeffrey Donbar leads the AFRL/PRAS effort to develop and apply tunable diode lasers for the scramjet engine testing.

# MIXING, CHEMICAL REACTIONS, AND COMBUSTION IN HIGH-SPEED TURBULENT FLOWS

AFOSR Grant F49620-01-1-0006

Paul E. Dimotakis  
*Graduate Aeronautical Laboratories*  
*California Institute of Technology, Pasadena, CA 91125*

## Summary/Overview

This research focuses on fundamental investigations of mixing, chemical-reaction, and combustion, in turbulent, subsonic, and supersonic flows, in support of high-speed air-breathing propulsion applications. It is comprised of an experimental effort; an analytical, modeling, and computational effort; and a diagnostics- and instrumentation-development effort.

## Technical discussion

Previous work on scramjet-type internal flows focused on mass-injection and heat-release effects on subsonic flows over a perforated ramp. Preliminary estimates of mixing at subsonic freestream speeds, based on a model by Dimotakis (1991, Eq. 23), have yielded mixed-fluid fractions in the shear-layer adjacent to the wall, roughly, 40% higher than for free shear layers. The higher value illustrates the benefits of the recirculation zone behind the ramp injector on mixing. Recent experiments focused on flows at transonic incoming freestream Mach numbers. Figure 1 is a schlieren visualization of this regime. Expanding slightly over the injection ramp, the incoming flow accelerates from  $M \cong 1.02$  to  $M \cong 1.05$ . Further downstream is a secondary mixing zone where injected fluid mixes with low-speed recirculation fluid. Flameholding benefits are expected from the lower strain rates encountered there, relative to the primary shear-layer above, for hydrocarbon-air and hydrogen-air scramjet combustion. Upper-guidewall pressure measurements are in accord with Mach numbers estimated from the flow-visualization data. Additional increases in inflow Mach number and improvements in diagnostics are in progress at this writing. This research is part of the Ph.D. work of M. Johnson.



Fig. 1. Supersonic flow with ramp injection. Incoming (top stream) Mach number,  $M_1 \cong 1.02$ .

Flame stability and flameholding investigations, motivated by scramjet issues, are also in progress. In particular, experiments are continuing on laminar-flame properties of premixed methane-, ethane-, and ethylene-air mixtures, at atmospheric pressure, over a range of equivalence ratios,  $\Phi$ , with a present focus on extinction strain rates against low-temperature walls; important for cold-wall quenching of hydrocarbon flames. The experiments utilize a stagnation-flow configuration, similar to counterflow flames, introduced by Law and coworkers (Wu & Law 1984, Law 1988, and Zhu *et al.* 1988), and rely on digital imaging of flame chemiluminescence, extensions to particle-streak velocimetry (PSV) for flow-field measurements, and independent jet-exit velocity measurements. Planar Laser Induced Fluorescence (PLIF) measurements of the reaction zone marking  $\text{CH}^*$  radical are implemented at this writing. Such data are useful in assessing and validating chemical kinetics mechanisms when simulated numerically with full chemistry and species transport models.

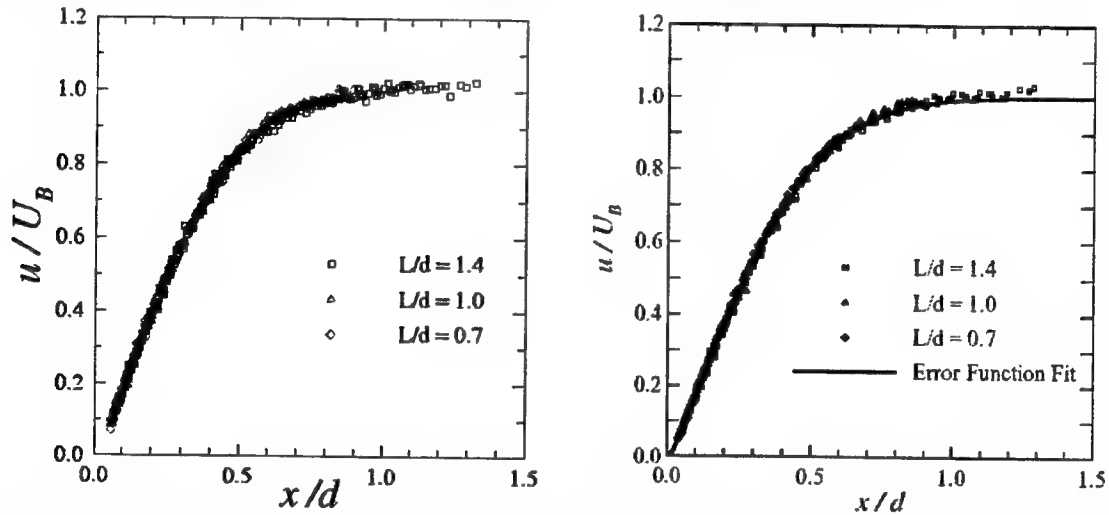


Fig. 2. (a) Centerline axial velocity profile experimental results,  $Re = 700$ . (b) Comparison of error-function fit to experimental data,  $Re = 1400$ .

A 1D model of an axisymmetric impinging jet flow is widely used in modeling laminar flames. Its reduced dimensionality allows full chemistry and species transport to be implemented without excessive computational cost. The model was extended to account for finite-diameter nozzle effects (Kee *et al.* 1988) for the study of laminar stagnation-flames. However, the 1D equations do not accurately describe a finite-diameter cold impinging jet at nozzle-plate separation distance ratios of 1, or greater. As these are the nozzle-plate separation ratios studied in this work, a detailed study of the impinging laminar jet is in progress. While this flow appears simple and is regarded as well documented, some new elements have emerged. For cold-flow impinging jets, the axial velocity profile along the jet centerline was found to be independent of the nozzle-stagnation plate separation distance, when scaled by the Bernoulli velocity,  $U_B$ , where,  $U_B^2 \equiv 2 \Delta p / [\rho (1 - (r_2/r_1)^4)]$ , with  $\Delta p$  the pressure drop across the nozzle,  $\rho$  the density, and  $r_2$  and  $r_1$  the radii of the nozzle exit and inlet, respectively. At flow velocities encountered in stagnation flames,  $\Delta p$  is of order  $10^{-8}$  bar and direct measurements require some care.

Figure 2a depicts the axial velocity profile of a  $Re = 700$  impinging jet, for three nozzle-plate separation distances. Collapsed velocity profiles are well characterized by a similarity expression (Kostiuk *et al.* 1993),  $u(x) = U_B \text{erf}[\alpha (x - \delta_w) / d]$ , where  $u(x)$  is the axial velocity,  $\alpha$  is a strain-rate parameter,  $x$  is the wall-normal distance,  $\delta_w$  a wall-displacement offset owing to the viscous boundary layer, and  $d$  the nozzle diameter. Only a few of these parameters are independent. A cold-flow profile is specified by  $U_B$  alone. An example of the single-parameter fit is in Fig. 2b. This will be exploited in simulating experiments in terms of an approximate 1D



simulation. This research is part of the Ph.D. thesis work of J. Bergthorson and is performed in collaboration with D. Goodwin.

Accompanying 1D simulations rely on a simulation package for reacting flows dubbed *Cantera* (Goodwin 2003). *Cantera* is characterized by improved computational efficiency, relative to other flame models currently in use, and can accommodate user-defined chemical-kinetics mechanisms, mixture-averaged or full-kinetic-detail transport models. It also calculates reaction-pathway diagrams at each location in the flame, allowing local details of the chemical kinetics to be investigated. Sample results for a methane-air flame using *Cantera* are given in Fig. 3.

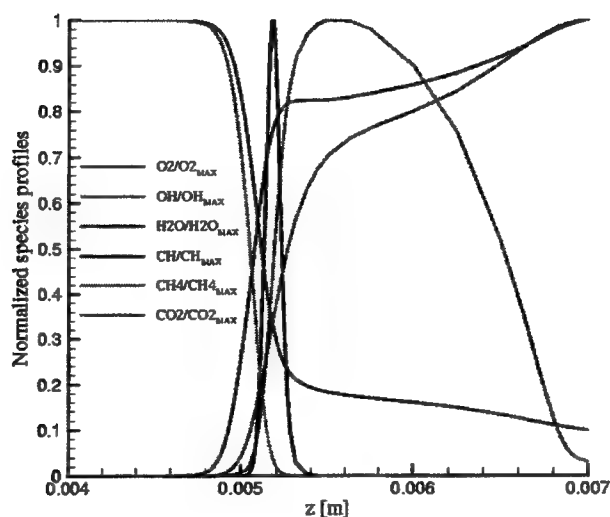


Fig. 3. Species profiles for components of interest in a methane-air flame ( $\Phi = 0.9$ ). 1D numerical simulation using the *Cantera* software package.

In addition to the 1D simulations, work is continuing on the development of 2D axisymmetric viscous simulations of stagnation flames, to complement the experimental effort. The code utilizes a modification and extension of the PRISM spectral-element code (Henderson & Karniadakis 1995), adapted for axisymmetric flow, and the accommodation of the complex inflow/outflow boundary conditions of the experimental geometry.

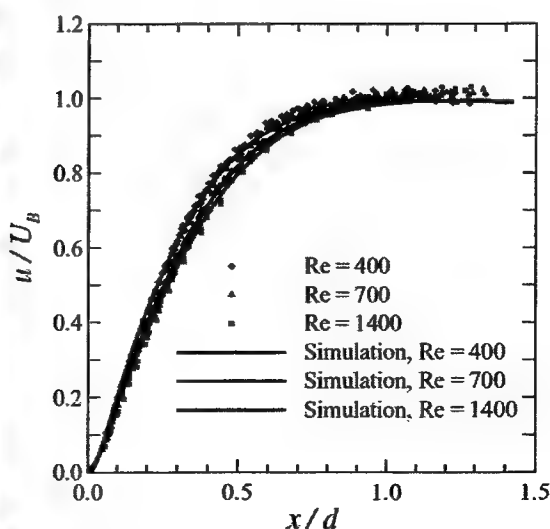
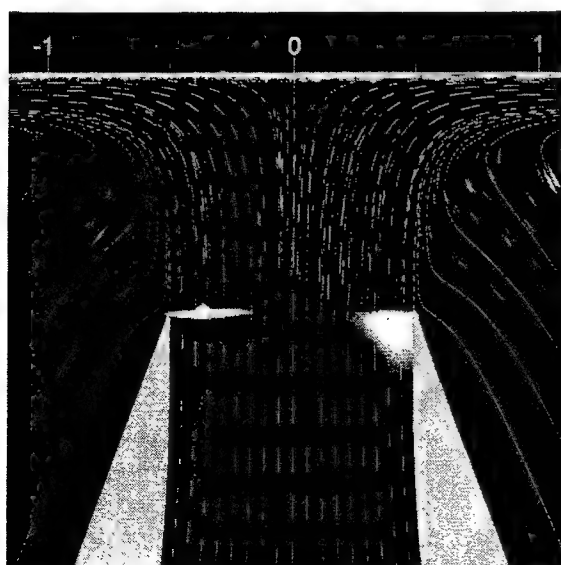


Fig. 4(a) Particle streak image detailing entrained flow with superimposed axisymmetric viscous calculation (yellow lines).  $Re = 700$ ,  $L/d = 1.0$ . (b) Comparison of calculated velocity profiles to experimental data detailing Reynolds number effects.

Simulations of non-reacting impinging-jet flow were completed and compared with experimental results. These simulations provide insight into the hydrodynamics of this flow. The unsteady Navier-Stokes equations are integrated in time from a quiescent state until the solution attains a steady-state flow condition. Figure 4a compares particle-streak-image data and streamlines from the axisymmetric viscous simulations. Good qualitative agreement can be seen, even in the entrainment region where velocities are low ( $< 0.02U_B$ ). Figure 4b compares the experimental data with the axisymmetric viscous calculations at  $L/d = 1.4$  for  $Re = 400$ , 700, and 1400. The differences between experimental and numerical results for these three cases are less than  $0.015 U_B$  root-mean-squared (rms), indicating that the choice of boundary conditions in the simulations is adequate. This research is part of the Ph.D. thesis work of K. Sone and is performed in collaboration with D. Meiron.

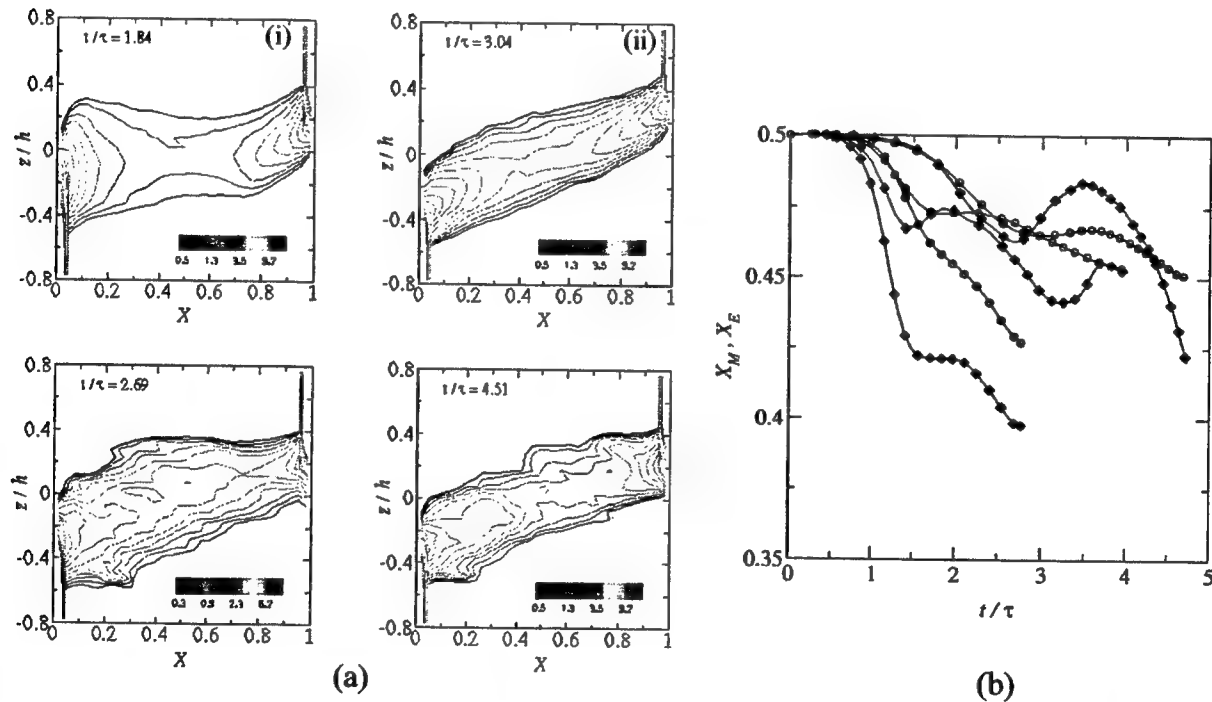


Fig. 5. (a) Probability density function of  $X$  vs.  $z/h$  for (i) Case A and (ii) Case C. Colored contours indicate values of  $p^X(X; z/h)$ . Contour intervals are exponentially spaced. (b)  $X_M$  (open circles) and  $X_E$  (filled diamonds) for Cases A (black), B (red), and C (blue).

Mixing by Rayleigh-Taylor (RT) instability is of intrinsic interest in a variety of contexts, including inertial-confinement fusion and supernovae. It is also dynamically significant because density is an active scalar. Direct numerical simulations (DNS) of incompressible miscible RT instability by Cook & Dimotakis (2001, 2002) have permitted the study of RT mixing without the restriction of small Atwood numbers,  $A \equiv (\rho_2 - \rho_1)/(\rho_2 + \rho_1)$ , or of unphysical numerical dissipation in simulations based on the Euler equations. Three simulations were completed, differing only in the initial perturbation spectra. In particular,  $k_A < k_B < k_C$  where  $k_A$ ,  $k_B$ , and  $k_C$  denote the wavenumber of the peak amplitude in the spectrum for Cases A, B, and C, respectively. Fig. 5a shows discrete approximations (32 bins) of  $p^X(X; z/h)$ , the probability density function (pdf) of the heavy-fluid mole fraction,  $X$ , as a function of the scaled inhomogeneous vertical coordinate,  $z/h$ . The origin of  $z$  is located at the mean position of the initial density interface (midplane). The mixing-zone width is,  $h = h_B - h_S$ , where  $\langle X \rangle(h_B) = 0.99$  and  $\langle X \rangle(h_S) =$

0.01 and angled brackets denote plane averages. The flow time scale is  $\tau = [L/Ag]^{1/2}$ , where  $L$  is the lateral dimension of the domain,  $A$  is the Atwood number, and  $g$  is the imposed acceleration. Although the simulations evolve differently, the final state is characterized by a broad composition range, with very little unmixed fluid able to penetrate the midplane. If the entrainment ratio,  $E$ , is defined as the volume of heavy fluid per unit volume of light fluid that is entrained into the mixing zone, then  $E = h_B/h_S$ . If all the entrained fluid is homogeneously mixed, the mean composition is  $X^E = E/(E + 1)$ . Fig. 4b shows the relationship between  $X^E$  and the actual mixed-fluid composition,  $X^M$ , computed from  $pX(X; z/h)$  (Koochesfahani & Dimotakis 1986). After the initial diffusive phase,  $X^E$  decreases to values less than 0.5.  $X^M$  follows similar trends, showing that the composition of mixed fluid is affected by the asymmetric growth and entrainment of the mixing zone. Asymmetric growth is a density-ratio effect, qualitatively explained by the higher terminal velocity of a spike compared with a bubble at the same density ratio (Youngs 1991, Ulon *et al.* 1995). This aspect of RT mixing cannot be captured by experiments or simulations conducted in the Boussinesq (low Atwood number) limit. The research on R-T mixing is part of the work by T. Mattner, in collaboration with A. Cook of LLNL.

Several enhancements were made to the KFS Camera system outlined in last year's report. One is minimization of the KFS CCD sensor noise. Figure 6 plots results from noise measurements. Binned values are for (2×2)-pixel binning to produce (512×512)-pixel images. The camera was then evacuated and the KFS CCD sensor was cooled to -38°C. This further reduced the noise for a 5 ms readout time to 25.8 e<sup>-</sup>/pixel. A reduction of the temperature reduces the CCD amplifier noise by the square-root of the absolute temperature and reduces CCD dark current exponentially (approximately a factor of 2 for every 10°C). To date, the KFS system has been used to record high framing-rate sequences of dynamic hydrocarbon-flame transitions and for atmospheric-turbulence wavefront phase measurements at the Palomar 200" telescope.

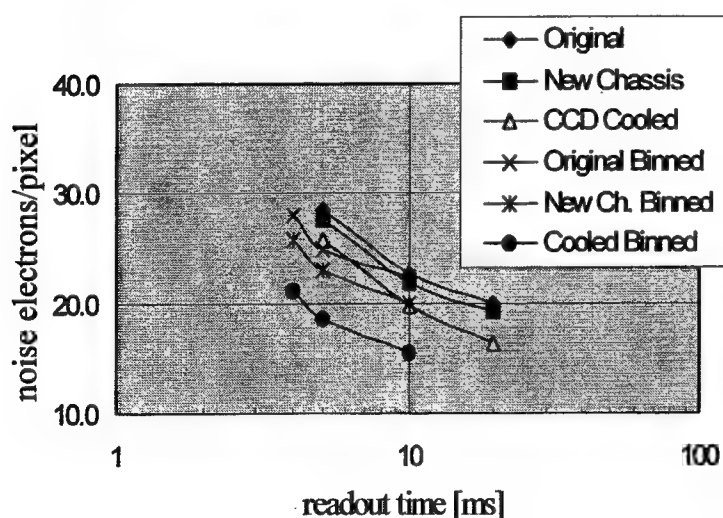


Fig. 6. 1024<sup>2</sup> imager noise performance

Further reductions in noise would exert significant leverage in the ability to detect low light-level signals. In the quest for lower noise yet, development is proceeding on a Hybrid Imaging Technology (HIT) sensor. The HIT sensor mitigates noise-bandwidth limitations in the KFS CCD by bump-bonding 2 CMOS processors chips (designed by G. Atlas of ImagerLabs) to the top & bottom of a CCD sensor (designed by M. Wadsworth of JPL) using indium balls. Each CMOS processor processes 128 channels from the CCD for a total of 256 channels. This should further reduce noise by  $\sim 8^{1/2}$ .

A new camera head is being designed and fabricated to accommodate the new HIT sensor as well as the current KFS sensor. The new camera head moves the shutter and power supply electronics outside of the evacuated enclosure to minimize CCD contamination problems. G. Katzenstein is designing the camera housing while D. Lang is designing the electronics. The new camera head is nearly complete and testing is expected to begin in May. The final

enhancement to the camera system is the development of a high-speed data link from the A/D converter boards to a disk-array.

Currently, the number of continuous frames acquired is limited by the amount of memory on the A/D converter boards (512 MB/board, for a total of 4 GB). This is sufficient for ~2700 frames ( $1024 \times 1024 \times 12$ -bits) without compression, or, approximately, 4000 to 8000 frames with lossless compression. Each A/D converter board has a high-speed auxiliary interface and D. Lang is designing an interface to a high-speed (128 MB/s) fiber-optic link (S-Link, developed at CERN). The S-Link will connect each of the 8 A/D converter boards to a disk storage array system (23TB total). The aggregate bandwidth will be 1 GB/s. This will allow recording of over  $10^6$  continuous frames at data rates of over 500 fps. This will permit 3D measurements and 3D measurements vs. time to be acquired in moderate to high Reynolds number turbulent flows.

## References

- Alon, U., Hecht, J., Ofer, D., & Shvarts, D. 1995 Power laws and similarity of Rayleigh-Taylor and Richtmyer-Meshkov mixing fronts at all density ratios. *Phys. Rev. Lett.* **74**, 534-537.
- Cook, A.W., & Dimotakis, P.E. 2001 Transition stages of Rayleigh-Taylor instability between miscible fluids. *J. Fluid Mech.* **443**, 69-99. Cook, A. W., & Dimotakis, P. E. 2002 Transition stages of Rayleigh-Taylor instability between miscible fluids. *J. Fluid Mech.* **457**, 410-411.
- Dimotakis, P.E. 1991 Turbulent Free Shear Layer Mixing and Combustion. *High Speed Flight Propulsion Systems*, in *Prog. Astro. & Aeronautics* **137**, Ch. 5, 265-340.
- Goodwin, D.G. 2003 An open-source, extensible software suite for CVD process simulation. *Proc. CVD XVI and EuroCVD Fourteen* (Electrochemical Society), in press.
- Henderson, R. D., & Karniadakis, G. E. 1995 Unstructured spectral element methods for simulation of turbulent flows. *J. Comp. Physics* **122**, 191-217.
- Kee, R.J., Miller, J.A., Evans, G.H., & Dixon-Lewis, G. 1988 A computational model of the structure and extinction of strained, opposed flow, premixed methane-air flames. *Proc. Combustion Institute* **22**, 1479-94
- Koochesfahani, M. M., & Dimotakis, P. E. 1986 Mixing and chemical reactions in a turbulent mixing layer. *J. Fluid Mech.* **170**, 83-112.
- Kostiuk, L.W., Bray, K.N.C., & Cheng, R.K. 1993 Experimental study of premixed turbulent combustion in opposed streams. Part I – nonreacting flow field. *Comb. and Flame* **92**, 377-395.
- Law, C.K. 1988 Dynamics of stretched flames. *Proc. Comb. Inst.* **22**, 1381-1402.
- Schlichting, H. 1960 *Boundary layer theory*. McGraw-Hill Book Company, Inc., New York.
- Wu, C.K., & Law, C.K. 1984 On the determination of laminar flame speeds from stretched flames. *Proc. Comb. Inst.* **20**, 1941-1949.
- Youngs, D. L. 1991 Three-dimensional numerical simulations of turbulent mixing by Rayleigh-Taylor instability. *Phys. Fluids* **3**, 1312-1320.
- Zhu, C.K., Egolfopoulos, F.N., & Law, C.K. 1988 Experimental and numerical determination of laminar flame speeds of methane/(Ar, N<sub>2</sub>, CO<sub>2</sub>)-air mixtures as a function of stoichiometry, pressure and flame temperature. *Proc. Comb. Inst.* **22**, 1537-1545.

# **THE LOW TEMPERATURE OXIDATION CHEMISTRY OF JP-8 AND ITS SURROGATES AT HIGH PRESSURE**

Contract No. DAAD19-03-1-0070; 44458-EG

David L. Miller and Nicholas P. Cernansky

Department of Mechanical Engineering and Mechanics  
Drexel University, Philadelphia, PA 19104

## **SUMMARY/OVERVIEW:**

An experimental program for the study of the ignition chemistry of JP-8 and its surrogates at high pressures began on June 1. The purpose of this project is to map the effects of chemical variations on the oxidation behavior of JP-8, and to participate in the development of an acceptable surrogate that matches the general behavior of JP-8. In this JP-8 mapping and surrogate development effort, selected JP-8's, distillate fuels, and neat distillate fuel components will be examined to develop comparative kinetic and mechanistic information in the low and intermediate temperature ranges (600 – 1000 K) and at elevated pressures (up to 20 atm). Similarly, the various proposed JP-8 surrogates, components, and their mixtures will be examined as well. These single and multiple component fuels will be oxidized in a pressurized flow reactor and stable intermediate and product species will be identified and quantified using permanent gas analyzers, gas chromatography, gas chromatography with mass spectrometry (GC/MS), and on-line Fourier Transform Infrared Spectrometry (FT-IR) in order to provide key mechanistic information. The experimental results will be used to develop appropriate detailed and reduced kinetic models for the ignition and oxidation of these fuels. Ultimately, these low and intermediate temperature experimental and modeling results will be coupled with the efforts of other research groups to provide a comprehensive understanding of the oxidation and combustion behavior of JP-8 and its surrogates.

## **OVERVIEW OF RESEARCH PROGRAM:**

### **Preignition Chemistry of JP-8's**

The first task of the research program examines the effects of fuel composition variations on the preignition oxidation process for JP-8 at conditions encountered in practical combustion devices. Several well-characterized samples of JP-8 from WPAFB and different refineries will be acquired and additional characterization work will be conducted as required. Important properties to be considered include: the relative fraction of each of the hydrocarbon functional groups, cetane number, and sulfur content. Reactivity mapping and survey studies will be conducted by exercising the flow reactor over a range of pressures (up to 20 atm), temperatures (600 - 1000 K), equivalence ratios, and diluent concentrations. During each experiment, a low and intermediate temperature reactivity map will be generated using online CO/CO<sub>2</sub> gas

analyzers. Analysis of these reactivity maps and the associated property data for each fuel sample will help elucidate the effects of chemical composition on the low and intermediate temperature chemistry of JP-8, and will help us select the specific fuels and conditions for more detailed examination. If during the course of this program, behavior is observed which can be explored more fully in our engine facilities, they will be used.

#### **Development of a "Standard" JP-8 Surrogate**

The second task involves participation in the development of a "standard" surrogate which can mimic the general combustion behavior of JP-8. However, due to the wide variations in cetane number, aromatic content, naphthene content, and percentage of other hydrocarbon functional groups in JP-8, there is a need to assure that these surrogates and models reflect the true nature of JP-8 and not just the specific sample of JP-8 used. During this task, the surrogates developed by other researchers, our own 5-component surrogate, and new surrogates developed from the knowledge gained from the first task will be examined in both the PFR facility and engine facilities and compared to the "average" preignition chemistry of JP-8. This will define the controlling factors and thus constraints on any surrogate if it is to adequately represent preignition behavior. Coupling of these constraints with those identified by other researchers who are examining other aspects of the combustion and emission behavior will lead to a "standard" JP-8 surrogate. Achieving this goal will require inter-laboratory testing and coordination, and several laboratories and researchers have indicated their willingness to participate. Overall, the identification of a standard JP-8 surrogate will greatly simplify and focus the experimental and modeling efforts.

#### **Preignition Chemistry of Distillate Fuel Components and Their Mixtures**

The third task of the research program examines the detailed preignition chemistry of key distillate fuel components and their mixtures at conditions encountered in practical combustion devices. The pressurized flow reactor will be operated at conditions of particular relevance identified in the first task, in order to generate species evolution profiles and other detailed experimental data. The initial studies will use the individual distillate fuel components of the proposed surrogates as the fuel, followed by their mixtures. Permanent gases will be analyzed online with continuous flow analyzers, and gas samples will be collected and stored in the heated multi-loop sampling valve for subsequent offline species analysis. These experiments and data, coupled with the appropriate analysis and kinetics modeling work, will help elucidate the effects of pressure and fuel structure on the low and intermediate temperature oxidation mechanism.

#### **Development of Chemical Kinetic Models**

The fourth task of the research program involves the development of detailed and reduced/skeletal chemical kinetic mechanisms and models which can simulate the experimental results and which can serve as tools for predicting ignition and emission characteristics. One of the primary goals of this study is to obtain mechanistic information and to gain insight into the detailed oxidation process and how it is affected by physical conditions. This will be accomplished by carefully selecting experimental conditions in order to isolate important features of the mechanism to be examined. By analyzing the intermediate and product species distributions, reaction paths and the relative importance of different reaction paths can be determined. Ultimately, the different experimental conditions employed will allow the mechanism to be examined over a wide range of conditions. The mixture experiments will allow

development of correlations relating fuel structure and composition to autoignition behavior as well as providing a test for the detailed mechanisms.





## ADVANCED SUPERCRITICAL FUELS

LRIR 93PR02COR

Principal Investigators: Tim Edwards, Chris Bunker, Tom Jackson

Air Force Research Laboratory  
AFRL/PRTG Bldg 490  
1790 Loop Rd N  
Wright Patterson AFB, OH 45433-7103

### SUMMARY/OVERVIEW:

Increases in aircraft and engine performance are increasing the heat load being transferred into an aircraft's primary coolant--the fuel. This research is aimed at understanding the limitations of operation of fuel heated to 480 C (900 F) and beyond. Important issues are expected to be thermal stability, injection/combustion properties, and fuel characterization.

### TECHNICAL DISCUSSION

#### **Thermal Stability**

Moving beyond the increases in thermal stability provided by the detergent/dispersant additives in JP-8+100 requires a better understanding of high temperature fuel oxidation and deposition processes. Attempts to interrupt the fuel auto-oxidation chain using hydroperoxide decomposers have been relatively unsuccessful [1]. Fuel system surface modifications have shown significant promise [2,3]. Fuel deoxygenation, although somewhat of a "brute force" approach, also contributes to deposition reduction. The use of the +100 additive, fuel deoxygenation, and surface coatings have enabled the increase of thermal stability in a "run-of-the-mill" JP-8 to the point that it was demonstrated to be better than JP-7 in a flowing 200 hr test at fuel temperatures of 700 F. Modeling efforts have shown good agreement with fuel oxidation profiles [2]; more work remains to adequately simulate deposition. One key challenge is the representation of the trace species responsible for fuel thermal stability -- how does one approximate the "average" or "typical" fuel for purposes of predicting fuel system component life? Earlier models have used total fuel sulfur as the correlating parameter -- it is known that this is inadequate due to the varying reactivity of the various types of sulfur (not to mention the neglect of other heteroatomic species). An alternative approach is to look at fuel polar species as a class to determine if this might be a better indicator of fuel thermal stability [4]. This work is ongoing and appears promising, but several "outlier" fuels have been identified -- fuels with high concentration of polar heteroatomic species but not the correspondingly-low thermal stability.

Above 900 F, thermal degradation of the bulk fuel leads to "endothermic" fuels. Current empirical models of endothermic fuel behavior do not take into account the change in fuel composition and properties that occurs with the cracking of the bulk fuel. A recent effort has corrected that problem for "mild" cracking [5]. Joint work with Tom Jackson on supercritical injection of high temperature fuel simulants for scramjet applications is reported in his abstract

for this meeting. A similar study for gas turbine conditions has been reported [6]. Judy Wornat's AFOSR work identifying the formation of large aromatics species as precursors to deposits indicates the path coking models for endothermic fuels need to take to model pyrolytic deposition.

### **Fuel-Quality Diagnostics [7-10]**

Efforts continue to develop chemical sensors capable of predicting fuel properties and fuel quality (in addition to the polar species diagnostics discussed above). Lab-scale measurements using fast-Gas Chromatography (fast-GC) coupled with empirical analysis to predict flash point, freeze point, and simulated distillation range are being transitioned to the field in collaboration with the AFPET (Air Force Petroleum Office) (Figures 3 and 4). Data obtained in the field will be fed back to AFRL to further enhance the empirical models and support development of chemometric-based models. Application of chemometrics to near-infrared data obtained for over 200 individual aviation fuels has also demonstrated the ability to predict flash point; however, the accuracy is currently below that of fast-GC. Near-IR offers potential long-term advantages over fast-GC due to its simple design, rapid scanning capabilities, and existence of field-level instruments. Further efforts to optimize the experimental method and improve prediction accuracy are underway.

Significant advances in the development of novel-semiconductor materials have been made. The materials are important due to their strong sensitivity to (*i.e.*; the electronic and optical properties can be modified by absorption of) hetero-atomic species known to be present in aviation fuel and responsible for poor thermal stability. Cadmium sulfide (CdS) particles with diameters on the order of 5 nm have been synthesized using a solution-based reverse-micelle procedure. The particles are then "processed" first by photolysis, then by a combined heat and vacuum treatment. The result is highly luminescent nanoparticles with quantum efficiencies on the order of 35% and spectral properties characteristic of trap states. Efforts to determine the chemical reactivity of the CdS nanoparticles with model hetero-atomic compounds are underway. Steady state and time-resolved luminescent quenching studies indicate strong interactions (Figure 5). Further work will focus on membrane technology to provide selectivity for specific chemical functionality and on-chip fabrication (MEMs devices) (Figure 6). Work in the area of biosensors is also continuing.

### **Novel Fuel Additives**

As described above, research is underway to develop additive technologies that are compatible with the thermal stability requirements of a JP-900 fuel (working temperature limit of 900 F). Current methodologies used to achieve JP-8+100 and under investigation for JP-8+225 (working temperature limits of 425 and 550 F, respectively) are thought to be inadequate for attainment of JP-900 goals. It is recognized that oxygen removal is the easiest way to achieve a JP-900 capable fuel. We are currently working on a novel application of nanotechnology—highly reactive core-shell nanoparticles—to deoxygenate fuel by chemical means. The advantages of nanotechnology are 1) nanoparticles possess very small sizes and thus very large surface areas, 2) nanoscale materials can be transported anywhere in an aircraft fuel system and not present difficulties with respect to filter plugging, and 3) nanoparticles can easily be made soluble in the non-polar environment of aviation fuel, thus making available a much larger area of chemistry to explore (*e.g.*, inorganic and organometallic compounds). Initial work on a first-generation JP-900 candidate has demonstrated temperature-activated reactivity (Figure 7) and

rapid deoxygenating with significantly reduce deposition levels (Figure 8). Future work will focus on testing the first candidate at 900 F, further development of environment triggered shell technology, and continued exploration of materials as the reactive core.

## References

- [1] DeWitt, M. J., and Zabarnick, S., "Development and Evaluation of Additives to Inhibit Oxidative Deposition of Jet Fuels," *ACS Petroleum Chemistry Division Preprints*, Vol. 47(3), 2002, pp. 183-186.
- [2] Ervin, J.S., Williams, T.F., Ward, T.A., and Bento, J., "Surface Deposition within Treated and Untreated Stainless-Steel Tubes Resulting from Thermal-Oxidative and Pyrolytic Degradation of Jet Fuel," submitted to *Energy and Fuels*, August 2002.
- [3] T. Dounghip, J. Ervin, T. Ward, T. Williams, S. Zabarnick, "Surface Deposition Within Treated and Untreated Stainless Steel Tubes Resulting from Thermal-Oxidative Degradation of Jet Fuel," *ACS Petrol. Chem. Div. Preprints* **2002**, 47, 204-207, 2002.
- [4] S. Zabarnick, R. Striebich, K. Straley, and L. Balster, Solid Phase Extraction Analysis of Polar Species in Jet Fuel," *ACS Petrol. Chem. Div. Preprints* **2002**, 47, 223-226, 2002.
- [5] Ward, T., Ervin, J. S., Striebich, R. C., Zabarnick, S., "Flow and Chemical Kinetics Simulations of Endothermic Fuels," 2003 ASME Fluids Engineering Division Summer Meeting Honolulu, Hawaii, July 6-10, 2003.
- [6] Dounghip, T., Ervin, J.S., Williams, T.F., and Bento, J., "Studies of Injection of Jet Fuel at Supercritical Conditions," *Ind. Eng. Chem. Res.*, Vol. 41, 5856-5866, 2002.
- [7] Qu, L., Martin, R. B., Huang, W., Fu, H., Zweifel, D., Lin, Y., Sun, Y-P., Bunker, C. E., Harruff, B. A., Gord, J. R., Allard, L. F., "Interactions of functionalized carbon nanotubes with tethered pyrenes in solution," *Journal of Chemical Physics*, Vol. 117(17), 8089-8094, 2002.
- [8] Sun, Y.-P., Rollins, H. W., Bandara, J., Meziani, J. M., Bunker, C. E., "Preparation and Processing of Nanoscale Materials by Supercritical Fluid Technology," Chapter 13 of *Supercritical Fluid Technology in Materials Science and Engineering-Syntheses, Properties, and Applications*, Y.-P. Sun, ed., Marcel Dekker, Inc., New York, 2002.
- [9] Bunker, C. E., Rollins, H. W., Sun, Y.-P., "Fundamental Properties of Supercritical Fluids," Chapter 1 of *Supercritical Fluid Technology in Materials Science and Engineering-Syntheses, Properties, and Applications*, Y.-P. Sun, ed., Marcel Dekker, Inc., New York, 2002.
- [10] Harruff, B. A.; Bunker C. E. "Spectral Properties of AOT-Protected CdS Nanoparticles: Quantum-Yield Enhancement by Photolysis" *Langmuir* 19(3) 893-897, 2003.

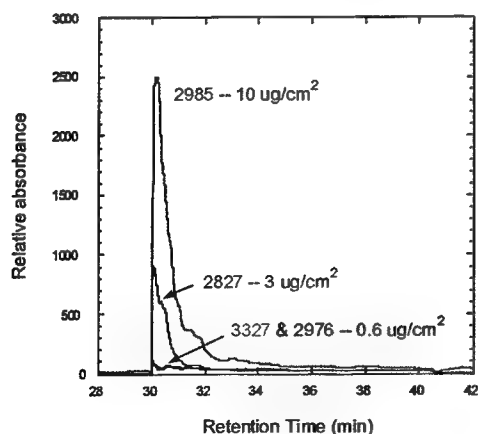


Figure 1. HPLC polar fractions from poor (2985), typical (2827), and excellent (3327 and 2976) jet fuels [4].

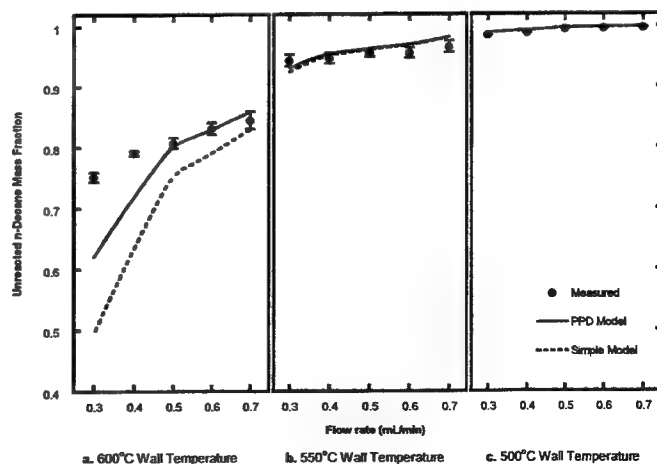


Figure 2. Comparison of Experimental versus Calculated n-Decane Degradation for Varying Steady State Wall Temperatures and Flow Rates [5].

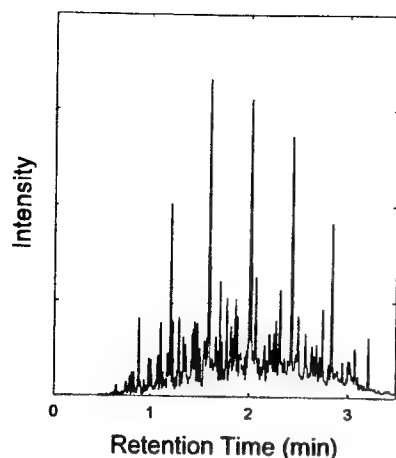


Figure 3. Fast-GC chromatogram obtained for JP-8 with a runtime under 3.5 min.

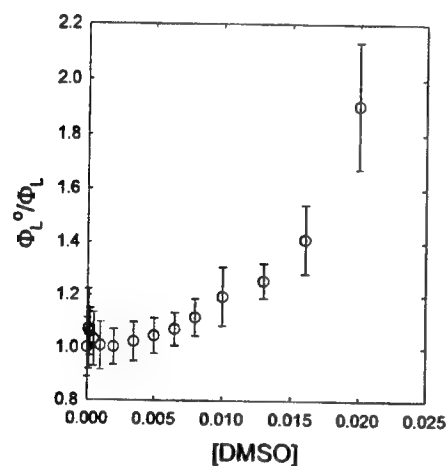


Figure 5. Stern-Volmer plot for the luminescence quenching of CdS nanoparticles by DMSO. Upward curvature indicates strong association.

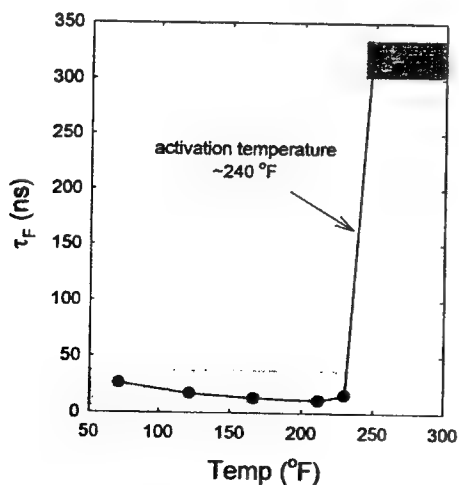


Figure 7. Fluorescence lifetime of pyrene in dodecane with the core-shell additive. Short lifetimes indicate presence of oxygen.

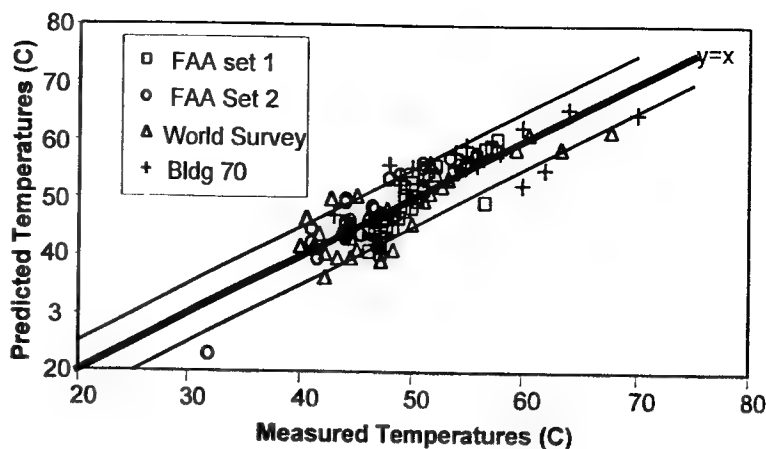


Figure 4. Measured vs. predicted flash point values for a series of aviation fuels based on fast-GC analysis and empirical modeling.

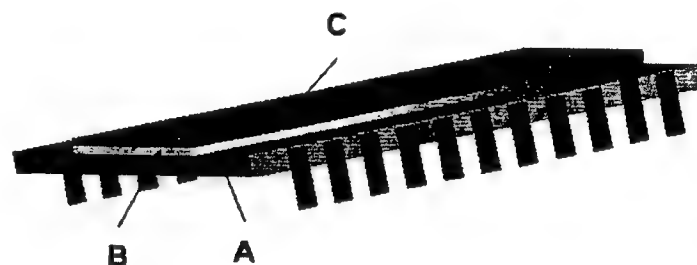


Figure 6. Cartoon representation of on-chip design of a CdS-based MEMs device with (A) chip substrate, (B) active chemical layer, and (C) chemical specific membrane.

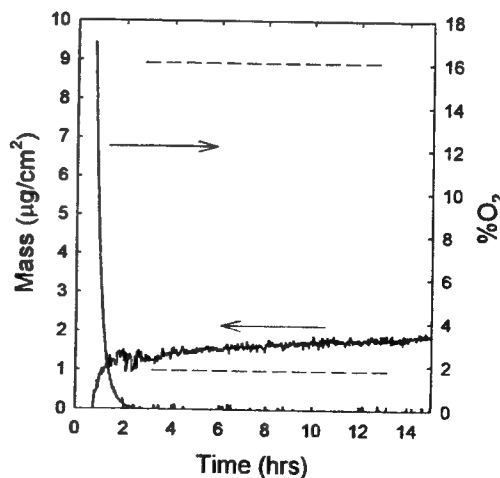


Figure 8. Quartz crystal microbalance analysis of JP-8 at 140°C with the core-shell additive. Top and bottom lines represents level of deposition observed for typical JP-8 and JP-8+100 fuels, respectively.

# EXPERIMENTAL AND DETAILED NUMERICAL STUDIES OF FUNDAMENTAL FLAME PROPERTIES OF GASEOUS AND LIQUID FUELS

(AFOSR Grant No. F49620-02-1-0002)

Principal Investigator: Fokion N. Egolfopoulos

*Department of Aerospace & Mechanical Engineering  
University of Southern California  
Los Angeles, California 90089-1453*

## SUMMARY/OVERVIEW

The main goal of this research is to provide fundamental data on the dynamic behavior of laminar flames for a wide range of conditions. The parameters that are considered include the fuel type, equivalence ratio, flame temperature, pressure, and combustion mode. The experimental data constitute a basis for partially validating the combustion chemistry of a large number of fuels ranging from hydrogen to gaseous and liquid hydrocarbons and alcohols. The understanding of the oxidation kinetics of such fuels is of immediate interest to the design of advanced air-breathing propulsion devices. Emphasis is given to kinetics regimes that have not been systematically probed in past flame studies and/or in which current knowledge of combustion chemistry appears to be inadequate. During the reporting period progress was made in the following: (1) Premixed flame extinction of lean and ultra-lean  $H_2$ /air flames. (2) Premixed flame extinction of mixtures of liquid  $CH_3OH$ ,  $C_2H_5OH$ ,  $n-C_7H_{16}$ , and iso- $C_8H_{18}$  fuels with air. (3) Non-premixed ignition of  $H_2$  and gaseous hydrocarbons. (4) Premixed ignition of liquid  $CH_3OH$ ,  $C_2H_5OH$ ,  $n-C_7H_{16}$ , and iso- $C_8H_{18}$  fuels. In all studies deficiencies of current state of the art chemical kinetics models were identified. Preliminary results suggest that revisions of the transport coefficients formulation can also have noticeable effects on the predictions of fundamental flame properties, especially for the highly diffusive  $H_2$  flames.

## TECHNICAL DISCUSSION

The studies include both experiments and detailed numerical simulations. The experiments are conducted in the opposed jet configuration that allows for the systematic determination of the fluid mechanics effects on flames and can be also modeled directly along its stagnation streamline. The experiments are performed in a variable pressure chamber. The reported measurements have been performed at  $p = 1 \text{ atm}$  through the use of a Digital Particle Image Velocimetry (DPIV) technique [1] and thermocouples. Raman and Rayleigh spectroscopy are about to be implemented for the non-intrusive sampling of temperature and species concentrations. The numerical simulations are performed through the use of a CHEMKIN-based counterflow code [2]. Several chemical kinetics schemes have been tested. Furthermore, a revised molecular transport subroutine library [3] has been tested for  $H_2$ /air flames.

### 1. Premixed Flame Extinction of Lean and Ultra-Lean $H_2$ /Air Mixtures

The oxidation kinetics of  $H_2$  were tested under fuel-lean conditions for which the presence of thermo-diffusional instabilities does not allow for the determination of laminar flame speeds. Under such conditions the flame temperatures are well below those encountered in hydrocarbon flames, and such temperatures are of relevance to the process of ignition. The extinction strain rates,  $K_{ext}$ , were determined and used to validate the kinetics, as it is known that both extinction and propagation are controlled by similar chain mechanisms [4]. Note that the presence of positive stretch suppresses the formation of cellular structures. Figure 1 depicts comparisons between the experimental and predicted  $K_{ext}$ 's by using the GRI30 [5] and Mueller et al. [6]  $H_2/O_2$  mechanisms. Both experiments and simulations were performed in the single-flame configuration in which a mixture jet counterflows against an ambient temperature air-jet. It is of interest to note that the agreements are not close and that there is a difference in the "slope" of the results. Furthermore, it can be seen that while the predicted  $K_{ext}$ 's by the two mechanisms "merge" at high temperatures they significantly deviate from each other at lower temperatures. The GRI30 mechanism appears to underpredict the  $K_{ext}$ 's of ultra-lean  $H_2$ /air flames by a factor of two (!) at low temperatures. At high temperatures, both mechanisms appear to overpredict the experimental  $K_{ext}$ 's by nearly 50%. The numerical simulations that are shown in Fig. 1 were performed by using a large number of grid points,  $N$ . It was found that by varying  $N$  from 300 to 2000-3000,  $K_{ext}$  could increase by as much as 25% reaching asymptotically the values that are reported in Fig. 1 as  $N \rightarrow \infty$ . Furthermore, a revised by Prof. Wang's group transport library subroutine [3] was tested for these flames and it was found that  $K_{ext}$  increases by approximately 10%; this work is in progress. While molecular transport has an effect on the results the observed differences must be largely caused by deficiencies in kinetics. Figure 2 depicts normalized sensitivity coefficients on  $K_{ext}$  for ultra-lean  $H_2$ /air flames, obtained by independently perturbing the pre-exponential factor of each reaction. The  $HO_2$  chemistry appears to have a noticeable effect on  $K_{ext}$  and uncertainties associated with the  $H+O_2+M \rightarrow HO_2+M$  may be responsible for the observed discrepancies.

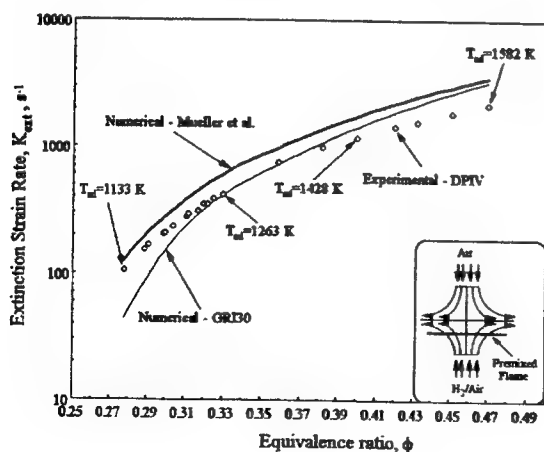


Fig. 1.  $K_{ext}$ 's for single  $H_2$ /air flames

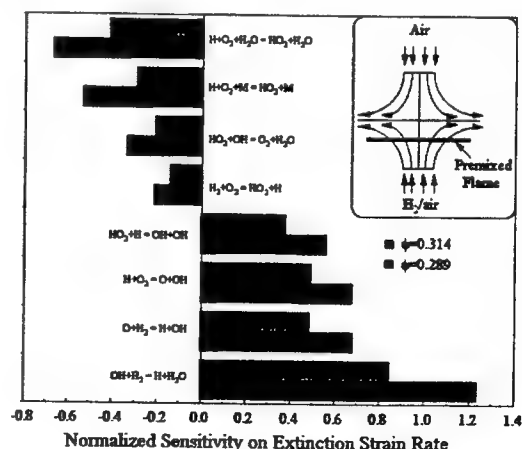


Fig. 2. Sensitivity analysis for single  $H_2$ /air flames

## 2. Premixed Flame Extinction of Mixtures of Liquid Fuels with Air

The extinction of mixtures of practical liquid fuels with air was also studied in the single flame configuration. The introduction of the liquid phase into the air under room temperature was achieved through the use of an evaporator and a high-precision liquid pump. The liquid is atomized into a stream of heated air and subsequently the temperature of the mixture is reduced to ambient. The liquid fuel exists in the vapor phase as long as its partial pressure is maintained below its vapor pressure at the prevailing ambient temperature. The liquid fuels that were tested are  $\text{CH}_3\text{OH}$ ,  $\text{C}_2\text{H}_5\text{OH}$ ,  $n\text{-C}_7\text{H}_{16}$ , and  $\text{iso-C}_8\text{H}_{18}$ . The  $K_{ext}$ 's of mixtures of those fuels with air at ambient temperature are shown in Fig. 3.

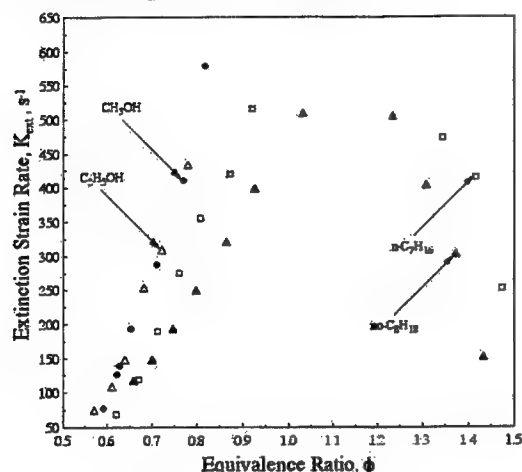


Fig. 3.  $K_{ext}$ 's for liquid fuels

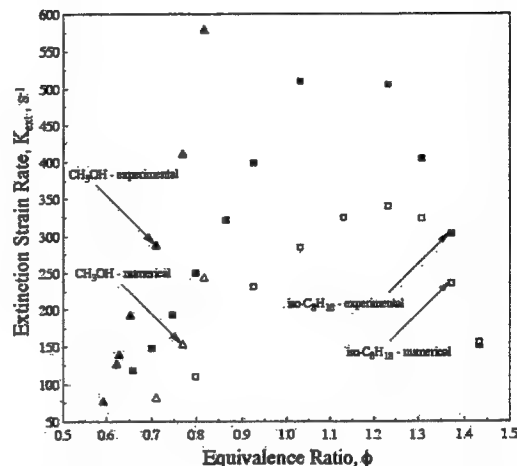


Fig. 4. Experimental and predicted  $K_{ext}$ 's

It is of interest to note that the  $K_{ext}$ 's of the alcohol fuels are noticeably higher than those of  $n\text{-C}_7\text{H}_{17}$ , and  $\text{iso-C}_8\text{H}_{18}$ , while there are minor differences between the measured  $K_{ext}$ 's of  $\text{CH}_3\text{OH}$  and  $\text{C}_2\text{H}_5\text{OH}$  flames. Furthermore, the  $n\text{-C}_7\text{H}_{16}$  flames are more resistant to extinction compared to  $\text{iso-C}_8\text{H}_{18}$  flames. These observations are important in terms of combustion stability. Numerical simulations of the  $K_{ext}$ 's shown in Fig. 3 are in progress and the results that have been obtained for  $\text{CH}_3\text{OH}$  and  $\text{iso-C}_8\text{H}_{18}$  flames are shown in Fig. 4. The mechanism of Curran and coworkers [7] was used for the simulations of the  $\text{CH}_3\text{OH}$  flames while the mechanism of Davis and Law [8] was used for the  $\text{iso-C}_8\text{H}_{18}$  flames. In both cases, the numerical simulations noticeably underpredict the experimental  $K_{ext}$  values.

## 3. Non-Premixed Ignition of $\text{H}_2$ and Gaseous Hydrocarbons

A new approach has been developed for ignition studies in the counterflow configuration. It includes the use of ultra-lean  $\text{H}_2$ /air flames as the ignition source. The hot excess air dominates the composition of the post-flame products, while minor amounts of  $\text{H}_2\text{O}$  are present. The temperature of those products can be controlled by either varying the  $\text{H}_2$ /air equivalence ratio or by adding small amounts of CO in cases in which higher ignition temperatures and low strain rates are required. Alternatively, in cases in which ignition temperatures below 1100 K are required a platinum screen is used at the burner exit to catalytically support  $\text{H}_2$ /air flames at such low temperatures. The temperature just downstream of the platinum screen is measured by a thermocouple and is used as boundary condition in the numerical simulations. The use of the

platinum screen is required for the ignition of  $H_2$ ,  $C_2H_4$ , and  $C_2H_2$  while the use of  $H_2$ /air flames at various equivalence ratios and with various amounts of added CO is required for the ignition of saturated hydrocarbons. Premixed ignition is achieved by counter-flowing the hot products against an air-jet in which the fuel is slowly added to the air stream. Non-premixed ignition is achieved by counter-flowing the hot products against a  $N_2$  jet in which the fuel is slowly added. The non-premixed ignition of  $H_2$ ,  $CH_4$ ,  $C_2H_6$ ,  $C_2H_4$ ,  $C_2H_2$ , and  $C_3H_8$  has been studied. Figure 5 depicts the effect of  $H_2$  and  $C_2H_4$  addition on the ignition of  $CH_4$  for a global strain rate,  $K_g = 44 \text{ s}^{-1}$ . These data were determined by using a  $\phi = 0.30$   $H_2$ /air flame as the ignition source, and by adding various amounts of  $H_2$  and  $CH_4$  in various mixtures of  $C_2H_4/N_2$ . These results are of relevance to the ignition response of the products of thermal cracking of endothermic fuels [e.g. 4]. The ignition promotion caused by  $H_2$  and  $C_2H_4$  is apparent. Preliminary numerical studies have shown that no mechanism can predict the experimental results shown in Fig. 5.

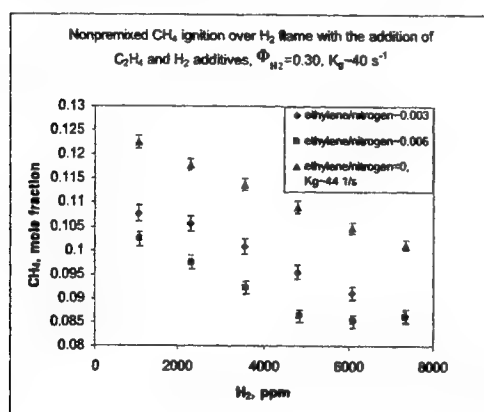


Fig. 5. Non-premixed ignition of gaseous fuels

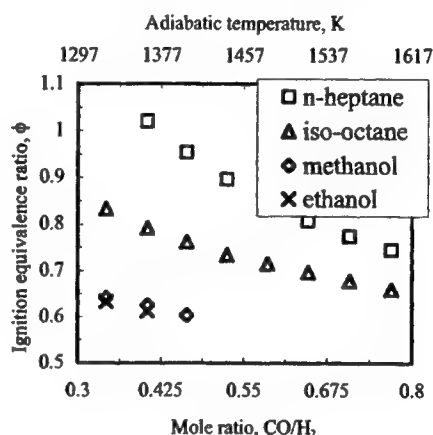


Fig. 6. Premixed ignition of liquid fuels

#### 4. Premixed Ignition of Liquid $CH_3OH$ , $C_2H_5OH$ , $n-C_7H_{16}$ , and $iso-C_8H_{18}$ Fuels

The premixed ignition of practical liquid fuels has been also studied. Representative results are shown in Fig. 6 and have been achieved by increasing the temperature of a  $\phi=0.256$   $H_2$ /air flame through CO addition. As expected, the higher is the temperature of the  $H_2$ /CO/air flame the lower is the ignition equivalence ratio of the test fuel. The greater ignition propensity of the alcohol fuels as well as that of  $iso-C_8H_{18}$  compared to  $n-C_7H_{16}$  is noticeable. Numerical simulations of these experiments are in progress.

#### REFERENCES

1. Dong, Y., Vagelopoulos, C.M., Spedding, G.R. & Egolfopoulos, F.N. *Proc. Combust. Inst.* **29**, in press (2002).
2. Egolfopoulos, F.N. & Campbell, C.S., *J. Fluid Mech.* **318**, pp 1-29 (1996).
3. Wang, H., Personal Communications (2003).
4. Egolfopoulos, F.N. & Dimotakis, P.E., *Combust. Sci. Tech.* **162**, pp. 19-36, (2001).
5. Bowman, C.T., Frenklach, M., Gardiner, W.R. & Smith, G. 1999 "The GRI 3.0 Chemical Kinetic Mechanism." [http://www.me.berkeley.edu/gri\\_mech/](http://www.me.berkeley.edu/gri_mech/).
6. Mueller, M.A., Kim, T.J., Yetter, R.A. & Dryer, F.L., *Int. J. Chem. Kin.* **31**, pp 113-119 (1999).
7. Curran, H., Personal Communications (2003).
8. Davis, S.G. & Law, C.K., *Proc. Combust. Inst.* **27**: 521-527 (1998).



# DROP/GAS INTERACTIONS OF DENSE SPRAYS

(AFOSR Grant No. F49620-02-1-0074)

Principal Investigator: G. M. Faeth

Department of Aerospace Engineering  
The University of Michigan  
3000 François-Xavier Bagnoud Bldg.  
Ann Arbor, Michigan 48109-2140, U.S.A.

## SUMMARY/OVERVIEW:

Turbulence generation and liquid breakup are being studied due to their relevance to the dense combusting sprays found in propulsion systems. Turbulence generation is the main source of turbulence in dense sprays; it consists of drop (particle) wake disturbances embedded in a turbulent interwake region. Both regions involve unusual flows that have received little attention in the past: the particle (drop) wakes are laminar-like turbulent wakes that are observed for intermediate Reynolds number spheres in turbulent environments; the turbulent interwake region consists of isotropic turbulence in the little-studied final decay period. Earlier work found the properties of these flows for monodisperse particle (drop) flows; current work is considering their properties for more practical polydisperse particle (drop) flows.

Secondary and primary liquid breakup are important because they are rate-controlling processes of dense sprays and fix the initial conditions of dilute sprays. Earlier experiments at large liquid/gas density ratios have shown that secondary drop breakup should be treated as a rate process and have provided the temporal properties of secondary drop breakup needed for this purpose; and have also shown that breakup of round nonturbulent liquid jets in crossflows is remarkably similar to the secondary breakup of drops. Current time-dependent numerical simulations are seeking drop breakup at small liquid/gas density ratios that are difficult to address using experiments; in addition, current measurements are considering the breakup properties of round nonturbulent liquid jets at large liquid/gas density ratios that are relevant to most propulsion applications using this atomization process, in more detail than before. In both cases, phenomenological analysis is being used to help interpret and correlate the results.

## TECHNICAL DISCUSSION

**TURBULENCE GENERATION.** Early studies showed that turbulence generation by particles (drops) involved particle wakes embedded in a turbulent interwake region (Parthesarathy and Faeth 1990a,b; Mizukami et al. 1992). Wu and Faeth (1993,1994,1995) subsequently showed that the wakes behaved like laminar wakes but with fast mixing due to the presence of turbulence (commonly referred to as "laminar-like turbulent wakes"). Subsequently, Chen et al. (2000) and Chen and Faeth (2000,2001) considering monodisperse particle flows, showed that the turbulent interwake region consisted of isotropic turbulence in the rarely observed final-decay period defined by Batchelor and Townsend (1948). The current work of Lee et al. (2003) seeks to extend these observations to the turbulent interwake region of more practical polydisperse particle flows, using wake-discriminating laser velocimetry.

Chen and Faeth (2001) developed an analogy between grid-generated isotropic turbulence and particle-generated isotropic turbulence, when both were in the final-decay period. This yielded a very useful correlation between relative turbulence intensities in the streamwise and cross-stream directions,  $(\bar{u}' \text{ and } \bar{v}')/U_p$ , where  $U_p$  is the mean streamwise velocity of the particles relative to the gas, and the dimensionless rate of dissipation of mechanical energy of the particles,  $D$ . During the present investigation, mixing rules were developed to extend these ideas

to polydisperse particle flows based in dissipation weighting of each particle size group. The resulting correlation of the measurements is illustrated in Fig. 1 which exhibits a universal correlation for both monodisperse and polydisperse sized particles according to the square root of  $D$ , as suggested by the theory.

Other experiments completed during this report period involved wake-discriminating measurements of energy spectra and characteristic length scales for the turbulent interwake region of polydisperse particle flows. A remarkable feature of these results was the large range of length scales observed (up to 1000:1) even though turbulence Reynolds numbers were small (less than 4). Also, energy spectra decayed according to the  $-5/3$  power of wave number just like conventional turbulence in spite of the unusual features of turbulence in the final-decay period; this latter behavior was shown to follow via the classical Kolmogorov derivation (Hinze, 1975) due to the large range of length scales in the flow. Present results for the ratios of the streamwise integral length scale,  $L_w$ , to the Taylor dissipation scale,  $\lambda$ , are plotted as a function of the turbulence Reynolds number,  $Re_\lambda$ , in Fig. 2. Results are shown for both conventional isotropic turbulence in the initial-decay period along with present results in the final-decay period. Surprisingly,  $L_w/\lambda$  decreases with increasing  $Re_\lambda$ , for interwake turbulence in the final-decay period, which is just opposite to the behavior of conventional turbulence. The interwake region also involves rates of turbulence dissipation up to 1000 times larger than conventional turbulence at comparable outer scales, accounting for past problems of turbulence models to predict the properties of this region (Lee et al., 2003). Finally, current work is seeking to resolve the structure of particle wakes in the final-decay period, in order to better understand the properties of this unusual turbulent flow.

**LIQUID BREAKUP.** Past experimental studies have established the temporal properties of secondary drop breakup (Chou and Faeth 1997; Chou et al. 1997; Dai and Faeth 2001; Faeth 1996; Hsiang and Faeth 1992, 1993, 1995) and have initiated studies of round nonturbulent liquid jet breakup in crossflow (Mazallon et al. 1999), both at large liquid/gas density ratios. Current work is considering secondary drop breakup at small liquid/gas density ratios as well as extending earlier studies of the primary breakup of nonturbulent liquid jets in crossflow at large liquid/gas density ratios.

Liquid drop breakup at small liquid/gas density ratios is being considered using time-dependent numerical simulations to reach conditions that are difficult to address by experiments. It was found that the traditional Hinze (1955) breakup regime plot was not convenient for treating the large viscous forces typical of high-pressure drop breakup; a better approach was to plot the ratio of drag/viscous forces,  $We^{1/2}/Oh$ , as a function of the ratio of surface-tension/viscous forces,  $1/Oh$ . These results are illustrated in Fig. 3; this approach yields an excellent correlation of existing measurements and demonstrates that effects of Reynolds number and liquid/gas density ratio on these properties are small providing a way to address the high-pressure sprays encountered in practical propulsion systems, see Aalburg et al. (2003a) for more details about this research.

Experimental results for nonturbulent liquid jets in crossflow were obtained using shock tube and wind tunnel tests. A surprising feature of these results is that breakup of liquid jets in crossflow yields a breakup regime map very similar to the classical Hinze (1955) map for the secondary breakup of drops, see Fig. 4. Other findings of these measurements include drop size and velocity distributions after breakup, and rates of liquid breakup, as a function of position along the liquid jet as well as measurements of the location of breakup of the liquid column as a whole. Phenomenological theories have been used to help interpret and correlate these measurements, see Sallam et al. (2003) and Aalburg et al. (2003b), for a more complete description of this research.

Current work involves additional pulsed holography measurements and numerical simulations of both secondary drop breakup and primary breakup of nonturbulent liquid jets.

## REFERENCES

- Aalburg, C.M. et al. (2003a) *AIAA J.*, submitted.  
Aalburg, C.M. et al. (2003b) *AIAA J.*, in preparation.  
Batchelor, G.K. and Townsend, A.A. (1948) *Proc. Roc. Soc. (London)* 194A, 527.  
Chen, J.-H. and Faeth, G.M. (2000) *AIAA J.* 38, 995.  
Chen, J.-H. and Faeth, G.M. (2001) *AIAA J.* 39, 180.  
Chen, J.-H. et al. (2000) *AIAA J.* 38, 636.  
Chou, W.-H. and Faeth, G.M. (1997) *Int. J. Multiphase Flow* 24, 889.  
Chou, W.-H. et al. (1997) *Int. J. Multiphase Flow* 23, 651.  
Dai, Z. and Faeth, G.M. (2001) *Int. J. Multiphase Flow* 27, 217.  
Faeth, G.M. (1996) *Proc. Combust. Inst.* 26, 1593.  
Hinze, J.O. (1955) *AIChE J.* 1, 289.  
Hinze, J.O. (1975) *Turbulence*, 2<sup>nd</sup> ed., McGraw-Hill, New York, p. 202 and p. 496.  
Hsiang, L.-P. and Faeth, G.M. (1992) *Int. J. Multiphase Flow* 18, 635.  
Hsiang, L.-P. and Faeth, G.M. (1993) *Int. J. Multiphase Flow* 19, 721.  
Hsiang, L.-P. and Faeth, G.M. (1995) *Int. J. Multiphase Flow* 21, 545.  
Lee, K. et al. (2003) *AIAA J.*, in press.  
Mazallon, J. et al. (1999) *Atom. Sprays* 9, 291.  
Mizukami, M. et al. (1992) *Int. J. Multiphase Flow* 18, 397.  
Parthesarathy, R.N. and Faeth, G.M. (1990a) *J. Fluid Mech.* 220, 485.  
Parthesarathy, R.N. and Faeth, G.M. (1990b) *J. Fluid Mech.* 220, 515.  
Sallam, K.A. et al. (2003) *AIAA J.*, submitted.  
Wu, J.-S. and Faeth, G.M. (1993) *AIAA J.* 31, 1448.  
Wu, J.-S. and Faeth, G.M. (1994) *AIAA J.* 32, 535.

Wu, J.-S. and Faeth, G.M. (1995) *AIAA J.* 33, 171.

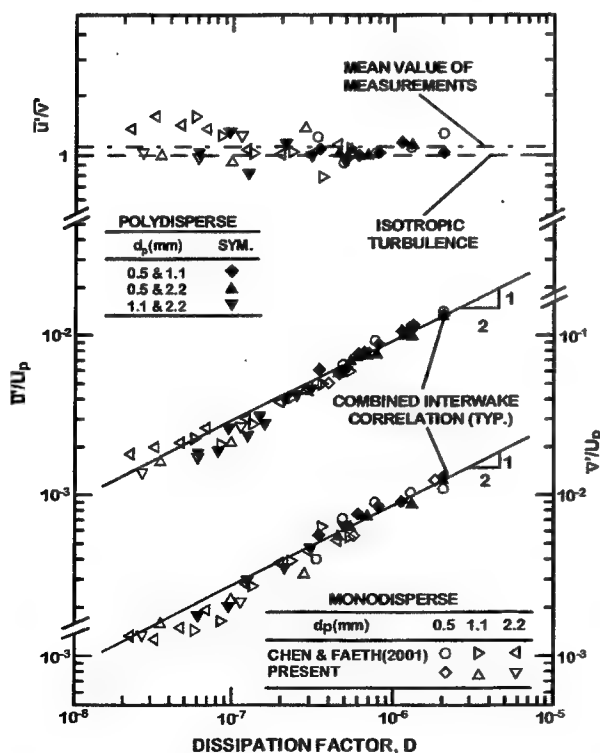


Fig. 1 Relative turbulence intensities as a function of the dissipation factor for the turbulent interwake region. From Lee et al. (2003).

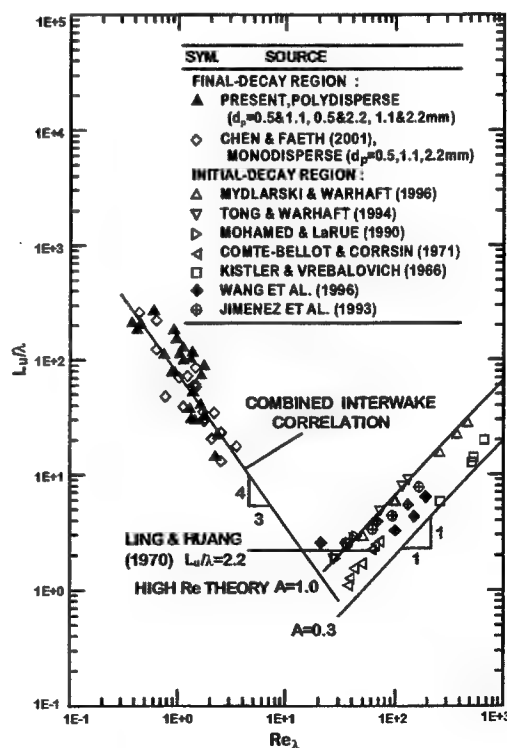


Fig. 2 Integral/dissipation length scale ratio as a function of turbulence Reynolds number. From Lee et al. (2003).

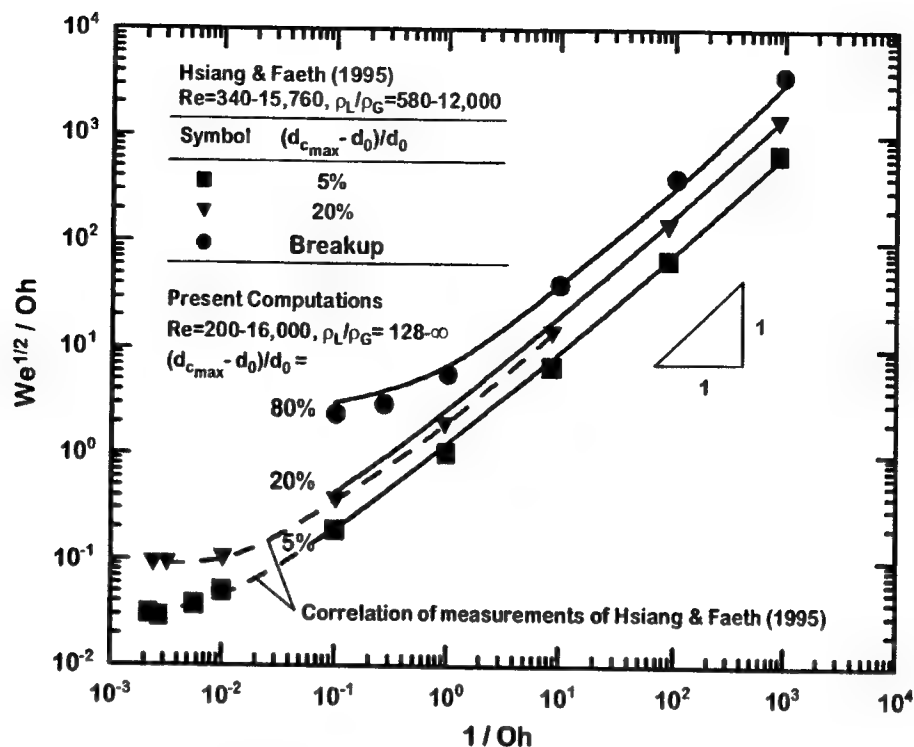


Fig. 3 Breakup regime boundaries for drops subjected to shock-wave disturbances in the drag/viscous force and surface-tension/ viscous force coordinate system. From Aalburg et al. (2003a).

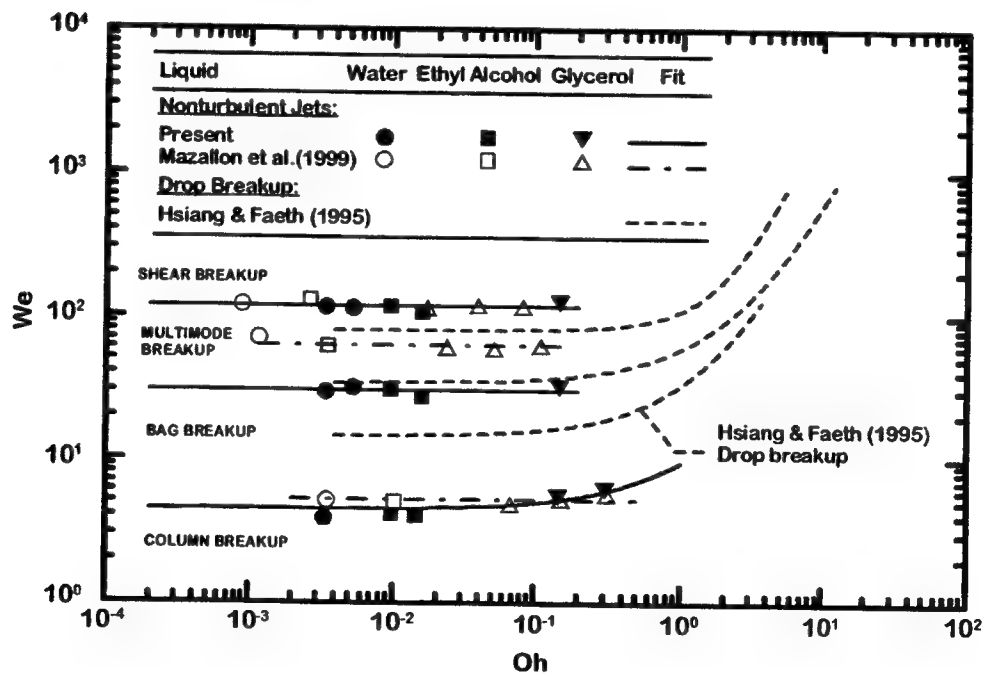


Fig. 4 Breakup regime boundaries for primary breakup of round nonturbulent liquid jets in gas crossflows. From Sallam et al. (2003).

# **ADVANCED STIMULATED SCATTERING MEASUREMENTS IN SUPERCRITICAL FLUIDS**

AFOSR Contract F49620-03-C-0015

Principal Investigator: Gregory W. Faris

SRI International  
Menlo Park, California 94025

## **SUMMARY/OVERVIEW**

This project uses stimulated scattering (stimulated Rayleigh, Brillouin, and Raman scattering) as a tool to investigate supercritical fluids. From the measurements, we can determine thermal, compressional, and compositional properties of supercritical fluids *in situ*. This research effort addresses the need for new diagnostics in the study of the supercritical and near-critical regimes, where low-pressure diagnostics do not work well.

## **TECHNICAL DISCUSSION**

### **Objectives**

The objectives of this research are to develop stimulated scattering as a diagnostic for supercritical fluids, and use this technique to improve our understanding of fluids in the supercritical state.

The study of supercritical fluids and flows requires new diagnostic techniques. Currently available techniques such as laser-induced fluorescence (LIF) and coherent anti-Stokes Raman scattering (CARS) are complicated by increased molecular interactions, leading to stronger quenching, larger absorption and refractive index, and incomplete understanding of the influence of local conditions on spectroscopic parameters such as linewidths, nonresonant background contributions, and quenching rates. We believe that stimulated scattering techniques hold great promise for studying supercritical fluids.

### **Stimulated Scattering**

Rayleigh, Brillouin, and Raman scattering occur commonly as spontaneous scattering. Rayleigh scattering results from refractive index variations due to thermal waves or diffusive density fluctuations and compositional fluctuations. Brillouin scattering results from refractive index variations due to sound waves or traveling density or pressure fluctuations. These scattering processes that arise from natural oscillation modes of materials can be used to determine the physical parameters responsible for those oscillations. When these collective modes are excited with a powerful laser, the mode oscillations can be driven so hard that they

grow exponentially. In this case, the oscillations cause stimulated scattering. The dominant advantage of stimulated scattering is that the scattered signal can be made arbitrarily large; otherwise, these processes produce extremely weak signals. By using a probe to measure the induced amplification, we can obtain very good quantitative results. This technique is distinct from the stimulated scattering that builds up from noise, in which case quantification is very difficult.

The large signals from stimulated scattering are particularly helpful for investigating Rayleigh and Brillouin scattering, where the weak signals available from spontaneous scattering are difficult to discriminate from background excitation light. Other advantages of stimulated scattering include excellent temporal resolution, and improved spectral resolution and signal-to-noise ratio. Furthermore, the use of two laser beams allows spatial registration and point measurement of local conditions.

With a single detection system, all three processes—Rayleigh, Brillouin, and Raman—can be measured. These processes together provide measurements of a wide range of material properties. Rayleigh scattering provides information on thermal properties, Brillouin scattering on compressional or elastic properties, and Raman scattering on chemical and compositional properties, density, and temperature. While spontaneous Brillouin and Raman scattering have been applied to supercritical fluids, the use of stimulated scattering for supercritical fluids is new.

## Experiment

We perform stimulated scattering measurements by producing strong scattering interactions using a pump laser and then probing the scattering using a second probe laser. As a pump laser we use an injection-seeded Nd:YAG laser and the probe laser is a tunable diode laser. The pump laser sets up an electric polarization oscillating at the characteristic frequency of a scattering mode of the material.<sup>1</sup> For strong laser driving, this polarization acts as a driving force, leading to amplification of both the material oscillation and the scattered optical wave. The optical amplification is detected as a gain or loss on the probe beam. The overlap volume of the pump and probe beams determines the spatial resolution. The stability of the probe and pump lasers has been optimized to allow for more reliable operation and narrower bandwidth, respectively. The cell is suitable for measurements in the supercritical and near-critical region.

## Results

The critical point for n-hexane occurs at a pressure 31 kPa and temperature of 234 °C. Examples of stimulated Rayleigh / Brillouin scattering spectra measured at 1064 nm in n-hexane near the critical temperature at three different pressures are shown in Fig. 1. The peaks to the left and right of each spectrum are the gain and loss Brillouin peaks, respectively. The central peak is the stimulated Rayleigh peak. Optical absorption enhances the Rayleigh peak and produced asymmetry to the Brillouin peaks. Also shown in Fig. 1 are fits to the data. These fits include

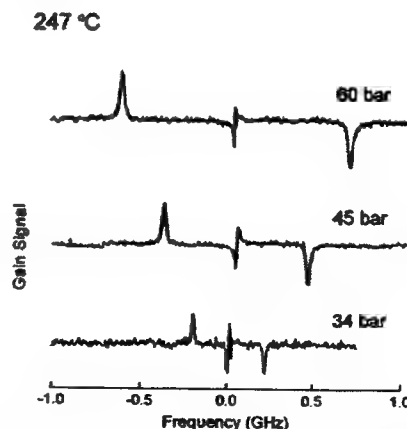


Figure 1. Stimulated scattering spectra at 1064 nm for three different pressures.

the appropriate lineshapes for each peak and the laser spectral width. Fits of this type enable the determination of linewidths, lineshifts, and peak heights. The electrostrictive Brillouin lineshape is described by the real part of the complex Lorentzian profile; the thermal Brillouin and Rayleigh lineshapes are described by the imaginary parts of a complex Lorentzian profile.<sup>2</sup> The measured lineshapes are given by the convolution of the Gaussian spectral lineshape of the Nd:YAG pump laser with these Lorentzian profiles. The following figures present stimulated Brillouin scattering properties for n-hexane at 1064 nm at sub-, near-, and supercritical conditions.

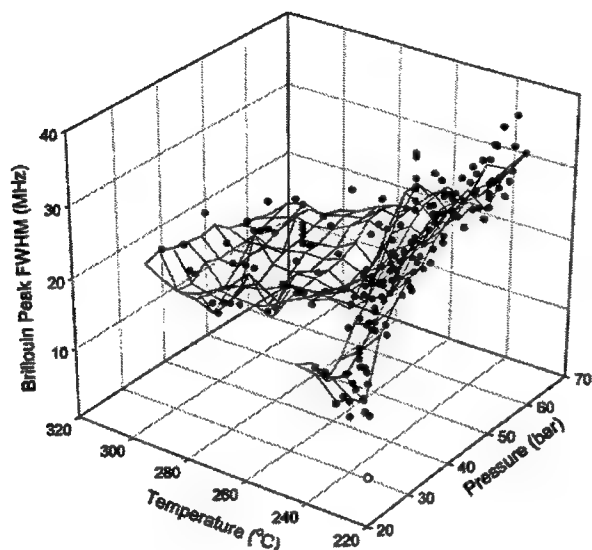


Figure 2. 3-D plot of stimulated Brillouin scattering widths.

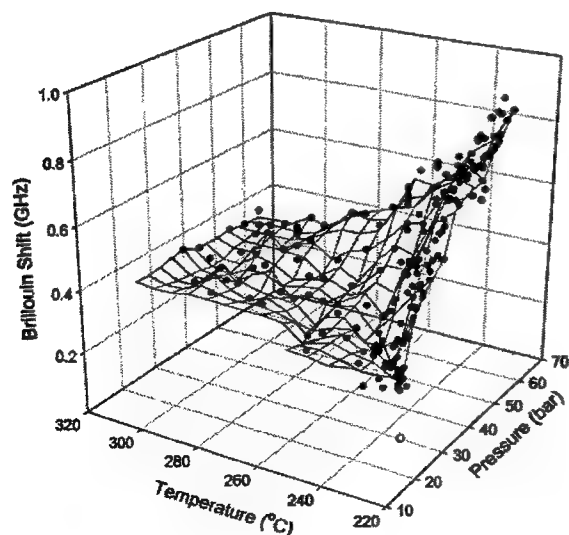


Figure 3. 3-D plot of stimulated Brillouin scattering shifts.

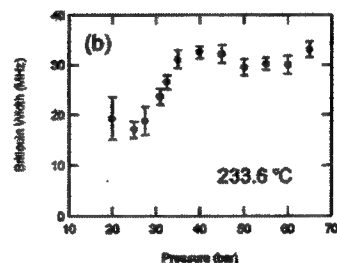
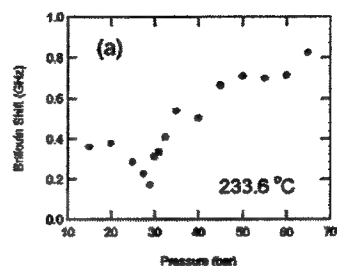


Figure 4. Effect of pressure on Brillouin scattering properties.

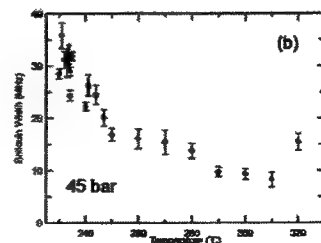
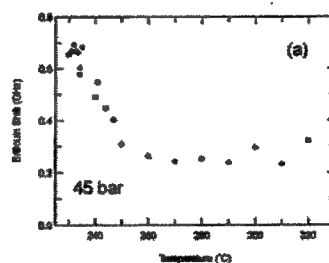


Figure 5. Effect of pressure on Brillouin Scattering properties.

Figures 2 and 3 present three-dimensional views of the Brillouin Doppler shifts and the Brillouin peak widths observed for n-hexane at 1064 nm in a wide range of temperature and pressure conditions. In both graphs, an open circle on the plane of the temperature-pressure coordinate system indicates the location of the critical point for n-hexane. The solid points correspond to the extracted values from our fits to the data. In both graphs, the scatter of the data points is representative of the experimental uncertainties. The uncertainty of the fit (one standard deviation) is typically 1% and 5% for the Brillouin Doppler shift and Brillouin peak width. However, repeated measurements at the same conditions show reproducibility to within approximately 10% and 20% for the Brillouin shift and width, respectively. The main source of experimental errors is the (unavoidable) existence of temperature and pressure fluctuations of the fluid under study. Our experiments for conditions ranging from ambient temperature and pressure to the supercritical state have clearly shown that these fluctuations become dramatically larger as the system approaches the critical point. The mesh surfaces shown in Figs. 2 and 3 have been created by numerical interpolation through the experimental points using commercially available software (Sigmaplot by SPSS Inc.). They are presented as a visual aid to the identification of trends in the experimental data. In both Figs. 2 and 3, the magnitude of the Brillouin shift and width exhibits a minimum in the region of the critical point. This observation is consistent with extreme values of the speed of sound and the acoustic damping rate attained near or at the critical point. We note that although our improved apparatus is successful in recording reliable spectra very close to the critical point, a limit exists within approximately a couple of bar and degrees °C, where critical opalescence and fluid fluctuations make measurements difficult. Consequently, the magnitude of the Brillouin shift and width could reach smaller values and even zero at the critical point.

Figures 4 and 5 show two-dimensional cross sections through the graphs of Figs. 2 and 3 that present a more clear view of the behavior of the Brillouin Doppler shift and Brillouin peak width as a function of temperature and pressure. The error bars shown for the Brillouin width correspond to one standard deviation, as extracted from the fits to the data. In the case of the Brillouin Doppler shift the error bars from the fit to the data are comparable to the size of the point markers.

Comparison of the widths, shifts, and heights of the electrostrictive Brillouin, thermal Brillouin, and thermal Rayleigh peaks with theory has showed consistency of the theory through the relationships between the heights and widths of the thermal Brillouin and thermal Rayleigh peaks. A remarkable feature in the Brillouin and Rayleigh measurements is the discontinuity in the observed properties that occurs near the critical point, as shown in the figures presented above.

## References

1. G. W. Faris, M. Gerken, C. Jirauschek, D. Hogan, and Y. Chen, "High-spectral-resolution stimulated Rayleigh-Brillouin scattering at 1  $\mu\text{m}$ ," *Opt. Lett.* 26, 1894-1896 (2001).
2. C. Jirauschek, E. M. Jeffrey, and G. W. Faris, "Electrostrictive and thermal stimulated Rayleigh spectroscopy in liquids," *Phys. Rev. Lett.* 87, 233902 (2001).



## PLASMA RESEARCH FOR AEROSPACE PROPULSION

LRIR Number -2308PBW/TH13

Principal Investigator: Biswa N. Ganguly

Air Force Research Laboratory, WPAFB OH

### SUMMARY/OVERVIEW:

Optical and electrical measurements performed in a short pulsed DC discharge of methane, argon and nitrogen mixtures are presented. Time-resolved voltage and current measurements reveal a rapid overvoltage breakdown followed by nearly steady-state operation at a relatively high reduced-electric-field strength for 50-100 Torr.cm discharge. Plasma emission measurements of  $H_\alpha$  Doppler width, CH A-X, and B-X, (0, 0) and vibrational overtone reveal the kinetic behavior of key dissociation fragments of  $CH_4$ .

### TECHNICAL DISCUSSION

Atomic hydrogen, hydrocarbon fragments and their radicals are important species for initiating ignition and sustaining stable flame propagation. Highly nonequilibrium plasma production of energetic reactive hydrocarbon fragments could have application in situations where more conventional means of promoting and sustaining combustion are degraded. One such situation is found in supersonic combustion (scramjet) propulsion systems where the flow speed is so high that mixing and reaction times are limited. Plasma torch ignitors have been widely investigated, and microwave discharges have been studied, both as means of providing reliable scramjet combustion. However, such approaches require multi-kilowatt electrical power inputs and are not easily volume scaleable. Pulsed dc glow discharges with high E/N can efficiently dissociate hydrocarbon with substantially lower power requirements. Here we describe our work to characterize such discharges in the context of possible combustion ignition applications. The experiments are carried out in a cylindrical pyrex chamber using parallel plate electrodes. A fast semiconductor high voltage switch produces the pulsed discharge over a range (10-800 Hz) of repetition rates. By adjusting the switch, discharges with continuously variable pulse durations ranging from 150 to 800 ns are produced. Measurements have been performed on mixtures of argon, nitrogen and methane at operating pressures of 30-100 Torr. A plot of E/N for argon/methane mixtures at 100 Torr is shown in figure 1. With increasing applied voltage, and power, emission from  $H^*$  and  $CH^*$  methane fragments increases linearly. Emission from  $CH^*$ ,  $C_2^*$  and  $CN^*$  also indicates high vibrational excitation. In the case of  $CH^*$  the vibrational distribution is non-thermal. In Figure 2, the (2, 2) hot band is clearly seen though the (1, 1) band remains buried by the (0, 0) band. Spectral simulation suggests a rotational temperature of 1200 K for this spectrum acquired near the cathode at 100 Torr. Kinetically hot H

atoms are also found near the cathode surface. The  $H_{\alpha}$  emission spectrum exhibits a distribution characterized by contributions from both cold and hot atoms. Figure 3 shows an acquired spectrum along with a simulation that consists of the following kinetic energy breakdown: 48% with 0.036 eV (thermal), 30% with 6.5 eV and 22% with 39 eV. These results are consistent with the dissociative excitation of H from the repulsive excited states of  $CH_4$  [1]. Using the technique of actinometry, an estimate of H-atom production during a discharge pulse can be made by comparing the  $H_{\alpha}$  emission from the methane discharge (Figure 4) to that from the very well characterized pure  $H_2$  discharge [2,3] under the same experimental conditions. Gap voltage, discharge power, and the resulting  $H_{\alpha}$  emissions from both pure hydrogen and methane discharges at 50 Torr using 6 kV pulser drive voltage were measured. The temporal behavior of the gap voltage and discharge power are very similar to the analogous case for discharges into methane, although both fall more rapidly in the hydrogen plasma during the later portion of the discharge pulse. The likely cause of the minor difference in temporal behavior is that the methane plasmas are slightly electron attaching whereas negative ion formation is absent in the hydrogen plasmas. The  $H_{\alpha}$  emission from the pure hydrogen discharge, shown in Figure 4, follows the discharge power pulse, identical to the temporal behavior of the  $H_{\alpha}$  emission from methane (lower plot in figure 4). The expression used to estimate H atom production in the  $CH_4$  discharges of interest can be written as,

$$[H]_{CH_4} \approx \frac{I_{H_{\alpha}}^{CH_4}}{I_{H_{\alpha}}^{H_2}} \frac{P_{H_2}}{P_{CH_4}} \frac{\sum_j A_{3j} + k_Q^{CH_4} [CH_4]}{\sum_j A_{3j} + k_Q^H [H_2]} \frac{2 \int X(E/N) P_{H_2} dt}{D_e V}. \quad (1)$$

where  $I_{H_{\alpha}}^{gas}$  - intensity of  $H_{\alpha}$  emission in a given discharge gas,  $P_{gas}$  - discharge power deposited into a given gas,  $A_{32}$ ,  $A_{3j}$  - Einstein coefficient for spontaneous emission for the indicated transition,  $k_Q^{gas}$  - quenching coefficient for  $H(n=3)$  atoms in a given gas,  $[H_2]$  - concentration of molecular hydrogen,  $[CH_4]$  - concentration of methane,  $X(E/N)$  - fraction of discharge power deposited into dissociation as a function of  $E/N$ ,  $D_e$  - energy required for dissociation, and  $V$  - discharge volume.

In this relation, the relevant quenching rate constants for  $H(n=3)$  atoms are  $2 \times 10^{-9} \text{ cm}^3/\text{s}$  in  $H_2$  and  $3.5 \times 10^{-9} \text{ cm}^3/\text{s}$  in  $CH_4$ , and the measured  $H_{\alpha}$  intensity profiles needed as inputs are shown in Figures 4. Using Equation (1), the H-atom production during a single discharge pulse into methane, under the same experimental conditions, is shown in the lower plot of the same Figure 4. For comparison purposes, the discharge pulse power and the associated  $H_{\alpha}$  emission are also shown in that plot. Note that the production rate is significantly higher during the brief high  $E/N$  early peak in the discharge power pulse which is typical in such fast pulsed overvolted discharges. Production of on the order of  $5 \times 10^{14}$  H atoms per cubic centimeter of discharge volume during a 400 ns discharge pulse is significant. The results are quite encouraging from the viewpoint of application to scramjet ignition and combustion augmentation. Verification of this actinometric estimate will require much more elaborate one and two-photon allowed laser induced fluorescence and/or mass spectrometric measurements.

#### References:

1. R.K. Janev and D. Reiter, Phys. Plasmas **9**, 4071 (2002).

2. R. Nagpal, B.N. Ganguly, P. Bletzinger and A. Garscadden, Chem. Phys. Lett. **257**, 386 (1996).
3. D. Pagnon, J. Amorim, J. Nahorny, M. Touzeau and M. Vialle, J. Phys. D. **28**, 1856 (1995).

### Figures

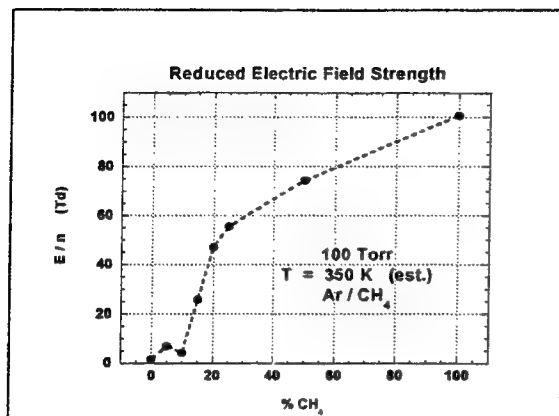


Figure 1. Reduced-electric-field strength as a function of methane mixture at fixed pressure and applied voltage

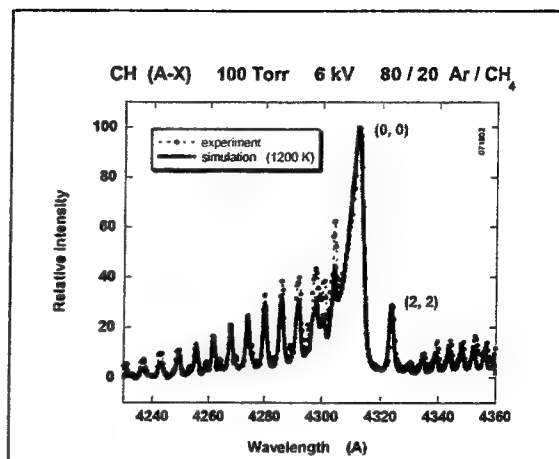


Figure 2. CH\* emission near the cathode. The (2,2) hot band is clearly seen in the spectra

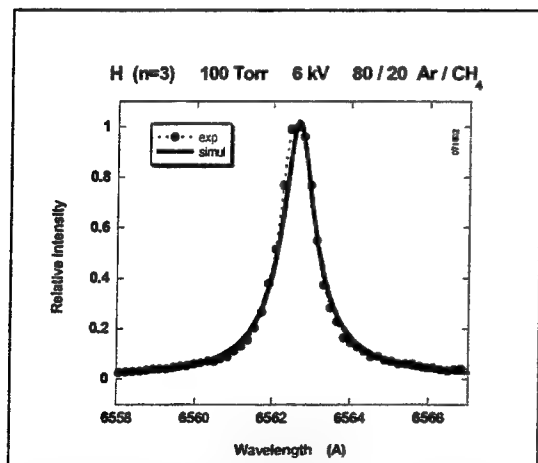


Figure 3. H\* emission (Balmer alpha) acquired near the cathode.

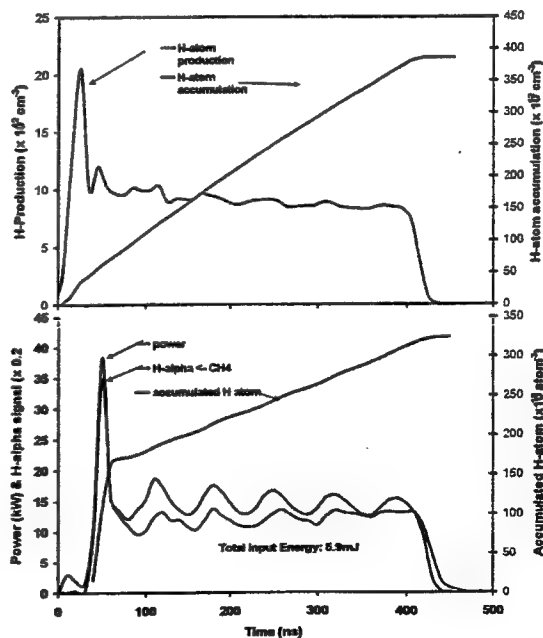


Figure 4. Actinometric measurement of H atom production in CH<sub>4</sub> high E/N discharge.



# SUB- AND SUPER-CRITICAL EVAPORATION AND COMBUSTION OF A MOVING DROPLET

DAAD 19-99-1-0116

Principal Investigator: George Gogos

University of Nebraska-Lincoln  
303 Canfield Administration Bldg  
Lincoln, NE 68588-2618

**SUMMARY:** We are conducting a comprehensive computational study of fuel droplet evaporation and combustion in sub- and super-critical ambient conditions under forced convection. An experimentally validated model for a moving spherical droplet that undergoes combustion has been developed. Transient numerical results were obtained for both suspended droplets (constant relative velocity) and for moving droplets. It is shown that the flame configurations present in a burning droplet are a function of the time histories of both the Reynolds number and the Damköhler number. With respect to high pressure and high temperature droplet vaporization, we have attempted to include deformation of a moving droplet. Our previous axisymmetric code (in spherical coordinates) cannot conveniently handle droplet deformation. We developed a new 2-D code in cylindrical coordinates for that purpose. At this point, the new code predicts results in agreement with experimental data (and with our previous code) when we turn off droplet deformation (low Weber numbers).

**TECHNICAL DISCUSSION:** Two major aspects of droplet evaporation/combustion have been studied and are discussed below.

**I. Numerical Simulation of Droplet Combustion Under Forced Convection** (with Dr. Daniel Pope and graduate student Kun Lu).

**Numerical Model:** The problem considered is that of a single-component liquid fuel (n-heptane) droplet undergoing evaporation and combustion in a hot, convective, low pressure, zero-gravity environment of infinite expanse. For a moving droplet, the relative velocity ( $U_\infty$ ) between the droplet and freestream is subject to change due to the influence of the drag force on the droplet. For a suspended droplet, the relative velocity is kept constant.

The governing equations for the gas-phase and the liquid-phase consist of the unsteady, axisymmetric equations of mass, momentum, species (gas-phase only) and energy conservation. Interfacial conservation equations are employed to couple the two phases. Variable properties are used in the gas- and liquid-phase. Multicomponent diffusion in the gas-phase is accounted for by solving the Stefan-Maxwell equations for the species diffusion velocities. A one-step overall reaction is used to model the combustion [1].

The governing equations are discretized using the finite volume and SIMPLEC methods. A colocated grid is adopted. Hyperbolic tangent stretching functions are used to concentrate grid points near the fore and aft lines of symmetry and at the droplet surface in both the gas- and liquid-phase. The discretization equations are solved using the ADI method with the TDMA used

on each line of the two alternating directions. Iterations are performed within each time-step until convergence is achieved. The grid spacing, size of the computational domain and time-step were tested to ensure that all solutions are independent of these parameters. A detailed discussion of the numerical model is given in [2,3].

**Results and Discussion:** The numerical model was used to investigate the combustion of a n-heptane droplet with an initial diameter ( $d_0$ ) of  $500 \mu m$ . Two cases were studied: a) a moving droplet, and b) a suspended droplet within a convective environment. The results presented here are for an ambient temperature ( $T_\infty$ ) of  $1000 K$ , an ambient pressure ( $P_\infty$ ) of  $1 atm$ , an initial droplet temperature ( $T_0$ ) of  $297 K$  and initial Reynolds numbers ( $Re_0$ ) of 8, 10 and 50.

Table 1 compares the lifetimes of both moving and suspended n-heptane droplets for the Reynolds numbers considered. The table contains interesting results that need to be explained. For example, the lifetime of a moving droplet with  $Re_0 = 50$  is longer than the lifetimes of moving droplets with initial Reynolds numbers of 8 and 10. Furthermore, for the same initial Reynolds number, the suspended droplet burns out faster than its moving droplet counterpart in two cases ( $Re_0 = 8, 50$ ), while for  $Re_0 = 10$ , the result is opposite. In the remainder of this section, the results presented in Table 1 will be discussed in more detail.

Figure 1 shows the time history of the dimensionless droplet diameter squared ( $d/d_0$ )<sup>2</sup>, Reynolds number, Damköhler number and evaporation constant ( $K$ ) for a suspended and a moving droplet with  $Re_0 = 8$ . The suspended and moving droplet developed envelope flames at approximately the same time ( $t = 30 ms$ ). Considering the droplet lifetimes (231 and 240 ms), this happened at a very early stage. Once the envelope flame formed, it remained for both droplets until the end of their lifetimes. Thus during most of the droplet lifetime, both the suspended and the moving droplet experience the same flame configuration. This implies that the two droplets will exhibit similar burning behavior and thus similar lifetimes. Figure 1(a) shows that to be true. The droplets in both cases have very similar diameter squared time histories.

$P_\infty = 1 atm$ $T_\infty = 1000 K$ $T_0 = 297 K$ $d_0 = 0.5 mm$	$Re_0 = 8$	Suspended	$t_d = 231 ms$
		Moving	$t_d = 240 ms$
	$Re_0 = 10$	Suspended	$t_d = 335 ms$
		Moving	$t_d = 243 ms$
	$Re_0 = 50$	Suspended	$t_d = 250 ms$
		Moving	$t_d = 316 ms$

**Table 1: n-heptane droplet lifetimes for suspended and moving droplets.**

Figure 1(b) shows the time history of the instantaneous Reynolds number ( $Re$ ) for both cases. Both Reynolds numbers decrease monotonically with time however, they decrease at different rates. The Reynolds number is defined as  $Re = d(t)U_\infty(t)/\nu_\infty$ , where  $d(t)$  and  $U_\infty(t)$  are the instantaneous droplet diameter and freestream velocity. The freestream velocity remains constant for the suspended droplet. As a result, the Reynolds number changes only with the droplet diameter. However, for the moving droplet, the droplet diameter decreases, and the droplet velocity decreases due to drag. Thus the Reynolds number for the moving droplet decreases faster than that for the suspended droplet.

The higher Reynolds number associated with the suspended droplet implies a stronger convection. This results in a higher evaporation constant for the suspended droplet than for the moving droplet as shown in Figure 1(d). At the beginning of the droplet lifetime, the evaporation constants for the two cases are very close and both increase rapidly due to the high temperature environment. A difference between the evaporation constants appears at about one tenth of the lifetime due to the difference in the convective strength for the two cases. At the

relatively low initial Reynolds number of 8, the difference in the evaporation constants between the suspended droplet and the moving droplet remains small during the entire droplet lifetime. As a result, the droplet lifetimes for the two cases are very close.

Figure 1(c) compares the instantaneous Damköhler numbers for the two cases. Here, Damköhler number is defined as:

$$Da = \frac{R(t)}{U_{\infty}(t)} A \rho_{\infty}^{a+b-1} W_f^{1-a} \left( \frac{1}{W_o} \right)^b \exp \left( - \frac{E_a}{R_u T_{\infty}} \right)$$

where  $R(t)$  is the droplet radius,  $W_o$  and  $W_f$  are molecular weights for the fuel and oxygen, and  $a$ ,  $b$ ,  $A$ , and  $E_a$  are constants. The Damköhler number is proportional to the ratio of droplet diameter to instantaneous freestream velocity. This ratio is the characteristic convective time-scale. Thus,  $Da$  is proportional to  $d(t)/U_{\infty}(t) = t_{conv}$ . Figure 1(c) shows that the Damköhler number for the suspended droplet decreases with time, while for the moving droplet case it increases slowly with time. The former result is expected since for the suspended case,  $U_{\infty}$  is constant while the droplet diameter decreases. This results in a monotonic decrease in  $Da$ . For the moving droplet case, both  $d(t)$  and  $U_{\infty}(t)$  decrease. The resulting trend in Damköhler number is not obvious. For  $Re_0 = 8$ , it seems that the droplet velocity decreases slightly faster than the droplet diameter.

For  $Re_0 = 50$ , both droplets ignite in the wake areas far downstream. After ignition, for the moving droplet case, the flame moves toward the droplet slowly, and finally forms an envelope flame (at approximately  $t = 270$  ms) near the end of its lifetime. For the suspended droplet, no envelope flame is developed throughout its lifetime, and the wake flame remains at approximately the same location for most of the droplet's lifetime. At  $t = 237$  ms the wake flame trailing the suspended droplet extinguishes. Thus, a pure evaporation process dominates in both cases. In the absence of envelope flames, the difference in Reynolds number histories between the two cases ( $Re$  is smaller for the moving droplet due to its deceleration) is the only cause for their different lifetimes shown in Table 1.

The combustion behavior for the two cases at  $Re_0 = 10$  is quite different from the cases discussed above. Although the Reynolds number for the suspended droplet is again higher than that for the moving droplet throughout the droplet lifetime, the lifetime of the suspended droplet is approximately 40% longer than that of the moving droplet. The big difference in droplet lifetimes, is caused by the difference in flame configurations. The moving droplet develops an envelope flame at an early stage ( $t = 40$  ms) of its lifetime. In contrast, the suspended droplet exhibits a transition flame (the flame partially surrounds the droplet) during most of the droplet lifetime. As a result, the front of the droplet is exposed to the ambient temperature, leading to a longer lifetime for the suspended droplet.

The trend in Damköhler number for  $Re_0 = 50$  and  $Re_0 = 10$  is the same as for  $Re_0 = 8$ , namely  $Da$  increases for the moving droplet and decreases for the suspended droplet. The flame configurations present in a burning droplet are a function not only of the Reynolds number, but of the Damköhler number as well. This is discussed more extensively in [4]. The results presented above for the three different Reynolds numbers seem to suggest that a moving droplet tends to develop an envelope flame at some stage during its lifetime, whereas a suspended droplet develops an envelope flame only at low initial Reynolds numbers.

**II. Evaporation of a Deformable Fuel Droplet under a Forced Convective Environment** (with Dr. Hongtao Zhang and graduate student Yuan Shi). Over this past year we developed a 2-D code in cylindrical coordinates to be able to handle droplet deformation.

A non-orthogonal, algebraically generated grid system was chosen. This choice was motivated by computational economy because it simplified the task of repeated grid regeneration

dictated by the constantly changing free surface shape. The non-orthogonal coordinates are defined with the  $\eta$ -coordinate direction following the radial lines and the  $\xi$ -coordinate direction following the 'tangential' lines. In the liquid phase, all lines radiated from a common origin at the midpoint of the original spherical droplet, and terminated at points distributed around the liquid/gas interface. In the gas phase the radial lines emerged from the same points that defined the termini of the liquid-grid radial lines at the liquid/gas interface, and extended to predetermined points along a fixed outer boundary.

The gas and liquid phase solutions are obtained by solving the unsteady equations of mass, species, momentum, and energy conservation in cylindrical coordinates, using a colocated grid. These equations are coupled via the conservation equations at the interface and are solved iteratively. Variable properties in the gas and liquid phase are calculated using appropriate high pressure correlations. The effect of gravity is neglected. The finite-volume and SIMPLEC methods are used to discretize the governing equations in the computational domain. Real gas effects are modeled using the Peng-Robinson equation of state.

At this point, the new code predicts results in agreement with experimental data (and with our previous code) when we "turn off" droplet deformation (low Weber numbers). Further debugging is needed to be able to handle droplet deformation which becomes important at higher Weber numbers.

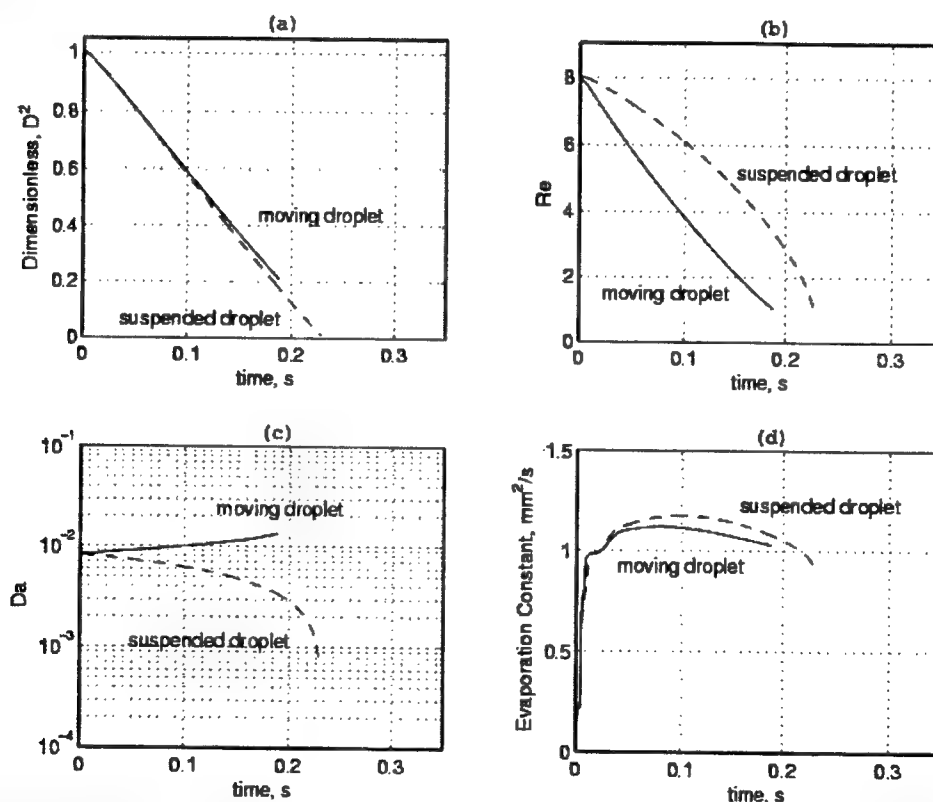


**Figure 1: Comparison between moving droplet and suspended droplet combustion for  $Re_0 = 8$  ( $d_0 = 500 \mu m$  and  $T_\infty = 1000 K$ ).**

## References

1. Westbrook, C. K. and Dryer, F. L., *Comb. Sci. and Tech.*, 27:31 (1981).
2. Lu, K., *M.S. thesis*, Mechanical Engineering, University of Nebraska-Lincoln, 2002.
3. Pope, D. N., *Ph.D. thesis*, Mechanical Engineering, University of Nebraska-Lincoln, 2001.
4. Pope, D. N., Lu, K. and Gogos, G., *Proceedings of the Third Joint Meeting of the U.S. Sections of The Combustion Institute*, Chicago, Ill., 2003.



# **SHOCK TUBE MEASUREMENTS OF IGNITION PROCESSES IN DIESEL-RELATED FUELS**

ARO Contract No. DAAD19-01-1-0597

Principal Investigator: Ronald K. Hanson

Mechanical Engineering Department  
Stanford University, Stanford CA 94305-3032

## **SUMMARY/OVERVIEW:**

We report results from the second year of a three-year program of basic research aimed at improving knowledge of the combustion kinetics behavior of diesel-related fuels. The work is intended to support efforts underway in other laboratories to improve diesel engine performance. Research is being conducted in two Stanford shock tube facilities and focuses on two topics: (1) measurements of shock-induced ignition time and individual species concentration time-histories during the combustion of diesel-related gas-phase fuels, and (2) fundamental studies of fuel sprays in a new aerosol shock tube using state-of-the-art optical diagnostic techniques.

## **TECHNICAL DISCUSSION:**

### **Ignition Time and Species Concentration Time-History Measurements**

Validation of hydrocarbon oxidation reaction mechanisms and development of new and improved reduced mechanisms require a reliable database of experimental combustion targets; such data are often drawn from experiments in shock tubes, flames or flow tube reactors. Though a limited amount of shock tube ignition time data presently exists for some fuels, these data exhibit substantial scatter and are of varying reliability. By contrast, data for stable species in flames or bench-top reactors have often been used to tune reaction mechanisms, but little or no data is available on transient radical species, such as OH or CH<sub>3</sub>, that play an important role in ignition processes. To help remedy these deficiencies, we are currently working to establish a new database of ignition time and radical species concentration time-history measurements to be acquired in shock tube studies of the major components of practical fuels and for surrogate fuel mixtures. This database will include studies of fuel components including n-alkanes, branched alkanes, alkenes, aromatics, and diesel surrogate mixtures.

We have measured ignition times and hydroxyl (OH) radical concentration time-histories behind reflected shock waves during the oxidation of three branched alkanes: iso-butane (2-methylpropane), iso-pentane (2-methylbutane), and iso-octane (2,2,4-trimethylpentane) over initial reflected shock conditions of 1177 to 2009 K, 1.10 to 12.58 atm, fuel mole fractions of 100 ppm to 1.25% and equivalence ratios of 0.25 to 2. Ignition times were measured using endwall CH emission, and OH concentrations were measured using narrow-linewidth ring-dye laser absorption of the R<sub>1</sub>(5) line of the OH A-X (0,0) band at 306.7 nm. These data provide a

unique database for the validation of detailed hydrocarbon oxidation mechanisms and hence contribute to improved understanding of propulsion fuels. See Figs. 1 and 2.

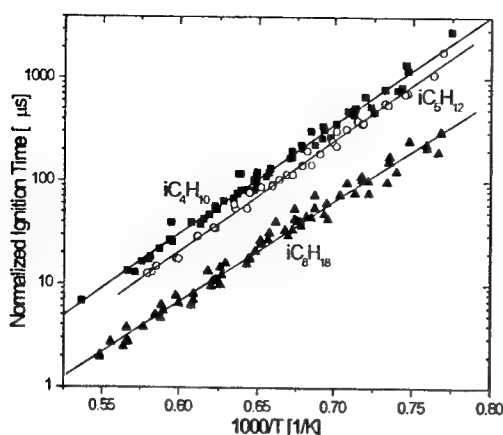


Figure 1. Correlated branched-alkane ignition times. All data normalized to 1 atm,  $\Phi = 1$ , and 21%  $O_2$ . Filled squares, iso-butane; open circles, iso-pentane; filled triangles, iso-octane; lines, correlations.

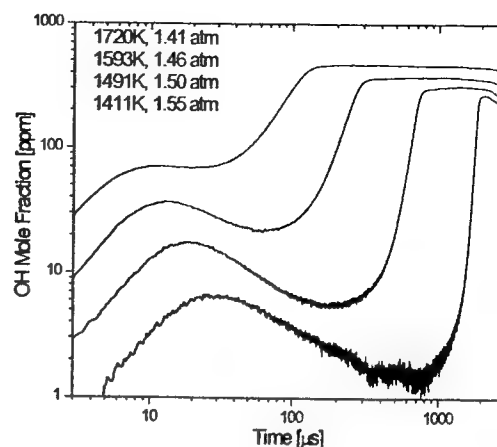


Figure 2. Iso-butane OH absorption data. Initial conditions: 0.1% iso-butane, 0.65%  $O_2$ . Upper trace 1720 K, lower trace 1411 K. Strong suppression of OH radical populations during the induction period before ignition is evident in the 1411 to 1593 K data.

The structure of the OH concentration time history data is similar for the three branched alkane fuels. After shock heating, fuel decomposition liberates H-atoms that react with  $O_2$  to form OH; shortly thereafter, the OH concentration decreases to an intermediate minimum before ignition, signaled by a rapid rise in the OH concentration. The structure of the OH concentration history during branched alkane oxidation is in contrast to previous work from our laboratory on n-alkane oxidation [Davidson et al. 2001]. During n-alkane oxidation the OH rises to a plateau prior to ignition rather than declining to a minimum. The strong suppression of OH during branched alkane oxidation, particularly at the lowest temperatures of this study, is one reason why branched alkanes inhibit knock in engine applications. Example OH concentration data are shown in Fig. 2 for iso-butane.

With the availability of OH concentration time-history data, comparisons of the measurements and models of the radical pool during ignition events can now be investigated. We performed sensitivity and contribution analysis for several published oxidation mechanisms for iso-butane, iso-pentane and iso-octane. Of particular note in this analysis is that the entire OH concentration time history shows very strong sensitivity to reaction (1)  $H + O_2 \rightarrow OH + O$ . Confidence in this rate coefficient has improved over the years, and recently Yu et al. (1994) put an uncertainty of only 9% on this rate over the temperature range 1336-3370 K. Despite the extensive efforts made to refine this rate, many current mechanisms still use the older rate coefficient recommended by Baulch et al. (1992); this rate varies by up to 30% over portions of the temperature range from the Yu et al. recommendation. Recent transition state calculations by Miller and Garrett (1997) also support the Yu et al. value for  $k_1$ . Simply changing  $k_1$  in these mechanisms to the Yu et al. value provides an improvement in terms of modeling our data. However, it is clear that other adjustments in the detailed model are needed to bring the model results into full agreement with our data.

## Shock Tube Studies of Fuel Sprays

Liquid fuels predominate in mobile energy-conversion systems such as gas turbines and internal combustion engines. Previous researchers have studied combustible sprays in shock tubes to learn about droplet breakup, evaporation, and ignition times, but these studies generally have applied commercial injectors that have wide droplet size distributions. Since the combustion of a two-phase mixture is strongly dependent on droplet heating and evaporation rates, the results have largely been qualitative in nature, obscured by details of the droplet size and spatial distribution, or have been quantitative only in specific situations. Our objective is to establish a facility that will permit the study of the interaction of shock waves and two-phase mixtures. These two-phase mixtures will be spatially uniform and will have a very narrow (nearly monodisperse) size distribution so that droplets of a specific size class can be studied independently. The interaction zone where the shock waves encounter the two-phase mixture will have wide optical access.

Work has been completed on the aerosol shock tube. We have modified an existing shock tube facility by adding a test section with a square cross-section (following a round-to-square transition section) and large flat windows to accommodate laser-sheet visualization and diode laser (absorption and extinction) diagnostics. Numerous pressure port locations are available for shock and detonation speed determination in the test section. Uniform spatial distributions of the aerosol in the initial gas mixture are introduced into the test section through large flush-mounted (when closed) valves in the end wall.

Mono-dispersed aerosols in the diameter range 0.5 - 10  $\mu\text{m}$  are produced for the shock tube using ultrasonic atomization. Droplet size measurements of the nebulizer spray have been obtained via a laser diffractometer and two-wavelength Mie laser scattering. Example droplet size distributions for several fluids are shown in Fig. 3. Narrow size distributions have been successfully generated in a variety of alkane fuels and water. Note that these distributions are substantially narrower than those obtained with a pressure-swirl atomizer.

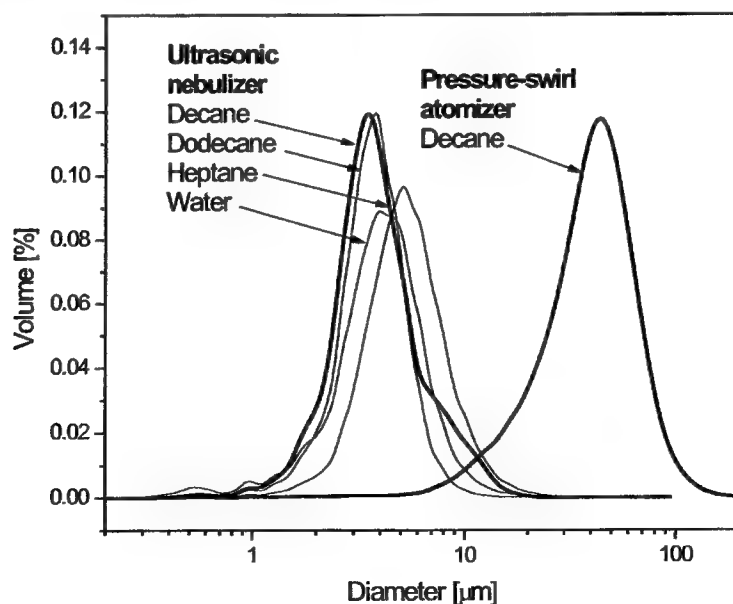


Figure 3. Comparison of volume pdf size distributions for decane, dodecane, heptane and water sprays produced by a ultrasonic nebulizer and a single fluid pressure-swirl atomizer.

The facility is nearing complete operation. Tests are underway to finalize the details of the aerosol injection system, e.g. to measure the spatial uniformity of the aerosol mixture in the tube, measure the aerosol settling time, and to adjust the inlet and exhaust valve timing to optimize the uniformity of the test mixture. The optical diagnostics, based on multi-wavelength extinction, are being transferred onto the shock tube. Initial tests are expected shortly.

### **Future Plans**

Future work in the development of the ignition time - species concentration database will include measurements of alkenes, aromatics, cyclo-alkanes, and double-bonded fuel decomposition intermediaries including 1,3-butadiene. Measurements of addition species, such as  $\text{CH}_3$ , will also be considered.

Future work with the aerosol shock tube will concentrate on shock tube measurements of the aerosol/shock wave interactions. These measurements will utilize laser sensors (developed under AFOSR and ONR sponsorship) to characterize fuel loading, aerosol time history, fuel vapor concentration and temperature, and ignition processes. Measurements of line-of-sight-averaged fuel droplet size, droplet volume fraction, and fuel vapor concentration with rapid time response using a sensor based on wavelength-multiplexing of five laser beams are planned. (This sensor will use three laser beams to measure droplet size (Sauter Mean Diameter) based on transmission measurements; and two beams to monitor vapor concentration based on differential absorption.)

### **CURRENT ARO-SPONSORED PUBLICATIONS:**

M. A. Oehlschlaeger, D. F. Davidson, J. T. Herbon, and R. K. Hanson, "*Shock Tube Measurements of Branched Alkane Ignition Times and OH Concentration Time Histories*," AIAA Paper 2003-0830, 41<sup>st</sup> AIAA Aerospace Sciences Meeting, Reno, January (2003).

D. F. Davidson, M. A. Oehlschlaeger, J. T. Herbon, and R. K. Hanson, "*Shock Tube Measurements of Iso-Octane Ignition Times and OH Concentration Time Histories*," Proceedings of the Combustion Institute 29: in press.

Horning D.C., Davidson D.F., and Hanson R.K., "*Study of the High-Temperature Autoignition of n-Alkane/O<sub>2</sub>/Ar Mixtures*," Journal of Propulsion and Power 18: 363-371 (2002).

# ADVANCED DIAGNOSTICS FOR REACTING FLOWS

AFOSR Contract No. 01-1-0145  
Principal Investigator: Ronald K. Hanson

Mechanical Engineering Department  
Stanford University, Stanford, California 94305-3032

## SUMMARY/OVERVIEW:

The goal of this research is to develop advanced laser-based diagnostics for non-intrusive measurements relevant to air-breathing combustion. The program emphasizes spectrally-resolved absorption using cw tunable IR lasers and planar laser-induced fluorescence (PLIF) using pulsed IR and UV laser sources. Detailed below is progress on several diagnostic concepts: ketone tracers for PLIF imaging; LIF at high pressure; IR PLIF for imaging IR-active gases; and wavelength-multiplexed strategies for fuel sensing. Also reported are high-temperature LIF measurements of  $\text{CO}_2$ , which have significant implications for UV-based combustion diagnostics.

## TECHNICAL DISCUSSION:

### Fuel Tracer Photophysics for Quantitative PLIF Diagnostics

Research on fuel tracers concentrates on experiments to elucidate the fundamental photophysical data needed to quantify absorption and fluorescence as a function of temperature, pressure, bath gas, and excitation wavelength. Past success in understanding the effects of these parameters on acetone has led to the development of PLIF techniques that instantaneously (and non-intrusively) measure temperature and acetone concentration in two dimensions under a variety of conditions (up to 1000 K and 16 bar). We have recently begun quantitative PLIF measurements of more realistic fuels and fuel surrogates. For example, our database now includes the absorption and fluorescence properties of 3-pentanone, (a slightly heavier ketone than acetone, more suited for tracking heavier hydrocarbons). In addition to its attractive physical properties, we have determined that 3-pentanone yields more signal per molecule than acetone and exhibits better temperature sensitivity under some conditions.

The data from our experiments along with data in the literature have been employed to build a semi-empirical, photophysical model to explain and predict a tracer's fluorescence behavior with changing temperature, pressure, and excitation wavelength. This endeavor has met with

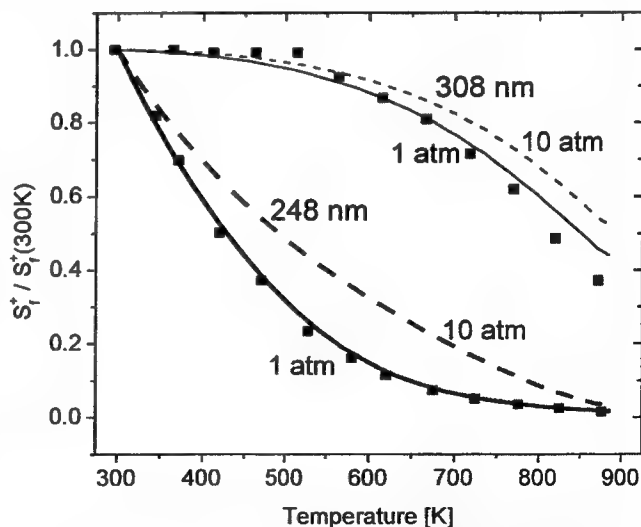


**Figure 1.** Modeled 3-pentanone fluorescence behavior (at constant mole-fraction, in nitrogen) as a function of temperature for 248 and 308 nm excitation at 1 and 10 atmospheres.

some success using both acetone and 3-pentanone. The usefulness of such a model is exemplified in Fig. 1. Smooth lines show model prediction of 3-pentanone's fluorescence behavior as a function of temperature for two excitation wavelengths and at two pressures in a nitrogen bath. Measured data is shown as discrete points. Exciting with 248 nm, one can see that temperature dependences may change with pressure; interpreting fluorescence signals at ten atmospheres should be quite different from interpretation at one atmosphere (although this has traditionally not been the case due to a lack of data at simultaneously elevated temperature and pressure). However, the temperature behavior does not change as much when using 308 nm excitation. Thus the model also shows ways by which we might mitigate or eliminate measurement error through the careful selection of excitation strategies in regions beyond where measured data is available.

## 2-D Images of Temperature and NO in Steady, High-Pressure Flames

Ability to understand and apply LIF of NO provides an effective diagnostics tool to measure instantaneous temperature fields as well as imaging of quantitative NO itself. However, high-pressure environments pose unique challenges to spectroscopic techniques as spectral features become collision-broadened and spectral interference from other species increases. In the past year we have expanded investigation of excitation strategies of NO LIF to include both the A-X (0,0) and A-X (0,1) transitions, where factors such as interference from O<sub>2</sub> LIF, signal intensity and temperature sensitivity have been quantitatively evaluated for stoichiometries between 0.83 and 1.2 and pressures up to 60 bar. Further extension of this study has lead to the development of a new multi-line temperature measurement strategy as well as quantitative imaging of NO. Shown in Fig. 2 are some of the temperature and quantitative NO measurements from this study. Among many correction parameters implemented in imaging of NO, a surprisingly large correction (~35%) resulted from the absorption of broadband UV from high temperature CO<sub>2</sub> across a 8mm flame. In the process of conducting this research, a highly accurate spectroscopic database for high-pressure NO has been developed.

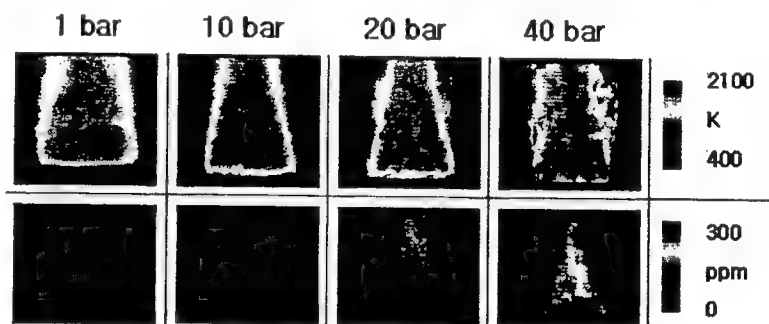


**Figure 2.** temperature fields (upper) and quantitative NO concentrations (lower) from a premixed methane/air flame using PLIF imaging of NO. 1000+ shots averaged in steady flame.

## IR PLIF using Vibrational Transitions

Many species important for combustion (CO, CO<sub>2</sub>, CH<sub>4</sub>, C<sub>2</sub>H<sub>4</sub>, and higher hydrocarbons) only have allowed, single-photon, electronic transitions in the vacuum ultraviolet, and thus do not permit visible or near-UV LIF diagnostics. However, infrared PLIF is possible using vibrational transitions if the molecule has an IR active mode. IR PLIF differs from traditional UV/Vis PLIF because excited vibrational levels have much longer radiative lifetimes than excited electronic systems, and there are often multiple mechanisms for vibrational relaxation. Therefore, detailed knowledge of vibrational energy transfer rates and processes is necessary for modeling of IR PLIF schemes and the quantitative interpretation of data. Building on our past success for CO and CO<sub>2</sub> IR PLIF schemes, we have begun IR PLIF of simple hydrocarbon fuels, CH<sub>4</sub> and C<sub>2</sub>H<sub>4</sub>.

## Two-Phase Fuel Diagnostics by Wavelength-Multiplexing

The development of multiphase diagnostics based on wavelength-multiplexed diode laser extinction has progressed to successful demonstration experiments to monitor droplet size and concentration using a three-wavelength extinction scheme and separate experiments to measure low concentrations of various hydrocarbon fuel vapors by differential absorption. Key virtues of our approach are 1) good prospects for near-real-time monitoring (better than 1  $\mu$ s), and 2) extension to multiphase combustion flows of near-IR diode laser absorption sensors for gas concentration. Fig. 3 illustrates vapor sensing in an ethanol spray for different droplet sizes. The differential vapor absorption signal ( $\Delta\tau_{\text{vapor}}$ ) begins to exceed the interference signal from droplets ( $\Delta\tau_{\text{drops}}$ ) after approximately 22% (13%) of the fuel evaporates for an initial droplet size of 4  $\mu$ m (5), even though for the range of wavelengths used, the droplet extinction exceeds vapor absorption over most of the droplet volume fraction range. Clearly the differential absorption technique considerably improves vapor detection sensitivity. The wavelength-multiplexed differential absorption sensor promises to be a powerful tool for near-real-time monitoring of combustion flows where fuel spray mixing, evaporation, and combustion are important.

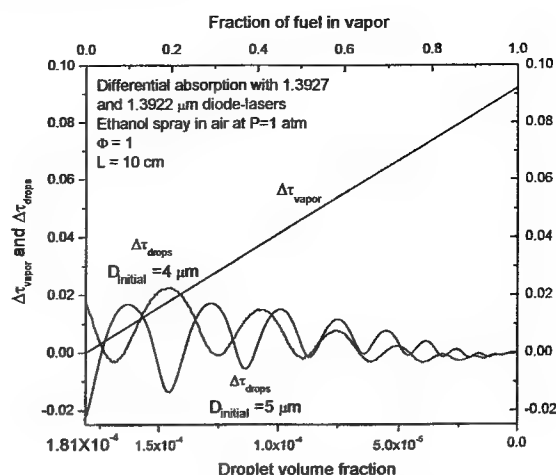


**Figure 3.** Comparison of differential vapor absorption and droplet extinction in ethanol sprays using the differential absorption technique for different initial droplet sizes.

## Development of CO<sub>2</sub> LIF

In the past year, we have learned that CO<sub>2</sub> becomes a strong UV absorber at high temperatures, prompting a search for subsequent LIF emission. We have since found strong evidence that the broadband (200-450nm) continuum emission with a faint superimposed band structure observed in high-pressure NO LIF is from CO<sub>2</sub>. Signal intensity variation with excitation wavelength, equivalence ratio and adiabatic flame temperature correlate well with absorption cross-section data taken with a UV kinetic spectrograph in our shock tube facility. Shown in Fig. 4 is LIF data taken in a CH<sub>4</sub>/O<sub>2</sub>/Ar and H<sub>2</sub>/O<sub>2</sub>/Ar flames; the strong Rayleigh peak and Raman from H<sub>2</sub>O is observed in both flames. The remaining broad-band fluorescence appears to be LIF of CO<sub>2</sub>. Although further characterization is required, initial results suggest promising opportunities for combustion diagnostics via CO<sub>2</sub> LIF.

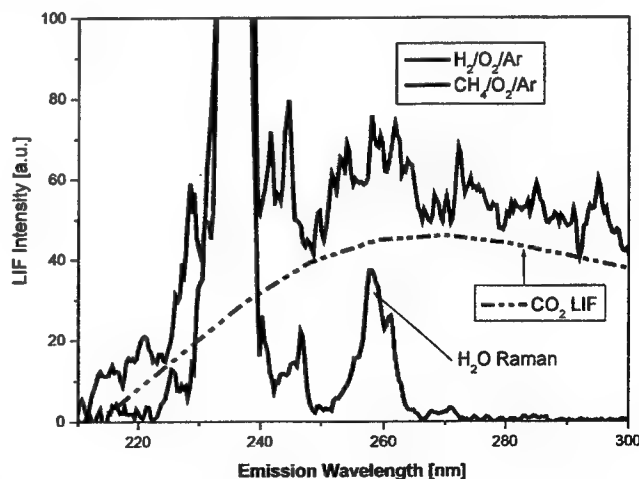


**Figure 4.** Emission spectra with 235.88-nm excitation in CH<sub>4</sub>/O<sub>2</sub>/Ar and H<sub>2</sub>/O<sub>2</sub>/Ar flames. (20 bar,  $\phi = 1.1$ ). The broadband CO<sub>2</sub> emission was extracted from the CH<sub>4</sub>/O<sub>2</sub>/Ar emission using spectral simulation fits of LIF emission components.



#### AFOSR-SPONSORED PUBLICATIONS:

1. J.T.C. Liu, R.K. Hanson, and J.B. Jeffries, "High-Sensitivity Absorption Diagnostic for NO<sub>2</sub> Using a Blue Diode Laser," *J. Quant. Spectros. Rad. Trans.* **72**, 655-664 (2002).
2. B.J. Kirby and R.K. Hanson, "Linear Excitation Schemes for IR PLIF Imaging of CO and CO<sub>2</sub>," *Applied Optics* **41**, 1190-1201 (2002).
3. W. Bessler, C. Schulz, T. Lee, J. B. Jeffries, and Ronald K. Hanson, "Strategies for Laser-Induced Fluorescence Detection of Nitric Oxide in High-Pressure Flames: I. A-X (0,0) Excitation," *Applied Optics* **41**, 3547-3557 (2002).
4. C. Schulz, J.D.Koch, D.F. Davidson, J.B.Jeffries, and R.K. Hanson, "Ultraviolet Absorption Spectra of Shock-Heated Carbon Dioxide and Water between 900 and 3050 K," *Chemical Physics Letters* **355**, 82-88 (2002).
5. W.G. Bessler, C. Schulz, T. Lee, D.-I. Shin, M. Hofmann, J.B. Jeffries, J. Wolfrum, and R.K. Hanson, "Quantitative NO-LIF Imaging in High-pressure Flames," *Applied Physics B* **75**, 97-102 (2002).
6. S. T. Sanders, D.W. Mattison, L. Ma, J.B. Jeffries, and R.K. Hanson, "Wavelength-Agile Diode-Laser Sensing Strategies for Monitoring Gas Properties in Optically Harsh Flows: Application in Cesium-Seeded Pulse Detonation Engine," *Optics Express* **10**, 505-514 (2002).
7. A. Ben-Yakar and R. K. Hanson, "Ultra-Fast-Framing Schlieren System for Studies of the Time Evolution of Jets in Supersonic Crossflows," *Experiments in Fluids* **32**, 652-666 (2003).
8. L. Ma, S.T. Sanders, J.B. Jeffries, and R.K. Hanson, "Monitoring and Control of a Pulse Detonation Engine Using a Diode-Laser Fuel Concentration and Temperature Sensor," *Proceedings of the Combustion Institute* **29**, (2002) in press.
9. C. Schulz, J.B. Jeffries, D.F. Davidson, J.D. Koch, J. Wolfrum, and R.K. Hanson, "Impact of UV Absorption by CO<sub>2</sub> and H<sub>2</sub>O on NO LIF in High-Pressure Combustion Applications," *Proceedings of the Combustion Institute* **29**, (2002) in press.
10. S.T. Sanders, D.W. Mattison, J.B. Jeffries, and R.K. Hanson, "Sensors for High-Pressure, Harsh Combustion Environments using Wavelength-Agile Diode Lasers," *Proceedings of the Combustion Institute* **29**, (2002) in press.
11. W.G. Bessler, C. Schulz, T. Lee, J.B. Jeffries, and R.K. Hanson, "Strategies for Laser-Induced Fluorescence Detection of Nitric Oxide in High-Pressure Flames: II. A-X (0,1) Excitation," *Applied Optics*, (2003) in press.
12. D.W. Mattison, C.M. Brophy, S.T. Sanders, L. Ma, L., K.M. Hinckley, J.B. Jeffries, and R.K. Hanson, "Pulse Detonation Engine Characterization and Control using Tunable Diode-Laser Sensors," *Journal of Propulsion and Power*, (2003) in press.
13. S.T. Sanders, D.W. Mattison, J.B. Jeffries, and R.K. Hanson, "Time-of-Flight Diode Laser Velocimeter using a Locally Seeded Atomic Absorber: Application in a Pulse Detonation Engine," *Journal of Shock Waves*, (2003) in press.
14. J.D. Koch and R.K. Hanson, "Temperature and Excitation Wavelength Dependences of 3-Pentanone Absorption and Fluorescence for PLIF Applications," *Applied Physics B*, (2003) in press.
15. W.G. Bessler, C. Schulz, T. Lee, J.B. Jeffries, and R.K. Hanson, "Strategies for Laser-Induced Fluorescence Detection of Nitric Oxide in High-Pressure Flames: III. Comparison of A-X Detection Schemes," *Applied Optics*, submitted (2003).
16. W.G. Bessler, C. Schulz, T. Lee, J.B. Jeffries, and R.K. Hanson, "Carbon Dioxide UV Laser-Induced Fluorescence in High-Pressure Flames," *Chemical Physics Letters*, submitted (2003).
17. Katharina Kohse-Hoeinghaus and Jay B. Jeffries (editors), *Applied Combustion Diagnostics*, Taylor and Francis, (2002).
18. M.G. Allen, E.R. Furlong, and R.K. Hanson, "Tunable Diode Laser Sensing and Combustion Control," in *Applied Combustion Diagnostics*, ed. K. Kohse-Hoinhaus and J.B. Jeffries, Taylor and Francis, 479-498 (2002).



# PLANAR IMAGE PARTICLE ANALYZER FOR WHOLE FIELD SPRAY APPLICATIONS

SBIR Program (Grant/Contract No.DAAD19-01-C-0011)

Principal Investigators(s): Cecil Hess, PhD and Ryder Nesbitt, SM

MetroLaser, Inc., 2572 White Road, Irvine, CA 92614-6236 ([chess@metrolaserinc.com](mailto:chess@metrolaserinc.com))

## SUMMARY/OVERVIEW

The purpose of this work is to develop a whole field measurement technique that is capable of simultaneously sizing multiple transparent droplets on a plane from scattered light features that are independent of laser beam intensity and obscuration. Last year, we reported on a digital holography technique to measure sprays. This year, we discuss a novel split-image digital photography technique that enables the measurement of larger particle size distributions over a larger field of view.

## TECHNICAL DISCUSSION

Light scattered by reflection and refraction from droplets immersed in a laser sheet is collected and split into two paths, which are simultaneously imaged onto and recorded by a CCD chip. The images recorded by the CCD can be analyzed to obtain data on particle size, location, and velocity within a two-dimensional area. Other related research in this field is based on photographic recordings of interference patterns<sup>1</sup>; holographic and photographic techniques measuring spots and fringes<sup>2</sup>; digital holography<sup>3</sup>; and the use of cylindrical optics to defocus and elongate particle images in one dimension and thus increase particle density measurement capability<sup>4</sup>. The technique reported here simultaneously measures particles from both their glaring spots and from the out-of-focus fringes, which provides a broad particle size measurement range and rapid data processing capability.

### Optical Setup

The system described here is called a Planar Image Particle Analyzer (PIPA). The general optical configuration of PIPA is given in **Figure 1**. In operation, a sheet of laser light illuminates transparent particles; each particle's reflected and refracted glare spots (manifestation of the scattered light) is collected by a doublet lens pair (DLP). The collection angle (between the sheet of laser light and the optical axis of the DLP) is chosen to provide a nearly equal intensity balance between the reflected

---

<sup>1</sup> Glover, A., Skippon, S., and Boyle, R., (1995) "Interferometric Laser Imaging for Droplet Sizing: A Method for Droplet-Size Measurement in Sparse Spray Systems", *Applied Optics*, Vol. 34, No. 36, pp. 8409-8421.

<sup>2</sup> Hess, C.F., (1998) "*Planar Particle Image Analyzer*", presented at 9<sup>th</sup> International Symposium on Application of Laser Techniques to Fluid Mechanics, Lisbon, Portugal, (July 13-16, 1998).

<sup>3</sup> Burke, J., Hess, C.F., and Kebbel, V., "Digital Holography for Whole Field Spray Diagnostics", presented at 11<sup>th</sup> International Symposium on Application of Laser Techniques to Fluid Mechanics, Lisbon, Portugal, (July 8-11, 2002).

<sup>4</sup> Maeda, M., Kawaguchi, T., Hishida, K., (2000) "Novel Interferometric Measurement of Size and Velocity Distributions of Spherical Particles in Fluid Flows", *Meas. Sci. Technol.* 11, L13-L18.

and refracted glare spots, requiring the use of the Scheimpflug angle geometry. A key feature of this setup is the use of a beam splitting cube (BC) to separate the light collected from particles into two optical paths: one for imaging the glare spots as 'spots' and the other for forming fringes from the out-of-focus glare spots. In the example below, the two light paths are imaged onto a single CCD chip. Clearly, multiple CCD chips can also be utilized for this technique.

### Spot Mode Imaging

Referring to **Figure 1**, the light in the 'spot path,' is imaged via the DLP, BC, mirror (M), and a prism (P) onto the camera's CCD chip (CCD). The images of particle glare spots are directed so as to fill one half of the CCD leaving the other half available for the 'fringe path.' **Figure 2**, below, is an image of a water droplet's reflected and refracted glare spots formed by the spot path. In this mode, the images of individual particles are relatively small, and for larger particles (for example, sized 40- $\mu\text{m}$  and larger) the distance between the two glare spots can be measured directly to accurately determine particle diameter. Also, by recording multiple spot mode images over time, in conjunction with a double-pulsed laser system, velocity data can be acquired.

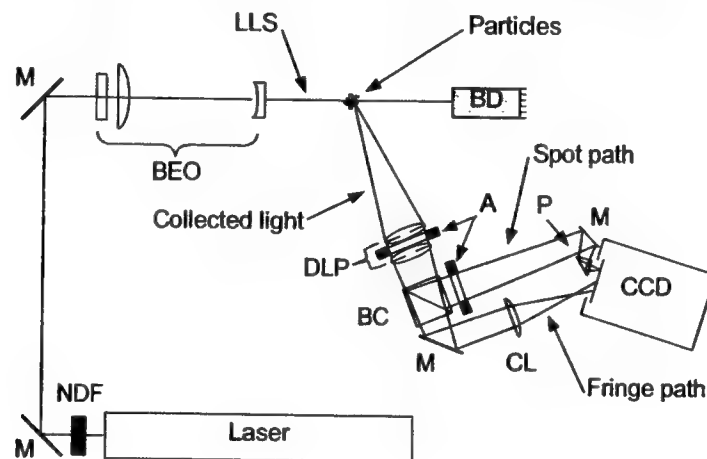


**Figure 1. Schematic of the Planar Image Particle Analyzer (PIPA).** Abbreviations: LLS, laser light sheet; M, mirrors; BEO, light sheet beam expanding optics; BD, beam dump; DLP, doublet lens pair; A, apertures; P, prism; CCD, digital camera; BC, beam splitting cube; CL, cylindrical lens; NDF, neutral density filter.

### Fringe Mode Imaging

In the second optical path, the 'fringe path,' light is directed and imaged onto the other half of the CCD via the DLP, BC, M and a cylindrical lens (CL). In this example, CL is orientated with its focusing power in the horizontal plane (parallel to the surface of the paper in **Figure 1**). In fringe path, which is based on a design invented by Keio University (Japan) and described by Maeda<sup>4</sup>, CL causes the horizontal component of the scattered light to focus slightly *in front* of the CCD, while the vertical component is essentially unaltered and continues converging toward the CCD as if being imaged by DLP alone. Thus, on the CCD, the horizontal component of particle glare spot images is *defocused*, while the vertical component is *focused*. For example, **Figure 3** is the same 33.6- $\mu\text{m}$  droplet in **Figure 2** as imaged by the fringe path. Smaller particles, sized 5 to 35- $\mu\text{m}$  in diameter, which are too small to be measured in spot mode, can be measured in fringe mode.



**Figure 2.** A 33.6- $\mu\text{m}$  water droplet imaged on the CCD by the 'spot path' showing the reflected and refracted glare spots.

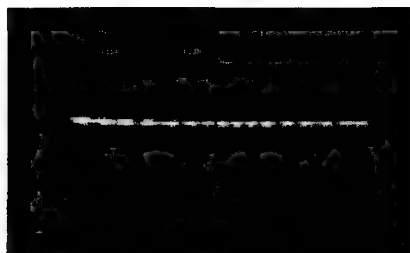


**Figure 3.** The same droplet in Figure 2 imaged on the CCD by the 'fringe path' showing the elongated a-focal fringe pattern formed on the CCD by the interference of the two glare spots.

### Spot/Fringe Image Correlation

Since the same particles are imaged on both sides of the CCD, it is necessary to track and correlate a particle's image in spot mode to its image in fringe mode. **Figure 4** is a PIPA image containing a realistic spray distribution of 5  $\mu\text{m}$  to 115  $\mu\text{m}$  water droplets, which has been adapted to illustrate the spot/fringe correlation regions. As discussed above, the vertical extent of particle images on the CCD are approximately the same for both fringes and spots, but the horizontal extent of the fringe images is much larger (**Figure 3**) due to the expansion provided by the cylindrical lens in the fringe path. Consequently, the FOVs captured by the two paths are slightly different. Thus, the image of a particle recorded at the far edge of the spot mode half of the CCD (left in **Figure 4**) may be only partially recorded in the fringe mode (right) side of the CCD.

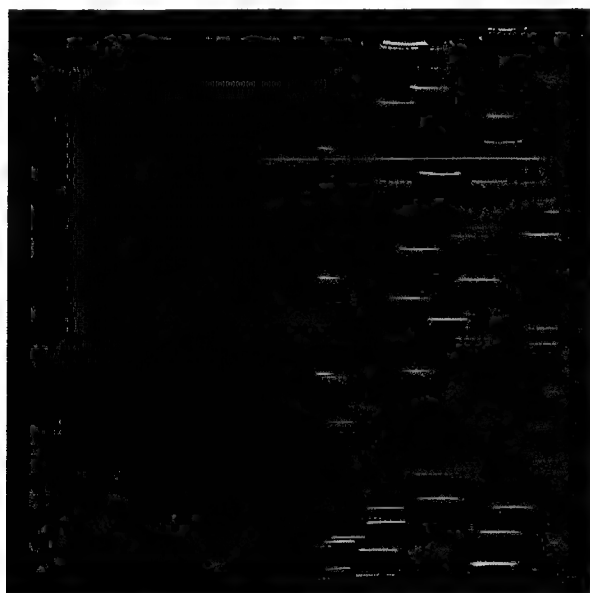


**Figure 4.** Image of 5  $\mu\text{m}$  to 115  $\mu\text{m}$  water droplets recorded by PIPA. Gray regions are outside of the spot/fringe correlation zone, and the white lines separate and show correlated spots and fringes.

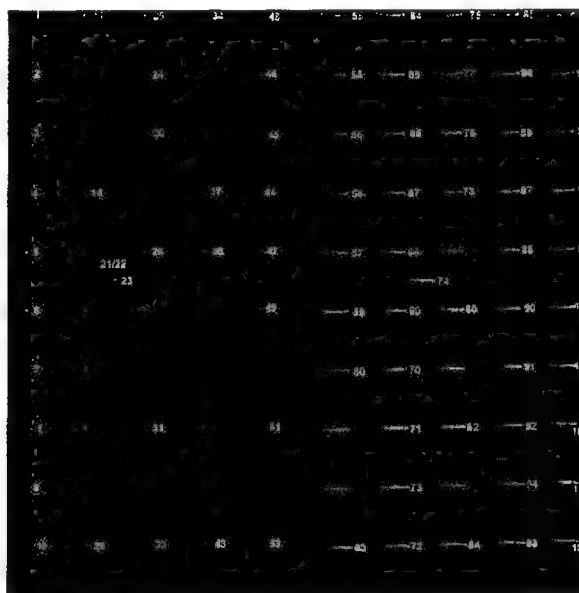


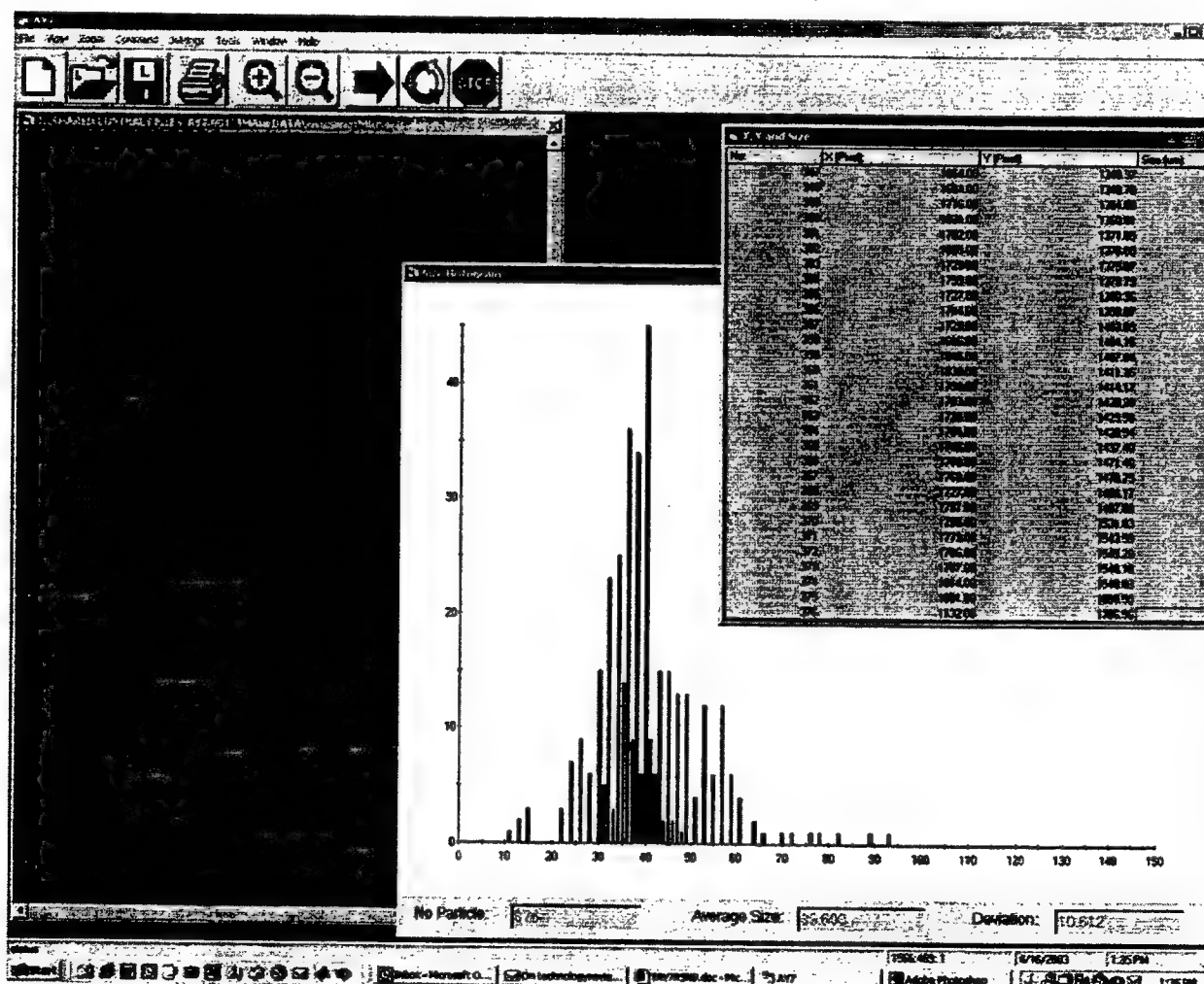
**Figure 5.** Image of a pinhole array used to generate a correlated spot to fringe image location correlation look up table (LUT).

A calibrated pinhole array was positioned in the laser light sheet, back-illuminated, and its image recorded by PIPA (**Figure 5**). The image was analyzed by PIPA's image analysis software PIPASOFT, which provided the X- and Y-coordinates of all the pinhole spot images and their corresponding expanded fringe images. Next, the spot and fringe location data were used to generate

a look up table (LUT) of correlated pinhole spot image locations to pinhole fringe image locations. Since the original pinhole array has only 53 correlated locations in the FOV, a linear interpolation algorithm was used to “fill in the blanks” and create a full resolution correlation LUT for every pixel in the image. In the end, the full resolution LUT enables the location of any particle in the spot mode side of the image to be correlated to a location in the fringe mode side of the image with an accuracy of  $\pm 2$  pixels. We turn now to a discussion of system software.

### Image Analysis Software

The program PIPASOFT was created to serve as a graphic user interface (GUI) for controlling the PIPA’s laser, image acquisition, data mapping & analysis, and data visualization & output functions. Figure 6 of PIPASOFT’s GUI shows the image display, particle size histogram and data table output windows. Additional functionality includes: the ability to accumulate particle size histograms from multiple images, graphic display of image intensity values to aid recording parameter setup, and 2D and 3D data visualization windows. PIPASOFT’s analysis algorithms can process both spot and fringes. The rapid image processing capability of PIPASOFT enables a 4-MB (2048x2048-pixel) image containing over 370 40- $\mu\text{m}$  glass micro spheres to be analyzed in less than one second.



# STABILIZATION AND BLOWOUT OF GASEOUS- AND SPRAY-JET FLAMES

ARO Grant/Contract Number: AMSRL-RO-RI 40131-EG

Principal Investigator: Kevin M. Lyons

North Carolina State University  
Department of Mechanical and Aerospace Engineering  
Raleigh, NC 27695-7910

## SUMMARY/OVERVIEW:

The focus of our efforts in this research program is to determine the underlying mechanisms that control flame stabilization and blowout in lifted spray flames. Extensive data exists for the characterization of gaseous diffusion flames as a result of past research performed by the combustion community. In these studies, mechanisms of stabilization, the role of premixing, and scalar dissipation have been examined to varying degrees in systems such as lifted laminar and turbulent diffusion flames. Recently, OH-PLIF measurements have been performed in our laboratory, along with smoke visualization, to investigate the single and double flame structures that exist in spray flames, along with high-speed visualization of the reaction zone. Current work in our laboratory is focusing on the temporal nature of the spray flame/flow interaction to understand how the double flame structure affects overall flame stability.

## TECHNICAL DISCUSSION:

### **Spray flame characterization utilizing OH-PLIF imaging, flame luminosity, and flow visualization**

Description and quantification of the phenomena that control two-phase combustion processes are of great interest [1,2], as most practical combustion devices initially introduce fuel in the liquid phase. The underlying mechanisms that control stabilization, extinction, and flame propagation are of great interest in spray flame research. Recent work has focused on turbulent lifted ethanol spray flames in annular air co-flow. OH Planar Laser-Induced Fluorescence and smoke-based flow visualization has been performed to observe reaction zone contours, oxidizer entrainment, and turbulent mixing in the near field of an atmospheric ethanol spray flame. Particular attention has been focused on the development and characteristics of the double flame structure that is unique to lifted spray flames. OH-PLIF facilitates imaging of the spray flame combustion structures with minimal attenuation or interference (primarily elastic

scattering from large fuel droplets). The instantaneous 2D images are used to both map out reaction zone contours and make observations on the effect of local fluid dynamics on the mode of combustion (diffusion or partially premixed) in the various regimes of the flame. Although the OH images provide excellent data for analyzing flame structures, further qualification of the results is required. Therefore, in order to better understand the entrainment and subsequent mixing of oxidizer with fuel vapor/droplets, smoke visualization has been performed (See Fig. 1). Incense smoke was injected into the low-speed co-flow and illuminated by a laser sheet to visualize the flow of air around and into the flame base with both a high-speed digital video camera and high-resolution color digital photography. Since the spray core is relatively cool, the smoke can be imaged well into the spray and the turbulent mixing of oxidizer and fuel is possible. This data is crucial in supporting the theories of flame structure morphology [3] and overall flame stabilization.

Contrary to the single flame structure observed in lifted non-premixed gaseous flames, the double flame structure in spray flames appears as two diverging flame fronts originating at the stabilization point, consisting of an outer diffusion flame with an inner structure that possesses partially premixed flame characteristics, especially at locations downstream of the leading edge (See Fig. 1). The inner flame structure burns primarily in a diffusion mode just inside the leading edge and evolves into a region indicative of partially premixed burning by the relatively wide regions of OH signal observed in the experimental data [4,5]. Flow visualization indicates that the development of the inner reaction zone is due to entrainment of ambient air into the spray core where it undergoes turbulent mixing along the shear layer created between the oxidizer flow and the momentum dominated region of the spray. The shear, or mixing, layer contains large scale vortical structures that possess small droplets that follow the gas phase flow faithfully (low Stokes flow) and vaporize easily. This mechanism aids in partial premixing of the fluid which creates a flammable mixture for inner zone combustion. Depending on the fuel spray characteristics and the co-flow velocity (affecting local stoichiometry), the inner structure can burn in both mixing controlled and partially premixed modes. Local extinction at the lowest axial locations of the inner flame structure, caused by high strain/scalar dissipation rates and quenching from droplets in the high momentum spray cone at the reaction zone interface, is thought to play an important role in partially premixed combustion at downstream locations due to extinction and re-ignition events. It is believed the larger droplets feed the outer reaction zone while the smaller, easily vaporized droplets sufficiently mix with entrained or co-flow air along the turbulent mixing layer to support partially premixed combustion at the inner reaction zone. One interesting observation was made for the two smallest fuel nozzles (without co-flow) analyzed in our studies. The case for no co-flow exhibited a unique "leading edge" phenomenon that is fundamentally different than the leading-edge structure observed in lifted gaseous diffusion flames. The presence of a single flame structure with no inner flame zone indicates that there is not sufficient air entrainment to support combustion, as verified through flow visualization. Once co-flow is introduced, the flame is lifted enough to entrain sufficient oxidizer for inner zone combustion, and high-speed video sequences reveal the turbulent recirculations responsible for the enhanced mixing of oxidizer with fuel vapor. In general, while low-speed co-flow

simply enhances the double structure with a minimal effect on liftoff height, the higher co-flow velocities create a well-lifted flame that exhibits a highly fluctuating stabilization point and an unsteady double structure. This spray flame research has provided insight into the nature of the flame structures and the effect that co-flow/air entrainment has on these structures. Current work is aimed at further quantifying spray flame mechanisms in order to understand how these near-field combustion structures are involved in the stabilization of turbulent spray flames. Developing a better understanding of spray flame stabilization will allow comparisons to be made to the better characterized phenomena associated with gaseous diffusion flames.

### **Spray and gaseous flame comparisons**

Observations of the leading edge characteristics in turbulent lifted gaseous [3] and spray flames [4] have been provided to compare and distinguish the mechanisms that govern the flame structure and stabilization in each respective combustion system [5]. In the methane flame, CH-PLIF has been performed simultaneously with both particle image velocimetry and Rayleigh scattering in two independent experiments. Single-shot OH-PLIF and flow visualization was performed in the ethanol spray flame. Each flame stabilizes in a zone of high mixing due to large-scale structures in the turbulent flow field. The leading edge of the lifted gaseous diffusion flame has been shown to oscillate between modes of stable upstream propagation and unstable downstream recession. The flame finds stability in regions of low-speed flow that are within the flammability limits. This so-called "leading-edge" combustion process is accomplished due to the fuel-lean premixed branch of the leading edge stabilizing the trailing diffusion flame through premixed flame propagation. The spray flame leading edge does not indicate the same variety of "leading-edge" combustion structure, but does develop a dual reaction zone (Figure 1 (d)). It is offered that flame stabilization in reacting sprays occurs where small droplets are available (to readily provide a mixable fuel vapor) and large-scale structures exist (which mix the fuel vapor with entrained air). The inner reaction zone develops along the turbulent shear layer. These main points compare and contrast flames stabilized in single and two-phase reacting flows. The authors believe these observations are timely, especially regarding the current emphasis of the combustion community on partially premixed combustion and triple flame structures. In addition, these results are pertinent in applications where a liquid or gaseous fuel may be considered for use in a practical device, and the best choice of fuel may depend upon the flame characteristics and stability desired. Future work includes modifying the spray dynamics in order to clarify how fuel properties (e.g., viscosity, surface tension, density), droplet size and velocity distribution, and oxidizer flow field affect leading edge combustion and stabilization. These research tasks will require diagnostic techniques that provide quantitative characterization of the turbulent flow field and reaction zones, such as with PIV or multiple-shot PLIF, and discriminate between different droplet size classes and liquid and gas phases.



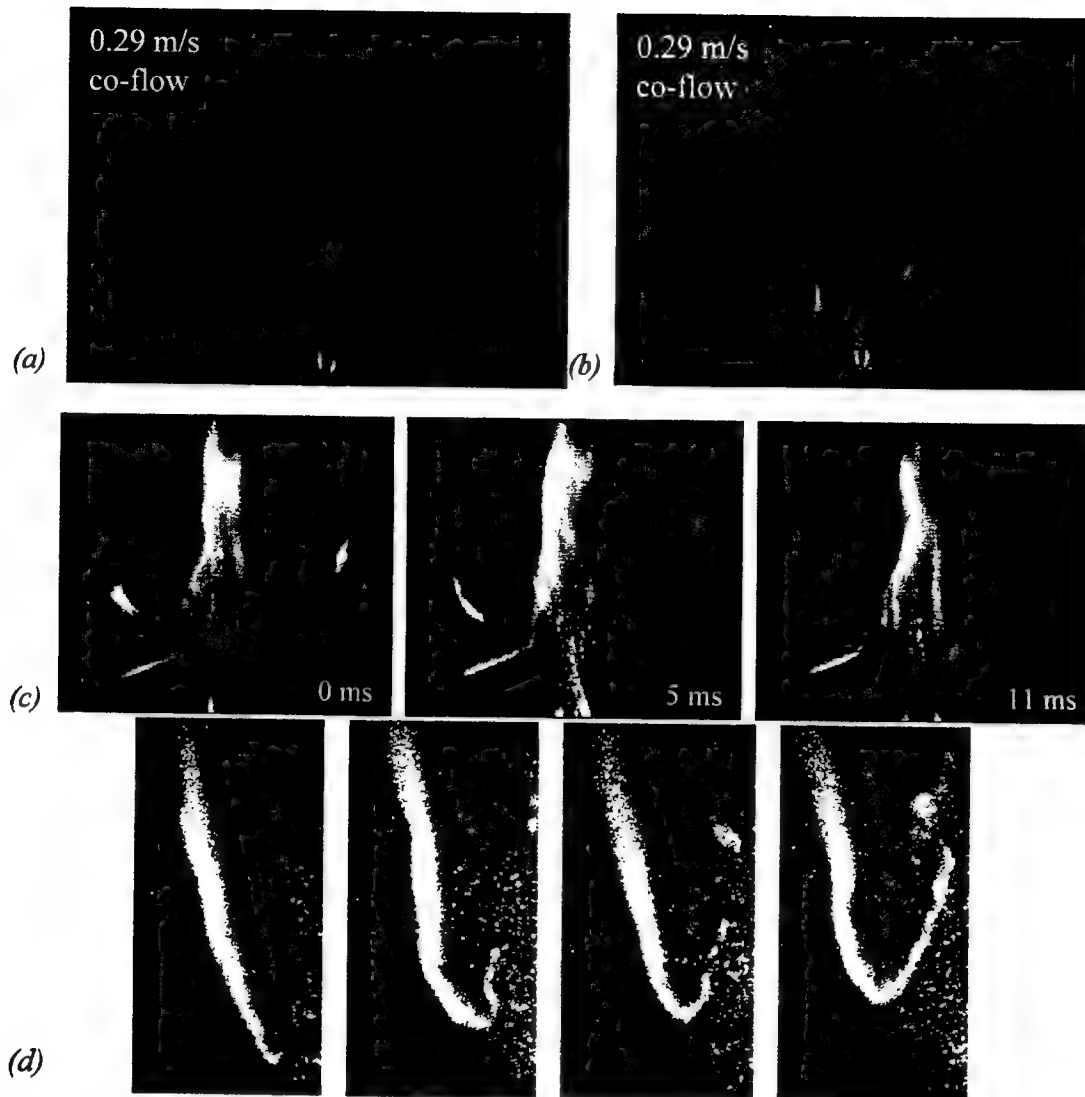


Fig. 1: Smoke visualization in spray flame with 0.29 m/s co-flow showing color digital photographs of (a) steady entrainment of smoke into spray, (b) dispersion of ambient gas flow into and around flame base, especially left side, (c) high speed digital video sequence of strong smoke entrainment and flow of smoke around the left flame leading edge and (d) OH-PLIF images showing development of double flame structure.

## References

1. Cessou, A., and Stepowski, D., Planar Laser Induced Fluorescence Measurement of [OH] in the Stabilization Stage of a Spray Jet Flame. *Combust. Sci. Technol.* **118** (1996) 361-381.
2. Stepowski, D., Cessou, A., and Goix, P., Flame Stabilization and OH Fluorescence Mapping of the Combustion Structures in the Near Field of a Spray Jet. *Combust. Flame* **99** (1994) 516-522.
3. Watson, K. A., Lyons, K. M., Donbar, J. M. and C. D. Carter Observations on the Leading Edge in Lifted Flame Stabilization, *Combustion and Flame* **119**(1999) 199-202.
4. Marley, S.K., Welle, E.J. and Lyons, K.M. , Combustion Structures in Lifted Ethanol Spray Flames, to appear: *ASME Journal of Engineering for Gas Turbines and Power*.
5. Marley, S. K., Watson, K. A. and Lyons, K. M. , Comparison Study on the Leading Edge in Lifted-Jet Gaseous vs. Spray Flames, under review: *Flow, Turbulence and Combustion*.



# **Autoignition and Burning Speeds of JP-8 Fuel at High Temperatures and Pressures**

**Grant No. DAAD19-01-1-0587**

**Hameed Metghalchi**

*Mechanical, Industrial and Manufacturing Engineering,  
Northeastern University,  
Boston, Massachusetts 02115*

## **Summary**

An experimental facility has been built to measure burning speed and study autoignition of JP-8 fuel at high temperatures and pressures. It includes two combustion chambers, spherical and cylindrical, optical set up and also a high temperature oven. Burning speed of fuel-oxidizer-diluent mixture is determined from the pressure rise during a combustion process using a thermodynamic model based on the conservation of mass and energy. Flame structure has been studied for gaseous fuel in the cylindrical vessel using a high speed CCD camera. Measurements have been done in these facilities for gaseous and liquid fuels over the wide range of temperature and pressure. Some of the results are presented in this report.

## **Technical Discussion**

### **1. Gaseous Fuel, methane-air-diluent mixtures:**

Measurements have been done for methane-air-diluent (In this study a mixture of 86 %  $N_2$  and 14 %  $CO_2$  is used) over the pressure range of 1-20 atm and temperature range of 298-650 K for equivalence ratios of 0.8-1.2. In the approach taken here, the pressure is the primary measurement. A thermodynamic analysis of the pressure time record that was used to calculate laminar burning speeds has been presented in the previous report. The measured values were compared to PREMIX code's theoretical predictions using GRI-Mech 3.0 mechanism. As it was expected, the agreement is very good at high temperature, low pressure condition. GRI-Mech 3.0 predicts higher values at high pressure, low temperature conditions.

Investigation of cracking or wrinkling has been done in the cylindrical chamber. In order to observe at what pressure the flame starts to become cellular, flames have been visualized in the cylindrical chamber. The burned gas volume and pressure relation has been plotted in Figure 1 for different mixtures. It can be seen that the effect of equivalence ratio, diluent percentage and initial pressure is very small on the behavior of this curve. The final pressure achieved in the combustion chamber is different for different mixtures.

The burning speeds along isentropes for stoichiometric methane-air-diluent mixtures with initial pressures of 1 atm and diluent of 0-15% are shown in Figure 2. The agreement between measured values and PREMIX calculations are good. Also in this figure, the power law fits to the experimental data have been shown along with the actual data. It can be seen that adding diluent decreases the burning speed and the final pressure achieved in the vessel becomes smaller. Mixtures with more diluent have lower flame temperature and consequently lower flame speed. In mixtures with high percentage of diluent, buoyancy can be significant. This can be detected using the ionization probes signals. In Figure 2 all the measured values are for smooth flames, therefore the measured values are the laminar burning speeds.

Shadowgraph photographs of flame propagation for stoichiometric methane-air-diluent mixtures with initial pressures of 1 atm and diluent of 0-15% ( $p_i = 1$  atm,  $T_i = 298$  K) are shown in Figure 3. Inside the cylindrical vessel, the pressure reaches approximately 5 times its initial

value before the flame hits the wall. It can be seen that throughout the whole experiments, the flame is smooth and spherical for all these mixtures.

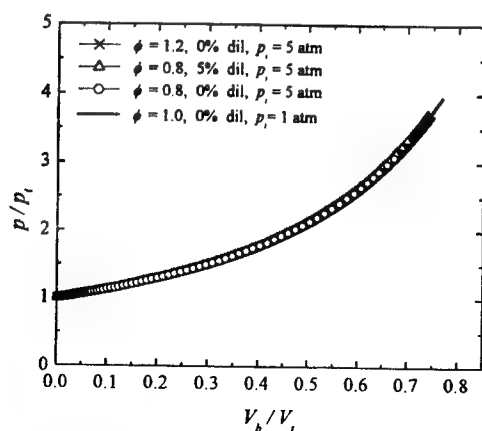
At high pressures, the flame front is cellular and instabilities can be observed even at smaller radii, as shown in Figure 4a. Shadowgraph photographs of flame propagation for stoichiometric methane-air-diluent mixtures with initial pressures of 5 atm and diluent of 0-15% ( $p_i = 5$  atm,  $T_i = 298$  K) are shown in Figure 4. Cellularities can be seen in methane-air mixture with no diluent at pressures around 7-8 atmosphere. By adding diluent to the mixture, part b-d of the figure, although the flames are still cracked, but they do not develop to any cellular structure. By adding diluent up to 15%, cracks become less but the effect of buoyancy can be observed.

Figure 5 shows the burning speed of stoichiometric methane-air-diluent mixture with initial temperature of 298 K, initial pressure of 5 atmospheres and diluent range of 0-15%. Again as we increase the amount of diluent the burning speed decreases. It can be observed that the agreement between measured values and PREMIX is good for mixtures with 5% diluent and higher. For methane-air mixture with no extra diluent, the measured values are higher than PREMIX. This again can be due to the instabilities in flame structure that increases the burning rate and consequently the measured values are higher than laminar burning speeds calculated by PREMIX. This has been verified in Figure 4a. As it has been discussed in the previous section, the flame becomes cellular for stoichiometric methane-air mixtures with initial pressure of 5 atm, at pressures around 7-8 atm.

## 2. Liquid Fuel, JP8-air mixtures:

During the past period construction of an oven was completed, where the spherical vessel can be housed. The spherical vessel can be heated up to 500 K. Liquid fuel is injected through a septum into a manifold inside the oven. A heated strain gauge in the oven was used to measure partial pressure of fuel in the vessel. A heated pressure transducer was used to measure pressure rise due to combustion. Mixtures of Stoichiometric JP8 and air have been burned at high initial temperatures and pressures. The purpose of these experiments was to determine the condition at which autoignition occurs. Figure 5 shows pressure versus time of a Stoichiometric mixture with initial pressure of 10 atmospheres and initial temperature of 490 K. It can be seen that autoignition occurred just before pick pressure as shown by pressure signal. In this case, autoignition occurred at 44 atmospheres of pressure and at 750 K.

It is anticipated for JP8 and air mixtures, both burning speed and the condition at which autoignition occurs will be measured next year.



**Figure 1-** Pressure ratio vs. ratio of burned gas volume to the total volume of combustion chamber for different mixtures of methane-air-diluent mixtures.

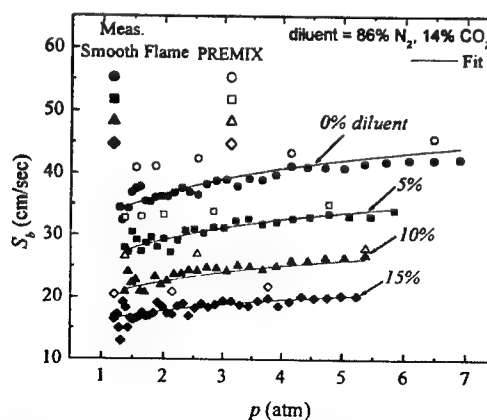


**Figure 2-** Comparison of burning speed of stoichiometric methane-air-diluent mixtures with those determined by PREMIX code along isentropes with initial pressure of 1 atm and initial temperature of 298 K, with different diluent percentage.

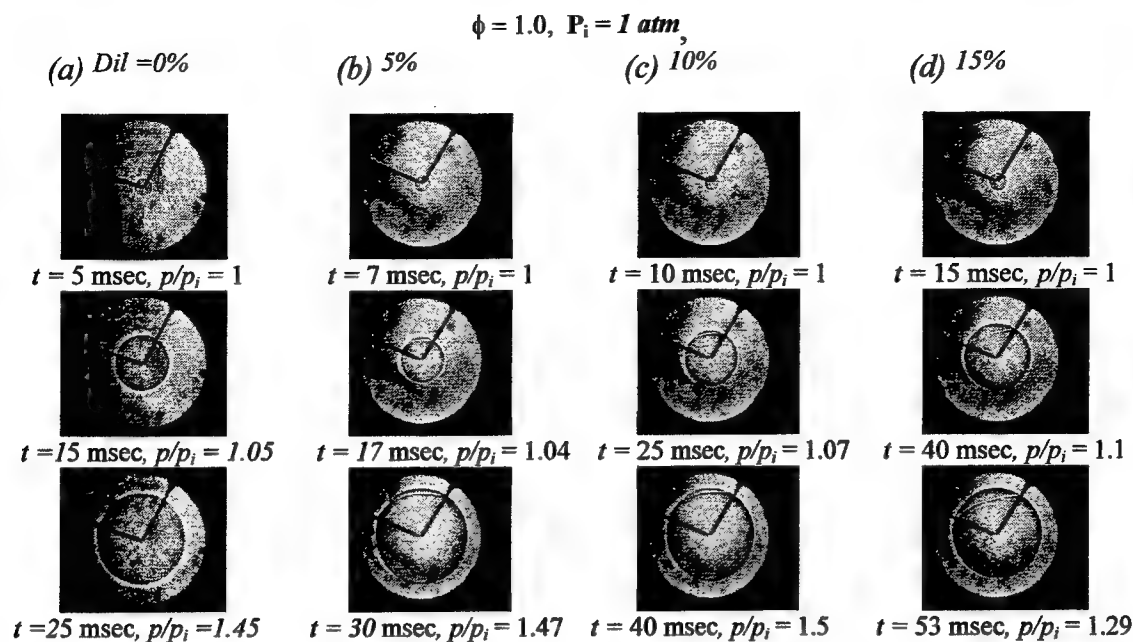


**Figure 3-** Flame propagation in cylindrical vessel, methane-air-diluent mixture,  $\phi = 1.0$ ,  $p_i = 1.0 \text{ atm}$  and  $T_i = 298 \text{ K}$ . (a) 0% diluent (b) 5% diluent (c) 10% diluent (d) 15% diluent.

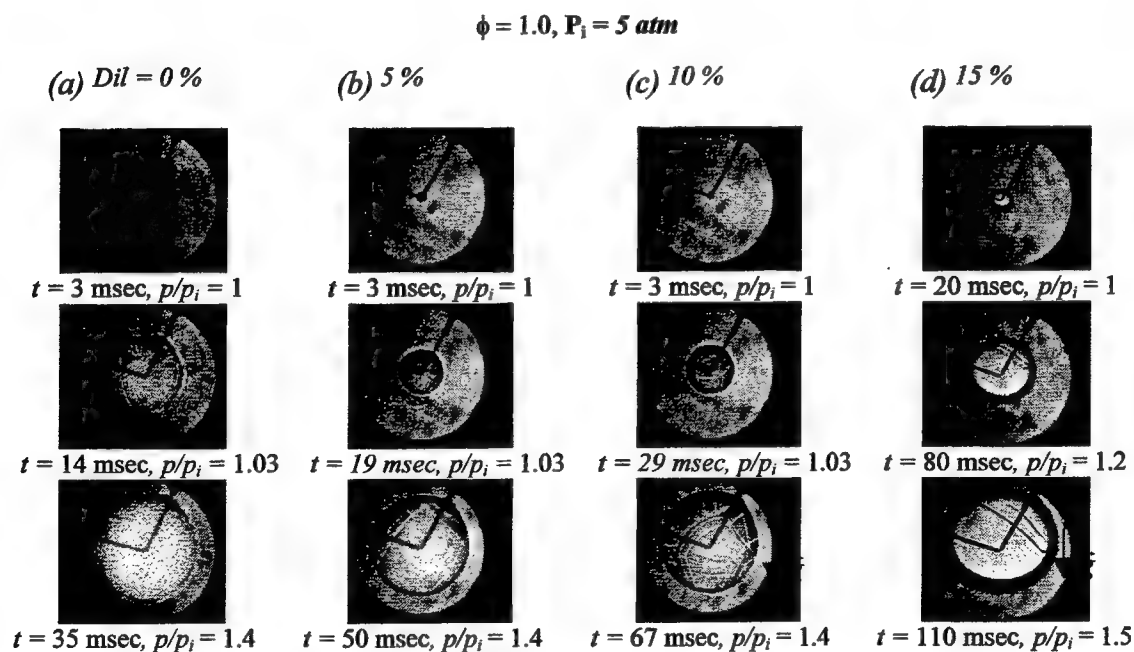


**Figure 4-** Shadowgraph pictures of flame propagation in the cylindrical chamber. Methane-air-diluent,  $\phi = 1.0$ ,  $p_i = 5.0 \text{ atm}$  and  $T_i = 298 \text{ K}$ . (a) 0% diluent (b) 5% (c) 10% (d) 15%.

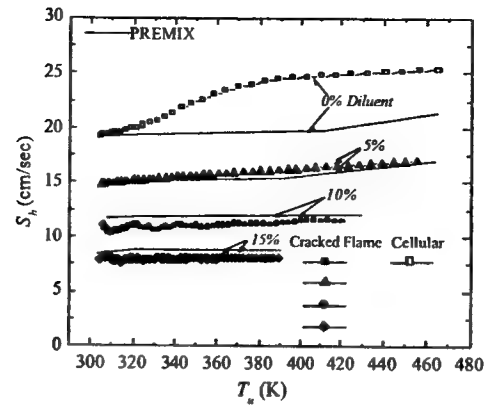


**Figure 5-** Comparison of burning speed of stoichiometric methane-air-diluent mixtures with those determined by PREMIX code along isentropes with initial pressure of 5 atm and initial temperature of 298 K, with different diluent percentage.

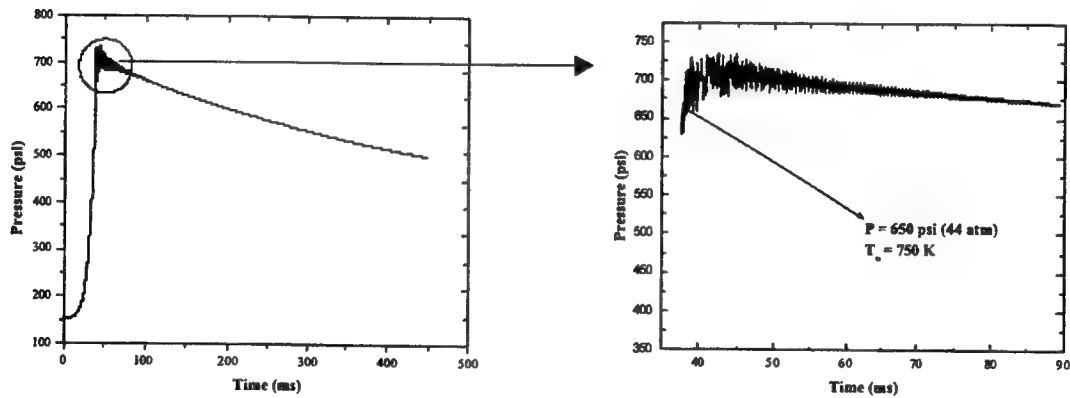


**Figure 6.** Pressure vs. Time for JP8-Air mixture,  $P_i = 10$  atm,  $T_i = 490$  K, and  $\Phi = 1$

# SOOT MORPHOLOGY IN UNSTEADY COUNTERFLOW DIFFUSION FLAMES

(ARO Grant/Contractor No. DAAD19-00-1-0429)

Principle Investigator: William Roberts

Department of Mechanical and Aerospace Engineering  
Campus Box 7910  
North Carolina State University  
Raleigh, NC 27695-7910

## SUMMARY/OVERVIEW:

The emission of particulate matter from turbulent diffusion flames, such as those found in Diesel engines, continues to be a serious concern to the US Army because of the strong IR signature emitted from hot soot and the detrimental effects of soot on human health. Both the temporal profile of the IR signature and the ill health effects are a function of the morphology of the soot. It is therefore desirable to control this morphology. However, before developing effective control strategies, a greater understanding of soot morphology in laboratory flames is necessary.

## TECHNICAL DISCUSSION:

The effort this year has focused on three inter-related subtasks, which will be described in some detail in the following paragraphs. All three tasks are in support of the overall goal of this project, which is an understanding of the processes controlling the morphology of soot generated in Diesel engines. The first subtask includes the measurement of soot morphology in a steady ethylene-air co-flow flame using a new planar laser light scattering technique. The second subtask concentrates on the measurement of polycyclic aromatic hydrocarbons (PAH) in an unsteady counterflow diffusion flame. The third subtask involves measuring soot volume fraction in high-pressure laminar co-flow diffusion flames.

Soot exists as agglomerated particles that may contain hundreds of primary spherules, which are typically on the order of 30-50 nm, in a fractal-like structure, with a fractal dimension less than 2. Rayleigh-Debye-Gans / polydisperse fractal aggregate (RDG/PFA) theory has been shown to accurately predict the angular dependence of scattered laser light in soot as well as other fractal-like particles and aerosols [1]. This technique has been used to successfully measure soot morphology in simple laminar and turbulent axisymmetric diffusion flames [2]. To determine all six morphological parameters, multi-angle scattering is required, but due to its time consuming nature, it may not be suitable to unsteady flames. One approach in overcoming this limitation is to make a number of assumptions regarding the fractal nature of the soot and the distribution of spherules per agglomerate. With these assumptions, the number of measurements

can be reduced to three: an extinction measurement and scattering measurements at two different angles. This approximate approach has achieved some success in axisymmetric flames [3, 4].

For the measurements in this subtask, propane and ethylene were burned in a well-documented co-annular burner [5]. Scattering measurements were made at 5° increments between 25° and 155°. The scattering/extinction system was calibrated using Rayleigh scattering from nitrogen. Soot volume fraction was measured as a function of height for both ethylene- and propane-air flames in the co-annular burner and compares well with previously published results obtained from this burner. Although there is considerable disagreement on the exact value of the fractal dimension ( $D_f$ ) for mature soot, the accepted range of  $D_f$  in laminar diffusion flames is between 1.6 and 1.8. One of the key assumptions in the approximate (two angle) RDG/PFA technique is that the fractal dimension is known. However, the measured  $D_f$  falls within the accepted range of values for mature soot only over a very narrow range. Low in the flame, in the inception zone, the early soot does not behave fractal-like at all, with a measured  $D_f$  of less than unity. As these particles are advected upstream and continue to grow and mature, they become more fractal-like. Conversely, the primary spherule diameter reaches a reasonable size fairly early in the flame, with diameters reaching approximately 10 nm at about 25% flame height in the ethylene flames and dropping to near 8 nm at 70% of the flame height before increasing again. The number of spherules per aggregate was observed to increase from approximately 50 at 25% flame height to approximately 250 at 75% flame height. This behavior is expected as the aggregates grow in size through clustering. Thus, techniques and approximations which have been validated for mature soot, are not necessarily appropriate for immature soot.

The second subtask involved the measurement of relative PAH concentrations in the unsteady counterflow diffusion flame burner. Given the importance of PAHs in both soot formation and growth processes and as a harmful pollutant itself, the study of PAHs generated during the combustion processes is very important. However, the study of PAH formation poses many difficulties, both experimentally and computationally. There are several methods available to detect PAHs. Conventional approaches to the analysis of PAHs deposited on the surface of particles require filter sampling, sample extraction, and enrichment procedures typically followed by gas or liquid chromatographic separation and detection by gas-chromatography and mass spectrometry or fluorescence or absorption spectroscopy.

Planar Laser Induced Fluorescence (PLIF) was used to determine relative concentrations in three different size classes of PAH. Considering the photophysical properties of PAHs, many researchers have suggested that the fluorescence at different emission wavelengths could be attributable to specific aromatic structures, i.e., the fluorescence wavelength distribution is dependent on the size of the PAH [6, 7], which means that with appropriate spectral filtering, different-sized PAHs maybe selectively detected.

Sgro et al. [8] found that the broad-band UV fluorescence centered around 320 nm is from carbonaceous material comprised of two-ring aromatics. Berlman [9] attribute the fluorescence spectra peaking in the UV at 300 nm to mono-ring aromatics (benzene and derivatives), and spectra peaking in the UV at about 350 nm to two-ring PAHs. Zizak et al. [10] found that the fluorescence centered near 400 nm is primarily from small PAHs composed of only two to three aromatic rings and fluorescence at 500 or 600 nm arising from larger PAHs, typically five rings or more. Therefore, for this research a 340 nm bandpass filter was chosen to

detect one- and two-ring PAHs, a 400 nm bandpass filter was chosen to detect three- and four-ring PAHs, and a 500 nm bandpass filter was chosen to detect five or more ringed PAHs.

Typical measurements of PAH size distributions made in the steady counterflow diffusion flame (CFDF) burner are shown in Fig. 1. Measurements were also made in the unsteady CFDF as a function of frequency and initial strain rate. The peak signal intensity is normalized by the steady state value and then plotted as a function of a Stokes parameter. This Stokes parameter, defined as the square root of the forcing frequency times  $\Pi$  normalized by the strain rate, indicates the frequency cut off at where the relative PAH concentration is no longer responding to the fluctuation in strain rate. As seen in Fig. 2, the smaller PAH molecules, identified by fluorescence at 340 nm has a more shallow slope than the larger PAH molecules, indicating that the smaller molecules remain coupled to the flow field oscillations at higher frequency fluctuations than the larger molecules.

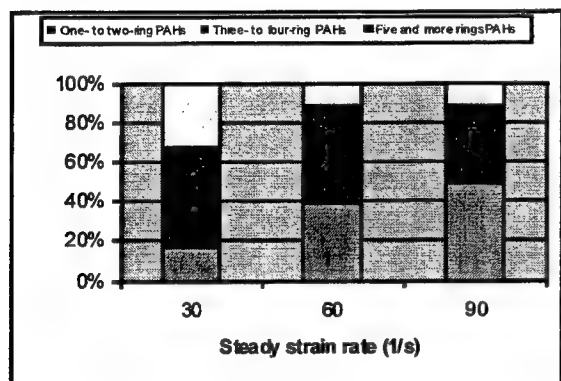


Figure 1. Contribution of different PAH class sizes as a function of steady strain rate (methane-air flame)

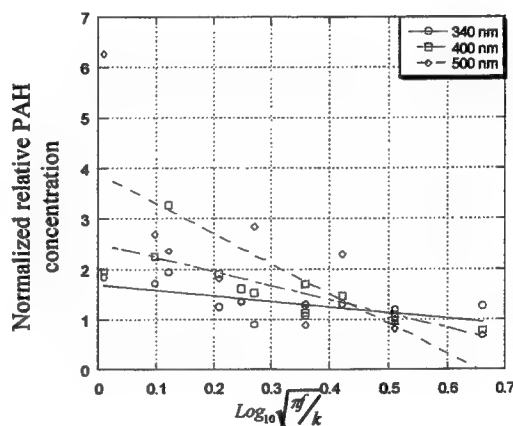


Figure 2. PAH response to strain rate fluctuations as a function of

The objectives of the third subtask are (1) to take laser light extinction measurements in a non-premixed laminar diffusion flame at elevated pressure as a means of providing calibration for the LII technique; (2) to employ the LII technique in a burner operating at elevated pressures; (3) to measure  $f_{sv}$  in a non-premixed laminar diffusion flame at elevated pressures up to 30 atmospheres. The small (4 mm diameter) co-flow flame is contained within a water-cooled pressure vessel. This vessel is capable of continuous operation at pressures up to 3.0 MPa and has three windows (7.6-cm diameter) for observation and non-intrusive diagnostics. The flame is relatively small compared to the volume of the chamber; therefore, air is used to purge the area surrounding the flame and the windows providing optical access.

To obtain spatially resolved, instantaneous  $f_{sv}$  measurements, Laser Induced Incandescence (LII) is employed. Briefly, the LII technique utilizes a very short duration output from a Nd:YAG laser to heat soot particles to near their vaporization temperatures. The thermal radiation emitted from these heated particles can then be related quantitatively to their volume fraction with appropriate calibration. This technique provides spatially resolved and

instantaneous  $f_{sv}$  measurements. The calibration will be done by measuring the extinction ratio of a second lower-powered laser. By assuming an axis-symmetric flame and using an image of the flame to accurately determine path length, the LII images and calibration data are used to obtain a quantitative image of  $f_{sv}$  throughout the flame [11, 12]. This spatially and temporally resolved  $f_{sv}$  information is necessary to determine such physical processes as the rates of primary particle formation, clustering, cluster-cluster agglomeration, and oxidation in diffusion flames.

The 1064 nm output from a Continuum Surelite III Nd:YAG is used to heat the soot particles; this particular wavelength is used to eliminate possible photochemical interferences [13]. The LII signal is collected with a Princeton Instruments ICCD camera with a 30 ns gate width; the gate delay for collection is 10 ns. To date,  $f_{sv}$  measurements have been made up to 3.0 MPa and are currently being quantified through corrections for laser sheet attenuation and signal absorption prior to calibration with light extinction measurements. Preliminary measurements indicate the soot volume fraction grows much faster than linear with pressure. There appear to be two distinct regimes, the first from atmospheric up to about 0.6 MPa, and then a second from 0.6 to 3.0 MPa. One of the difficulties in the extinction measurements is that the particles become very large and the extinction to scattering ratio changes with pressure. This issue is also being addressed.

#### References:

1. G. M. Faeth and U. O. Koylu, *Combust. Flame* **108** (4-6) (1995) 207-229.
2. U. O. Koylu, *Combust. Flame* **109** (3) (1997) 488-500.
3. U. O. Koylu, *Chem. Phy. Proc. Comb.* (1999) 324-327.
4. S. De Iuliis, F. Cigoli, S. Benecchi, and G. Zizak, *Applied Optics* **37** (1998) 7865-7874.
5. R. J. Santoro, H. G. Semerjian, and R. A. Dobbins, *Combust. Flame* **51** (2) (1983) 203-218.
6. A. Ciajolo, R. Ragucci, B. Apicella, R. Barbella, M. de Joannon, and A. Tregrossi, *Chemosphere* **42** (2001) 835-841
7. R. L. Vander Wal, K. A. Jensen, and M. Y. Choi, *Combust. Flame* **109**:399-414 (1997)
8. L. A. Sgro, P. Minutolo, G. Basile, and A. D'Alessio, *Chemosphere* **42** (2001) 671-680
9. I. B. Berlman, (1971) *Handbook of Fluorescence Spectra of Aromatic Molecules*, Second ed. Academic Press, New York.
10. G. Zizak, F. Cignoli, G. Montas, S. Benecchi and R. Donde, *Recent Res. Devel. in Applied Spectros.*, **1**(1996) 17-24
11. M. Y. Choi and K. A. Jensen, *Combust. Flame* **112**, 485-491 (1998).
12. M. E. DeCroix and W. L. Roberts, *Combust. Sci. Tech.* **160**, 165-189 (2000).
13. R. L. Vander Wal, *Appl. Opt.* **35**, 6548-6559 (1996).



# CHEMICAL-KINETIC CHARACTERIZATION OF AUTOIGNITION AND COMBUSTION OF DIESEL AND JP-8

(Grant/Contract Number DAAD19-99-1-0259)

Principal Investigator: Dr. Kalyanasundaram Seshadri

Department of Mechanical and Aerospace Engineering  
University of California at San Diego  
La Jolla, California 92093

## SUMMARY/OVERVIEW:

The objective of the research is to obtain a fundamental understanding of the physical and chemical mechanisms of autoignition and combustion of diesel and JP-8 in non premixed systems. Detailed chemical kinetic mechanisms that describe combustion of many of the components in diesel and JP-8 are not available and are unlikely to be developed in the near future. As a consequence the research was focused on developing the necessary scientific knowledge for developing surrogate for diesel and JP-8. The experimental part of the research was performed employing the counterflow configuration. The fuels tested were *n*-heptane, *n*-decane, *n*-dodecane, *n*-hexadecane, cyclohexane, methylcyclohexane, toluene, and *o*-xylene because they represent the types of fuels in diesel and JP-8.

## TECHNICAL DISCUSSION:

### *The Structure of Nonpremixed n-Decane Flames*

*n*-Decane is considered to be a component of surrogate fuels for diesel and JP-8. An experimental and numerical study was performed to elucidate the structure and mechanisms of extinction and autoignition *n*-decane flames in strained laminar flows under nonpremixed conditions. Experiments were conducted on flames stabilized between two counterflowing streams. The fuel-stream was a mixture of prevaporized *n*-decane and nitrogen, and the oxidizer stream was a mixture of air and nitrogen.

Concentration profiles of  $C_{10}H_{22}$ ,  $O_2$ ,  $N_2$ ,  $CO_2$ ,  $CO$ ,  $H_2O$ ,  $CH_4$ ,  $C_2$ -hydrocarbons,  $C_3$ -hydrocarbons, and  $C_4$ -hydrocarbons, were measured. The measurements were made by removing gas samples from the reaction zone using a quartz microprobe and analyzing them in a gas chromatograph. The microprobe with an outer diameter of 166 microns and an inner diameter of 83 microns was employed. The gas chromatograph was equipped with a 4.5 ft molecular sieve (80/100 mesh) column and a 12 ft Porapak Q column. The molecular sieve column was used for separating  $H_2$ ,  $O_2$ ,  $Ar$ ,  $N_2$ ,  $CH_4$ , and  $CO$ . The Porapak Q column was used for separating all other species. Temperature programming and valve switching were employed to optimize the separation performance of both columns. The

mole fractions of species in the gas mixture was determined using a thermo-conductivity-detector (TCD) and a flame-ionization-detector (FID). The expected accuracy for the maximum concentrations of most species is expected to be better than  $\pm 10\%$ . This includes species that can be clearly identified on either the FID or TCD-detector. Hydrogen gives a weak signal on the TCD-detector and it is estimated to be accurate to  $\pm 25\%$ . The expected accuracy for water is assumed to be  $\pm 20\%$ . Figure 1 shows the mole fraction of  $C_{10}H_{22}$ ,  $O_2$ ,  $CO_2$ ,  $H_2O$ , and  $CO$  as a function of distance. The points in Fig. 1 represent measurements and the lines are results of numerical calculations.

The temperature profile was measured using an uncoated Pt-Pt13%Rh (Type R) thermocouple. The wire diameter was 25 microns and the bead diameter was 90 microns. The measurement was corrected for radiation by assuming spherical shape of the bead and a constant emissivity of 0.2. Catalytic effects were neglected. The absolute accuracy of the temperature measurement is expected to be better than  $\pm 80$  K. Figure 2 shows experimental data on the temperature field in the nonpremixed *n*-decane flame. The triangles in Fig. 2 represent the raw-data of the measured temperature, the spheres represent the temperature corrected for radiation. The lines are results of numerical calculations using detailed chemistry.

Critical conditions of extinction were measured for various *n*-decane concentrations in the fuel stream. The oxidizer stream was air. For a certain composition of the reactant streams, a flame was established, and the the strain rate was increased until extinction is observed. Critical conditions of autoignition were measured for a mole fraction of *n*-decane equal to 0.15. The oxidizer stream was air, and it was heated until autoignition is observed.

Numerical calculations were performed using detailed chemistry, applying the same boundary conditions as in the experiments. A detailed chemical kinetic mechanism made up of 347 reversible reactions among 66 species was employed. The flame structure and critical conditions of extinction and autoignition were calculated. The numerical results were compared with experiments as shown in Figs. 1 and 2.

### *Extinction and Autoignition of Liquid Hydrocarbon Fuels*

This section describes research on combustion of hydrocarbon fuels and fuel mixtures. Figure 3 shows the mass fraction of oxygen in the oxidizing stream,  $Y_{O_2}$ , as a function of the strain rate at extinction for a number of liquid hydrocarbon fuels. The fuel marked as diesel was obtained at a local service station. The symbols in Fig. 3 represent measurements, the lines are best fits to the experimental data. Figure 3 shows that the critical conditions of extinction of *iso*-octane, hexadecane, and a mixture of 70 % decane and 30 % xylene are similar to that of diesel. Figure 4 shows the oxidizer temperature,  $T_{0,1}$ , as a function of the strain rate, at autoignition for various liquid fuels. Figure 4 shows that in comparison to diesel, decane is easier to ignite while a mixture of 80 % decane and 20 % xylene is more difficult to ignite. Comparison of Figs. 3 and 4 show that although the critical conditions of extinction of *iso*-octane, hexadecane, and a mixture of 70 % decane and 30 % xylene are similar to that of diesel, the critical conditions of autoignition for these fuels and fuel mixture are not similar to that of diesel. This illustrates the challenges in developing surrogate fuels.

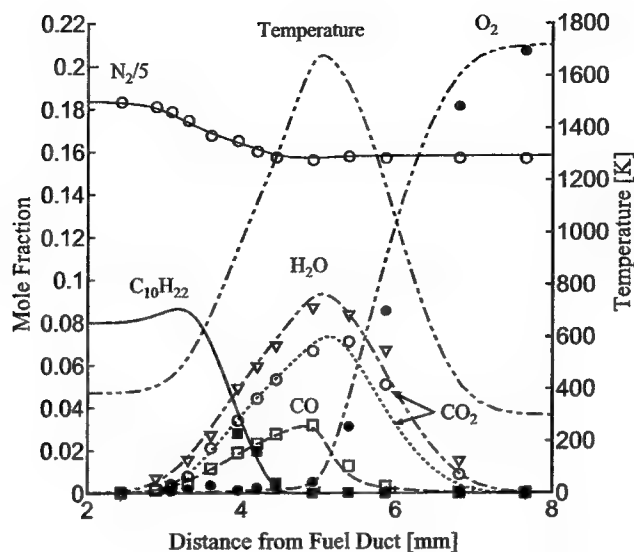


Figure 1: Experimental data showing the mole fraction of  $C_{10}H_{22}$ ,  $O_2$ ,  $CO_2$ ,  $H_2O$ , and  $CO$  as a function of distance. The points represent measurements and the lines are results of numerical calculations.

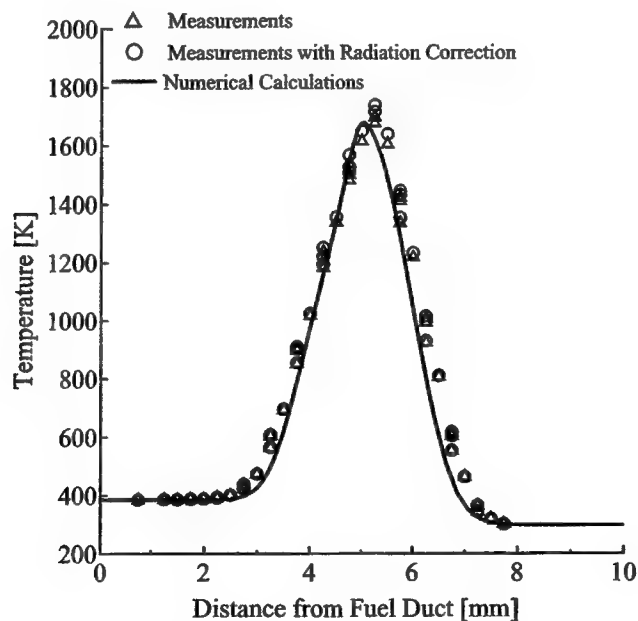


Figure 2: Temperature measurement in a nonpremixed  $n$ -decane flame. The triangles represent the raw-data of the measured temperature, the spheres represent the temperature corrected for radiation. The lines are results of numerical calculations using detailed chemistry.

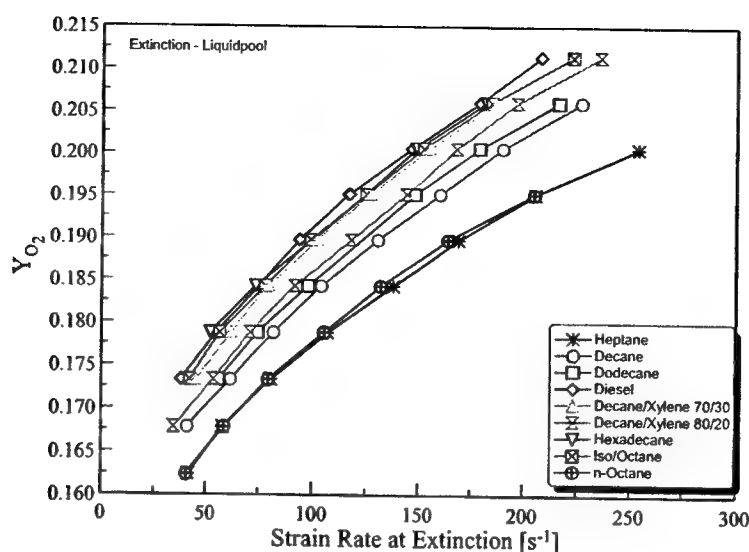


Figure 3: Experimental data showing the mass fraction of oxygen in the oxidizing stream,  $Y_{O_2}$ , as a function of the strain rate,  $as^{-1}$  at extinction. The symbols represent measurements. The lines are best fits to the experimental data.

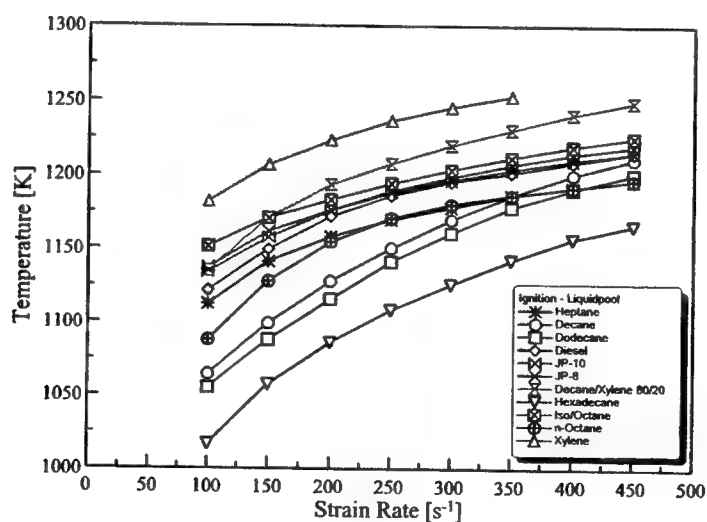


Figure 4: Experimental data showing the oxidizer temperature,  $T_{0,I}$ , as a function of the strain rate, at autoignition. The symbols represent measurements. The lines are best fits to the experimental data.

# DEVELOPMENT AND OPTIMIZATION OF A COMPREHENSIVE KINETIC MODEL OF HYDROCARBON FUEL COMBUSTION

(Grant/Contract Number F49620-01-1-0144)

Principal Investigator:

Hai Wang

Department of Mechanical Engineering  
University of Delaware, Newark, DE 19716

## SUMMARY/OVERVIEW:

The objective of this research program is to develop a comprehensive, predictive, and detailed kinetic model of hydrocarbon combustion for aeropropulsion simulations. During the reporting period progress has been made in a number of areas, including (1) revision of the  $H_2/CO$  reaction chemistry, (2) a systematic optimization of the  $H_2/CO$  reaction model; (3) compilation of a new diffusion coefficient database. These projects represent the two key ingredients that are necessary for the success of the overall research program: (a) an accurate physico-chemical property database for combustion kinetics, and (b) a unified and optimized kinetic model for higher aliphatic and aromatic fuel combustion.

## TECHNICAL DISCUSSION:

### 1. Revision of $H_2/CO$ Combustion Chemistry

The reaction mechanism of  $H_2/CO$  oxidation is the kinetic foundation for the combustion of all hydrocarbons. In our previously compiled reaction mechanism [1], the  $H_2/CO$  submodel was based on the GRI-Mech. Over the last two or three years, there have been renewed interest in the rate constants of the key radical-chain termination reaction  $H+O_2+M = HO_2+M$ . Kinetic parameters newly made available show marked differences from those in early literature compilations. These new kinetic parameters gave us an urgent reason to re-examine the  $H_2-CO$  combustion model. In addition, the downward revision of the enthalpy of formation of OH may also exhibit a marked influence on the overall reaction kinetics of  $H_2$  combustion. The current work was also motivated by the fact that the  $H_2$ -submodel of the GRI-Mech has not been optimized against a large body of  $H_2$  combustion data.

The objectives of the present study are (1) to update the  $H_2-CO$  combustion reaction model on the basis of recent kinetic data, and (2) to optimize the  $H_2-CO$  model against available experimental data. Special attention has been placed on the capability of the model to predict ultra-lean  $H_2$ /air flames that correspond to a kinetics regime relevant to hydrocarbon ignition.

The revised, trial reaction mechanism consists of 14 species and 41 elementary reactions [2], and uses the revised diffusion coefficients of [3]. All rate constants have been re-evaluated and, when necessary, updated. The trial kinetic model was tested against over 60 sets of  $H_2/CO$  combustion experimental data, including shock-tube ignition delay time, laminar flame speed, and the species profiles in turbulent flow reactors and in premixed burner-stabilized flames. Representative results of  $H_2$  combustion are shown by the dotted lines in Figures 1-5. Also shown in the figures are the predictions made using the Mueller-Kim-Yetter-Dryer (MKYD)

reaction model (dashed lines). Our trial model has also been tested against the oxidation of mixtures of  $H_2$  and CO with generally good agreement. These results are not shown here. In addition, the trial model has been tested against new extinction strain rates of ultra-lean  $H_2$ -air flames, and the results are reported in [4].

In Figures 1-3, selected ignition delay comparisons show that reaction model predicts the experimental data reasonably well. The trial model yields the upward curvature towards lower temperatures as expected from the experimental observations.

Figure 4 shows experimental and computed laminar flame speeds of  $H_2$ -air mixtures at the atmospheric pressure. The trial model is found to be in a close agreement with the experimental data. The trial model tends to over predict the  $H_2$ - $O_2$ -He flame speeds at elevated pressures. The discrepancies are clearly due to kinetics as a previous study showed that the uncertainty in the transport coefficients cannot account for the observed differences.

Figure 5 shows representative results obtained for the species profiles during  $H_2$  oxidation in a turbulent flame reactor under three pressures, 0.3, 3.0, and 15.7 atm. It is seen that the model well captures the experimental features.

## 2. Mechanism Optimization

The validation tests carried out using the trial model demonstrated that this model is comprehensive and qualitatively accurate. The remaining discrepancies were then be resolved by a systematic optimization of model parameters with respect to a large set of target data, about 30 in all, that range from the global combustion properties of ignition delay and flame speed, to the more detailed species profiles during  $H_2$  oxidation in flames and flow reactors. On the basis of sensitivity analyses, 27 rate parameters were considered as active. Response surfaces were developed using the methodology developed recently [5]. Optimization shows that an improvement of the trial reaction model could be achieved within the rate parameter uncertainty space. Compared to the trial model, the optimized reaction model predicts better the experimental data, as seen by the solid lines in Figures 1-5. The currently optimized reaction model also resolves some of the stubborn cases that the MKYD model was not able to closely predict, as seen in Figures 2, 3 and 5.

Although the optimization results seem to be satisfactory, we realized that given the experimental uncertainty in the optimization targets, the optimization does not yield a unique, global minimum in the rate parameter uncertainty space. For this reason, the "optimized" model should be represented by a hypersurface on which every point (or rate parameter combination) is equally valid. We are developing a methodology that can express mathematically the hypersurface.

## 3. Diffusion-Coefficient Compilation

Our recent studies (e.g. [3]) showed that there are marked disagreements between diffusion coefficients obtained from first-principle calculations and those obtained from the empirical mixing rules of collision diameter and well depth. Therefore, it may be necessary to explicitly specify the pair diffusion coefficients in flame simulations. We compiled a list of diffusion coefficients for key pairs on the basis of our own studies as well as the results available in the literature. These pairs include H-He, H- $H_2$ ,  $H_2$ -He, H-Ar, H- $O_2$ , H- $N_2$ ,  $H_2$ - $N_2$ ,  $N_2$ - $N_2$ , and  $H_2$ - $H_2$ . The corresponding parameters used in the multi-component transport formulations were also calculated for these pairs. The list will expand to include CO,  $CO_2$ , and hydrocarbons in the next two years. The SANDIA transport library code was revised to include the possibility of externally specified diffusion coefficients. Both the database and transport library code are available for use upon request.

## AFOSR SPONSORED PUBLICATIONS:

1. Law, C. K., Sung, C. J., Wang, H., and Lu, T. F. "Development of comprehensive detailed and reduced reaction mechanisms for combustion modeling," *AIAA Journal*, in press, 2003 (invited review article).
2. Davis, S. G., Joshi, A. Wang, H., and Egolfopoulos, F. N. "A comprehensive and optimized kinetic model of  $H_2/CO$  combustion," Third Joint Meeting of the US Sections of the Combustion Institute, Chicago, March 2003, paper A8.
3. Middha, P., Yang, B., and Wang, H. "A first-principle calculation of the binary diffusion coefficients pertinent to kinetic modeling of hydrogen-oxygen-helium flames," *Proceedings of the Combustion Institute*, in press.
4. Dong, Y., Andac, G. M., Egolfopoulos, F. N., Davis, S. G., and Wang, H. "Experimental and numerical studies of flame extinction: validation of chemical kinetics," Third Joint Meeting of the US Sections of the Combustion Institute, Chicago, March 2003, paper PK8.
5. Davis, S. G., Mhadeshwar, A. B., Vlachos, D. G., and Wang, H. "A new approach to response surface development for detailed gas-phase and surface reaction kinetic model development and optimization," *International Journal of Chemical Kinetics*, submitted, 2002.
6. Hirasawa, T., Sung, C. J., Joshi, A., Yang, Z., Wang, H. and Law, C. K. "Determination of laminar flame speeds of fuel blends using digital particle image velocimetry: ethylene, *n*-butane, and toluene flames," *Proceedings of the Combustion Institute*, in press.

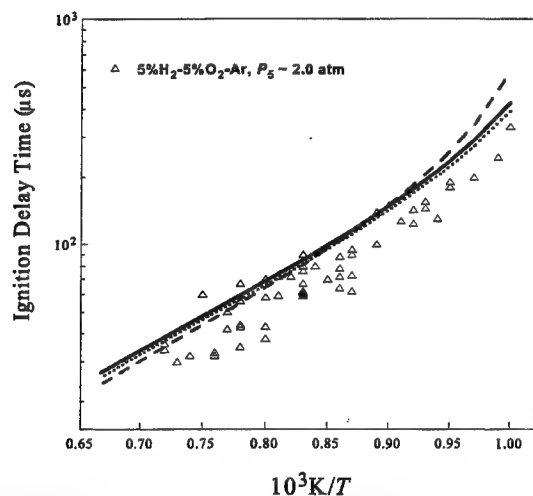


**Figure 1.** Experimental (symbols) [Cheng, R. K. and Oppenheim, A. K., *Combust. Flame* 58, 125-139 (1984).] and computed (line) ignition delay times of a  $6.67\%H_2 + 3.33\%O_2 + 90\%Ar$  mixture behind reflected shock waves ( $P_5 \sim 1.9$  atm). Dotted line: trial model; solid line: optimized model; dashed line: MKYD model.

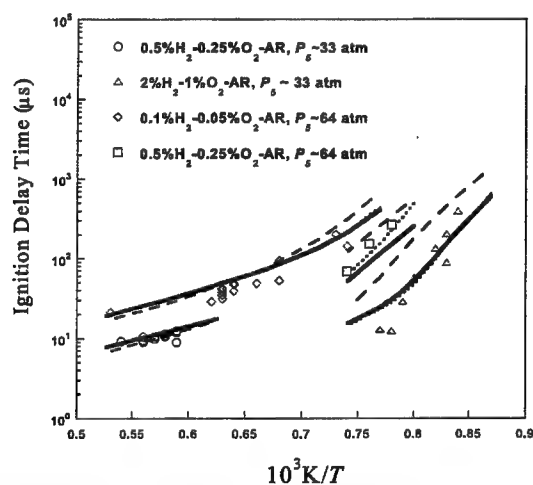


**Figure 2.** Experimental (symbols) [Peterson, E. L., Davidson, D. F., Rohrig, M. and Hanson, R. K., *20th Intl. Symp. Shock Waves*, 1996, pp. 941-946.] and computed (lines) delay times of maximum rate of  $[OH]$  absorption change for  $H_2-O_2-Ar$  mixtures behind reflected shock waves. Dotted line: trial model; solid line: optimized model; dashed line: MKYD model.

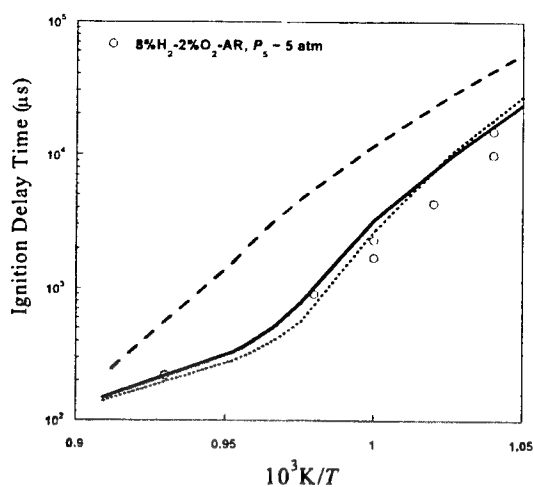


**Figure 3.** Experimental (symbols) [Skinner, G. B. and Ringrose G. H., *J. Chem. Phys.* 42, 2190-2192, (1965).] and computed (line) ignition delay times. Dotted line: trial model; solid line: optimized model; dashed line: MKYD model.

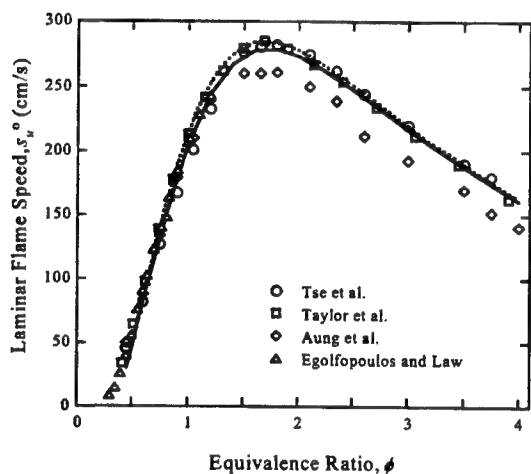


**Figure 4.** Experimental (symbols) [Tse, S. D., Zhu, D. L., and Law, C. K., *Proc. Combust. Inst.* 28, 1793-1800 (2000); Taylor, S. C., "Burning Velocity and the Influence of Flame Stretch," Ph.D. thesis, University of Leeds, 1991; Aung, K. T., Hassan, M. I., and Faeth, G. M., *Combust. Flame* 109, 1-24, (1997); Egolfopoulos, F. N. and Law, C. K., *Proc. Combust. Inst.* 23, 333-340 (1990)] and computed (line) laminar flame speed of  $H_2$ -air mixtures at the atmospheric pressure. Dotted line: trial model; solid line: optimized model.

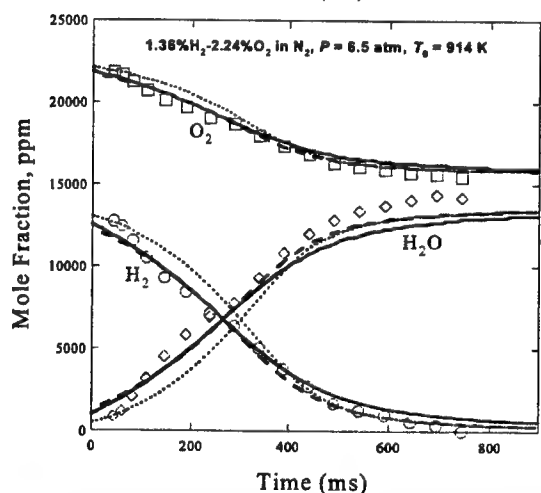
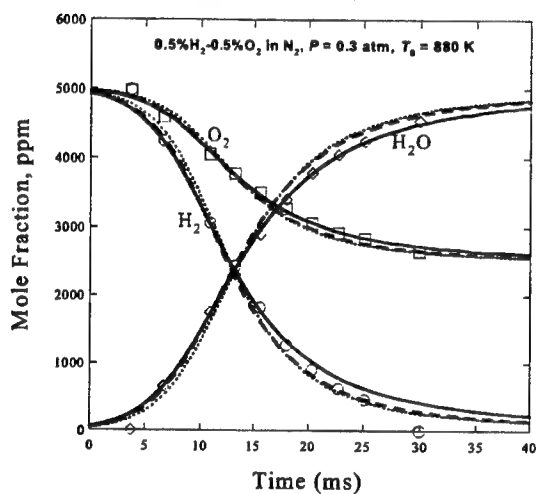
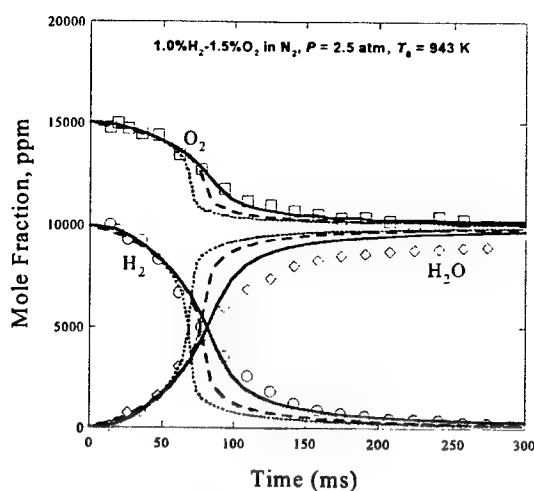


**Figure 5.** Experimental (symbols) [Mueller, M.A., Kim, T.J., Yetter, R.A. and Dryer, F. L. *Int. J. Chem. Kin.*, 31, 113 (1999).] and computed (lines) species profiles of  $H_2$  oxidation in a turbulent flow reactor. Dotted line: trial model; solid line: optimized model; dashed line: MKYD model.



## *Invitees*

Dr. Ajay Agrawal  
Aerospace and Mechanical Engineering  
University of Oklahoma  
865 Asp Avenue, Room 212  
Norman, OK 73019  
(405) 325-1754  
FAX: 325-1088  
aagrawal@ou.edu

Dr. M.S. Anand  
Rolls-Royce Corporation  
P.O. Box 420  
Speed Code T14  
Indianapolis, IN 46206-0420  
(317) 230-2828  
FAX: 230-3691  
m.s.anand@rolls-royce.com

Dr. William Anderson  
AMSRL-WT-PC  
U.S. Army Research Laboratory  
Aberdeen Proving Ground, MD 21005-5066  
(410) 278-9992  
DSN: 298-9992  
FAX: 278-7333  
willie@arl.army.mil

Dr. Kurt Annen  
Aerodyne Research, Inc.  
Manning Park Research Center  
45 Manning Road  
Billerica, MA 01821-3976  
(978) 663-9500 x234  
FAX: 663-4918  
kannen@aerodyne.com

Dr. Chris Atkinson  
Dept. of Mechanical & Aerospace Engineering  
West Virginia University  
P.O. Box 6106  
Morgantown, WV 26506-6106  
(304) 293-4111  
FAX: 293-2582

Mr. Steve Beckel  
Pratt and Whitney  
M/S 715-83  
P.O. Box 109600  
West Palm Beach, FL 33410-9600

Dr. Josette Bellan  
Jet Propulsion Laboratory  
4800 Oak Grove Drive  
MS 125-109  
Pasadena, CA 91109  
(818) 354-6959  
FAX: 393-5011  
josette.bellan@jpl.nasa.gov

Dr. Michael Berman  
AFOSR/NL  
4015 Wilson Boulevard, Room 713  
Arlington, VA 22203-1954  
(703) 696-7781  
DSN: 426-7781  
FAX: 696-8449  
michael.berman@afosr.af.mil

Dr. William Berry  
Director for Research  
Defense Research & Engineering  
3040 Defense Pentagon  
Washington, DC 20301-3040

Dr. Thomas Beutner  
AFOSR/NA  
4015 Wilson Boulevard, Room 713  
Arlington, VA 22203-1954  
(703) 696-6961  
DSN: 426-6961  
FAX: 696-8451  
thomas.beutner@afosr.af.mil

Dr. Robert Bill  
Propulsion Directorate  
Army Research Laboratory  
NASA Glenn Research Center  
21000 Brookpark Road, MS 77-12  
Cleveland, OH 44135-3191  
(216) 433-3703  
FAX: 433-3000  
robert.c.bill@lerc.nasa.gov

Dr. Mitat Birkan  
AFOSR/NA  
4015 Wilson Boulevard, Room 713  
Arlington, VA 22203-1954  
(703) 696-7234  
DSN: 426-7234  
FAX: 696-8451  
mitat.birkan@afosr.af.mil

Dr. Kevin Bowcutt  
North American Aircraft Division  
Rockwell International Corp.  
P.O. Box 3644  
Seal Beach, CA 90740-7644

Mr. Andreja Brankovic  
Flow Parametrics, LLC  
15 Debra Drive  
Bear, DE 19701  
(302) 838-7368  
FAX: 838-7369  
brankov@flowparametrics.com

Dr. R.C. Brown  
Aerodyne Research, Inc.  
Manning Park Research Center  
45 Manning Road  
Billerica, MA 01821-3976  
(978) 663-9500  
FAX: 663-4918

Dr. Walter Bryzik  
Propulsion Systems Division  
USA Tank-Automotive Command  
ATTN: AMSTA-TR-R, MS 121  
Warren, MI 48397-5000  
(810) 574-6461  
FAX: 574-5054  
bryzik@cc.tacom.army.mil

Dr. John D. Buckmaster  
Department of Aerospace Engineering  
University of Illinois  
Urbana, IL 61801

Dr. T.D. Butler  
MS B-210 T-DO: Theoretical Division  
Los Alamos National Laboratory  
Los Alamos, NM 87545  
(505) 667-4401  
FAX: 665-4055  
tdbutler@lanl.gov

Dr. H.F. Calcote  
ChemIon Inc.  
159 Philip Drive  
Princeton, NJ 08540  
(609) 921-6891  
FAX: 921-6891  
calcote@alumni.princeton.edu

Dr. George Caledonia  
Physical Sciences, Inc.  
20 New England Business Center  
Andover, MA 01810  
(508) 689-0003  
FAX: 689-3232

Mr. Donald Campbell  
NASA Glenn Research Center  
21000 Brookpark Road  
Mail Stop 3-2  
Cleveland, OH 44135  
(216) 433-2929  
FAX: 433-5266

Dr. Herb Carlson  
AFOSR/CA  
4015 Wilson Boulevard, Room 713  
Arlington, VA 22203-1954  
(703) 696-7550  
DSN: 426-7550  
FAX: 696-9556  
herb.carlson@afosr.af.mil

Dr. Campbell Carter  
AFRL/PRA  
1950 Fifth Street  
Building 18, Room D224  
Wright-Patterson AFB, OH 45433-7251  
(937) 255-7203  
DSN: 785-7203  
campbell.carter@wpafb.af.mil

Dr. Len Caveny  
13715 Piscataway Drive  
Ft. Washington, MD 20744  
(301) 292-5319  
FAX: 292-3724  
lcaveny@compuserve.com

Dr. Nicholas Cernansky  
Mechanical Engineering Department  
Drexel University  
32nd and Chestnut Streets  
Philadelphia, PA 19104-2884

Dr. Chine I. Chang  
Director  
U.S. Army Research Office  
P.O. Box 12211  
Research Triangle Park, NC 27709-2211  
(919) 549-4203  
DSN: 832-4203  
FAX: 549-4348  
jchang@aro-emh1.army.mil

Dr. Harsha Chelliah  
Department of Mechanical, Aerospace and  
Nuclear Engineering  
University of Virginia  
Charlottesville, VA 22903-2442  
(804) 924-6037  
FAX: 982-2037  
harsha@virginia.edu

Dr. Jacqueline Chen  
Sandia National Laboratories  
P.O. Box 969, MS 9051  
Livermore, CA 94551-0969  
(510) 294-2586  
FAX: 294-1012  
jhchen@sandia.gov

Dr. S.Y. Cho  
Department of Mechanical and  
Aerospace Engineering  
Princeton University  
Princeton, NJ 08544-5263

Dr. M.B. Colket  
United Technologies Research Center  
411 Silver Lane, MS 129-29  
East Hartford, CT 06108  
(860) 610-7481  
(860) 658-9502  
FAX: 610-7593  
colketmb@utrc.utc.com

Dr. S.M. Correa  
GE Corp. Research & Development  
P.O. Box 8, K1ES112  
Schenectady, NY 12301  
(518) 387-5853  
FAX: 387-7258  
correa@crd.ge.com

Dr. Werner Dahm  
Department of Aerospace Engineering  
The University of Michigan  
3056 FXB 2140  
Ann Arbor, MI 48109-2140  
(734) 764-4318  
(734) 761-2026  
FAX: 763-0578  
wdahm@umich.edu

Mr. Eugene Danielson  
U.S. Army Tank-Automotive and  
Armaments Command  
ATTN: AMSTA-TR-R - MS 121  
Warren, MI 48397-5000

Dr. Ron Davis  
Chemical Science and Technology Lab  
National Institute of Standards & Technology  
Building 221, Room B312  
Gaithersburg, MD 20899

Dr. Peter A. DeBarber  
MetroLaser  
2572 White Road  
Irvine, CA 92614  
(949) 553-0688  
FAX: 553-0495  
debarber@deltanet.com

Dr. Paul Dimotakis  
California Institute of Technology  
1201 East California Boulevard  
MC 301-46  
Pasadena, CA 91125  
(626) 395-4456  
(626) 794-2594  
FAX: 395-4447  
dimotakis@caltech.edu

Dr. Glenn Diskin  
NASA Langley Research Center  
Hypersonic Airbreathing Prop. Branch  
MS 197  
Hampton, VA 23681-2199  
(757) 864-6268  
FAX: 864-7923  
g.s.diskin@larc.nasa.gov

Dr. Gregory Dobbs  
United Technologies Research Center  
Silver Lane, Mail Stop 90  
East Hartford, CT 06108  
(860) 610-7145

Dr. James F. Driscoll  
Department of Aerospace Engineering  
University of Michigan  
3004 FXB Building  
Ann Arbor, MI 49109-2118  
(734) 936-0101  
FAX: 763-0578  
jamesfd@umich.edu

Dr. J. Philip Drummond  
NASA Langley Research Center  
Mail Stop 197  
Hampton, VA 23681-0001  
(757) 864-2298  
FAX: 864-7923  
j.p.drummond@larc.nasa.gov

Dr. C. Dutton  
Department of Mechanical and Industrial Engineering  
University of Illinois  
Urbana, IL 61801

Dr. Tarek Echekki  
Dept. of Mechanical & Aerospace Engineering  
North Carolina State University  
2601 Stinson Drive - Campus Box 7910  
Raleigh, NC 27695-7910  
(919) 515-5238  
FAX: 515-7968  
techekk@eos.ncsu.edu

Dr. J.T. Edwards  
AFRL/PRTG  
1790 Loop Road, N  
Building 490  
Wright-Patterson AFB, OH 45433-7103  
(937) 255-3524  
DSN: 785-3524  
FAX: 255-1125  
james.edwards@wpafb.af.mil

Dr. Fokion N. Egolfopoulos  
Department of Mechanical Engineering  
University of Southern California  
Olin Hall 400B  
Los Angeles, CA 90089-1453  
(213) 740-0480  
FAX: 740-8071  
egolfopo@almaak.usc.edu

Dr. G.M. Faeth  
Department of Aerospace Engineering  
University of Michigan  
3000 FXB Building  
Ann Arbor, MI 48109-2140  
(734) 764-7202  
FAX: 936-0106  
gmfaeth@umich.edu

Dr. Parviz Famouri  
Department of Computer Science and  
Electrical Engineering  
West Virginia University  
P.O. Box 6109  
Morgantown, WV 26506  
(304) 293-0405 x2530  
pfamouri@wvu.edu

Dr. Gregory W. Faris  
Molecular Physics Laboratory  
SRI International  
333 Ravenswood Avenue  
Menlo Park, CA 94025-3493  
(650) 859-4131  
FAX: 859-6196  
gregory.faris@sri.com

Dr. Partick Farrell  
Engine Research Center  
1500 Engineering Drive  
University of Wisconsin  
Madison, WI 53706  
(608) 263-1686  
farrell@engr.wisc.edu

Dr. Farley Fisher  
National Science Foundation  
4201 Wilson Boulevard  
CTS/Room 525  
Arlington, VA 22230  
(703) 292-8371  
ffisher@nsf.gov

Dr. David E. Foster  
Engine Research Center  
University of Wisconsin  
1500 Engineering Drive  
Madison, WI 53706  
(608) 263-1617  
foster@engr.wisc.edu

Dr. Bish Ganguly  
AFRL/PRPE  
2645 Fifth Street, Suite 13  
Wright-Patterson AFB, OH 45433-7919  
(937) 255-2923  
DSN: 785-2923  
FAX: 656-4095  
biswa.ganguly@pr.wpafb.af.mil

Dr. Richard G. Gann  
Building and Fire Research Laboratory  
National Institute Of Standards & Technology  
100 Bureau Drive, Stop 8650  
Gaithersburg, MD 20899-8650  
(301) 975-6866  
FAX: 975-4052  
rggann@nist.gov

Dr. Alan Garscadden  
AFRL/PR  
1950 Fifth Street, Building 18A  
Wright-Patterson AFB, OH 45433-7251  
(937) 255-2246  
DSN: 785-2246  
FAX: 986-4657  
alan.garscadden@pr.wpafb.af.mil

Dr. Kresimir Gebert  
BKM, Inc.  
5141 Santa Fe Street  
San Diego, CA 92109  
(858) 270-6760  
bkm-inc@worldnet.att.net

Mr. R. Giffen  
Aircraft Engine Group  
General Electric Company  
Neumann Way  
Cincinnati, OH 45215

Dr. Sharath Girimaji  
Department of Aerospace Engineering  
Texas A&M University  
College Station, TX 77843-3141  
(979) 845-1674  
FAX: 845-6051  
girimaji@aero.tamu.edu

Dr. Peyman Givi  
Department of Mechanical Engineering  
University of Pittsburgh  
644 Benedum Hall  
Pittsburgh, PA 15261  
(412) 624-9605  
FAX: 624-4846  
givi@engr.pitt.edu

Dr. Irvin Glassman  
Department of Mechanical and  
Aerospace Engineering  
Princeton University  
Princeton, NJ 08544-5263  
(609) 258-5199  
(813) 442-1118  
FAX: 258-5963  
glassman@princeton.edu

Dr. George Gogos  
Department of Mechanical Engineering  
University of Nebraska, Lincoln  
Lincoln, NE 68588-0656  
(402) 472-3006  
ggogos1@unl.edu

Dr. Judah Goldwasser  
Mechanics Division, Code 333  
Office of Naval Research  
800 North Quincy Street  
Arlington, VA 22217-5660  
(703) 696-2164  
DSN: 426-2164  
FAX: 696-2558  
goldwaj@onr.navy.mil

Dr. James Gord  
AFRL/PRTS  
1790 Loop Road, N  
Building 490  
Wright-Patterson AFB, OH 45433-7103  
(937) 255-7431  
DSN: 785-7431  
FAX: 656-4570  
james.gord@pr.wpafb.af.mil

Dr. Jay P. Gore  
School of Mechanical Engineering  
Purdue University  
1003 Chaffee Hall  
West Lafayette, IN 47907-1003  
(317) 494-1500  
FAX: 494-0530

Dr. Larry Goss  
Research Applications Division  
Systems Research Labs, Inc.  
2800 Indian Ripple Road  
Dayton, OH 45440-3696  
(513) 252-2706

Dr. Richard Gould  
Department of Mechanical and  
Aerospace Engineering  
P.O. Box 7910  
North Carolina State University  
Raleigh, NC 27695-7910  
(919) 515-5236  
FAX: 515-7968  
gould@eos.ncsu.edu

Dr. Frederick Gouldin  
Department of Mechanical and  
Aerospace Engineering  
Cornell University  
Ithaca, NY 14853-5692  
(607) 255-5280  
fcg2@cornell.edu

Dr. Mark Gruber  
AFRL/PRA  
1790 Loop Road, N  
Wright-Patterson AFB, OH 45433-7251  
(937) 255-2175  
DSN: 785-2175  
FAX: 656-4659  
mark.gruber@afrl.af.mil

Dr. Brian K. Gullett  
U.S. Environmental Protection Agency  
National Risk Management Research Laboratory  
Air Pollution Technology Branch (MD-65)  
Research Triangle Park, NC 27711  
(919) 541-1534  
FAX: 541-0290  
gullett.brian@epa.gov

Dr. Rajendra Gupta  
Department of Physics  
University of Arkansas  
226 Physics Building  
Fayetteville, AK 72701  
(501) 575-5933  
rgupta@comp.uark.edu

Dr. Mark A. Hagenmaier  
AFRL/PRA  
1950 Fifth Street  
Building 18, Suite 10  
Wright-Patterson AFB, OH 45433-7251  
(937) 255-5210  
DSN: 785-5210  
FAX: 476-4659  
hagenma@possum.appl.wpafb.af.mil

Dr. Nabil S. Hakim  
Director, Advanced Engineering  
Detroit Diesel Corporation  
13400 W. Outer Drive, R03-B  
Detroit, MI 48239-4001  
(313) 592-7455  
FAX: 592-5906

Dr. Robert D. Hancock  
AFRL/PRTS  
1790 Loop Road, N  
Building 490  
Wright-Patterson AFB, OH 45433-7103  
(937) 255-6814  
DSN: 785-6814  
FAX: 255-1125  
hancockr@ward.appl.wpafb.af.mil

Dr. Ronald Hanson  
Mechanical Engineering Department  
Stanford University  
Building 530, Room 112  
Stanford, CA 94305-3030  
(650) 723-4023  
FAX: 725-4862  
hanson@me.stanford.edu

Dr. Naeim Henein  
Department of Mechanical Engineering  
Wayne State University  
2121 Engineering Building  
Detroit, MI 48201  
(313) 577-3887  
FAX: 577-8789  
henein@me1.eng.wayne.edu

Dr. Cecil F. Hess  
MetroLaser  
2572 White Road  
Irvine, CA 92614  
(949) 553-0688  
FAX: 553-0495  
chess@metrolaserinc.com

Mr. Robert Holland  
United Technologies Chemical  
Systems Division  
P.O. Box 49028  
San Jose, CA 95161-9028  
(408) 224-7656

Dr. Tian-Sen Huang  
Prairie View A&M University  
P.O. Box 307  
Prairie View, TX 77446-0307  
(936) 857-2859  
FAX: 857-2850  
ts\_huang@pvamu.edu

Dr. Lawrence Hunter  
Applied Physics Laboratory  
Johns Hopkins University  
Johns Hopkins Road  
Laurel, MD 20707-6099  
(301) 953-5000 x7406

Dr. Frank Hurley  
U.S. Army Research Office  
P.O. Box 12211  
Research Triangle Park, NC 27709-2211  
(919) 549-4432  
DSN: 832-4432  
FAX: 549-4310  
hurley@aro-emh1.army.mil

Dr. Farhad Jaber  
Department of Mechanical and  
Nuclear Engineering  
Kansas State University  
Manhattan, KS 66506  
(785) 532-5619  
FAX: 532-7057  
jaberi@mne.ksu.edu

Dr. Thomas Jackson  
AFRL/PRSC  
1950 Fifth Street  
Building 18  
Wright-Patterson AFB, OH 45433-7251  
(937) 255-2175  
DSN: 785-2175  
FAX: 656-4659  
thomas.jackson@afrl.af.mil

Dr. Jeff Jagoda  
School of Aerospace Engineering  
Georgia Institute of Technology  
Atlanta, GA 30332-0150  
(404) 894-3060  
jeff.jagoda@aerospace.gatech.edu

Dr. Jay Jeffries  
Mechanical Engineering Department  
Stanford University  
Thermophysics Division, Building 520  
Stanford, CA 94305-3032  
(650) 736-0007  
FAX: 723-1748  
jeffries@navier.stanford.edu

Mr. Gordon Jensen  
Chemical Systems Division  
United Technologies  
P.O. Box 49028  
San Jose, CA 95161-9028  
(408) 365-5552

Mr. Jeff Jensen  
Kaiser-Marquardt  
16555 Staycoy Street  
Van Nuys, CA 91406

Mr. Craig Johnston  
Lockheed Advanced Dev. Company  
Lockheed-Martin Corporation  
1011 Lockheed Way  
Palmdale, CA 93599-7212

Dr. Walter Jones  
AFOSR/NA  
4015 Wilson Boulevard, Room 713  
Arlington, VA 22203-1954  
(703) 696-8457  
DSN: 426-8457  
FAX: 696-8451  
walter.jones@afosr.af.mil

Dr. John Kelly  
Altex Technologies Corporation  
650 Nuttman Road, Suite 114  
Santa Clara, CA 95054  
(408) 980-8610

Dr. G.B. King  
Department of Mechanical Engineering  
Purdue University  
West Lafayette, IN 47907-1288  
(765) 494-6518  
kinggb@ecn.purdue.edu

Dr. Merrill K. King  
NASA Headquarters  
Code UG  
300 E Street, SW  
Washington, DC 20546  
(202) 358-0817  
FAX: 358-3091  
mking1@mail.hq.nasa.gov

Dr. David E. Klett  
Mechanical Engineering Department  
North Carolina Agricultural and  
Technical State University  
Greensboro, NC 27401-3209

Dr. Charles Kolb  
Aerodyne Research, Inc.  
Manning Park Research Center  
45 Manning Road  
Billerica, MA 01821-3976  
(978) 663-9500  
FAX: 663-4918

Dr. Kenneth Kuo  
Department of Mechanical Engineering  
Pennsylvania State University  
University Park, PA 16802  
(814) 865-6741  
FAX: 863-3203

Dr. Ming-Chia Lai  
Department of Mechanical Engineering  
Wayne State University  
Detroit, MI 48202

Dr. John Larue  
Department of Mechanical Engineering  
University of California  
Irvine, CA 92717

Dr. Allan Laufer  
Office of Energy Research  
U.S. Department of Energy  
19901 Germantown Road  
Germantown, MD 20874  
(202) 903-5820  
allan.laufer@oer.doe.gov

Dr. Normand Laurendeau  
School of Mechanical Engineering  
Purdue University  
West Lafayette, IN 47907-1288  
(765) 494-2713  
FAX: 494-0539  
laurende@ecn.purdue.edu

Dr. C.K. Law  
Department of Mechanical and  
Aerospace Engineering  
Princeton University  
Princeton, NJ 08544-5263  
(609) 258-5271  
FAX: 258-6233  
cklaw@princeton.edu

Dr. C.C. Lee  
Environmental Protection Agency  
Cincinnati, OH 45268  
(513) 569-7520

Dr. Calvin Lee  
Applied Research Division  
Natick Research, Development & Engr. Ctr.  
Kansas Street  
Natick, MA 01760-5017  
(508) 233-4267  
FAX: 233-5000  
calvin.k.lee@us.army.mil

Dr. Anthony Leonard  
Graduate Aeronautical Labs  
California Institute of Technology  
Pasadena, CA 91125  
(626) 395-4465

Dr. Arthur Lewis  
Aerospace Mechanics Division  
University of Dayton Research Institute  
300 College Park  
Dayton, OH 45469-0110  
(937) 229-4235  
FAX: 229-4251

Dr. Goang Liaw  
Department of Civil Engineering  
Alabama A&M University  
P.O. Box 367  
Normal, AL 35762  
(205) 851-5565

Dr. Timothy Lieuwen  
School of Aerospace Engineering  
Georgia Institute of Technology  
Atlanta, GA 30332-0150  
(404) 894-3041  
FAX: 894-2760  
tim.lieuwen@aerospace.gatech.edu

Dr. Mark A. Linne  
Division of Engineering  
Colorado School of Mines  
Golden, CO 80401  
(303) 273-3609  
FAX: 273-3278  
mlinne@mines.edu, mark.linne@forbrf.lth.se

Dr. Charles L. Liotta  
Department of Chemical Engineering  
Georgia Institute of Technology  
Atlanta, GA 30332-0100  
(404) 853-9344  
FAX: 894-6956

Dr. Lyle N. Long  
Department of Aerospace Engineering  
Pennsylvania State University  
233 Hammond Building  
University Park, PA 16802  
(814) 865-1172  
FAX: 865-7092  
lnl@psu.edu

Dr. Kevin Lyons  
Department of Mechanical and  
Aerospace Engineering  
North Carolina State University  
P.O. Box 7910  
Raleigh, NC 27695  
(919) 515-5293  
FAX: 515-7968  
lyons@eos.ncsu.edu

Dr. Bruce MacDonald  
Research Applications Division  
Systems Research Labs, Inc.  
2800 Indian Ripple Road  
Dayton, OH 45440-3696  
(513) 252-2706

Mr. Nick Makris  
SA-ALC/SFT  
Kelly AFB, TX 78241-5000  
AV945-8212  
FAX: 945-9964

Dr. David Mann  
U.S. Army Research Office  
P.O. Box 12211  
4300 South Miami Boulevard  
Research Triangle Park, NC 27709-2211  
(919) 549-4249  
DSN: 832-4249  
FAX: 549-4310  
dmann@arl.army.mil

Dr. Nagi Mansour  
Computational Fluid Mechanics  
Branch, RFT 202A-1  
NASA Ames Research Center  
Moffett Field, CA 94035  
(415) 604-6420

Dr. John Marek  
NASA Glenn Research Center  
21000 Brookpark Road  
Mail Stop 5-11  
Cleveland, OH 44135-3127  
(216) 433-3584  
FAX: 433-3000  
cecil.j.marek@lerc.nasa.gov

Dr. Jay Martin  
Engine Research Center  
University of Wisconsin, Madison  
1500 Engineering Drive  
Madison, WI 53706  
(608) 263-9460  
FAX: 262-6707  
martin@enr.wisc.edu

Dr. James McDonald  
Chemistry Division  
Naval Research Laboratory  
Code 6110  
Washington, DC 20375-5342  
(202) 767-3340  
DSN: 297-3340

Dr. A.M. Mellor  
Mechanical & Materials Engineering Dept.  
Vanderbilt University  
512 Kirkland Hall  
Nashville, TN 37240  
(615) 343-6214  
FAX: 343-6687

Dr. Lynn Melton  
Programs in Chemistry  
University of Texas, Dallas  
P.O. Box 830688  
Richardson, TX 75083-0688  
(972) 883-2913  
(972) 680-2163  
FAX: 883-2925  
melton@utdallas.edu

Dr. Suresh Menon  
School of Aerospace Engineering  
Georgia Institute of Technology  
270 Ferst Drive  
Atlanta, GA 30332-0150  
(404) 894-9126  
FAX: 894-2760  
suresh.menon@aerospace.gatech.edu



Dr. Hameed Metghalchi  
Mechanical, Industrial and  
Manufacturing Dept. 334SN  
Northeastern University  
360 Huntington Avenue  
Boston, MA 2115  
(617) 373-2973  
FAX: 373-2921  
metghal@coe.neu.edu

Dr. Michael M. Micci  
Department of Aerospace Engineering  
Pennsylvania State University  
233 Hammond Building  
University Park, PA 16802  
(814) 863-0043  
(814) 692-8751  
FAX: 865-7092  
micci@henry2.aero.psu.edu

Dr. Andrzej Miziolek  
Army Research Laboratory  
AMSRL-WT-PC  
Aberdeen Proving Ground, MD 21005-5066  
(410) 278-6157  
FAX: 278-6094  
miziolek@arl.army.mil

Dr. H.C. Mongia  
Manager, Combustion Technology  
GE Aircraft Engines  
One Neumann Way, M/D A404  
Cincinnati, OH 45215-6301  
(513) 243-2552  
FAX: 243-2538  
hukam.mongia@ae.ge.com

Dr. Arje Nachman  
AFOSR/NM  
4015 Wilson Boulevard, Room 713  
Arlington, VA 22203-1954  
(703) 696-8427  
DSN: 426-8427  
FAX: 696-8450  
arje.nachman@afosr.af.mil

Dr. Herbert Nelson  
Code 6110, Chemistry Division  
Naval Research Laboratory  
4555 Overlook Avenue, SW  
Washington, DC 20375-5342  
(202) 767-3686

Dr. Elaine Oran  
LCP&FD, Code 6404  
U.S. Naval Research Laboratory  
4555 Overlook Avenue, SW  
Washington, DC 20375-5344  
(202) 767-2960  
FAX: 767-4798  
oran@lcp.nrl.navy.mil

Dr. T.E. Parker  
Engineering Division  
Colorado School of Mines  
Golden, CO 80401-1887  
(303) 273-3657  
FAX: 273-3602  
tparker@mines.colorado.edu

Dr. Phillip H. Paul  
Sandia National Laboratories  
P.O. Box 969, MS 9051  
Livermore, CA 94551-9051  
(510) 294-1465  
FAX: 294-1012  
phpaul@sandia.gov

Dr. Lisa Pfefferle  
Department of Chemical Engineering  
Yale University  
New Haven, CT 06520-8286  
(203) 432-2222  
FAX: 432-7232  
pfefferle@htcre.eng.yale.edu

Dr. Emil Pfender  
Department of Mechanical Engineering  
The University of Minnesota  
125 Mechanical Engineering  
Minneapolis, MN 55455

Dr. Heinz G. Pitsch  
Department of Mechanical Engineering  
Stanford University  
Building 500, Room 500M  
Stanford, CA 94305-3035  
(650) 725-6635  
FAX: 725-7834  
h.pitsch@stanford.edu

Dr. Robert Pitz  
Department of Mechanical and  
Materials Engineering  
Vanderbilt University  
Nashville, TN 37235  
(615) 322-0209  
FAX: 343-8730  
pitzrw@ctrvan.vanderbilt.edu

Dr. S.B. Pope  
Department of Mechanical and  
Aerospace Engineering  
Cornell University  
Ithaca, NY 14853-7501  
(607) 255-4314  
FAX: 255-1222  
pope@mae.cornell.edu

Dr. David Pratt  
AFRL/VAS  
Building 45 Annex  
2130 Eighth Street, Suite 1  
Wright-Patterson AFB, OH 45433-7542  
(937) 255-5042  
DSN: 785-5042  
FAX: 656-7915  
david.pratt@va.af.mil

Dr. Martin J. Rabinowitz  
NASA Glenn Research Center  
21000 Brookpark Road, Mail Stop 5/10  
Cleveland, OH 44135-3191  
(216) 433-5847  
FAX: 433-5588  
marty@lerc.nasa.gov

Dr. Larry Rahn  
Sandia National Laboratories  
7011 East Avenue  
Mail Stop 9056  
Livermore, CA 94551-0969  
(510) 294-2091  
FAX: 294-2276  
rahn@sandia.gov

Dr. Mohan K. Razdan  
Rolls-Royce Company  
P.O. Box 420  
Speed Code T10B  
Indianapolis, IN 46206-0420  
(317) 230-6404  
FAX: 230-3691  
mohan.razdan@rolls-royce.com

Mr. Robert Reed  
Sverdrup Technology, Inc.  
AEDC  
1099 Avenue C  
Arnold AFB, TN 37389-9013  
(615) 454-4648  
DSN: 340-4648  
FAX: 454-6317

Dr. Rolf D. Reitz  
Mechanical Engineering Department  
University of Wisconsin  
1500 Johnson Drive  
Madison, WI 53706  
(608) 262-0145  
FAX: 262-6717

Col. Steven Reznick  
AFOSR/CD  
4015 Wilson Boulevard, Room 713  
Arlington, VA 22203-1954  
(703) 696-7555  
DSN: 426-7555  
FAX: 696-9556  
steven.reznick@afosr.af.mil

Dr. Kyung T. Rhee  
Department of Mechanical and  
Aerospace Engineering  
Rutgers, The State University of NJ  
Piscataway, NJ 08854-0909  
(732) 445-3651  
ktrhee@jove.rutgers.edu

Dr. James Riley  
Mechanical Engineering Department  
University of Washington  
Seattle, WA 98195  
(206) 543-5347  
73671.737@compuserve.com

Dr. William Roberts  
Department of Mechanical and  
Aerospace Engineering  
Box 7910  
North Carolina State University  
Raleigh, NC 27695-7910  
(919) 515-5294  
FAX: 515-7968  
wrobert@eos.ncsu.edu

Mr. Gerald A. Roffe  
GASL  
77 Raynor Avenue  
Ronkonkoma, NY 11779

Dr. W.M. Roquemore  
AFRL/PRTS  
1790 Loop Road, N  
Building 490  
Wright-Patterson AFB, OH 45433-7103  
(937) 255-6813  
DSN: 785-6813  
FAX: 656-4570  
melr@ward.appl.wpafb.af.mil

Dr. Daniel Rosner  
Department of Chemical Engineering  
Yale University  
New Haven, CT 06520-8286  
(203) 432-4391  
FAX: 432-7232  
daniel.rosner@yale.edu

Dr. John Ross  
Department of Chemistry  
Stanford University  
Stanford, CA 94305-3032  
(650) 723-9203

Dr. Gabriel Roy  
Mechanics Division, Code 1132  
Office of Naval Research  
800 North Quincy Street  
Arlington, VA 22217-5660  
(703) 696-4406  
DSN: 426-4406  
FAX: 696-0934  
roy@ocnr-hq.navy.mil

Dr. Robert C. Ryder  
Flow Parametrics, LLC  
15 Debra Drive  
Bear, DE 19701  
(302) 838-7368  
FAX: 838-7369  
rryder@flowparametrics.com

Mr. Kurt Sacksteder  
NASA Glenn Research Center  
21000 Brookpark Road, MS 500-217  
Cleveland, OH 44135  
(216) 433-2857

Dr. Michael Salkind  
President, Ohio Aerospace Institute  
22800 Cedar Point Road  
Cleveland, OH 44142  
(440) 962-3001  
FAX: 962-3120  
michaelsalkind@oai.org

Dr. Mohammad Samimy  
Mechanical Engineering Department  
Ohio State University  
206 West 18th Street  
Columbus, OH 43210-1107  
(614) 422-6988  
(614) 848-9439 (2<sup>nd</sup> phone)  
FAX: 292-3163  
msamimy@magnus.acs.ohio-state.edu

Dr. G.S. Samuelsen  
Department of Mechanical and  
Aerospace Engineering  
University of California  
Irvine, CA 92697-3975  
(949) 824-5468

Dr. Lakshmi Sankar  
School of Aerospace Engineering  
Georgia Institute of Technology  
Atlanta, GA 30332  
(404) 894-3014

Dr. Domenic Santavicca  
Propulsion Engineering Research Center  
Pennsylvania State University  
106 Research Building East - Bigler Road  
University Park, PA 16802-2320  
(814) 863-1863

Dr. R.J. Santoro  
Department of Mechanical Engineering  
Pennsylvania State University  
University Park, PA 16802-2320  
(814) 863-1285  
FAX: 865-3389  
rjs2@email.psu.edu

Dr. Sutanu Sarkar  
Department of Applied Mechanical  
and Engineering Science, MC 0411  
University of California  
La Jolla, CA 92093-0411  
(858) 534-8243  
FAX: 534-7599  
ssarkar@ucsd.edu

Dr. John Schaefer  
Energy and Environmental Division  
Acurex Corporation  
555 Clyde Avenue  
P.O. Box 7555  
Mountain View, CA 94039

Dr. Frederick Schauer  
AFRL/PRTS  
1790 Loop Road, N  
Building 490, Room 104  
Wright-Patterson AFB, OH 45433-7103  
(937) 255-6462  
DSN: 785-6462  
FAX: 255-1125  
frederick.schauer@wpafb.af.mil

Dr. Peter Schihl  
Propulsion Systems Division  
USA Tank Automotive Command  
ATTN: AMSTA-TR-R, MS 121  
Warren, MI 48397-5000  
FAX: 574-5054  
schihlp@tacom.army.mil

Dr. Lyle Schwartz  
AFOSR/CC  
4015 Wilson Boulevard, Room 713  
Arlington, VA 22203-1954  
(703) 696-8457  
DSN: 426-7551  
lyle.schwartz@afosr.af.mil

Dr. Ernest Schwarz  
Propulsion Systems Division  
USA Tank-Automotive Command  
ATTN: DRSTA-RGD  
Warren, MI 48397-5000  
(810) 574-5656  
FAX: 574-5054  
schwarze@cc.tacom.army.mil

Mr. Lee Scuderi  
McDonnell Douglas Aerospace  
P.O. Box 516  
St. Louis, MO 63166-0516

Dr. Jerry Seitzman  
School of Aerospace Engineering  
Georgia Institute of Technology  
Atlanta, GA 30332-0150  
(404) 894-0013  
FAX: 894-2760  
jerry.seitzman@ae.gatech.edu

Dr. Kalyanasundaram Seshadri  
Center for Energy and Combustion Research,  
0407  
University of California  
La Jolla, CA 92093-0407  
(619) 534-4876  
seshadri@ames.ucsd.edu

Dr. Robert Shaw  
Division of Chemical and Biological Sciences  
U.S. Army Research Office  
Research Triangle Park, NC 27709-2211  
(919) 549-0641

Dr. Adam Siebenhaar  
Aerojet Propulsion Division  
P.O. Box 13222  
Sacramento, CA 95813-6000

Dr. Gupreet Singh  
U.S. Department of Energy  
1000 Independence Avenue, S.W.  
Washington, DC 20585  
(202) 586-2333  
FAX: 586-4166  
gupreet.singh@hq.doe.gov

Dr. William Sirignano  
Department of Mechanical and  
Aerospace Engineering  
University of California  
Irvine, CA 92697-3975  
(949) 824-3700  
FAX: 824-3773  
sirignan@uci.edu

Mr. Davey Smith  
Northrop Grumman Corporation  
B-2 Division Dayton Office  
2850 Presidential Dr., Suite 100  
Fairborn, OH 45324

Dr. Gregory Smith  
Department of Chem Kinetics  
SRI International  
333 Ravenswood Avenue  
Menlo Park, CA 94025-3493  
(415) 859-3496

Dr. James Smith  
Department of Chemical Engineering  
University of Alabama in Huntsville  
Huntsville, AL 35899  
(256) 824-3594  
smithje1@uah.edu

Dr. Kenneth A. Smith  
Department of Chemical Engineering  
Massachusetts Institute of Technology  
Room 66-540  
Cambridge, MA 02139  
(617) 253-1973  
FAX: 253-2701  
kas@mit.edu

Dr. Judi Steciak  
University of Idaho, Boise  
800 Park Boulevard  
Boise, ID 83712-7742  
(208) 364-4080  
FAX: 387-1246  
jsteciak@uidaho.edu

Dr. David Stewart  
Department of Theoretical and Applied  
Mechanics  
University of Illinois  
Urbana, IL 61801

Dr. Geoffrey J. Sturgess  
Innovative Scientific Solutions, Inc.  
2786 Indian Ripple Road  
Dayton, OH 45440-3638  
(937) 252-2706  
FAX: 656-4652  
gsturgess@aol.com

Dr. B. Sturtevant  
Engineering and Applied Science Dept.  
California Institute of Technology  
Pasadena, CA 91125

Dr. G. Sullins  
Applied Physics Laboratory  
Johns Hopkins University  
Johns Hopkins Road  
Laurel, MD 20707-6099  
(301) 953-5000

Dr. Rodney Tabaczynski  
Director, Power Train Research Lab  
Ford Motor Research Laboratory  
3623 Scientific Research Lab  
P.O. Box 2053  
Dearborn, MI 48121-2053  
(313) 322-8930

Dr. Douglas Talley  
AFRL/PRSA  
10 East Saturn Boulevard  
Edwards AFB, CA 93524-7660  
(661) 275-6174  
DSN: 525-6174  
FAX: 275-6245  
douglas.talley@ple.af.mil

Dr. Jefferson W. Tester  
M.I.T. Energy Laboratory  
Massachusetts Institute of Technology  
Room E40-455  
Cambridge, MA 02139  
(617) 253-3401  
FAX: 253-8013  
testerel@mit.edu

Dr. Julian Tishkoff  
AFOSR/NA  
4015 Wilson Boulevard, Room 713  
Arlington, VA 22203-1954  
(703) 696-8478  
DSN: 426-8478  
FAX: 696-8451  
julian.tishkoff@afosr.af.mil

Dr. Chenning Tong  
Mechanical Engineering Department  
Clemson University  
248 Fluor Daniel EIB  
Clemson, SC 29634-0921  
(864) 656-7225  
FAX: 656-4435  
ctong@ces.clemson.edu

Dr. Michael Trenary  
Department of Chemistry  
The University of Illinois  
Chicago, IL 60680

Dr. James Trolinger  
MetroLaser  
2572 White Road  
Irvine, CA 92614  
(949) 553-0688  
FAX: 553-0495  
jtrolinger@vmsa.oac.uci.edu

Dr. Timothy Troutt  
Department of Mechanical Engineering  
Washington State University  
Pullman, WA 99164-2920

Dr. Gretar Tryggvason  
Department of Mechanical Engineering  
& Applied Mechanics  
The University of Michigan  
2350 Hayward, Room 2250  
Ann Arbor, MI 48109-2125  
(734) 763-1049  
FAX: 764-4256  
gretar@umich.edu

Dr. Frank Tully  
U.S. Department of Energy  
19901 Germantown Road, SC-141  
Germantown, MD 20874  
(301) 903-5998  
frank.tully@science.doe.gov

Dr. A.D. Vakili  
Space Institute  
University of Tennessee  
Tullahoma, TN 37388

Dr. Mark Valco  
Propulsion Directorate  
Army Research Laboratory, MS 49-1  
NASA Glenn Research Center  
Cleveland, OH 44135-3127  
(216) 433-3717  
FAX: 433-2182  
aamark@lims01.lerc.nasa.gov

Dr. David Van Wie  
Applied Physics Laboratory  
The Johns Hopkins University  
11100 Johns Hopkins Road  
Laurel, MD 20723-6099  
(240) 228-5194  
FAX: 228-5850  
david.vanwie@jhuapl.edu

Dr. Ian Waitz  
Department of Aeronautics and Astronautics  
Massachusetts Institute of Technology  
77 Massachusetts Avenue, Bldg. 33-207

Cambridge, MA 02139-4307  
(617) 253-0218  
FAX: 258-7566  
iaw@mit.edu

Dr. Joe Wander  
AFRL/MLQL  
139 Barnes Drive, Suite 2  
Tyndall AFB, FL 32403-5323  
(904) 283-6240  
DSN: 523-6240  
FAX: 283-6064  
jwander@mlq.af.mil

Dr. Hai Wang  
Department of Mechanical Engineering  
University of Delaware  
Newark, DE 19716  
(302) 831-2421  
FAX: 831-3619  
hwang@me.udel.edu

Dr. Zhicheng Wang  
Clark Atlanta University  
223 James P. Brawley Drive, SW  
Atlanta, GA 30314  
(404) 880-6125  
FAX: 880-6615  
zhicheng\_wang@hotmail.com

Dr. Charles Westbrook  
Lawrence Livermore National Laboratories  
P.O. Box 808  
Livermore, CA 94551  
(925) 422-4108  
FAX: 422-2644  
westbrook1@llnl.gov

Dr. Phillip R. Westmoreland  
Department of Chemical Engineering  
University of Massachusetts  
Amherst, MA 01003  
(413) 545-1750  
(413) 545-2507  
FAX: 545-1647  
westm@ecs.umass.edu

Dr. James Whitelaw  
Department of Mechanical Engineering  
Imperial College of Science and Technology  
London SW7 2BX, UK

Dr. Forman Williams  
Center for Energy and Combustion Research,  
0310  
University of California  
La Jolla, CA 92093-0310  
(858) 534-5492  
(858) 534-4285  
FAX: 534-7720  
fwilliams@ucsd.edu

Dr. Skip Williams  
AFRL/VSXT  
29 Randolph Street  
Hanscom AFB, MA 01731  
(781) 377-2076  
FAX: 377-7091  
skipw@plh.af.mil

Dr. Bernard T. Wolfson  
Wolfson Associates International  
4797 Lake Valencia Boulevard West  
Palm Harbor, FL 33563  
(813) 786-3007

Dr. Mary J. Wornat  
Department of Chemical Engineering  
Louisiana State University  
South Stadium Drive  
Baton Rouge, LA 70803  
(225) 578-7509  
FAX: 578-1476  
mjwornat@lsu.edu

Dr. J.M. Wu  
Space Institute  
University of Tennessee  
Tullahoma, TN 37388

Dr. Vigor Yang  
Propulsion Engineering Research Center  
The Pennsylvania State University  
111 Research Building East  
University Park, PA 16802-2320  
(814) 863-1502  
FAX: 865-4784  
vigor@arthur.psu.edu

Dr. Richard Yetter  
Department of Mechanical and Nuclear  
Engineering  
Pennsylvania State University  
State College, PA 16802  
(814) 863-6375  
rayetter@psu.edu

Dr. Joseph Zelina  
AFRL/PRTS  
1790 Loop Road, N  
Building 490, Room 109  
Wright-Patterson AFB, OH 45433-7251  
(937) 255-7487  
DSN: 785-7487  
joseph.zelina@wpafb.af.mil

Dr. Ben Zinn  
School of Aerospace Engineering  
Georgia Institute of Technology  
Atlanta, GA 30332-0150  
(404) 894-3033  
FAX: 894-2760  
ben.zinn@aerospace.gatech.edu